# Design and Development of Hybrid Nanomaterials for Efficient Photocatalysis

*A dissertation submitted in partial fulfilment of requirements for the degree of*

**Doctor of Philosophy**

**By**

**Thongam Debika Devi**

(Reg. No. 176151105)


**School of Energy Science and Engineering**

**Indian Institute of Technology Guwahati**

**Guwahati- 781039, Assam, India**

# *Dedication*

*I proudly dedicate this thesis to my loving parents and brothers who have supported me day and night which made me able to get this honour.*

School of Energy Science and Engineering
Indian Institute of Technology Guwahati

## Certificate

This is to certify that the research work incorporated in this thesis entitled, "**Design and Development of Hybrid Nanomaterials for Efficient Photocatalysis**" is carried out by me under the guidance of **Dr. Harsh Chaturvedi** at the School of Energy Science and Engineering, Indian Institute of Technology Guwahati, Guwahati, Assam, India as the partial fulfillment for the award of Doctor of Philosophy. In keeping with the general practice of reporting scientific observations, due acknowledgments have been made wherever the work described is based on the findings of the investigations. I further declare that this work has not been submitted in part or full to any other university or institute for the award of any degree or diploma.

**Thongam Debika Devi**
Reg. No. 176151105,
School of Energy Science and Engineering,
Indian Institute of Technology Guwahati
Guwahati-781039, Assam, India

# भारतीय प्रौद्योगिकी संस्थान गुवाहाटी

# Indian Institute of Technology Guwahati

North Guwahati, Guwahati,
PIN- 781039, ASSAM, INDIA
Phone: +91 361 2583000 Extn 2702, 2582702
Fax: +91 3612690 762 (Institute), 2582749 (Department)


## Certificate

---

This is to certify that the thesis entitled, "**Design and Development of Hybrid Nanomaterials for Efficient Photocatalysis**" is submitted by **Thongam Debika Devi (Reg. No. 176151105),** a student of the School of Energy Science and Engineering, Indian Institute of Technology Guwahati, Guwahati, Assam, India as the partial fulfilment for the award of Doctor of Philosophy under the guidance and supervision of Dr. Harsh Chaturvedi (Late). The research work documented in this thesis has not been submitted in part or full to any other university or institute for the award of any degree or diploma.


**Member Secretary, SPPC**

**Dr. Pankaj Kalita**

Associate Professor,

School of Energy Science and Engineering,

Indian Institute of Technology Guwahati

Guwahati-781039, Assam, India

**Dr. Harsh Chaturvedi (Late)**

Assistant Professor,

School of Energy Science and Engineering,

Indian Institute of Technology Guwahati

Guwahati-781039, Assam, India

# Acknowledgment

With another sunrise added to my calendar, I still dream, run, and hope for the best every morning. Although 24 hours seem short, I still find time to enjoy every second and sing my song “I Have a Dream and a Song to Sing”. With those aborted fragmented dreams and failed experiments, I still stand tall and firm by the grace of God.

Through this piece of paper, I feel delighted to express my heartfelt gratitude and appreciation to my dear ones— family, guru, friends, and lab-mates who have played a part in this journey of five years. They say parents are the first Gods whom we can see, so first and foremost, I would like to bow my head to the only living God, my parents who gave me the wings to fly with freedom, a ground to stand and always by my side. Secondly, I would like to express my sincere and profound gratitude towards my supervisor Dr Harsh Chaturvedi for giving me the chance to work with him in his lab. His constant instruction, scientific guidance, positive responses, countless opportunities, and provision have made this dissertation possible. I feel fortunate to have him as my supervisor who has provided sovereignty in my research, believing in me and his guidance to mend at times of lost motivation, and for his endless support and motivation during my research work. I am also grateful to Dr. Pankaj Kalita, my academic supervisor for his kind assistance and support, without whose effort my PhD would be incomplete. In addition, I am extremely appreciative of the efforts he put forth to conduct the vital viva voce and other necessary procedures for the successful completion of this journey.

I would like to extend my gratitude to my doctoral committee Prof. Pranab Goswami, Prof. Vaibhav V. Goud, and Dr Akshai Kumar Alape Seetharam for their insightful observations and suggestions. Their valuable inputs, advice, and comments provided a space for improving my research in many areas.

I express my appreciation and gratitude to the head, technical staff, non-technical staff, and authorities of the School of Energy Science and Engineering for providing the research and analytical facilities required for my research work. I am thankful to the Ministry of Education (MoE), Govt. of India, for the financial assistance in the form of a scholarship to pursue my doctoral degree. Further, I owe an immense debt of gratitude to the authorities of Central Instruments Facility (CIF), their staff particularly, and the student operators for helping in my

sample analysis. These facilities have made my doctoral thesis possible to complete. I also extend my gratitude to the Centre for Nanotechnology, Department of Chemistry, Chemical Engineering, and Department of Physics for providing the facilities. I am also thankful to the academic affairs, student affairs, and finance sections of IIT Guwahati for their kind help and advice in their respective roles.

I am fortunate to be able to have my friends and lab-mates to share my achievements and this journey, for their love, patience, and understanding. I thank my friends for their constant moral support, research discussions, motivation, and help in crucial times. Without our chai breaks and runaway trips, this PhD journey would have been a difficult one. I also thank my childhood best friend who is very supportive at every step and overwhelms me with positive vibes, sharing happy and memorable moments. I extend my thanks to other friends who have helped me with research work and creating happy memories. Their unwavering support has been my rock, and I am forever grateful for their belief in me.

Last but not least, I want to convey my heartfelt gratitude to everyone who has contributed directly or indirectly to this work and the journey itself. Your contributions, no matter how modest, were not overlooked and are highly appreciated.

In the end, I bow my head towards the almighty God for the blessings that have bestowed upon me in showing me the correct way, giving me the strength to chase my dream, and for being all in all happy, with failure, and success.

# Abstract

Water, a universal solvent, is our life and its degradation in quality has imposed a major threat to the health and environment due to the disposal of untreated wastewater directly or indirectly to the water bodies with emerging contaminants. Photocatalytic advanced oxidation processes (AOP) using reactive oxygen species ROS ($OH^-$, •OH, $H_2O_2$, $HO_2$•, $O_2$•$^-$, $O_2^{2-}$) provide complete removal of these recalcitrant and persistent pollutants by using nanomaterials under an activating source. The light-matter interaction and charge carrier transfer dynamics in a photosystem play a major role in AOP. Although charge transfer plays a significant role in performance manipulation, other main controllable photocatalyst properties— engineering catalyst composition, shape & size, surface structures, electronic properties, using catalyst support, etc.— all possess roughly equal significance for all catalytic applications. However, its real-time application is limited by the use of high-power light sources to trigger the reaction system and its limited performance. Thus, the main goal of this thesis work is to understand and address these bottlenecks: (a) designing photocatalyst to harvest natural light, (b) developing heterostructure photocatalyst for enhanced efficiency by developing interfacial charge transfer, and (c) studying and discovering ways to enhance charge transfer by manipulating heterostructure photocatalyst responsive to natural sunlight.

The chemical synthesis approach and the green synthesis method were utilized in the first stage of the research to determine an effective way of synthesizing ZnO nanoparticles. Although the green synthesis method is environmentally friendly and cheap, the synthesized nanoparticles are found to have a zinc-biomolecule complex which becomes ineffective for further use. In the chemical synthesis method, the use of various zinc precursors and synthesis methods affects the nanoparticle properties, which in turn affects their photocatalytic performance. The ZnO nanoparticle synthesized using a zinc sulphate source and precipitation method provided the smallest crystallite size and ZnO nanoparticles synthesized using an acetate source and hydrothermal method exhibited the largest crystallite size nanoparticles. Also, to investigate the nature of ZnO in different solvents and synthesis techniques, mainly DMF, solvothermal, or precipitation methods, various ZnO nanoparticles were synthesized differing in physical as well as chemical properties like; crystallinity, morphology, etc. Depending on the solvent properties, unique morphological

structures- cauliflower, hydrangea, and petals are obtained with the variation in synthesis medium and methods. This part of the study aims to focus on the three main hurdles in photocatalytic AOP for water treatment: (i) designing natural sunlight active photocatalyst, (ii) replacing the triggering source of UV or artificial sunlight with natural sunlight, (iii) reusing of face-mask fabric as a substrate for anchoring photocatalyst thus replacing the slurry system. Our work also emphasized on developing a novel way of reusing the ever-increasing face-mask disposal because of the coronavirus pandemic. DMF acts as a structure-directing agent forming petals-like structures acting as the building block for flower formation by self-assembly and orientated-attachment process because of the DMA's ability to bind with positive charge $Zn^{2+}$. The ZnO photocatalysts-coated face-mask fabric is used as the floating photocatalyst for RhB degradation under natural sunlight illumination, thus removing the additional process of the photocatalyst retrieval process. A similar degradation efficiency of 91% dye removal in 100 min is obtained as compared with the slurry system triggered by UV light illumination of 99% by the ZnO samples prepared in DMF solvent. ZnO photocatalysts synthesized using DMF solvent show better performance and degradation rate due to the synergy of the formation of surface defects, oxygen interstitial, open sites, and higher surface exposure by the petal-like structures. The synergy of the defect formation, petals-like morphologies, and larger pore size and volume resulted in exhibiting higher degradation efficiencies under UV and sunlight irradiation.

The charge transfer dynamics and interaction between ZnO and three different electronically different SWCNTs; metallic-SWCNT (m-SWCNT), semiconducting-SWCNT (s-SWCNT), and pristine-SWCNTs (p-SWCNT that contains both metallic and semiconduction SWCNT) are studied through the critical coagulation concentration (CCC). The physicochemical and morphological properties of the ZnO functionalized SWCNTs: m-SWCNT+ZnO, s-SWCNT+ ZnO, and p-SWCNT+ZnO are analyzed by advanced characterization techniques. In the functionalization and composites formation, ZnO sub-nano particles are attached and anchored on SWCNT surfaces, thereby forming a heterojunction interface, exhibiting distortion-dislocation and strain. Evidence of charge transfer between SWCNT and ZnO is observed with an increase in charge carrier lifetime from 3.31 ns (ZnO) to 4.76 ns (s-SWCNT+ZnO) and an increase in metallicity is seen in s-SWCNT+ZnO. Due to the variation in dielectric values and electronic properties of SWCNTs, the CCC values that indicate optimum interaction between SWCNT and ZnO coagulant obtained have differed— m-SWCNT (1.9E-4), s-SWCNT (3.4E-4), and p-SWCNT

(2E-4). The study of interaction and charge transfer dynamics between different SWCNTs and ZnO are extended to the ZnO nanoparticles self-assembled onto the SWCNT surface via a chemical synthesis method where SWCNTs act as an anchor for ZnO nanoparticles. In comparison to the bare ZnO, SWCNTs induce structurally negligible changes on the SWCNT/ZnO heterostructure nanoparticles. The broad absorption PL emission spectra and ESR analyses show the presence of defects in heterostructures that are attributed to interstitials and oxygen/zinc vacancies, as well as charge transfer. These defect sites are also generated by the liberation of DMF molecules bound to the ZnO surface, which act as a structure-directing agent and surfactant. These defects are found to enhance the photocatalytic degradation efficiency of RhB by achieving complete degradation in 100 mins under natural sunlight by using face-mask fabric coated with ZnO and SWCNT/ZnO heterostructures. Due to charge transfer and separation in the SWCNT/ZnO heterojunction interface, the charge carrier lifetime increases. This increase in charge carrier lifetimes enhances RhB degradation, and the highest degradation rate of 0.0278 $min^{-1}$ is obtained by using m-SWCNT/ZnO-coated floating fabrics. By showing 99% degradation efficiency in direct sunlight after the $5^{th}$ cycle, the generated samples—ZnO and SWCNT/ZnO heterostructures—are discovered to be stable and recyclable. After being exposed to UV radiation for five cycles, the samples remain stable and recyclable with no deterioration in efficiency. OH• radicals and holes ($h^+$) were discovered to play important roles in the photocatalytic degradation of RhB using the SWCNT/ZnO samples. Concerning the band edge locations with the oxidation and reduction potentials of ROS for the AOP, potential reactions and charge transfer mechanisms between ZnO and SWCNT in the SWCNT/ZnO heterostructure are revealed.

In continuation to enhance the charge transfer dynamics and reduce exciton recombination, for an approach to enhance the charge carrier's lifetime, other nanomaterials are incorporated and doped with the pristine ZnO semiconductor oxide nanoparticles. To explore further dependence of photocatalytic performance on the charge transfer dynamics and pathways on heterostructure interface, Type I ZnO/$Fe_3O_4$ and Type II ZnO/$TiO_2$ composite heterostructures are prepared and analyzed. Type II ZnO/$TiO_2$ composite heterostructures show greater photocatalytic performance with a photodegradation rate of 0.014 $min^{-1}$ as compared to that of Type I ZnO/$Fe_3O_4$ due to the presence of defects and faster electron diffusion from the ZnO to the $TiO_2$ with charge carrier lifetime of 7.125 ns. In Type I ZnO/$Fe_3O_4$ heterostructure photocatalyst, a lower photodegradation rate of 0.011 $min^{-1}$ is shown due to the involvement of one surface in the photocatalytic redox

reaction. The larger energy band level difference between ZnO and $Fe_3O_4$ in the heterojunction interface might also contribute to slowing down the charge transfer diffusion in the heterostructure interface giving rise to a lower charge carrier lifetime of 6.236 ns.

Further, the dependence of charge transfer pathways on the photocatalytic performance is studied using the g-$C_3N_4$/ZnO heterojunction interface that showed the Z-scheme charge transfer pathway. Photocatalytic performance by the single photocatalyst g-$C_3N_4$, ZnO, binary photocatalyst g-$C_3N_4$/ZnO, ZnO/SWCNT, g-$C_3N_4$/SWCNT, and ternary photocatalyst g-$C_3N_4$/ZnO/SWCNT are also investigated. The synthesized photocatalysts showed responsiveness to natural sunlight and were used for the photocatalytic degradation of RhB with a detailed analysis of the charge transfer mechanisms in the heterojunction interface for the effective generation of ROS. The energy band structures and positions of the individual photocatalyst g-$C_3N_4$ and ZnO were estimated using the Tauc plot study and UPS spectra. In the photocatalytic degradation of RhB under natural sunlight, the addition of IPA enhances the efficiency from 95% to 99%. The degradation efficiency of g-$C_3N_4$+$H_2O_2$ is higher as compared to that of bare g-$C_3N_4$. In the case of ZnO photocatalyst, with the addition of IPA and $H_2O_2$ into the reaction medium, the degradation efficiencies decreased from 82% to 36% and 46% respectively. With the formation of g-$C_3N_4$/ZnO heterojunction interface, Z-scheme charge transfer pathways are formed based on the band edge positions. In the Z-scheme charge transfer in g-$C_3N_4$/ZnO heterojunction interface, photogenerated $e^-$s and $h^+$s played a crucial role in the g-$C_3N_4$ and ZnO respectively for the photocatalytic degradation of RhB under natural sunlight. This reporting degradation experiment method exempted the use of an external triggering light source and continuous stirring process during the reaction process, thus overcoming the energy consumption setback and reducing cost consumption while using cheap and less toxic photocatalysts— ZnO and carbon-based photocatalysts.

# Contents

# List of Figures

# List of Tables

# Nomenclature

## Abbreviation

| | |
|---|---|
| **AOP** | Advanced Oxidation Processes |
| **BET** | Brunauer–Emmett–Teller |
| **BJH** | Barrett-Joyner-Halenda |
| **CB** | Conduction Band |
| **CBM** | Conduction Band Minima |
| **CCC** | Critical Coagulation Concentration |
| **DCA** | Diffusion-Controlled Aggregation |
| **DEG** | Diethylene Glycol |
| **DI $H_2O$** | Deionization Water |
| **DLVO** | Derjaguin−Landau−Verwey−Overbeek |
| **DMA** | Dimethylacetamide |
| **DMF** | N, N-Dimethyl formamide |
| **EDL** | Electric Double Layer |
| **EDX** | Energy Dispersive X-ray |
| **EG** | Ethylene Glycol |
| **ESR** | Electron Spin Resonance |
| **FESEM** | Field Emission Scanning Electron Microscopy |
| **FETEM** | Field Emission Transmission Electron Microscope |
| **FTIR** | Fourier Transform Infrared Spectrometer |
| **FWHM** | Full Widhth Half Maxima |
| **HRTEM** | High-Resolution Transmission Electron Microscope |
| **IPA** | Isopropyl Alcohol |
| **JCPDS** | Joint Committee on Powder Diffraction Standards |
| **m-SWCNTs** | metallic- Single-Walled Carbon Nanotubes |
| **NBE** | Near band edge |
| **NTs** | Nanotubes |
| **PL** | Photoluminescence |

| | |
|---|---|
| **p-SWCNTs** | pristine- Single-Walled Carbon Nanotubes |
| **RBM** | Radial Breathing Mode |
| **RCA** | Reaction-Controlled Aggregation |
| **RhB** | Rhodamine B |
| **ROS** | Reactive Oxygen Species |
| **SAED** | Selected Area Electron Diffraction |
| **SH** | Schulze-Hardy rule |
| **SHE** | Standard Hydrogen Electrode |
| **SSP** | Size-Strain Plot |
| **s-SWCNTs** | semiconducting- Single-Walled Carbon Nanotubes |
| **SWCNTs** | Single-Walled Carbon Nanotubes |
| **TEM** | Transmission Electron Microscope |
| **TRPL** | Time-resolved Photo Luminescense |
| **UPS** | Ultraviolet Photoelectron Spectroscopy |
| **UV** | Ultra Violet |
| **UV-Vis** | Ultra Violet-Visible |
| **VB** | Valence Band |
| **VBM** | Valence Band Maxima |
| **XPS** | X-ray photoelectron spectroscopy |
| **XRD** | X-Ray Diffraction |

## Notations

| | | | |
|---|---|---|---|
| **°C** | Degree Celsius | **ml** | Milli litre |
| **$\bullet O_2^-$** | Superoxide Anion Radical | **mM** | Milli molar |
| **Å** | Angstrom | **μm** | Micro metre |
| **am** | Ante meridiem | **nm** | Nanometre |
| **cc/g** | Cubic Centimetre Per Gram | **ns** | Nanosecond |
| **cm** | Centimetre | **$OH^-$** | Hydroxyl Ion |
| **$C_t$** | Concentration at Time t | **OH•** | Hydroxyl Radical |
| **d-spacings** | Interplaner spacing | **pH** | Potential of Hydrogen |
| **$e^-$** | Electron | **pm** | Post meridiem |

| | | | |
|---|---|---|---|
| **$E_{CB}$** | Conduction Band Edge Positions | **ppm** | Parts per million |
| **$E_{CBM}$** | Energy of conduction band minima | **$R^2$** | correlation value |
| **$E_e$** | Energy of free electron | **rpm** | Rotations per minute |
| **$E_g$** | Energy Bandgap | **$S_{11}$** | first-order optical transitions for semiconducting-SWNTs |
| **$E_{VB}$** | Valence band edge positions | | |
| **$E_R$** | Repulsive electrostatic repulsion | **$S_{22}$** | second-order optical transitions for semiconducting-SWNTs |
| **eV** | Electron volt | **$S_{33}$** | third-order optical transitions for semiconducting-SWNTs |
| **$E_{VBM}$** | Energy valence band maxima | **t** | Time |
| **gm** | Gram | **V** | Volt |
| **h** | | **W** | Watt |
| **$h^+$** | Holes | **ε** | Dielectric constant |
| **$HO_2$•** | Hydroperoxyl Radical | **$E_H$** | High Binding Energy Cut Off |
| **hr** | Hour | **$E_L$** | Low Binding Energy Cut Off |
| **$I_D$** | D-band intensity | **$E_F$** | Fermi Energy |
| **$I_{G-}$** | $G^-$ band intensity | | |
| **$I_{G+}$** | $G^+$ band intensity | | |
| **klux** | Kilo lux | | |
| **k** | Degradation rate constant | | |
| **l** | litre | | |
| **$M_{11}$** | First-order optical transitions for metallic-SWNTs | | |
| **$m^2/g$** | square meter per gram | | |
| **$M_{22}$** | second-order optical transitions for metallic-SWNTs | | |
| **min** | Minute | | |

## Sample naming

| | |
|---|---|
| **$ZnO_{sa}$** | ZnO synthesised from zinc sulphate source with aloe vera extracts |
| **$ZnO_{aa}$** | ZnO synthesised from zinc acetate source with aloe vera extracts |
| **$ZnO_{sl}$** | ZnO synthesised from zinc sulphate source with lemon extracts |
| **$ZnO_{al}$** | ZnO synthesised from zinc acetate source with lemon extracts |
| **$ZnO_{dds}$** | ZnO synthesised using DEG solvent with solvothermal method |
| **$ZnO_{ddp}$** | ZnO synthesised using DEG solvent with precipitation method |
| **$ZnO_{DDp}$** | ZnO synthesised using DMF solvent with precipitation method |
| **$ZnO_{Dws}$** | ZnO synthesised using DMF+$H_2O$ solvent with solvothermal method |
| **$ZnO_{Dwp}$** | ZnO synthesised using DMF+$H_2O$ solvent with precipitation method |
| **SWCNT+ZnO** | SWCNT and ZnO composites prepared with sonication method |
| **SWCNT/ZnO** | ZnO nanoparticles self-assembled onto the SWCNT surfaces |

# Chapter 1

# Introduction and Literature Review

In today's millennium, the demand for catalyst material is soaring sky-high for its crucial importance and contribution. It is impossible to picture a world without a catalyst for its tremendous involvement in industries, material decompositions, chemical reactions, fuel generations and we human beings are run by catalyst activities called enzymes. Due to the limited resources of fossil fuels obtainable worldwide, catalyst materials have been playing a major role in minimizing energy consumption in the processes of converting inputs to outputs easily, efficiently, and effectively. Some remarkable applications of photocatalysts include water splitting,[1] conversion of solar energy into light using photovoltaics/ solar cells,[2] transforming harmful gases into reusable fuels like $CO_2$ to methanol,[3] water treatment and purification,[4] photochromic glasses,[5] generation of green fuels,[6] self-cleaning glasses,[7] GHGs capturing cement,[8] hydrogen gas production,[9] and so forth[10,11]. Therefore, due to the increasing rate of pollution of water/ air/ food, etc., the use of advanced catalyst nanomaterial to mitigate problems is becoming a focal point in this 21$^{st}$ century.

The exploration of catalyst materials and methods or activities to improve existing catalytic mechanisms has been attracting major attention but is believed to have grown into maturation (in lab-scale implementations). Some desirable properties of photocatalyst nanomaterials are high selectivity, easy separation, mass production, recyclability, solubility, applicability on a large scale, desirable reaction conditions, stability, cost-effectiveness, bio-compatibility, reproducibility, etc. which assist in evolving low-grade catalyst to highly efficient hybrid catalyst. Among these, researchers focus on the four most important aspects: activity, selectivity, stability, and toxicity. As an approach for hybrid photocatalyst, enzymes/ homogeneous catalyst is anchored to the heterogeneous catalyst, giving a unified advantage of the high selectivity of homogeneous/ enzymes catalyst and easily retractable capability of heterogeneous nature.[12] These photocatalysts are tuned and optimized by different approaches like designing synthesis routes, nanoparticle morphologies, defect engineering, elemental doping, framing heterostructures, customizing bandgap, etc. These catalysts are triggered for the reaction by various external forces like electromagnetic waves (UV/sunlight/visible light)— photocatalysis,[13,14] electric field— electrocatalysis,[1,15] sound— sonocatalysis,[16,17] a

combination of light and electric field— photoelectrocatalysis,[18,19] heat— thermocatalysis,[20,21] and so forth[22] as a main source of energy. Based on simplicity and efficiency, catalysis reaction activated by light, photocatalysis is one of the easiest, facile, and widely used techniques. This process is also used to analyze molecular or atomic-light interactions, catalytic reaction processes, and chemical kinetics. Therefore, over the past decades, the efforts and focuses of the researchers have shifted from developing new photocatalysts to understanding photocatalytic reaction dynamics extensively to increase efficiency for the existing materials for large-scale commercial applications.

The analysis of the mechanisms behind different catalytic reactions and material-material/ material-activator interactions is becoming a scientific hub. As photocatalysis is based on an advanced oxidation process, the light-matter interaction for the production of reactive oxygen species (ROS) plays the role of the foundation for photocatalysis in combating pollutants. To modify and enhance the photocatalysis reaction rate, different strategies like bandgap engineering techniques, doping, and coupling with dissimilar elements/ compounds making hybrid photocatalysts are applied.

## 1.1 On the genesis of catalysis

The use of catalyst materials started without our knowledge but consciously the concept appeared when a catalyst was used in the fermentation method to produce alcohol from sugar. The report of using first known inorganic catalysts was reported in the year 1552 by Valerius Cordus, using $H_2SO_4$ for increasing catalytic conversion rate.[23,24] Figure 1.1 shows the illustration of the journey of a catalyst from an infant stage to its maturation stage. The catalysis reactions are broadly categorized into three types, homogeneous, heterogeneous, or surface catalysis, and bio-catalysis or enzymatic catalysis. Apart from these categories, catalysis may fall under environmental catalysis and hybrid/ composite catalysis. Homogeneous catalysis reactions take place entirely in the same or uniform phase with the catalyst, whereas heterogeneous catalysis reactions take place at different phases like the solid-liquid, solid-gas interface. Unlike homogeneous catalysis which is single-sited comprising catalytically active atoms, the heterogeneous catalyst has a well-defined structure, and the reaction is multi-sited where various active sites like edge, defect, face, etc. are involved simultaneously.[25] Enzymatic catalysis is outstanding because of its high catalytic potential (highly selective and mild reaction conditions at room temperature), but enzymatic catalysis is sensitive, unstable, and often demolished in the reaction which adds to its prejudice. Therefore, after analyzing these

catalyst categories, the main approach to developing a new catalyst is to club the main favorable assets of each catalyst category like effectiveness from homogeneous, tuneable properties from heterogeneous, and bio-compatibility from the enzymatic catalyst.[26,27]

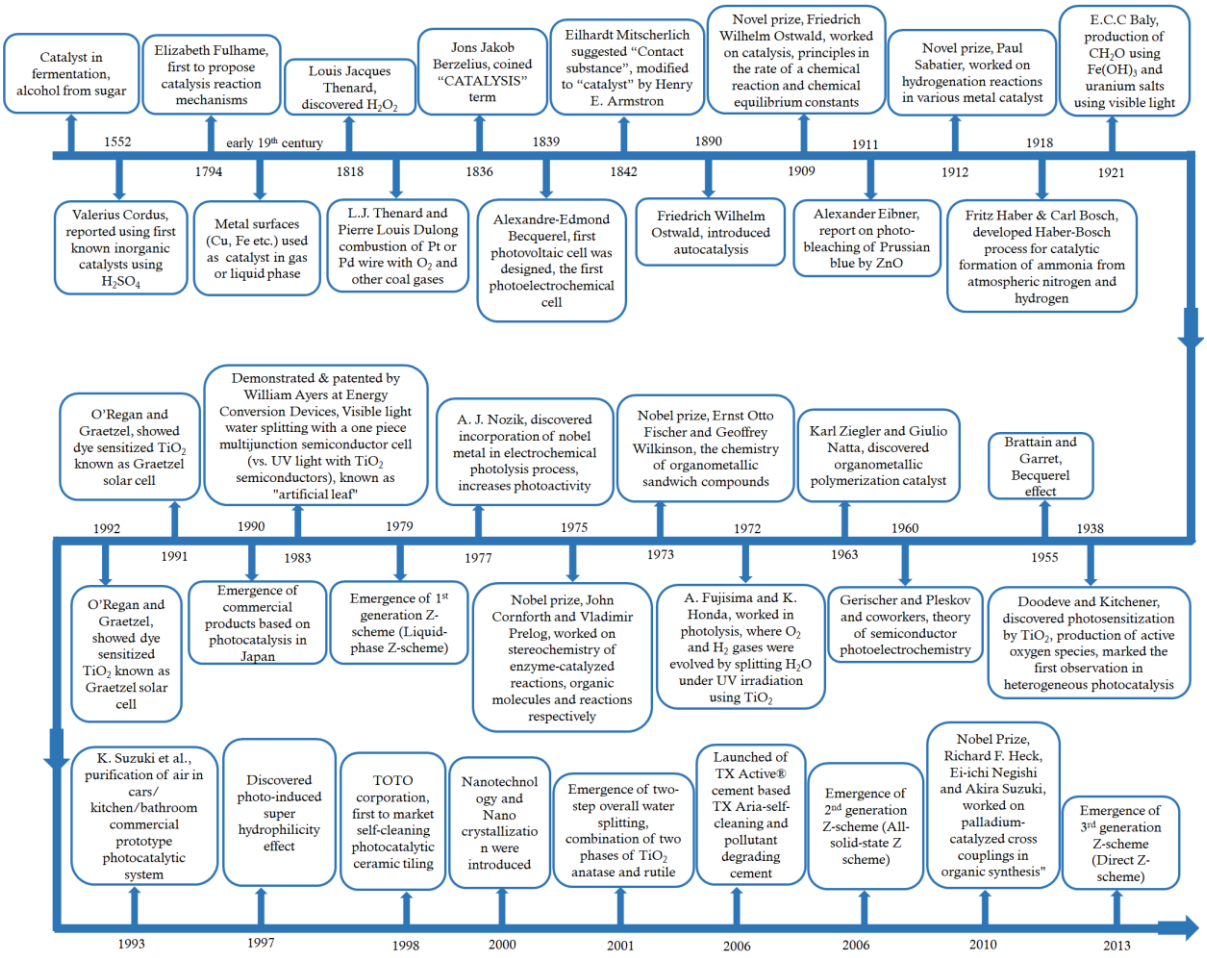


*Figure 1.1 illustrates the historical background in chronological order of the advancement in catalysis and its related field*

## 1.2 Heterogeneous photocatalysis

A chemical reaction accelerated by a catalyst in the presence of light is acknowledged as a photocatalysis reaction, which is also known as artificial photosynthesis. Photocatalysis is a combination of photochemical and catalysis reactions inspired by natural photosynthesis process and mimics the same, where a synthetic material acts as a catalyst in place of a biological catalyst (chlorophyll). In short, the photocatalysis process has evolved from photolysis and photochemical reactions. In the early age, around the 1900s, the study of photocatalysis was focused mainly on the formation of formaldehyde as a reaction intermediate in the reaction process by imitating the natural photosynthesis process.[27–30] Apart from the convenience, efficiency, and comfort provided by homogeneous photocatalysis, due to

hindrances and difficulty in identifying and establishing reaction mechanisms, photocatalysis steered from homogeneous to heterogeneous or hybrid/ complex photocatalysis.[31–33] Starting from the study of chemical reactions and kinetics, the generation of in-situ $H_2O_2$ during the catalysis process is the main step for the implementation of the photocatalysis process in various fields (ex. energy generation and pollution mitigation).[34,35] In 1918, E.Baur[34] explained the mechanism of photolysis where a molecular potential difference was seen when the light was subjected to affect the chemical reaction. Therefore, photolysis was regarded as molecular electrolysis. G.S.Egerton[36,37] and D.Ashton et al.[38] had studied elaborately the photochemical degradation of cotton and textile materials via photochemical oxidation reaction in the presence of inorganic pigments like ZnO, $TiO_2$, Cu. The group studied the role of $H_2O_2$ production broadly when water was oxidized under the illumination of electromagnetic radiation. However, the main eye-opening breakthrough in photocatalysis occurred when A.Fujishima and K.Honda's[1] conjoint work in photolysis, was published in 1972. In their work, $O_2$ and $H_2$ gases are evolved by splitting $H_2O$ under UV irradiation using a $TiO_2$ single crystal catalyst electrode, carving the milestone of photocatalysis[1]. Therefore, photocatalysis reactions induced by semiconductor oxides have been a major study area from an early age until now.

***Heterogeneous photocatalyst classifications***

Photocatalysts can be of different types based on a certain aspect according to the convenience and implementation like compositions, sizes, dimensions, electrical properties, or others. Xiaogang et al.[30] grouped photocatalysts into six categories based on constituent materials—traditional semiconductor, molecular, plasmonic, 2D, quantum dots, and traditional semiconductor-based photovoltaic-assisted photocatalyst. N.Serpone et al.[39] A.V Emeline et al.[40] summarized photocatalysts based on time and material, grouped into generations—first, second, and third, and proposed concepts of photoactive materials with multi-photon excitation capability, selective photoexcitation, and heterojunctions. In the review article by Fernando et al.[41], the advancements of photocatalytic material from single-phase semiconductors to mixed bi-functional material were discussed. By studying heterogeneous catalysis, G.M.Schwab and K.Gossner[42] classified photocatalysts based on their structure; metals, supported metal catalysts, and oxide catalysts.[43] Continually, H.Ren et al.[44] and Y.Boyjoo et al.[45] classified photocatalyst materials based on their composition; binary, complex metal oxides, metal sulfides, and metal-free materials. Due to the emergence of countless photocatalyst materials, it becomes difficult to categorize properly and is found to be subtle to the club most materials

explicitly in a certain group. Yet this review article attempts to consolidate photocatalyst materials into eleven categories based on the type and composition of the material, covering almost every type of photocatalyst. The categories are: Oxides,[46,47] Sulfides,[48,49] Nitrides,[50,51] II-VI,[52] Halides,[19,53] III-V,[54] Doped material,[55,56] Carbon-based,[57,58] Elemental/ Metal NPs,[59,60] Molecular organic frameworks,[61] and other complex structures are collectively known as Composites/ Hybrids[53,62]. The photo-catalyst material in each category can be of unary (ex. one-element oxide; ZnO[13]), binary (ex. two-element oxide; $CoFe_2O_4$[63]), tertiary (ex. three-element oxide; $AgBiW_2O_8$[64]), and multi-elemental[65] (shown in Table 1.1).

*Table 1.1 Classification of photocatalysts based on compositions and their examples*

| **Sl. No** | | **Unary Oxide** | **Binary Oxide** | **Tertiary Oxide** |
|---|---|---|---|---|
| 1. | Oxides | $TiO_2$, ZnO, $WO_3$, $ZrO_2$, $CeO_2$, $Bi_2O_3$, $MnO_2$, $Fe_3O_4$, $Fe_2O_3$, MgO, $Al_2O_3$, $Ag_2O$, $Ga_2O_3$, $SnO_2$, CuO, $V_2O_5$ | $SrTiO_3$, $Bi_2WO_6$, $BiVO_4$, $CaNbO_3$, $BaBiO_3$, $Ag_2WO_4$, $Ag_3VO_4$, $K_2WO_4$, $K_4Nb_6O_{17}$ | $Co_xZn_{1-x}Fe_2O_4$, $AgBiW_2O_8$, |
| 2. | Sulfides | ZnS, CdS, CdZnS, SnS, $Cu_2ZnSnS_4$, $Co_3S_4$, $ZnInS_4$, $InS_2$, $CdInS_4$ | | |
| 3. | Halides | AgX, CsX, $RhX_3$, $PbX_2$, $CsPbX_3$, $MAPbI_3$ | | |
| 4. | Nitrides | BN, $Mo_2N$, MoN, $Co_xN$, TiN, $Ta_3N_5$, WN, $LaTaON_2$, $Fe_xN$, $Ni_3N$, $EuWON_2$, $CaTaO_2N$, $BaTaO_2N$, $EuNbO_2N$ | | |
| 5. | II-VI | ZnX and CdX (X=O, S, Se, and Te) | | |
| 6. | III-V | BN, InGaP, GaN, GaP, GaAs, Al-Ga-In-N, (GaIn)P/GaAs, GaAs/AlGaAs, InP, InAs | | |
| 7. | Elemental or Metal NPs | Ag, Cu, C, Au, Al, Pt, Bi, Co, Fe nanoparticles/ nanowires | | |
| 8. | Doped | $Au@SiO_2@Fe_2O_3$, AgBr@Ag, (Au/Ag/Fe/Cu/Co/Mn)-ZnO, (Au/Ag/Fe/Cu/Co/Mn/Se)-$TiO_2$, (metal, non-metal, rare-earth elements doping) | | |
| 9. | Carbon-based | Graphene, Carbon nanotubes, reduced graphene oxide, graphene Quantum dots, $TiO_2$/GQD, g-$C_3N_4$/$SnS_2$, g-$C_3N_4$, graphene oxide-BiOBr | | |
| 10. | MOFs | Metal (Fe, Cr, Co, Cu, Ag)- terephthalates | | |
| 11. | Composites/ Hybrids | ZnO decorated $Fe_2O_3$, Core-shell: $NiFe_2O_4@TiO_2$, $Fe_3O_4@TiO_2$, $MoS_2@CoFe_2O_4$, $BiOBr@BiOI@Fe_3O_4$, $Bi_2O_2CO_3@BiOCl$ | | |

The new heterogeneous photocatalysts emerge by manipulating certain like bandgap, carrier transport, crystallinity, surface area, and stability based on the applications and the requirements. These heterogeneous photocatalysts display divergent optical, magnetic, physical, and chemical properties as the constituents vary from organic to inorganic, metals to non-metals/ rare-earth elements, intrinsic (undoped)-extrinsic (doped), and others. Tuning particles shape, structure and sizes, microns to nano-size morphologies; 0D (quantum dots),[57,58] 1D (rods, tubes, wires),[46,66] 2D (thin films),[57,67] 3D (nanowire bundles, bulk powders),[13,68] and other complex structures[69,70] mostly alter bandgap energies. This alteration in the bandgap results in inducing unique responses to the interaction of light as light-matter interaction phenomena is a very delicate process. This is easily hindered by even a single change in composition, type of material, or change in reaction parameters. Therefore, the main focused area of photocatalyst properties is to have large visible spectral absorbance, high-energy conversion efficiency, and maximum charge generation-separation rates.

***Fundamental principles and mechanisms of heterogeneous photocatalysis***

The heterogeneous photocatalysis includes a variety of reactions: oxidation, reduction, de-hydrogenation, radical formation, etc. occurring in semiconductor surfaces where a wide range of weakly bound chemical adsorbates undergo light-initiated-induced redox reactions. The photocatalysis process is carried out in different media for different implementations like gas-phase ($CO_2$ reduction or GHG mitigation), solid-phase (solar to energy conversion), and liquid-phase or aqueous solution (dye degradation/ wastewater treatment). For water pollution mitigation, the photocatalytic reaction takes place in photocatalyst materials that are dispersed in a pollutant-containing medium or on a photocatalyst that is anchored in a substrate. The execution of this kind of reaction takes place in a batch reaction system for analyzing particular photocatalyst material under a known quantity of reaction conditions. The batch reaction system primarily uses powder catalyst dispersing in the medium through stirring or sonication (stirring throughout the process to prohibit agglomeration), acknowledging its simplicity and uncomplicated reaction step explorations. Furthermore, the catalyst material is also maneuvered in different forms like electrodes,[57] powders,[13] fabric,[71] floating forms,[62], and many others[72]. The liquid phase photo-catalysis process follows five predominant steps (illustrated in Figure 3): (a) Catalyst introduction in the contaminated liquid medium, (b) Adsorption of contaminant molecules on the catalyst surface, (c) Oxidation/ reduction reaction

of the contaminants, (d) Desorption of product molecules from the catalyst surface, and (e) Removal of products from interface region.[4]

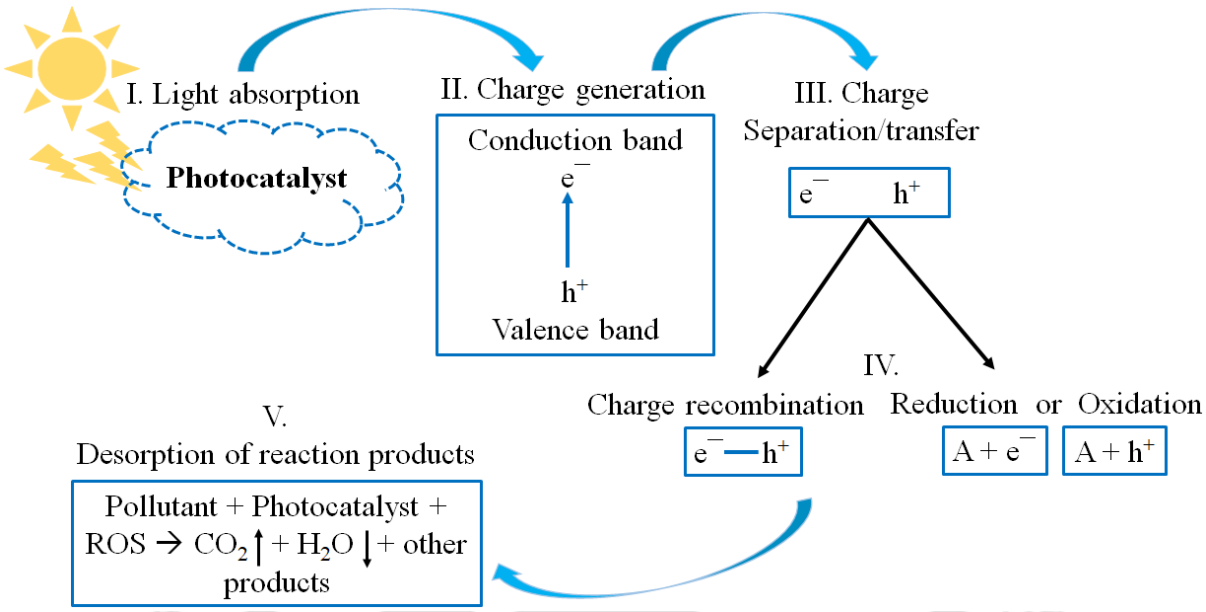


*Figure 1.2 Stepwise photocatalysis process illustration*

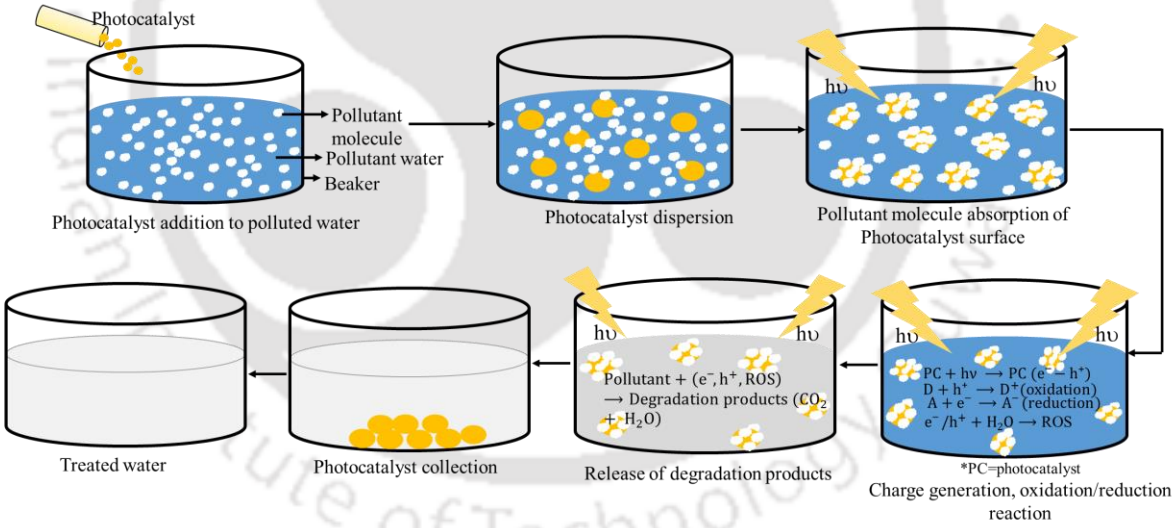


*Figure 1.3. Stepwise demonstration of liquid phase photocatalysis process*

Regardless of innumerable photocatalysts, photocatalysis processes predominantly revolve around these five pivotal phases (illustrated in Figure 1.2) and two reaction pathways. The five phases are (i) Light absorption or harvesting, (ii) Excitation and exciton/ charge generation, (iii) Charge separation-transfer-migration, (iv) Charge recombination, or Oxidation-reduction processes, and (v) Desorption of reaction products from the catalyst surface or reaction medium.[4,73–75] The two reaction pathways for the photocatalytic reactions are: (a) Direct

pathways, where photogenerated charge carriers are separated and trapped by pollutant molecules or surface defects consequently forming radicals, and (b) Indirect pathways, where photo-generated charge carriers are used to produced ions and radicals (ROS) by reacting with water molecules.[76,77] For photo-degradation of contaminants, advanced oxidative process (AOPs) provides complete oxidation of pollutants and mineralizing them into less harmful components by generating strong oxidants or oxidizing species (like •OH radicals, superoxide radicals), called reactive oxygen species triggered by an external force. Some of the pollutant molecules like $Cl^-$, $SO_4^{2-}$, $Al^{3+}$, $Cu^{2+}$, $CN^-$, phosphates, and others, present in the wastewater also act as charge carriers and attack the unsaturated bonds of the pollutants.[78] The elimination of pollutant molecules occurs through a complete/ partial breakdown of conjugated unsaturated bonds by charged particles and radicals generated, collectively known as ROS.[79] In the case of complete mineralization, pollutants are degraded into less harmful products like $CO_2$, $H_2O$, or alcohol and gases with the formation of numerous reaction intermediates.[79,80]

Photocatalysis reaction is initiated by photo-absorption and photo-excitation by the photocatalyst when incident photon energy is equal to or greater than photocatalyst bandgap ($E_g$) (i.e., $h\upsilon \geq E_g$; where $\upsilon$=frequency of incident light and h=Planck's constant). This photoexcitation creates an electronic vacancy, hole ($h^+$) in the valence band edge by exciting an electron ($e^-$) in the conduction band edge (*Photocatalyst* + $h\upsilon \rightarrow$ *Photocatalyst* ($e^- + h^+$)). These photogenerated $e^-$—$h^+$ pairs are called an exciton pair that carries energy. Correlated motion of $e^-$s and $h^+$s is not associated with electronic current. Exciton pairs can be of loosely or strongly bounded $e^-$—$h^+$ pairs with the Coulomb attractive interactions. The loosely bound excitons are known as Wannier-Mott exciton or free excitons, which are typically observed in semiconductor nanocrystals (quantum dots) and the exciton wavefunction is delocalized. The free movement of Wannier-Mott excitons is limited by the particle or crystal size (because of its large radius and ease of dissociation). The strongly bound excitons (small-radius excitons) are known as Frenkel excitons and are normally demonstrated in the aggregates of organic dyes.[57,81] The $h^+$ then initiates further interfacial $e^-$ transfer and the reaction rate is determined by the reaction of $h^+$s with a substrate, as carrier trapping is a fast phenomenon. These transferred photogenerated $e^-$—$h^+$ pairs are noticeably powerful to induce various oxidation and reduction processes of the surface adsorbed chemical substances forming singly oxidized $e^-$ donor ($D + h^+ \longrightarrow D^+$) or singly reduced $e^-$ acceptor ($A + e^- \longrightarrow A^-$) or witness surface recombination emitting radiative or non-radiative energy.[74] Table 1.2 provides a series of photocatalytic reactions decentralized in a simple semiconductor catalyst surface.

*Table 1.2. Major possible reactions in a photocatalysis reaction for the generation of charge carriers and reactive oxygen species for the degradation and mineralization of pollutants*

| | |
|---|---|
| $Pollutant + h^+ \longrightarrow Oxidation;$ | $Pollutant + e^- \longrightarrow Reduction;$ |
| $h^+ + H_2O \longrightarrow h^+ + \bullet OH;$<br>$e^- + O_2 \longrightarrow O_2^{\bullet -}$ ;<br>$2HO_2^{\bullet} \longrightarrow H_2O_2$ ; | $h^+ + OH^- \longrightarrow \bullet OH$ ;<br>$O_2^{\bullet -} + h^+ \longrightarrow HO_2^{\bullet}$ ; |
| $H_2O_2 + O_2^{\bullet -} \longrightarrow \bullet OH + OH^- + O_2$ ;<br>$H_2O_2 + h\boldsymbol{\nu} \longrightarrow 2 \bullet OH$ ; | $H_2O_2 + h^+ \longrightarrow O_2 + 2h^+$ ;<br>$H_2O_2 + e^- \longrightarrow \bullet OH + OH^-$ ; |
| $O_3 + e^- \longrightarrow O_3^{\bullet -}$;<br>$O_3 + h\nu \longrightarrow O_2 + O \bullet$ ; | $O_3^{\bullet -} + H^+ \longrightarrow HO_3^{\bullet -}$ ;<br>$O \bullet + H_2O \longrightarrow 2 \bullet OH$ ; |
| $Fe^{3+} + H_2O + h\nu \longrightarrow Fe^{2+} + \bullet OH + H^+$ | |
| $\boldsymbol{Pollutant + (e^-, h^+, ROS) \longrightarrow Degradation\ products\ (CO_2, H_2O, \ldots)}$<br>**ROS: $O_2$•-, •OH, $OH^-$, $HO_2$•, $H_2O_2$** | |

Although many researchers claim and debate the use of photocatalytic water in real-time wastewater treatment, some researchers are still working to understand the limitations in large-scale applications as well as to invent new efficient reactors. S.Loeb et al.[82] published an article in 2019 on the advancement of the Photocatalytic Water Treatment technology debating its applicability in the large scale application and whether it is worth further study. The study also pointed out that despite focusing on the application of this photocatalysis in municipal water treatment operations, ignoring the immense technology transfer problems and creating academic hype. Also, in E.Cates's short point-of-view article on the position of photocatalytic water treatment application, it was pointed out that the need to design a photocatalytic treatment system is greater than focussing on the catalyst[83]. However, Panasonic's successful development in producing 'Photocatalytic Water Purification Technology' in 2014 to generate drinking water with the use of $TiO_2$ photocatalyst and UV rays from sunlight to detoxify the polluted water gave us hope to be able to design a system for large-scale wastewater treatment applications. So, in recent years, the focus has been made on developing an efficient photocatalytic water treatment reactor using the already existing and well-known photocatalyst— mostly ZnO and $TiO_2$ in the inorganic semiconductor section while g-$C_3N_4$ and graphene or graphene oxide in the carbon-based photocatalyst category[84,85]. O.Baaloudj et al. proposed a pilot scale design of a sustainable and cost-effective photocatalytic treatment system by employing selenite $Bi_{12}TiO_{20}$ as a photocatalyst and tested by degrading three different antibiotics—cefixime, cefaclor, cefuroxime with maximum 94% degradation efficiency within 210 min[86]. Researchers are also using 3D printing like inkjet printing,

stereolithography, selective laser sintering, and direct ink writing for the immobilization of the photocatalyst nanoparticles for wastewater treatment by using novel photocatalytic reactor designs in different structures with high accuracy using polymer, ceramics, or porous hierarchical structures[85,87]. In the research paper by N.Jorge et al., natural organic coagulants, potassium persulfate, and photo-Fenton process were used to treat the winery wastewater which showed a cheaper method with high dissolved organic carbon removal by replacing metal salt coagulants with the natural organic coagulants[88]. *Thymus daenensis* and Stachys pilifera Benth extract mediated ZnO/carbon nanofiber composites for the photocatalytic degradation of tetracycline with 93.65±2.1% in ultrapure water and 81.28±2.1% in general hospital influents[89]. Other high-efficiency techniques have also been reported by many researchers using different approaches and materials— heteroatoms doped g-$C_3N_4$ with $ZnFe_2O_4$ and graphene oxide[90], MXene composite[91], hybrid organic–inorganic membranes[92], nanocomposite filters[93], optimized packed bed photoreactor[94], piezo-photocatalytic wastewater treatment system[95], solar-driven photothermal photocatalysis[96], linear fresnel photoreactor photocatalytic wastewater treatment system[97], etc.

## 1.3 Band gap engineering

The transfer of photogenerated charge carriers to surface-adsorbed pollutant molecules occurs when the Fermi level and redox potential of the absorbed molecules equilibrate or more positive than the energy levels of the valence band maxima to act as an electron donor or more negative than the minimum energy level of the conduction band. Because of the surface potential developed between the semiconductor and electrolyte interface (known as the Schottky barrier), an interfacial electric field is generated driving $e^-$s and $h^+$s in opposite directions. This charge carrier separation inhibits recombination causing band flattening at the solid-liquid interface. This surface potential also induces charge carriers to drive toward the surface trapping sites, by either migration or diffusion. As every catalyst surface has unique electrical, physical, and chemical properties, it possesses a distinct number of trapping active sites and responses uniquely to the charge carriers or pollutants. These sites are the bait or launching sites for charge particles or carriers like anions, cations, and contaminant molecules, which are either organic or inorganic that attach through chemisorption or physisorption processes by weak van der Waal's force of attraction. The efficiency and effectiveness of these reactions are indicated by the quantum yield, "*it is the number of molecules of a given pollutant degraded per photon of radiation absorbed*" or "*It is the ratio of the number of molecules*

*undergoing dissociation by several photons absorbed by the solution*". The efficiency is altered by tuning major factors like bandgap, catalyst compositions, catalyst loading concentration, surface defects, surface properties, shape and size, pH of the reaction medium, and light source.

Apart from tinkering with photocatalysts in physical properties like porosity, surface area/surface charges, induced defect, and varied morphologies, bandgap engineering is considered one of the best and most efficient approaches agreed by many to improve photocatalysis efficacies by enhancing major reaction steps.[98–100] The bandgap engineering is done in three ways: shifting (lifting) valence band maxima, shifting (dropping) conduction band minima, and introduction of new bands between valence band maxima and conduction band minima (illustrated in Figure 1.4-a, b, c).[101,102]

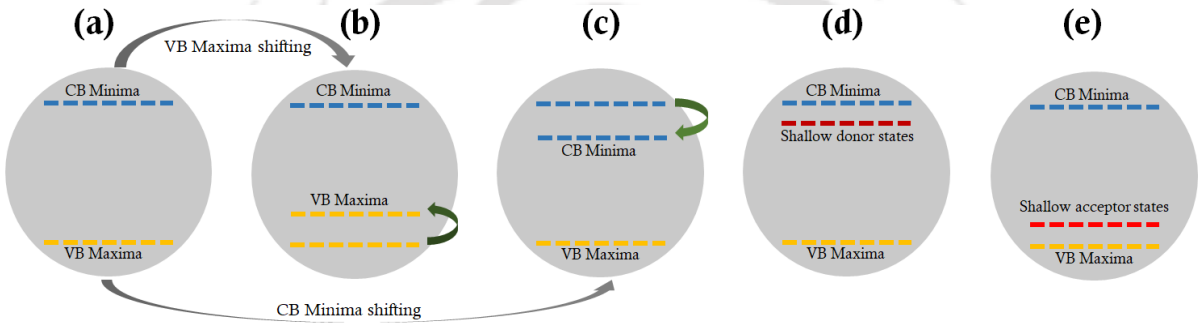


*Figure 1.4. The shift of energy band in band-gap engineering, (a) general CBM minima and VBM maxima of a photocatalyst, (b) shifting/uplifting of VBM maxima, (c) shifting/downshift of CBM minima, (d) introduction of donor state below the CBM minima, (e) introduction of acceptor state above the VBM maxima*

The main approach to engineering the bandgap of a photocatalyst is to broaden solar light absorption spectra from UV to Visible region, which enhances the density of charge generation resulting in boosting photo-reactivity and charge separation. Therefore, for selecting a photocatalyst for an efficient and higher quantum yield application, the principal step is to choose a matching bandgap with the activating light source, competence in excitation and generation of $e^{-}$—$h^{+}$ pairs, charge separation, and environment friendliness.[5,43,73]

## 1.4 Doping and metal-incorporated photocatalyst

One of the embryonic approaches to enhance photocatalytic reaction and band gap engineering is by doping process, introducing co-catalyst materials/ sensitizers, and others. Doping can be grouped into four types: (i) Self-doping, (ii) Metal doping, (iii) Non-metal doping, and (iv) Co-doping. In association with different types of doping, mid-gap energy states are established

between the conduction band minima and valence band maxima (shown in Figure 4 a, b). In metal ion-doped semiconductor oxides, reduction reaction primarily occurs through electron transfer reaction to the metal ions via single or multiple steps, additionally, interfacial charge transfers and separation The presence of surface defects suppresses charge carrier recombination, acting as a reaction site.[14,73,103,104] Also in a doped photocatalyst material, dopants act as trappers for the photo-generated $e^-$s and $h^+$s; trappings, and de-trapping of $h^+$s and $e^-$s (shown by a series of reactions in Table 1.3).[105,106]

*Table 1.3. Role of defects and surface defects in photocatalysis reaction in charge transfer*

| | |
|---|---|
| Trapping | $(Dopant)^{n+} + e^- \longrightarrow (Dopant)^{(n-1)+}$ , $(Dopant)^{n+} + h^+ \longrightarrow (Dopant)^{(n+1)+}$ |
| De-trapping | $(Dopant)^{n+} + hv \longrightarrow (Dopant)^{(n-1)+} + h^+$, $(Dopant)^{n+} + hv \longrightarrow (Dopant)^{(n+1)+} + e^-$ |
| Surface defects (SD) | $SD + h^+ \longrightarrow (SD)^+$, $(SD)^+ + e^- \longrightarrow SD$, $(SD)^+ + dye \longrightarrow (SD-dye)^+$ |

However, not all alterations in a photocatalyst yield positive results as the introduction of dopants into a pristine semiconductor may slow down the reaction processes due to an increase in the recombination of $e^-$—$h^+$ pairs in the dopant sites.[43,76] W.J.Yin et al.[102] widely studied bandgap and band edge modification using generalized gradient approximation (also validated by hybrid density function method) by substituting/ co-doping certain percentages of O and Ti from $TiO_2$. It was found that the concentration of dopants affects bandgap and band edge positions. The binding energy of co-doped material is calculated by[102]:

$$E_b = E(D_{Ti}) + E(A_O) - E(D_{Ti} + A_O) - E_{TiO_2}$$

where: $E(D_{Ti})\ and\ E(A_O)$ are total energies with donor and acceptor on Ti and O sites, $E_{TiO_2}$ is the total energy of $TiO_2$.

In the case of semiconductor-metal heterostructure photocatalyst, a space charge region called the Schottky barrier is formed in the interface. The alignment of the Fermi level to attain equilibrium takes place in the interface by flowing $e^-$s from material with a higher Fermi level or lower work function to a lower Fermi level or higher work function forming an electric field in the contact region.[59,107,108] Here, metal with higher work function acts as $e^-$ trappers and makes itself excessively negatively charged, consequently making the corresponding semiconductor positively charged in excess. Therefore, these $e^-$ trapping phenomena assist in improving exciton separation and inhibit in-charge carrier recombination. For example, Ag nanoparticles in AgBr or AgCl, produce surface plasmon resonance-induced electric fields developed in the metal and semiconductor contact region. This phenomenon enhanced

photocatalytic activity in sunlight illumination by transferring e⁻s from Ag metal to semiconductor AgBr, equilibrating Fermi levels (shown in Figure 1.5).[59]

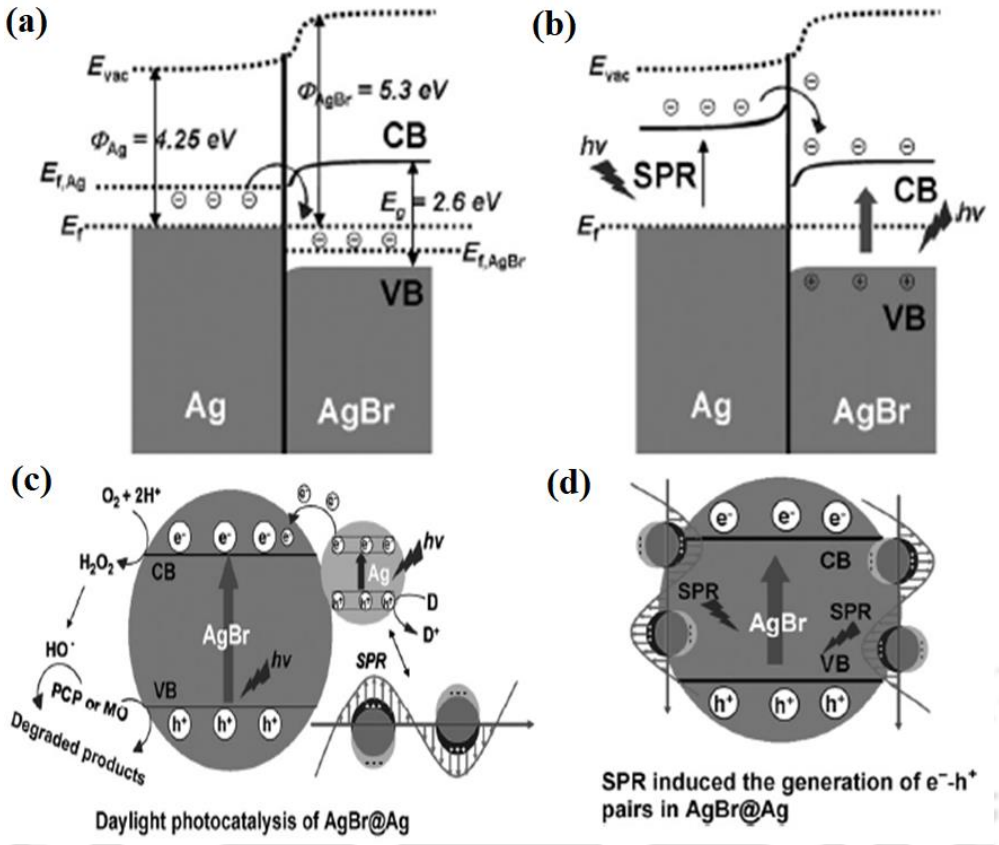


*Figure 1.5. Charge transfer mechanism between energy levels in Ag nanoparticles doped in AgBr (a) energy level before daylight illumination, (b) charge transfer and separation after daylight illumination with surface plasmon resonance phenomenon in Ag nanoparticles, (c) photocatalysis in AgBr@Ag in the presence of daylight illumination, and (d) surface plasmon resonance induced charge carriers generations in AgBr@Ag[59]*

One of the hot emerging photocatalyst materials is plasmonic material, where noble metal nanoparticles like Ag, and Au, are incorporated with another photocatalyst to form a complex hybrid photocatalyst. These plasmonic photocatalysts are known to absorb solar energy and form an internal electric field when illuminated by the light of sufficient energy where charge generation takes place followed by a similar photo-redox mechanism to that of conventional reaction mechanisms. The localized surface plasmon resonance originates when the incident light wavelength is greater than the size of the metal nanoparticles, and free e⁻s oscillate in the nanoparticle surfaces in phase with the incident electromagnetic field.[30,107,109] Here, charge carriers are separated by the developed surface plasmon resonance electric field, increasing the quantum efficiency and with the direct e⁻ transfer from plasmonic metal to the counter material.[60,107]

## 1.5 Charge transfer dynamics in heterostructure hybrid photocatalyst

Shifting to multicomponent photocatalyst, suitable band edge materials are integrated forming hybrid heterostructures. The hybrid multicomponent photocatalyst improves light absorption efficiency and optimizes the charge separation-recombination process where one material acts as a photosensitizer for the other material. This heterojunction is conceivably in between semiconductor-semiconductor, semiconductor-metal, metal-metal, and metal-insulator. Here, semiconductors can be organic or inorganic, and depending on their majority charge carriers, they can be n-type or p-type. Hence, heterojunctions are the combination of n and p-type semiconductors, forming n-n, p-p, n-p/ p-n heterojunctions.[5,110,111]

In a few cases of heterostructures, semiconductors are assumed to be insulators when partnered with less bandgap material since absorption of light is limited to the UV region of the electromagnetic spectrum and has less electronic properties.[5,39,112] In n-p/ p-n type heterojunction, one n-type semiconductor is in contact with another p-type semiconductor forming a heterojunction interface with space charge region developed by $e^-$s and $h^+$s diffusion in opposite directions, thereby creating a built-in electric potential. This built-in potential uplift charge transfer rate, eliminating recombination and increasing carrier lifetime. The potential drive $e^-$s from a higher conduction energy level to a lower conduction energy level and $h^+$s will transfer from the lower valence level to the higher valence band level. Succinctly, the mechanisms of $e^-$—$h^+$ transfer from one material to another strongly depend upon work function or conduction band and valence band levels, with the type of triggering reaction-oxidation or reduction. In heterostructures, charge transfer encounters less barrier, and therefore due to the built-in potential and band matching, a greater number of $e^-$s and $h^+$s migrate in the opposite directions, thereby amplifying photo-redox reactions. However, to construct an efficient heterojunction, constituting materials should acquire matching bandgap or potential.[59,100,113]

T. Xie et al.[111] illustrated band alignment and charge separation between n-type $SrFe_{12}O_{19}$ and p-type $Bi_2O_3$ heterojunction; $e^-$s were transferred from n-type to p-type and $h^+$s from p-type to n-type (shown in Figure 1.5). The magnetic field generated inside the magnetic component further cooperated in propelling photogenerated $e^-$s and $h^+$s, thereby complementing each other.[111] The optical band gap of n-n type hetero-structured $ZnFe_2O_4$/$BiVO_4$ falls to be in between the bandgap of an individual component and photons are absorbed by less bandgap

material ($ZnFe_2O_4$), where $e^-$s are transferred to less negative conduction band material ($BiVO_4$) to the counter component.[110]

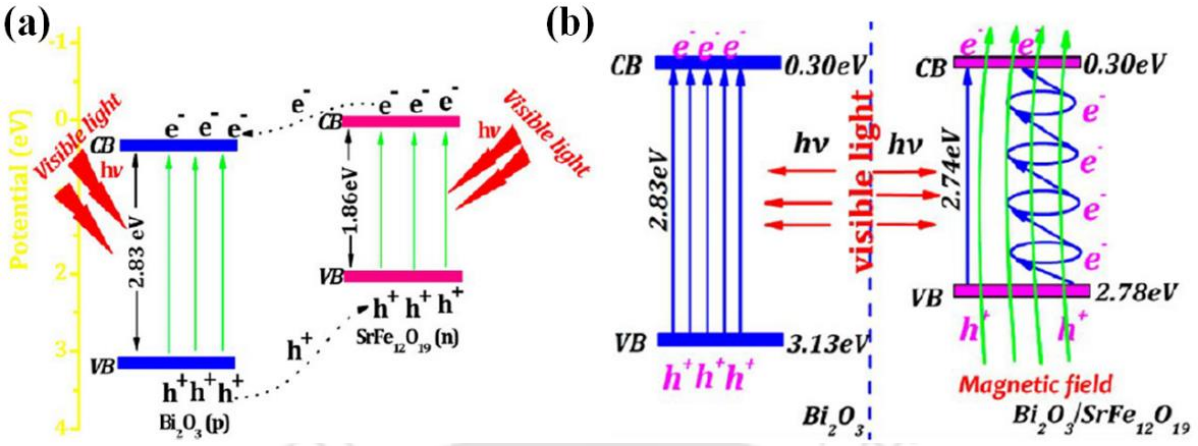


*Figure 1.6. Heterojunction between p-type $Bi_2O_3$ and n-type $SrFe_{12}O_{19}$ (a) charge transfer between the junction and (b) energy level matching and photoinduced electrons flow under visible light irradiation [96]*

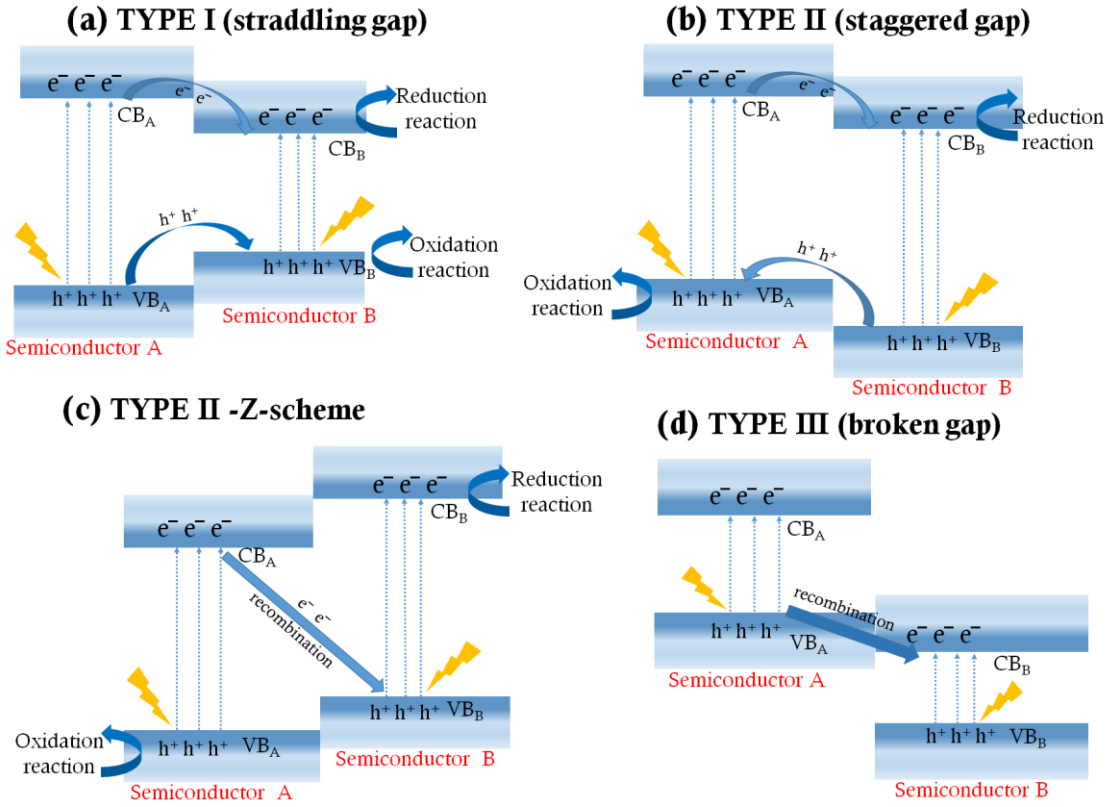


*Figure 1.7. Different types of heterostructures and redox reactions associated with the charge transfer between semiconductor A and semiconductor B, (a) Type I (straddling gap), (b) Type II (staggered gap), (c) type II - direct Z-scheme, and (d) Type III (broken gap).*

Based on the charge excitation-separation and conduction band minima-valence band maxima alignment of the constituting semiconductor materials where the discontinuity or band offset

lies, semiconductor-semiconductor heterostructures are of four types. They are shown in Figure 1.7 with semiconductor A and semiconductor B: (i) Type I (straddling gap), (ii) Type II (staggered gap), (iii) Type II (direct Z-scheme), and (iv) Type III (broken gap). Thus, due to the presence of band-offset, charge carriers experience a potential barrier in the junction and therefore can control the motion and flow of charge carriers. In Type I straddling gap semiconductor heterojunction, the CB and VB of one semiconductor show more positive and more negative respectively as compared to the counter semiconductor material. Therefore, photoexcited $e^-$s are transferred from the more negative CB to less negative CB, and $h^+$s are transferred from more positive VB to less positive VB between the two comprising semiconductors (from semiconductor A to semiconductor B).[114]

In contrast to Type I heterojunction where photoexcited $h^+$s and $e^-$s are transferred from one semiconductor to the corresponding semiconductor (example: $TiO_2/BiVO_4$[115]), Type II heterostructures transfer photoexcited $h^+$s and $e^-$s in opposite directions. The charge transfer in Type II heterojunctions may follow two different pathways: conventional and direct Z-scheme, as shown in Figure 1.6 (b and c). The oxidation and reduction reaction takes place in different semiconductor surfaces for Type II heterostructures while the redox reaction for Type I heterostructure takes place in a single semiconductor surface, therefore charge separation and involvement of charge carriers in a redox reaction are more in Type-II heterostructures. The above-mentioned p-p, n-p/ p-n, and n-n heterojunctions are introduced and designed under the Type II heterojunction category.[116] The photoexcited $e^-$s in the more negative CB transfer either to the less negative CB (conventional charge transfer, example $CuWO_4/Mn_3O_4$[117]) or to the VB of the counter material (direct Z-scheme, example g-$C_3N_4/TiO_2$ heterostructure. And, these $e^-$s recombined with the $h^+$s, thereby, increasing photoexcited $e^-$- $h^+$ separation, generating more $e^-$s and $h^+$s for reductive and oxidative reactions, resulting in the enhancement of photocatalytic efficiency.[118]

The Type III heterostructures are quite different from the above types as the chances of charge transfer between the dissimilar semiconductors are rare, therefore losing the significance of engineering heterostructures.[116] The $h^+$s of semiconductor A recombine with the photoexcited $e^-$s of semiconductor B and the redox reaction takes place on different semiconductor surfaces.[114] With the development of different catalyst types, the major concern of retrieving and reusability of catalyst was solved by using magnetic-based catalyst materials like ferrites catalyst for its easy magnetic separation, e.g. n-n heterogeneous structure of $ZnFe_2O_4$ and $BiVO_4$.[110] Apart from multi-component photocatalyst and doping, size variation is further one

of the major influencing factors of bandgap manipulation. It is noted that the band gap increases and is quantized with the decrease in particle sizes by the localization of energy bands and edges.[13,119]

In a photocatalytic system, the efficiency depends on the kinetic competition of the unproductive (recombination) and the productive steps— excitation and generation of Coulomb-bound electron-hole pair, charge separation, transfer, and redox reactions. Thus, the charge carrier dynamics are calculated by using the Time-resolved photoluminescence spectroscopy (TRPL) and determined the timescales of these photophysical processes, thereby providing room for improvement and the root cause of the limitations. To enhance photocatalytic performance, increasing the charge carrier lifetimes is very important to generate more charge carriers and reactive oxygen species for photocatalytic experiments. The artificial photosynthesis process is a complex multi-proton and electron process with slow rates where proton reduction takes in microseconds and water oxidation in seconds. Therefore, to increase the charge carrier lifetimes, the formation of a junction is needed to improve the charge carrier separation and transfer across the heterojunction interface. Due to the formation of the inbuilt potential and band bending in the interface, it improves the charge separation and transfer in a heterojunction interface with the help of the built-in potential driving force, thus increasing the yield. In TRPL, a time-correlated single photon counting technique is commonly used, where the sample is excited by a short light or laser pulse that generates a histogram. The histogram is built of the time delay between the photoexcitation and the detection of the photon emitted, representing the decay of the excited state. Over time, the PL intensity will be proportional to the time-dependent concentration of the excess photogenerated charges. This PL decay also gives information about charge transfer and charge trappings. The PL decay curve is often fitted to multiexponential models but sometimes depends upon the material— molecular systems have a first-order or single exponential fit while in semiconductor materials the decay kinetics show a complex nature. Due to the bimolecular nature of a material, the charge recombination, trapping, and transport resulted in non-exponential decay. Thus, from the TRPL analysis, the average lifetime of the photoexcited electrons of the material is calculated using two different methods or formulas—(i) intensity-weighted lifetimes and (ii) amplitude-weighted lifetimes. However, to measure different emissive state populations and to know the extent of charge transfer in a heterojunction interface, amplitude-weighted lifetime is mostly used and the intensity-weighted method is mainly used to determine the average time that a material remains in the excited state[120,121].

## 1.6 Carbon-based photocatalyst

Another development in the field of hybrid photocatalysts has been a carbon-based heterogeneous catalyst as an approach towards environmental friendliness and availability despite the well-accepted contribution of pure carbon-based materials. These catalysts are essentially composites of two or more semiconductor compounds co-partnered with carbon nanotubes (multi-walled or single-walled),[122] carbon quantum dots,[123] two-dimensional graphene with quantum dots[57,58] or graphite composites,[57] graphitic carbon nitride, and reduced graphene oxides[124]. The carbon-based heterogeneous photocatalysts are organic and known for their potential green catalyst; surface porosity properties of carbon-based materials are an asset in providing trapping active sites and modulating electrical properties of the composite, as carbon-based materials are conductive. Apart from enhancing photocatalytic properties, it acts as an anchoring surface or template for other partnered elements or compounds.[57,122,123]

Carbon-based materials have desirable electronic properties and can act as an $e^-$ transmitting channel photogenerated by the semiconductor nanomaterials, thereby enhancing $e^-$—$h^+$ separation/transfer, increasing charge carrier lifetime by inhibiting recombination. Single-Walled Carbon Nanotubes (SWCNTs) possess unique optical and electronic properties which highly depend upon the carbon nanotube diameter and chirality, the (n, m) values. That is, every distinct (n, m) nanotube has unique interband energy displaying specific electronic properties. SWCNTs with $|n-m|=3i$ or $|n-m|=3i\pm1$, where i=integer, are metallic or semiconducting respectively in nature[125]. The charge transfer in SWCNTs or MWCNTs coupled with semiconducting oxides like ZnO, $MoS_2$, $TiO_2$, and polymers has been studied widely[126–129]. In ZnO/MWCNT heterostructure, the MWCNT promotes interfacial $e^-$ transfer by acting as an $e^-$ acceptor. This process enhances $e^-$—$h^+$ separation in the composites, showing similar semiconductor-metal heterojunction characteristics where photogenerated $e^-$s of semiconductors are transferred to the carbon-based material, suppressing the recombination process[6,130,131]. Among numerous heterogeneous photocatalysts, carbon-based semiconductor oxide nanomaterials like $TiO_2$ or ZnO in heterojunction with reduced-graphene oxides, CNTs, carbon nitride, and graphene/carbon dots, etc. have successfully employed and shown promising results for various applications like sensors, demineralizing water contaminants, $CO_2$ reduction, and water splitting[126,132–139]. In ternary CNT/$TiO_2$/ZnO composites, the synergetic effect of individuals enhanced the photocatalytic degradation performance while largely depending upon the amount of main light-absorbing photocatalyst ZnO[137]. However, in

the CNT/ZnO/rGO ternary composite, the incorporation of CNTs enhanced the photo-catalytic activity by increasing light absorption and reduction of charge recombination[140]. Due to the high aspect ratio of CNTs and surface areas, the ZnO/CNT composites showed higher degradation efficiency as compared with the bare ZnO nanoparticles[141,142]. The enhancement of photocatalytic performance in the CNT/semiconductor oxides is well known, but the impact of the type of SWCNTs which are metallic and semiconducting on the charge transfer dynamics needs to be studied exclusively.

Graphitic carbon nitride (g-$C_3N_4$) has attracted much attention because of its potential to serve as a photocatalyst because of its cheap, metal-free, non-toxic material properties, easy preparation, and suitable physicochemical and thermodynamic properties. Among the family of carbon nitrides, g-$C_3N_4$ is the most stable allotrope under ambient conditions. g-$C_3N_4$ is a polymeric semiconductor with a similar layered structure to graphene. Considering the complicated synthesis method of graphene, g-$C_3N_4$ might be considered as a breakthrough in sustainable photocatalysts development. It is easily prepared by the condensation or direct heating of nitrogen-rich organic compounds- urea, melamine, cyanamide, and dicyandiamide at 500–650ºC. Depending on the condensation temperature, the band gap of g-$C_3N_4$ is 2.6–2.8 eV absorbing UV and blue light by the inter-band transition. It can be activated by UV light and the visible spectrum of the solar irradiation. Although, g-$C_3N_4$ has low oxidant ability due to the upper edge of the valence band, its electronic properties, morphology, optical, and structural properties are easily tunable. However, it has a strong reduction ability due to the highly negative conduction band value and is responsible for photogenerated electrons. g-$C_3N_4$ is known to show high recombination of photoinduced electrons and holes, leading to diminished photocatalytic efficiency. Thus, modifications in the properties or composite formations are needed to enhance the photocatalytic activity.

## 1.7 Parameters Affecting AOP

One of the simplest and fundamental ways to engineer photocatalyst properties like optical, electrical, size, and morphology is to adopt variable synthesizing routes and preparation parameters. In conjunction with material properties, factors like pH, concentration, type of pollutants, amount of catalyst loading, and inclusion of charge ion scavengers are also major factors for revising demineralization or degradation of pollutants with high efficacies (shown in Figure 1.9).

It is prominent that photocatalysis reaction efficiency is the synergy of all these properties and considering single properties confines solely in that singular material and reaction conditions by keeping other characteristics as constants.

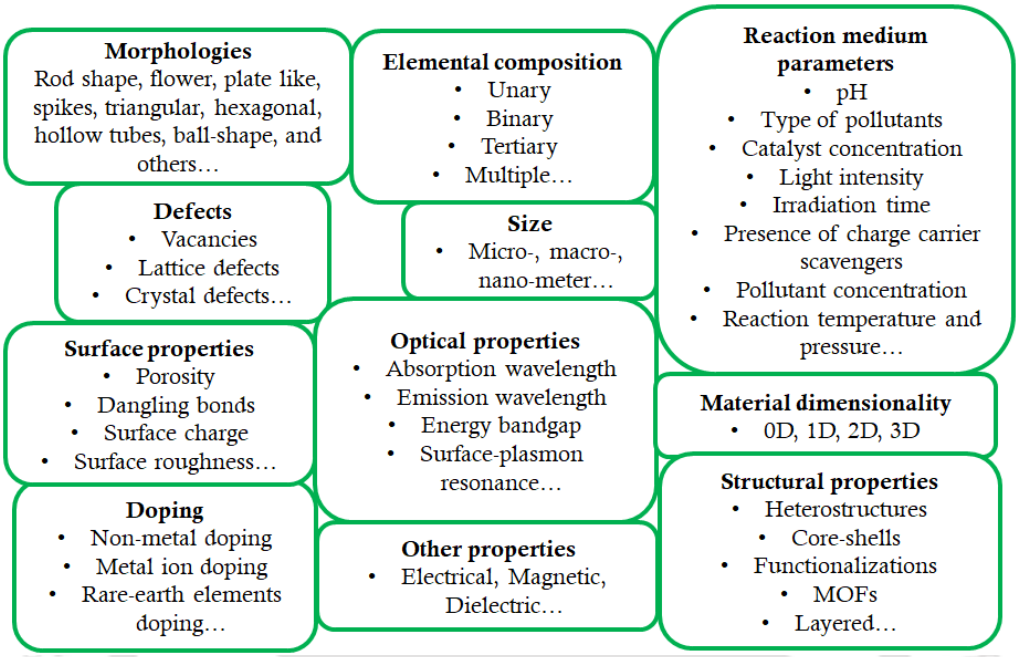


*Figure 1.8 Photocatalysis depending on factors*

## 1.8 Objectives of the thesis

It is found that fewer studies have been done based on SWCNT-based photocatalyst materials, this work will focus on the use of carbon nanotubes (CNTs) and g-$C_3N_4$ functionalized by semiconductor oxides (ZnO and $TiO_2$) as carbon-based material possess unique properties like SWCNTs have both metallic and semiconducting properties. The interaction of light with SWCNT and semiconductor oxides will be studied through the phenomena of plasmons, excitons, charge generation-separation-transfer will be analyzed, and the effect of dielectric property, dimensions, surface property, and functionalization techniques like self-assembly. The following is the proposed work:

(i) Experiment designing using parameter optimization.

(ii) Synthesizing semiconductor oxides based on parameter optimization.

(iii) Synthesizing semiconductor oxides functionalized with metallic-SWCNTs (m-SWCNT), semiconducting-SWCNTs (s-SWCNT), pristine-SWCNTs (p-SWCNTs or the as synthesized SWCNTs that contain both m-SWCNT and s-SWCNT) and g-$C_3N_4$.

(iv) Study the PC activity of the prepared samples under the influence of natural sunlight.

(v) To explore the concepts of light interaction and charge transfer dynamics.

(vi) Experimental lab work and compare theory and practical data.

## 1.9 Outline of the thesis

**Chapter 1** provides a brief introduction and literature review based on the research work— heterogeneous photocatalysis and charge transfer dynamics in a heterostructure interface. This chapter starts from the genesis of catalysis to heterogeneous photocatalysis, the classification of heterogeneous photocatalysts used for the advanced oxidation process. The fundamental principles and mechanism of the heterogeneous photocatalysis based on the advanced oxidation process of water treatment are explained in detail. To increase the performance of the photocatalyst and to harvest sunlight energy, different photocatalyst engineering approaches- band gap engineering, doping, and composite formations are also discussed in the literature review. The charge transfer dynamics in the photocatalysis are explained from a single compound to the charge transfer in the heterostructure interface to inhibit the charge carrier recombination. Other than the transition metal oxides, carbon-based photocatalysts are also explored. Lastly, the parameters affecting the AOP were discussed followed by the introduction to the objectives of this thesis work.

The detailed nanoparticle preparation methods, precursors, and chemicals used to synthesize photocatalyst nanomaterials, and the advanced technologies used to characterize the synthesized nanoparticles are provided in **Chapter 2**. The formulae used to calculate throughout the material analysis are also explained.

**Chapter 3** focuses on optimizing the reaction parameters— the use of precursor, synthesis method, reaction medium, etc. The choice of synthesis method— green synthesis method and chemical synthesis method. Aloe vera and lemon extracts were used as the reducing agents to synthesize ZnO nanoparticles in the green synthesis method. In the chemical synthesis method, two different zinc precursors— zinc acetate and zinc sulfate were used with two different synthesis methods—hydrothermal and precipitation methods. The effect of the use of variable chemical components on the ZnO crystal, optical, surface, and morphological properties was studied in detail. To engineer the surface and optical properties for visible light harvesting, different reaction mediums—DMF and DEG were used. The influence of the synthesis medium on creating crystal/ surface defects, morphologies, charge carrier lifetimes, and its effect on

photocatalytic efficiency were discussed. The photocatalytic performances were studied by using ZnO-coated fabric as the face mask fabric exposed to natural sunlight.

**Chapter 4** discusses the formation of ZnO composites with three different types of SWCNTs— metallic, semiconducting, and pristine. Two different methods were used to form the composites— simple sonication and self-assembly of ZnO nanoparticles on the SWCNTs surface during ZnO synthesis. The interaction of the ZnO nanoparticles with different SWCNTs was investigated through the critical coagulation concentration using ZnO as the coagulant in the stably dispersed SWCNT suspensions. In the self-assembly mode, the ZnO nanoparticles are made to self-assemble onto different SWCNTs during the precipitation method. The charge transfer dynamics on the ZnO/SWCNT heterojunction interface were studied with the calculation of charge carrier lifetimes and compared with the simple ZnO nanoparticles. The performance of the synthesized ZnO/SWCNTs on the photocatalytic performance using nanoparticles coated face mask fabric as the floating photocatalyst under the exposure of natural sunlight.

**Chapter 5** explores and compares different charge transfer pathways— Type I, Type II, and Z-scheme charge transfer pathways. The effect of different charge transfer pathways on the photocatalytic performance is compared and evaluated. Two different composites— Type I—ZnO/$Fe_3O_4$, Type II— ZnO/$TiO_2$, and Z-scheme g-$C_3N_4$/ZnO. ZnO/$Fe_3O_4$ and ZnO/$TiO_2$ composite heterostructures were prepared by chemical precipitation method using procured $TiO_2$ and $Fe_3O_4$ nanoparticles and zinc source was added in the $TiO_2$ and $Fe_3O_4$ suspension in the precipitation method. The g-$C_3N_4$/ZnO composite heterostructure was prepared by simple sonication method where g-$C_3N_4$ was prepared by thermal decomposition method and ZnO nanoparticles were taken from Chapter 3. The charge transfer in the heterojunction interface was analyzed and explained in detail. The performance of the synthesized nanoparticles was evaluated by the photocatalytic degradation of RhB under natural sunlight. The dominant reactive species partaking in the AOP were determined based on the band edge positions and with the use of different scavengers.

The performance and impact of the charge transfer pathways on the photocatalytic efficiency were compared in **Chapter 6**. In this chapter, the efficiency of the synthesized nanoparticles is categorized and compared in two categories— under the influence of UV light and natural sunlight. The performances are also compared with other nanoparticles.

**Chapter 7** concludes the findings of all the work done and displays the future perspectives of the thesis. The scope of implementing the thesis research on the large-scale application of water treatment under the influence of natural sunlight is presented in the future scope section.

# Chapter 2

# Materials, Methods, and Characterization Techniques

## 2.1 Materials

*Table 2.1 The chemicals used in every experiment were used without further treatments*

| Chemical | Make | Chemical | Make |
|---|---|---|---|
| $ZnSO_4.7H_2O$ | Nice Chemical (p) Ltd. | N, N-Dimethyl formamide | Finar |
| $Zn(CH_3COO)_2.2H_2O$ | HiMedia | Diethylene glycol (DEG) | HiMedia |
| NaOH flakes | Nice Chemicals (p) Ltd. | Hydrazine monohydrate, $N_2H_4.H_2O$ | Finar |
| metallic-SWCNT | Nano Integris-IsoNanotubes | Ethylene Glycol | HiMedia |
| semiconducting-SWCNT | Nano Integris-IsoNanotubes | Absolute ethanol | Finar |
| pristine-SWCNT | Nano Integris-IsoNanotubes | Isopropyl alcohol | Finar |
| $FeCl_3$ | HiMedia | 36 W UVC | Lago, LX36HR |
| Titanium Isopropoxide | Sigma Aldrich | Disposable 3 Ply Surgical Mask | Asgard Melt-Blown Fabric |
| Melamine | HiMedia | Rhodamine B (RhB) | SRL Pvt. Ltd |
| $Fe_3O_4$ | Sigma Aldrich | $TiO_2$ | Sigma Aldrich |

## 2.2 Preparation Methods

### *2.2.1 Green synthesis of ZnO using aloe vera and lemon extract*

**Preparation of aloe vera extract**

The aloe vera for these experiments was grown in a flowerpot at IIT Guwahati hostel. The freshly obtained aloe vera leaves were washed thoroughly three to four times using DI $H_2O$, cut into small pieces by using a clean knife, and added to 100 ml of DI $H_2O$. The mixture was

boiled under continuous stirring using a magnetic stirrer in a hot plate stirrer for 2 hr at 100˚C. The solution was made to cool down at room temperature before filtering the leave remains using a double-folded muslin cloth. The extract was ready to use for ZnO preparation.

**Preparation of lemon extract**

The lemons were bought from the local market and washed several times using DI $H_2O$. The clean lemons were cut into half using a clean knife and the juice was squeezed out in a beaker followed by filtration using a folded muslin cloth to remove pulps and solid mixtures. The lemon extract was ready to use as a reducing agent.

*Table 2.2. Detailed preparation steps of ZnO using the green synthesis method*

| Sl. No. | Sample | Method | Zinc source | Reducing agent | Synthesis procedure |
|---|---|---|---|---|---|
| **1.** | $ZnO_{aa}$ | Green source + hydrothermal | 2 grams of $Zn(CH_3COO)_2.2H_2O$ | Aloe vera extract (boiled in DI $H_2O$) | 80 ml of aloe vera boiled extract + 2 grams of $Zn(CH_3COO)_2.2H_2O$ → 15 mins stirring at 50°C → solution shifted to 100 ml Teflon at 200°C for 12 hr. Precipitate was taken after centrifugation and washing several times with DI $H_2O$→ dried in hot air oven overnight at 100 °C |
| **2.** | $ZnO_{sa}$ | Green source + hydrothermal | 2 grams of $ZnSO_4.7H_2O$ | Aloe vera extract (filtered boiled in DI $H_2O$) | Same as $ZnO_{aa}$ but change the zinc source to $ZnSO_4.7H_2O$ |
| **3.** | $ZnO_{al}$ | Green source + hydrothermal | 2 grams of $Zn(CH_3COO)_2.2H_2O$ | Lemon extract (filtered freshly cut and squeezed) | 2 grams of $Zn(CH_3COO)_2.2H_2O$ + 100 ml of DI $H_2O$ at 96 °C and stirred for 5 mins → 3 ml of lemon extract was added → 15 mins stirring at 50°C → solution shifted to 100 ml Teflon at 200°C for 12 hr. Precipitate was taken after centrifugation and washing several times with DI $H_2O$→ dried in hot air oven overnight at 100 °C |
| **4.** | $ZnO_{sl}$ | Green source + hydrothermal | 2 grams of $ZnSO_4.7H_2O$ | Lemon extract (Freshly cut and squeezed) | Same as $ZnO_{al}$ but change the zinc source to $ZnSO_4.7H_2O$ |

**Green synthesis of ZnO nanoparticles**

Here, ZnO nanoparticles are synthesized by the hydrothermal method to explore ZnO properties. Two different zinc sources are used: $Zn(CH_3COO)_2.2H_2O$ and $ZnSO_4.7H_2O$. In all the sample preparation, DI $H_2O$ was used throughout the experiments as a reaction medium, cleaning, or washing process. Table 2.2 shows the detailed preparation steps all followed by calcined at 500 ˚C for 4 hr and Figure 2.1 shows the naming representation of synthesized ZnO nanoparticles. The ZnO nanoparticles precipitates are not formed in the case of the precipitation method and hence are excluded from this paper. The reason may be attributed to the lesser-known reducing ability of the bio-molecules as compared to the chemical reducers. Therefore, the ZnO nanoparticles are difficult to form within the given time interval (2 hr). Figure 2.1 shows the preparation steps of ZnO nanoparticles (a) with aloe vera extract and (b) with lemon extract.

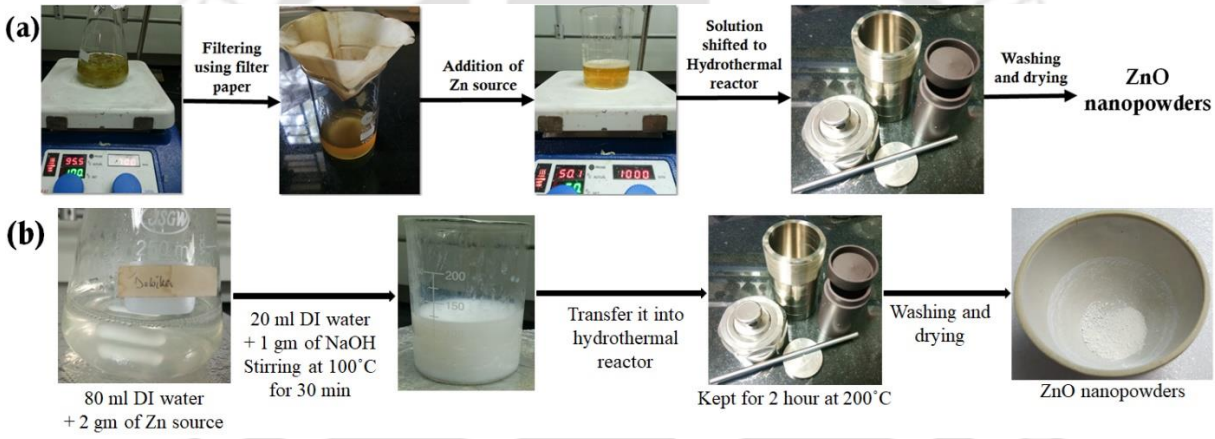


*Figure 2.1 shows the illustrations of (a) ZnO preparation using aloe vera broth extract via the hydrothermal method and (b) ZnO preparation using lemon fruit extract via the hydrothermal method*

***2.2.2 Preparation of ZnO nanoparticles with different zinc sources and synthesis method***

Four different ZnO nanopowders were synthesized using facile chemical precipitation and hydrothermal methods to investigate the effect of zinc source precursor type and synthesis method on the physical, chemical, and optical properties of ZnO. Here, $ZnSO_4.7H_2O$ and $Zn(CH_3COO)_2.2H_2O$, which are readily soluble in water, were used as zinc sources and NaOH flakes were used as a reducing agent in the aqueous reaction medium (DI $H_2O$) without further purifications or treatments. Here, 10 mM of zinc source was dispersed in 80 ml DI $H_2O$ at 80-85 ℃ and stirred for 15 min to dissolve the zinc precursor. In parallel, a 20 ml aqueous solution of 1 g NaOH was prepared using sonication at room temperature. The NaOH solution was added dropwise into the zinc solution and stirred for 15 min. For the precipitation method, the

solution was kept stirring for 2 hr at 80-85 ℃. For the hydrothermal method, the solution was transferred to the Teflon-lined autoclave keeping for 2 hr at 200 ℃ in a hot air oven. The solution was cooled down at room temperature. The precipitate was collected and washed several times with DI $H_2O$ using centrifugation at 5000 rpm to remove unwanted compounds. The collected samples were dried in a hot air oven overnight at 100 ℃. DI $H_2O$ was used throughout the experiments for reaction medium and cleaning purposes. The dried ZnO nanopowders were collected and stored for further use. The samples were labeled as $ZnO_{sh}$, $ZnO_{ah}$, $ZnO_{ap}$ and $ZnO_{sp}$. The suffix letters in ZnO indicate the type of zinc source and synthesis method: s= $ZnSO_4.7H_2O$ source, a= $Zn(CH_3COO)_2.2H_2O$ source, h= hydrothermal method, and p= precipitation method. An elaborate sample preparation procedure is illustrated in Figure 2.2 for both synthesis methods.

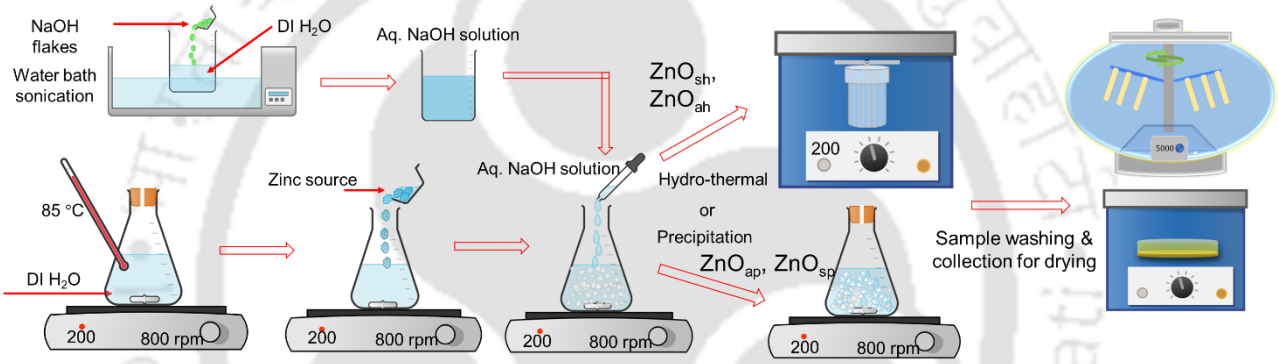


*Figure 2.2 ZnO synthesis procedure via hydrothermal and precipitation method with two different zinc sources— $ZnSO_4.7H_2O$ and $Zn(CH_3COO)_2.2H_2O$*

### ***2.2.3 Synthesis of nano-flowers and introducing defects***

Concerning the chemical components and the conditions mentioned in Table 2.3, the five distinct ZnO photocatalysts are synthesized. Figure 2.3 illustrates the preparation steps of these five different ZnO morphologies by differing synthesis mediums (DEG, DMF, $H_2O$), and methods (Solvothermal, Precipitation). To prepare $ZnO_{dds}$, in an 80-90 °C preheated 60 ml DEG solvent, 10 mM $Zn(CH_3COO)_2.2H_2O$ was added in vigorous stirring for 30 min. Simultaneously, for the reducing agent solution, 10 ml DEG and 40 mM $N_2H_4.H_2O$ were mixed and added slowly into the main zinc precursor solution. The solution was kept for 30 min stirring to form uniform nuclei. For the solvothermal method, the solution was transferred to a Teflon-lined autoclave and kept in a hot air oven for 3 hr at 150 °C. Whereas, for the precipitation method, the solution was kept stirring at 80-90 °C for 3 hr. The solution was cooled at room temperature and washed several times to remove the impurities/residues with

DI $H_2O$. The washed precipitate was dried overnight. The remaining four ZnO samples: $ZnO_{ddp}$, $ZnO_{DDp}$, $ZnO_{Dws}$, and $ZnO_{Dwp}$ were prepared following the same protocol by using the specifications mentioned in Table 2.3. The first suffix in the sample naming denotes the main solvent: d=DEG, D=DMF, the middle suffix letter denotes the solvent used to mix $N_2H_4.H_2O$ reducing agent: d=DEG, d=DMF, w=$H_2O$, and the last letter denotes the type of method: s= solvothermal, p= precipitation. All five samples were calcined at 500 °C for 4 hr.

*Table 2.3. Parameters for preparing five different ZnO nanoparticles with variable solvents and synthesis methods*

| **$ZnO_{dds}$** | **$ZnO_{ddp}$** | **$ZnO_{DDp}$** | **$ZnO_{Dws}$** | **$ZnO_{Dwp}$** |
|---|---|---|---|---|
| 60 ml DEG at 85-90 °C Solvothermal (3 hr autoclave at 200°C) | 60 ml DEG 85-90 °C Precipitation (3 hr stirring 85-90 °C) | 60 ml DMF Preheat 85-90 °C Precipitation (3 hr stirring at 85-90 °C) | 60 ml DMF Preheat 85-90 °C Solvothermal (3 hr autoclave at 200 °C) | 60 ml DMF Preheat 85-90 °C Precipitation (3 hr stirring at 85-90 °C) |
| 10 mM zinc acetate 10 ml DEG+40 mM $N_2H_4.H_2O$ | 10 mM zinc acetate 10 ml DEG+ 40 mM $N_2H_4.H_2O$ | 10 mM zinc acetate 10 ml DMF+40 mM $N_2H_4.H_2O$ | 10 mM zinc acetate () 10 ml $H_2O$+40 mM $N_2H_4.H_2O$ | 10 mM zinc acetate 10 ml $H_2O$+40 mM $N_2H_4.H_2O$ |
| Calcined 4 hr at 500°C | Calcined 4 hr at 500°C | Calcined 4 hr at 500°C | Calcined 4 hr at 500°C | Calcined 4 hr at 500°C |

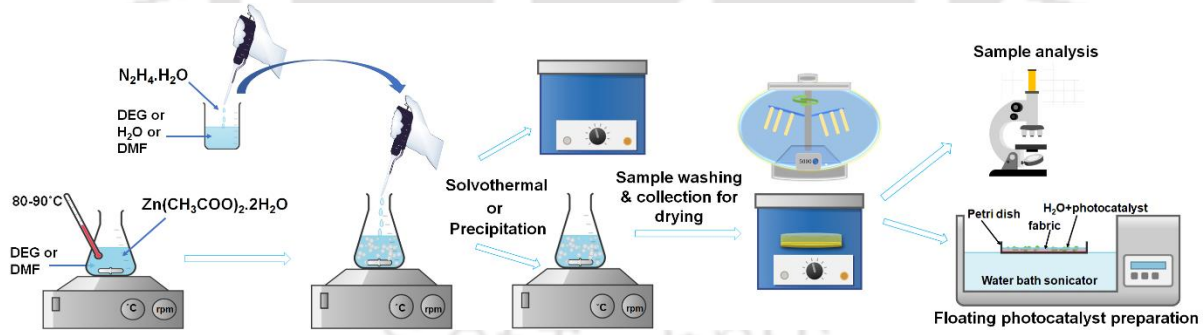


*Figure 2.3. Illustration of different ZnO preparations with the variation in synthesis medium and method*

### ***2.2.4 Functionalization of electronically different SWCNTs by ZnO***

For surface functionalization and determining critical coagulation concentration (CCC) of electronically and optically different SWCNTs: m-SWCNT, s-SWCNT, and p-SWCNT that were procured from Nano Integris-IsoNanotubes, ZnO prepared in Section 2.2.2 synthesized using sulfate source and hydrothermal method with the smallest crystallite size was used. 50

mg of ZnO was added to 2 ml of ~4.16 mM of each m-SWCNT, s-SWCNT, and p-SWCNT suspension. The solutions were sonicated at room temperature for 4 hr and the precipitates were collected by centrifugation and dried in a hot air oven for further use (Figure 2.4). The samples were labeled as m-SWCNT+ZnO, s-SWCNT+ZnO, and p-SWCNT+ZnO for m-SWCNT, s-SWCNT, and p-SWCNT respectively.

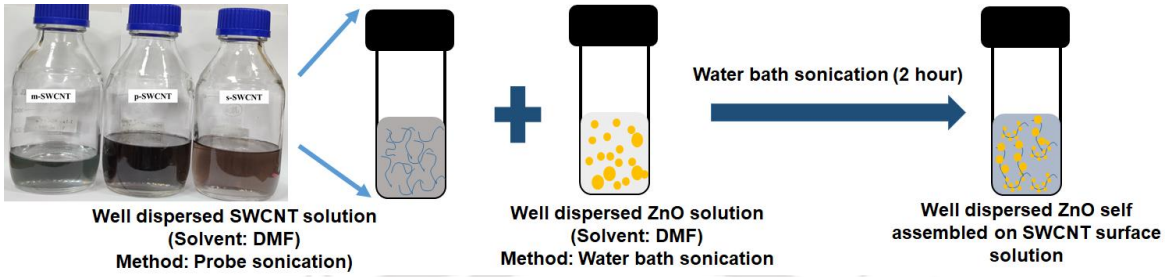


*Figure 2.4. Functionalization of electronically different SWCNTS- metallic, semiconducting, and pristine SWCNTs by ZnO*

### ***2.2.5 Synthesis of ZnO self-assembly on electronically different SWCNTs***

In continuation with the charge transfer study in ZnO functionalized SWCNTs and SWCNT+ZnO composites, here, ZnO nanoparticles are self-assembled and grown directly on electronically different SWCNTs; m-SWCNTs, s-SWCNTs and p-SWCNTs surfaces by facile chemical method. In this, 25 ml of DMF was taken as a solvent for the reaction as SWCNTs are stably dispersed in DMF. A 5 ml of pre-prepared 83 mM m-SWCNTs suspension was mixed in the previous SWCNT suspension. The solution was preheated at 80-85 °C with continuous stirring before adding 2 mM $Zn(CH_3COO)_2.2H_2O$ and kept for 15 min stirring. Simultaneously, a 5 ml aqueous solution of 4 mM $N_2H_4.H_2O$ was prepared, used as a reducing agent, and assisted in $Zn(OH)_2$ nuclei formation. The $N_2H_4.H_2O$ aqueous solution was added dropwise to the main solution and stirred at 800 rpm for 3 hr at 80-85 °C. A whitish precipitate formed was collected and washed 3 to 4 times with DI $H_2O$ to remove the impurities or remaining unwanted chemical compounds and ions. The collected precipitate was dried overnight at 150 °C in a hot air oven followed by 4 hr calcination at 500 °C in a muffle furnace. The sample was named m-SWCNT/ZnO for further study and analysis. The above same reaction procedures were followed for the remaining self-assembled ZnO on s-SWCNTs and p-SWCNTs. The composites were named s-SWCNT/ZnO and p-SWCNT/ZnO for further study.

### *2.2.6 Synthesis of composite heterostructures:*

To synthesize ZnO/$Fe_3O_4$ and ZnO/$TiO_2$ composite heterostructure, 500 mg of the procured $Fe_3O_4$ and $TiO_2$ nanoparticles were dispersed in the DEG solvent separately by sonication and preheat at 80-90 °C. In the $Fe_3O_4$ and $TiO_2$ nanoparticles suspensions, 10 mM of $Zn(CH_3COO)_2.2H_2O$ were added slowly and stirred for 30 min. Simultaneously, two 40 mM $N_2H_4.H_2O$ + 10 ml DEG were prepared by mixing. The $N_2H_4.H_2O$ solutions were added slowly to the two reaction mixtures. The solutions were stirred for 3 hr at 80-90 °C and the precipitates were collected by centrifugation. The collected precipitates were washed three or four times with the DI $H_2O$ and dried in the oven overnight at 150 °C.

### *2.2.7 Synthesis of g-$C_3N_4$/ZnO nanocomposite*

#### Preparation of g-$C_3N_4$

Graphitic carbon nitride, g-$C_3N_4$ nanoparticles are synthesized by direct thermal polymerization. 3.12 gm of melamine was kept in a crucible in a muffle furnace for 4 hr at 500 °C. The yellowish g-$C_3N_4$ powders were collected after the furnace came down to room temperature naturally and were kept for further use.

#### Preparation of g-$C_3N_4$/ZnO composite

The prepared ZnO nanoparticles by using a solvothermal method using DMF as the solvent in Section 2.2.3 was used to prepare the g-$C_3N_4$/ZnO composite. g-$C_3N_4$ and ZnO are mixed in a 1:1 weight ratio and dispersed in 20 ml DI $H_2O$ by ultrasonication for 1 hr at room temperature. The g-$C_3N_4$/ZnO composite was collected by centrifugation and dried the sample for further use.

#### Preparation of g-$C_3N_4$/ZnO/SWCNT composite

The prepared g-$C_3N_4$/ZnO composite is then mixed with the 5 ml of preprepared 1 mg/20 ml SWCNT solution by ultrasonication for 2 hr. The ternary composite was collected and dried in a hot air oven for further use.

## 2.3 Characterization Tools

*Table 2.4 characterization tools*

| Sl no. | Instrument | Make and model |
|---|---|---|
| 1. | 9 KW powder X-ray diffraction (XRD) Spectroscopy | Rigaku RINT 2500 TTRAX III, X-ray wavelength Cu-kα, λ= 1.5406 Å, 45 kV, 112 mA |
| 2. | Raman Spectrometer 532 nm laser | Horiba Scientific LabRAM HR Evolution |
| 3. | Sigma Field Emission Scanning Electron Microscopy | Sigma 300 FESEM, Zeiss-Sigma 300 model |
| 4. | Gemini Field Emission Scanning Electron Microscopy | Gemini 300 FESEM |
| 5. | Field Emission Scanning Electron Microscope (FESEM) with OXFORD EDS | Zeiss, Model: Sigma |
| 6. | Transmission Electron Microscope | JEOL, Model: JEM 2100 |
| 7. | Electron Spin Resonance (ESR) Spectrometer | JEOL, Model: JES-FA200 |
| 8. | Vibrating Sample Magnetometer (VSM) | Lakeshore, Model:7400 series |
| 9. | Picosecond Time-resolved and Steady State Luminescence Spectrometer | Edinburg Instruments, Model: Lifespec II & FSP 920. |
| 10. | Surface Area and pore size analyzer and high-pressure surface analyzer | Quantachrome Instruments, Autosorb, IQ MP, & Micromeritics Instrument Corporation |
| 11. | Fourier Transform Infrared Spectrometer | Perkin Elmer (BX) FTIR |
| 12. | UV - VIS - NIR Spectrophotometer, UV-Visible Spectrophotometer | Perkin Elmer (Lambda 950) Hitachi/Shimadazu/Agilent / Perkin Elmer |
| 13. | UV-Vis absorption spectroscopy | Agilent Technologies, Cary Series |
| 14. | Photoluminescence spectroscopy | Horiba, Fluoromax -4C |
| 15. | XPS | PHI 5000 VersaProbe III, kα source, Aluminum anode |

## 2.4 Photocatalytic Advanced Oxidation Process of RhB

To check the photocatalytic AOP and compare the efficiency and performance, for all the samples 50 ml of 10 ppm RhB dye solution was taken.

### ***2.4.1 Under the UVC light (Dispersion process)***

Under UV light, photocatalytic degradation of 50 ml 10 ppm RhB solution was performed. In this experiment, 50 mg of the photocatalyst were dispersed in RhB solution were illuminated vertically with UVC light with continuous stirring. 1 ml samples were collected every 20 min time interval.

### ***2.4.2 Under natural sunlight (Dispersion process)***

Under natural sunlight (August, October, November) photocatalytic degradation of 50 ml 10 ppm RhB solution was performed for the photocatalyst solution to investigate photocatalyst stability and reusability without centrifugation and just by exposing the photocatalyst mixed RhB. 1 ml samples were collected every 20 min time interval without further centrifugation

### ***2.3.3 Under natural sunlight (Floating photocatalyst process)***

Substrate use: The Asgard Melt-Blown Fabric Disposable 3-Ply Surgical Mask was used for the photocatalytic AOP to anchor the nanoparticles. The mask has ISI class 2 mask made by continuous polypropylene fibers joined consisting of three layers: (a) outer layer: hydrophobic non-woven fabric, (b) middle: high-density filter, and (c) inner: hydrophilic non-woven fabric. For our experiment, an ethanol-treated face mask is taken (inner and outer layer fabrics), cut into 7 cm diameter, and dip-coated with the nanoparticles.

The prepared nanoparticles were coated on two 7 cm face-mask fabrics (Asgard Melt-Blown Fabric Disposable 3 Ply Surgical Mask) to act as a floating photocatalyst (Shown in Figure 2.5). For this process, the fabric was dip-coated with 50 mg nanoparticles each and made to be evenly coated and absorbed onto the fabric surface by sonicating and drying for further use. The natural sunlight-triggered photodegradation experiment was performed on a clear sunny day with an average solar power ranging from 60 klux to 120 klux by floating the nanoparticles-coated face-mask fabric. 1 ml samples were collected every 20 min time interval. The collected samples were analyzed by UV-Vis absorption spectroscopy without further centrifugation to evaluate the performance and charge transfer of ZnO, m-SWCNT/ZnO, s-SWCNT/ZnO, and p-SWCNT/ZnO heterostructures.

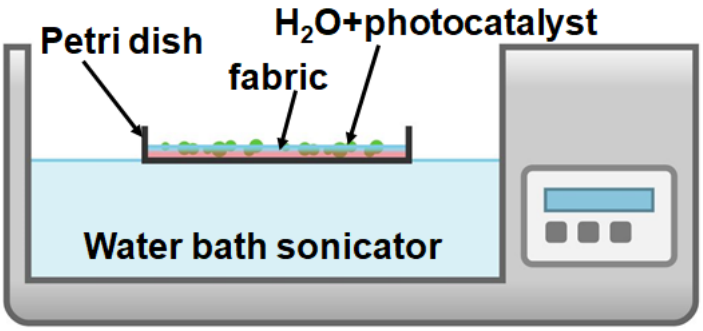


*Figure 2.5. Preparation of floating photocatalyst*

## 2.5 Cycle test

Five cycle tests under UV light and natural sunlight were performed for the photocatalytic degradation of 50 ml 10 ppm RhB solution to investigate photocatalyst stability and reusability. For UV light, 65 mg of the photocatalyst were dispersed in RhB solution and were illuminated vertically with UVC light with continuous stirring. For the natural sunlight, the experiments were done between 10 am to 2 pm by selecting a clear sky. Assays in the natural sunlight were conducted by dispersing 50 mg of photocatalysts and directly exposing it to natural sunlight without stirring. To reuse the photocatalyst following every cycle, it was collected and dried.

## 2.6 Parameter effect test

To investigate the influence of photocatalyst dosage on AOP efficiency, different doses of the photocatalyst were tested under UV light irradiation. Additionally, ethanol, a hydroxyl radical scavenger, was added to the system at different concentrations to investigate the predominant charge carrier affecting the photocatalytic AOP efficiency. Also, IPA and $H_2O_2$ were used to see the effect on the AOP process.

## 2.7 Calculations

### ***2.7.1 X-Ray Diffraction parameter calculation***

The crystallite sizes of the nanoparticles were calculated using the Debye-Scherrer formula,

$$D = \frac{0.9\lambda}{\beta cos\theta}$$

where, D=crystallite size (nm), λ= X-ray wavelength Cu-kα, λ=1.5406 Å, β= full-width half maxima, θ=angle in radian.

In Size Strain Plot analysis (SSP), the XRD peak broadening is the combined effect of strain-induced (Gaussian function) and crystallite size-induced broadening (Lorentzian function). The size strain plot is plotted by $d_{hkl}^2\beta_{hkl}cos\theta$ in x-axis against $(d_{hkl}\beta_{hkl}cos\theta)^2$ in y-axis, calculation by using the formula[143,144]:

$$(d_{hkl}\beta_{hkl}cos\theta)^2 = \frac{k\lambda}{D}(d_{hkl}^2\beta_{hkl}cos\theta) + \frac{\varepsilon^2}{4}$$

where, k=constant, ε=strain, $d_{hkl}$=lattice distance between the hkl plane, $\beta_{hkl}$=full-width half maxima of instrumental corrected broadening, θ=Brag's angle. The information on the lattice strain and crystallite sizes are given by the slope and intercept of the SSP plot respectively. The negative and positive slopes indicate the presence of lattice shrinkage and tensile strain in the lattice[143,144].

Intensity ratio $\boldsymbol{i = \frac{I_{(101)}}{I_{(002)}}}$

where $I_{(101)}$, $I_{(002)}$ are the intensities of the ZnO (101) and (002) peaks.

### ***2.7.2 Band gap and band edge calculation***

The optical energy band gap of the photocatalyst is calculated from the Tauc's plot by using,

$$\alpha h\vartheta = A(h\vartheta - E_g)^n;\ A = Constant = (^{e^2}/_{nch^2m_e^*})(2m_r)^{\frac{3}{2}}$$

where, α=absorption coefficient ($cm^{-1}$), hν=photon energy (eV), n= constant depending upon the electron transition =1/2 for direct allowed transition, =2 for indirect allowed transition, $E_g$= optical band gap energy (eV), $m_e^*$= effective mass, $m_r$= reduced mass of the charge carriers.

The valence band and conduction band edge positions of the photocatalysts are calculated by using the Mulliken electronegativity theory:

$$E_{VB} = \chi - E_e + \frac{E_g}{2};\ E_{CB} = \chi - E_e - \frac{E_g}{2}$$

where χ= geometric mean of the Mulliken electronegativity of the constituent atoms in the semiconductor =5.89 eV, $E_e$=energy of free electron vs hydrogen =~4.5 eV, $E_g$=bandgap energy (eV).

### *2.7.3 Charge carrier lifetime calculation*

The electron decay lifetimes of the samples were calculated by using Pico Second Time-Resolved Fluorimeter (Make: Eddinburg Instruments, Model: Lifespec II) with an instrumental resolution of ±2ps in the 0-50 ns time range, excited by 375 nm laser.

In TRPL, Time-resolved photoluminescence spectroscopy, the an intense laser pulse is used for optical excitation to attain nonequilibrium electron and hole densities and the excess carriers ($n(t_0) = n_{tot}(t_0) - n_{eq}(t_0)$; where $n_{tot}(t_0)$ = total carrier density, $n_{eq}(t_0)$=equilibrium carrier density, at the end of laser pulse excitation $t_0$) relax by recombination to equilibrium. The recombination process includes (a) radiative- emission of photons by electron-hole recombination or band-to-band transition, and (b) non-radiative- dissipating the energy through heat by recombination. The decay emission and recombination can be mono-molecular, bi-molecular, tri-molecular, or higher molecular recombination involving one, two, three, and a higher number of carriers respectively.

The non-radiative decay rate i.e., Shockley-Read-Hall (SRH) recombination, is described by the mono-molecular process given by,

$R_{non} = An_{tot}(t)$; where A=non-radiative decay proportionality constant (A>0)

As the radiative recombination involves electron-hole pair for band-band recombination, a bi-molecular process, the radiative recombination rate is given by,

$R_{rad} = Bn_{tot}(t)p_{tot}(t)$; where B= radiative decay proportionality constant (B>0)

In addition to the radiative and non-radiative SRH recombination, Auger recombination, a tri-molecular process is also an important recombination process involving electron-hole pair and other electron or hole carriers. The Auger recombination rate is given by,

$R_{Aug} = C^1 n_{tot}^2(t)p_{tot}(t) + C^2 p_{tot}^2(t)n_{tot}(t)$; where $C^1$ and $C^2$ are Auger decay proportionality constant

Thus, the total recombination rate for an optical relaxation is given by,

$$R_{tot} = -\frac{dn}{dt} = R_{non} + R_{rad} + R_{Aug}$$

$$-\frac{dn}{dt} = An_{tot}(t) + Bn_{tot}(t)p_{tot}(t) + C^1 n_{tot}^2(t)p_{tot}(t) + C^2 p_{tot}^2(t)n_{tot}(t);$$

In the initial period of high excitation, the total carrier density is similar to the excess carrier density and $n_{tot}(t)=n(t)=p(t)$. Thus, the total rate of carrier recombination is deduced to,

$$-\frac{dn}{dt} = An(t) + Bn^2(t) + Cn^3(t);$$ also known as ABC equation.

The PL recombination or decay curves were fitted using exponential one- or multi-component fit using

$I = \sum_{i=1,2,3\ldots} I\ exp(\frac{t}{\tau_i})$; i=2 for bi-exponential fit, i=3 for tri-exponential fit…

The average charge carrier lifetime (nanoseconds) for multi-exponential fit is calculated by[145]:

$$\tau_i = \sum_{i=1,2,3..} B_i\tau_i^2 \,/\, \sum_{i=1,2,3,..} B_i\tau_i$$

where i=no. of fitting component, $B_i$=amplitude, $\tau_i$=decay time.

The lifetimes of the samples are calculated by two different methods,

Amplitude-weighted; $\tau_{avg}^{amp} = \sum_{i=integer} \frac{a_i\tau_i}{a_i}$

Intensity-weighted lifetimes: $\tau_{avg}^{int} = \sum_{i=integer} \frac{a_i\tau_i^2}{a_i\tau_i}$;

where $a_i$=intensity ratio factor for $i^{th}$ component. The quality of fitting is determined by the value of $\chi^2$ equals to or nearly equal to 1.

***2.7.4 Photocatalytic advanced oxidation process parameters calculation***

The degradation rate is calculated from the Langmuir Hinshelwood mechanism using the formula:

$$\ln\left({}^{C_0}/_{C_t}\right) = kt$$

$C_0$=concentration at time t=0, $C_t$= concentration at time t.

The linear fitting curve of the $\ln(\frac{C_0}{C_t})$ plot against the irradiation time in minutes gives the highest correlation value ($R^2$) of 0.99, an indication of good curve fitting. The photocatalytic degradation efficiencies of all the experiments are calculated using:

$$\eta(\%) = \frac{C_0 - C_t}{C_0} \times 100$$

where $C_0$= initial concentration, $C_t$= concentration at time t.

The degradation rate of all samples is determined from the experimentally obtained data by plotting $\ln(C_0/C_t)$ on the y-axis against time (minutes) on the x-axis for both UV and natural sunlight-assisted photocatalytic degradation. The points were fitted using linear curve fitting by following the pseudo-first-order reaction rate kinetics model given by,

$$\ln\left({}^{C_0}/_{C_t}\right) = kt$$

where t=time in minute, k=degradation rate constant ($min^{-1}$).

### ***2.7.5 ZnO growth kinetics in different solvents***

The distinct nucleation and crystal growth in these variable conditions resulted in the change of ZnO properties. The formation of ZnO nanoparticles in a chemical bottom-up approach includes major five steps: (a) dissociation of the precursor into ions, (b) nuclei formation, (c) growth, (d) aggregation, and (f) coarsening.

In a colloidal system, the nanoparticle's stability and interaction are described by the Derjaugin-Landau-Verway-Overbeek (DLVO) theory. For stable dispersion, attractive van der Waals interaction ($E_A$) is counterbalanced by repulsive electrostatic repulsion ($E_R$)[146,147]i.e. total energy ($E_T$) is given by:

$$E_T = E_A + E_R$$

However, in the case of nanoparticle assembly, other interaction mechanisms like dipole-dipole, van der Waals, and coulombic interaction should also be considered[146,147].

As the aggregation in a colloidal system, a surface charge function depends on the medium ionicity, polarity, pH, and temperature, the growth of the nanoparticles in different solvents is analyzed using coulombic interaction which induces repulsive forces, and the Coulombs law for interaction is given by[146,147]

$$E_R = \frac{q_1 q_2}{4\pi\varepsilon r}$$

where $q_1$, $q_2$=two-particle charge values, ε=medium dielectric constant, r=distance between two particles.

From the above equation, the repulsive Coulombic force is proportional to the particles' charge value and inversely proportional to the solvents' dielectric constant. In this paper, as no surfactants or ligands were used for ZnO synthesis, the surface charge of ZnO nanoparticles

depends upon the solvent polarity[148]. For nanoparticle aggregation, the attractive force is given by the van der Waals interaction depending upon the solvent volume and precursor amount used. The van der Waals interaction for two spherical particles in a given system is given by[146]:

$$E_A = -\int dv_1 \int dv_2 \frac{q^2\lambda}{r^6}$$

where $v_1$, $v_2$ =volumes of the two particles, q=atomic concentration, r=distance between the two particles, λ=van der Waal constant. The contributing factors of $E_A$ viz. solvent volume and precursor amount have been kept constant for the preparation of five different ZnO samples, hence, the contribution of $E_A$ is considered the same. Therefore, the main influencing factor, $E_R$ depending upon the solvent properties (dielectric constant) plays a major role in ZnO nanoparticle growth kinetics. The solvents' intrinsic properties- dielectric constant, polarity, dipole moment, viscosity, and density are given in Table 2.5.

*Table 2.5 Intrinsic physicochemical properties of the solvents used*

| | **Dielectric constant (ε)** | **Polarity** | **Dipole moment (D in C.m)** | **Viscosity (mP.sec)** | **Density (g/mL)** |
|---|---|---|---|---|---|
| **DEG** | 31.69 | 0.713 | 2.31 | 35.7 | 1.118 |
| **DMF** | 36.71 | 0.386 | 3.86 | 0.92 | 0.944 |
| **$H_2O$** | 80.4 | 1 | 1.84 | 1.0016 | 0.998 |

# Chapter 3

# Green Synthesis and Choice of Precursor: Optimization of Parameters

## Part A: Green synthesis of ZnO nanoparticles using aloe vera and lemon extracts

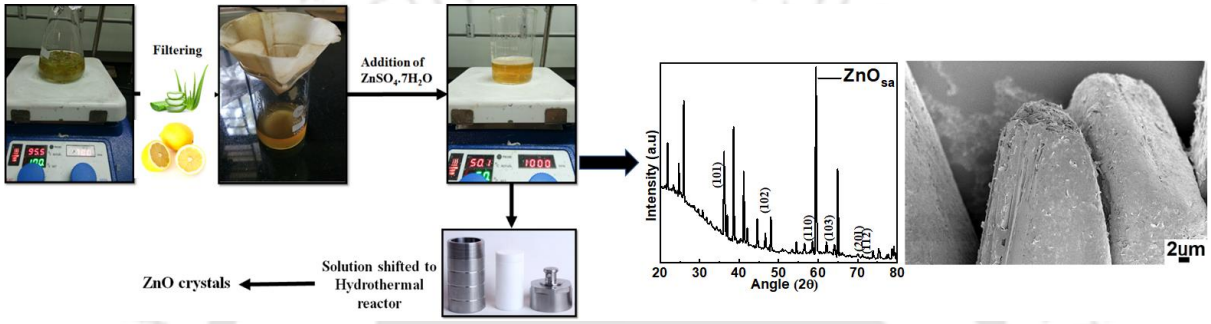


***Graphical abstract of Part A***

*Thongam, D. D.; Chaturvedi, H. Effect of Biochemical Compounds on ZnO Nanomaterial Preparation Using Aloe Vera and Lemon Extracts. Mater. Today Proc. 2020, 44, 4299–4304. https://doi.org/10.1016/j.matpr.2020.10.548.*

### 3.1 Green synthesis

Plants and microbes are two examples of the endless supply of bio-applicable life that nature provides. Due to their unlimited resources, biocompatibility, simplicity, cost-effectiveness, and ability to combat the rise in environmental degradation brought on by chemicals and compounds of emerging concern, the use of these natural sources for the synthesis of nanoparticles has emerged as an intriguing area of study. By following the nanobiotechnology approach, using different parts of the plant extracts like leaves (tulsi[149], Coriandrum Sativum[150], aloe vera[151]), flowers (Hibiscus sabdariffa[152], Cassia auriculata[153],), fruits (guava, orange, fig, lemon), and others [154], these nanoparticles are synthesized. Both lemon (*Citrus limon*) and aloe vera (*Aloe Barbadensis*) are widely recognized for their curative effects and are readily available. In addition to the plants' inherent antibacterial qualities, the biomolecules found in these plants can function as reducing, capping, and stabilizing agents in the production of nanoparticles[155]. Approximately 99% of aloe vera is water, with the remaining 1% consisting

of various substances such as fat and water-soluble vitamins, minerals, enzymes, non-enzymatic systems, amino acids, terpenoids, sterols, and other chemicals. Citric acid, ascorbic acid, polyols, and amine-free amino acids are just a few of the carboxylic acids found in lemons, which are also known for their antioxidant and nutritional benefits. Fruit peel extracts are also a good source of proteins and flavonoids.

In the first half of this chapter, we first examine how plant extracts, specifically those derived from lemon fruit and aloe vera, can shed light on the production of ZnO nanoparticles. The nanoparticles are synthesized using: (1) chemical precipitation method, and (2) hydrothermal processes with two different zinc sources: (1) zinc acetate ($Zn(CH_3COO)_2.2H_2O$), and (2) zinc sulphate ($ZnSO_4.7H_2O$). With the use of aloe vera extracts in the precipitation method, ZnO precipitates were not formed. Therefore, only ZnO samples synthesized using the hydrothermal method and the combination of acetate source/sulphate source and lemon/aloe vera extracts are considered to investigate the feasibility and effectiveness of the green synthesis approach. Here, $ZnO_{sa}$ indicates ZnO synthesized using sulphate source "s" using aloe vera extract "a". Similarly, $ZnO_{aa}$ indicates ZnO(acetate source, aloe vera), $ZnO_{sl}$(sulphate source, lemon extract), and $ZnO_{al}$ (acetate source, lemon extract.)

### ***3.1.1 Structural and morphological analysis***

Figure 3.1.1 (a-d) shows the XRD spectra of the synthesized samples: $ZnO_{sa}$, $ZnO_{aa}$, $ZnO_{sl}$, and $ZnO_{al}$. Analyzing the XRD spectra, the existence of additional peaks indicates the presence of impurities in the sample with a sign of incomplete ZnO crystal formation (JCPDS-00-036-1451 for pure ZnO). These impurity peaks may have originated from the biomolecules present in the lemon and aloe vera extracts. However, the identification of the impurity peaks corresponding to certain biomolecules is still on the dark side. To investigate the elements, present in the samples, elemental analysis was carried out (EDX analysis) and is shown in Figure 3.1.1 (e, f), and its corresponding atomic % of the elements present is summarised in Table 3.1.1. The $ZnO_{sa}$ synthesized using aloe vera extract showed the presence of Zn, O, and C with an atomic % of 21.1, 66.5, and 12.4% respectively for spectrum 1. The ZnO sample prepared using lemon fruit extract shows traces of Na, Mg, and Ca in 2.3, 0.1, and 0.1 atomic % respectively with the major constituents of Zn, O, and C at 10.7, 40.1, and 46.7 atomic %. These showed the carbon and other elements contributed from the organic carbons and minerals present in aloe vera and lemon extract.

*Table 3.1.1 Elemental compositions of $ZnO_{sa}$ and $ZnO_{al}$*

| Elements | Atomic % Spectrum 1 | Atomic % Spectrum 2 | Atomic % Spectrum 1 | Atomic % Spectrum 2 |
|---|---|---|---|---|
| | $ZnO_{sa}$ | | $ZnO_{la}$ | |
| **Zn** | 21.1 | 20.2 | 10.7 | 8.2 |
| **O** | 66.5 | 20.2 | 40.1 | 42.1 |
| **C** | 12.4 | 14.9 | 46.7 | 45.7 |
| **Na** | | | 2.3 | 2.9 |
| **Mg** | | | 0.1 | 0.4 |
| **Ca** | | | 0.1 | 0.7 |

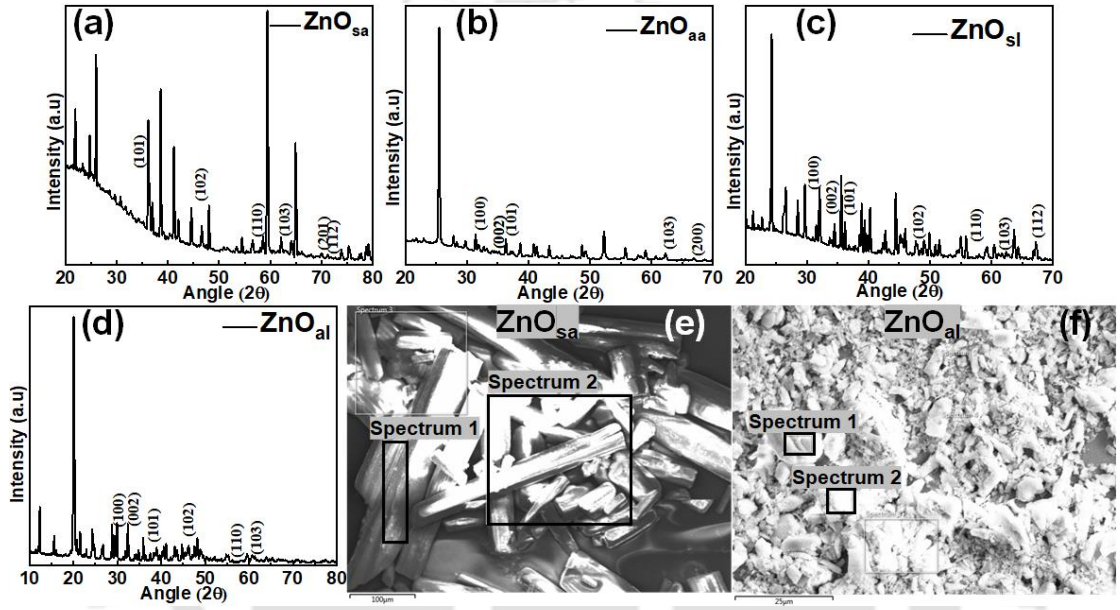


*Figure 3.1.1 shows the XRD pattern of (a) $ZnO_{sa}$, (b) $ZnO_{aa}$, (c) $ZnO_{sl}$, and (d) $ZnO_{al}$, EDX data of (e) $ZnO_{sa}$, and (f) $ZnO_{al}$*

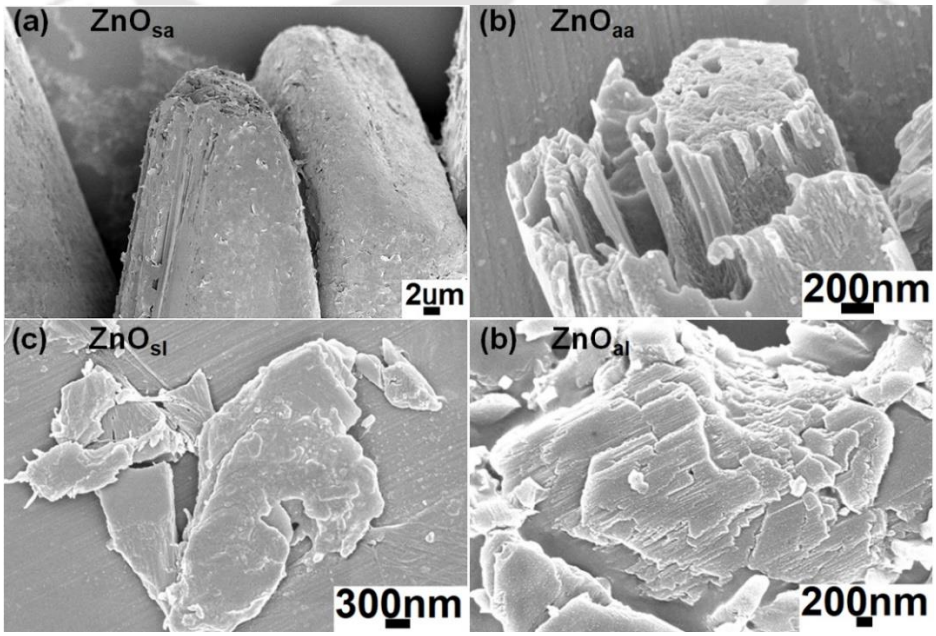


*Figure 3.1.2 FESEM images of (a) $ZnO_{sa}$, (b) $ZnO_{aa}$, (c) $ZnO_{sl}$, (d) $ZnO_{al}$*

The FESEM images of the ZnO samples are shown in Figure. 3.1.2 (a-d). The morphologies do not have definite shapes and sizes but show a cluster of chunk particles with rough mineral-like surfaces. As the particles do not exhibit a definite morphology and show chunk particles, the smallest to largest size ranges from 200 nm to 5 μm.

### ***3.1.2 Results and Discussion of the green synthesized ZnO***

Lemon is high in carboxylic acids, including citric acid, ascorbic acid, polyols, amine-free amino acids and proteins, and flavonoids (molecular structure shown in Figure 3.1.3). Citric acid and flavonoid carboxylate, hydroxyl, and amine groups combine with metal ions ($Zn^{2+}$) in the reaction media to generate complex compounds and structures[154,156]. In addition to their function as stabilizing/capping agents, the citric acids, ascorbic acid, limonoids, and flavonoids found in lemon extracts also function as reducing agents to regulate the size, shape, and physical characteristics of Zn compounds. The citric acid present in lemon, as compared to ascorbic acid, is recognized for its high reducing activity, and its concentration impacts the size and shape of the resulting sample[157–159]. Here, the $Zn^{2+}$ ions from the $Zn(CH_3COO)_2.2H_2O$ and $ZnSO_4.7H_2O$ dissociation chelate with the citrate ions to form hexa-hydric and penta-basic rings through the carboxyl and hydroxyl groups. These complexes formed undergo dehydration and esterification to form stable compounds in addition to the $Zn(OH)_2$[157]. Thus, the presence of biomolecules—citric acids, ascorbic acids, and flavonoids induces in generating polymorphism in the ZnO samples. This polymorphism is evident from the XRD spectra shown in Figure 3.1.1 (a, b, c, d); however, the illustration of the final compound structure is difficult owing to the complex ingredients of the biomolecules present in the plant extracts. In certain instances, these Zn complexes can be inferred into ZnO crystals by subjecting them to intense heat applications at 400°C, thereby creating ZnO crystal[156]. The direct ionic interaction between the $Zn^{+2}$ ion and the biomolecules may have prevented the ZnO complexes from being converted into pure ZnO crystals in this case.

Similarly, aloe vera leaf extract-produced ZnO samples exhibit crystal impurities, and establishing a reaction phenomenon is difficult since it involves several complicated biological chemicals, contrary to those prepared using a specific chemical reductant like NaOH or KOH. The bioactive compounds present in aloe vera contain functional groups— amines, hydroxyl, and carbonyl. These functional groups cross-linked with the charged metal ions ($Zn^{2+}$) to form metal complexes[154,158,159]. The aloe vera extracts contain bioactive compounds like saccharides, amino acids, enzymes, lipids, sterols, etc. Among these bioactive compounds, the organic

moieties containing phenolic groups are known to be involved in $TiO_2$ synthesis[154]. In Figure 3.1.4, we see a plausible reaction process for nanoparticle production that involves activating metal ions from dissociating metal precursors. A slow dissociation is initiated by the biomolecules present because of the plant extract's limited reduction capabilities, marking the initial nucleation phase. Through the functional groups and π-electrons by weak van der Waals force or ionic bonding, the metal ions interact and legate with the biomolecules present. Following the nucleation, the size of the nanoparticles grows through the growth process[158,160]. Thus, the nanoparticle size depends upon the plant extract concentration and its reducing ability.

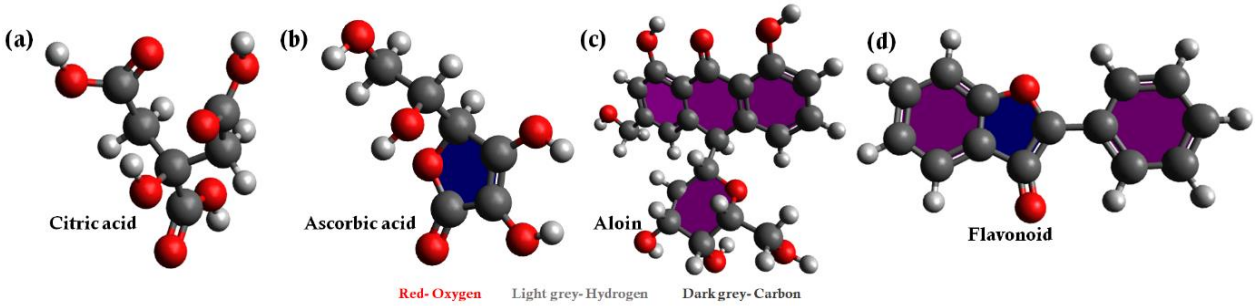


*Figure 3.1.3 Molecular structure of (a) Citric acid, (b) Ascorbic acid, (c) Alion, and (d) Flavonoid*

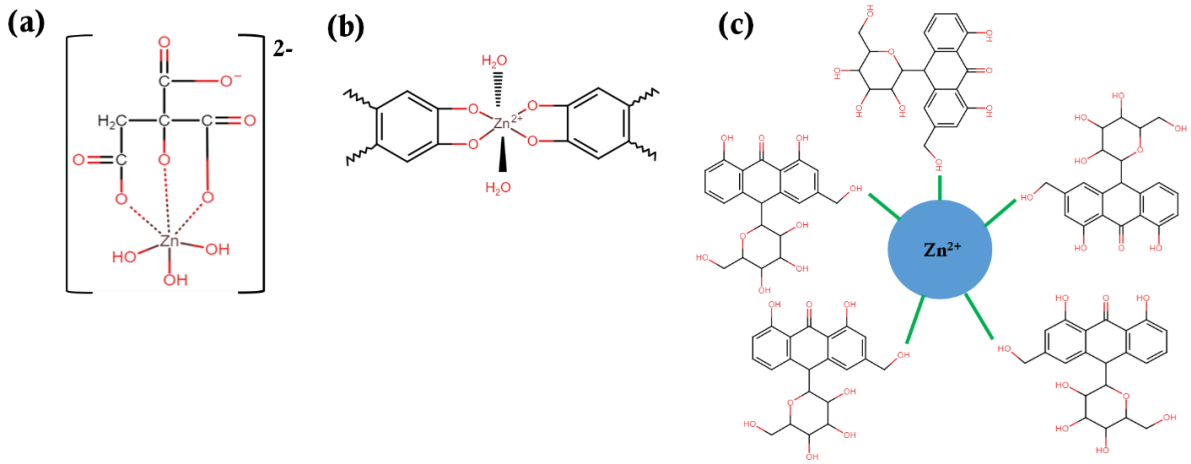


*Figure 3.1.4 illustrates the complex formation with the biomolecules (a) citric acid present in lemon extracts[161], (b) aromatic hydroxyl groups[159], and (c) aloin (polyphenol) present in aloe vera extract (adapted from [162])*

The metal ions surrounded by the biomolecule complexes undergo hydrolysis and reversed micellization, and form the final metal ion complex. The surrounding biomolecules in the metal-ion complex act as the surfactant and agglomeration of nanoparticles are inhibited[159]. These polymeric complexes stayed chelated on the ZnO surface which is evident from the XRD analysis[159]. Some of the advantages of using biomolecules apart from bio-compatibility are:

biomolecules act as (i) surface modifier[158], (ii) stabilizing agents to inhibit agglomeration by creating a barrier from steric or electrostatic repulsions, (iii) electron shuttles for the metal ion reduction[159], and (iv) template/ structure-directing agent[159].

Figure 3.1.4 illustrates a plausible hypothesis for the formation of zinc complexes with the biomolecules present in lemon and aloe vera extracts- (a) citric acid from lemon extracts[158,161], (b) aromatic hydroxyl groups[159] and (c) aloin (polyphenol) from aloe vera extract[162]. As these biomolecules have strong chelating ability, they are readily attached and adsorbed onto the nanoparticle's surfaces forming complex structures. Hence, although green synthesis is biocompatibility, the nanoparticle formation mechanisms are still unclear. From the study, the green synthesis is not found to be suitable due to the formation of the Zn complex with the biomolecules present in aloe vera and lemon fruit extracts. The biomolecules are persistent to remove through repeated washing, drying, and calcination.

### ***3.1.3 Findings of Part A (Green Synthesized ZnO)***

- Because of the availability, biocompatibility, and presence of bioactive compounds, aloe vera, and lemon fruit were used as a reducing agent to synthesize ZnO nanoparticles by hydrothermal method.
- As lemon is rich in carboxylic acids, polyols, proteins, and flavonoids, and aloe vera is rich in phenolic compounds, the bioactive compounds form the metal complex through the linkage of metal ions ($Zn^{2+}$) and the functional groups of the biomolecules. This showed the presence of impurities, which originated from the biomolecules.
- Thus, from the analysis, the green synthesis is not found to be suitable for high-quality metal oxide synthesis due to the formation of the Zn complex with the biomolecules present in aloe vera and lemon fruit extracts.

## Part B: Optimization of reaction parameters

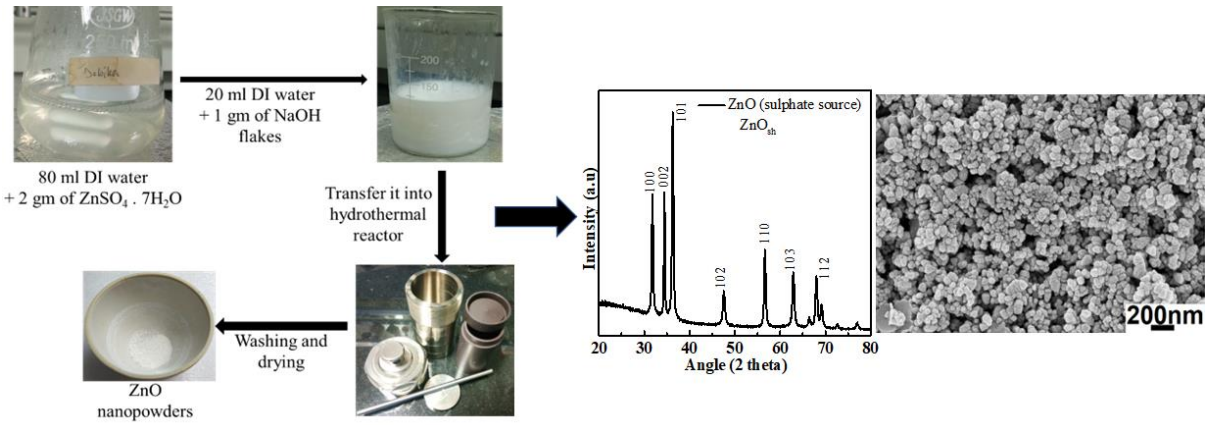


***Graphical Abstract of Part B***

## 3.2. Choice of precursor: Zinc Acetate or Zinc Sulphate

"Actions and reactions are always the forces in pairs", we have all learned from our childhood, "if we apply any force, there will always be a reaction". The same physiology applies in our kitchen and laboratory. What ingredients we choose to prepare something will henceforth change the outcome. Thus, to tune and control the properties of a material to synthesize in a chemical laboratory, the ingredients selection and modus operand will eventually exhibit in the outcome of the product. Based on the criteria of the application for maximum efficiency and performance, the properties of the ZnO are tuned by controlling the above-mentioned ingredients known as precursors and modus operand i.e., preparation methods. Some controllable properties of ZnO include particle sizes, morphologies, surface, optical, electronic, and crystal properties. The change in the synthesis medium in a bottom-up chemical synthesis process will thereby affect the ZnO properties.

### ***3.2.1 Structural and morphological analysis***

The four ZnO nanoparticles ($ZnO_{sh}$, $ZnO_{ah}$, $ZnO_{ap}$, $ZnO_{sp}$ where the suffix s: zinc sulphate source, a: zinc acetate source, h: hydrothermal, p: precipitation method) were prepared using different synthesis methods (hydrothermal and precipitation) and different zinc sources ($ZnSO_4.7H_2O$ and $Zn(CH_3COO)_2.2H_2O$). $ZnO_{sh}$ and $ZnO_{sp}$ exhibited the formation of porous rough surface quasi-spherical morphologies by aggregating smaller sub-nano-sized ZnO particles forming larger particles (Figure 3.2.1 a, d). The ZnO nanoparticles synthesized by similar zinc sulphate sources exhibited similar morphologies. All the particle sizes vary from 100 nm to 200 nm. Unlike the $ZnSO_4.7H_2O$ source, ZnO synthesized from

$Zn(CH_3COO)_2.2H_2O$ shows a non-uniform shape and size distribution. The flake structure formation in $ZnO_{ah}$ of ~200 nm along with nano aggregates (Figure 3.2.1 b) is possibly due to the stable growth environment maintained in hydrothermal reaction.

The comparative XRD analysis of $ZnO_{sh}$, $ZnO_{ah}$, $ZnO_{ap,}$ and $ZnO_{sp}$ samples shown in Figure 3.2.2 a confirms good crystallinity with hexagonal wurtzite phase structure of space group $P6_3mc$ and no impurity peaks were present (JCPDS-00-036-1451). ZnO synthesized by hydrothermal method; $ZnO_{sh}$ and $ZnO_{ah}$ show higher 2θ degrees peak shift, broadening of FWHM in $ZnO_{sh}$ as compared to $ZnO_{sp}$ and $ZnO_{ap}$ (Figure 3.2.2 b). This behavior coincides with the increasing crystallite sizes and is possibly contributed by the changes in lattice parameters which resulted in the variation of crystallite sizes[163]. ZnO of similar synthesis methods; $ZnO_{ap}$ & $ZnO_{sp}$, and $ZnO_{sh}$ & $ZnO_{ah}$ show the same peak positions (Figure 3.2.2 b). The bond length and bond radii are changed due to the presence of lattice strain/ lattice-mismatched causing changes in the crystal structures, a diversion from the intrinsic wurtzite hexagonal structure. The peak shift towards the higher 2θ degrees indicates the compaction occurred in the unit cell and vice versa and a decrease in the lattice parameter[164,165]. With the increase in lattice strain and peak shift to lesser 2θ degrees, the crystallite sizes reduce, which correctly falls for these synthesized samples. Due to the uniform distribution of temperature and pressure in the hydrothermal method, the crystal growth took place continuously and uniformly for $ZnO_{ah}$ and $ZnO_{sh}$. In the precipitation method ($ZnO_{sp}$ and $ZnO_{ap}$) due to continuous stirring, the crystals undergo stress-strain and 2θ peak shifts to a lesser angle than that of hydrothermal with the reduction in crystallite sizes (calculated using Debye-Scherrer's formula) from 29 to 26 nm and 27 to 19 nm for acetate and sulphate source respectively. The crystallite sizes of different ZnO are found to be in the order of $ZnO_{ah} > ZnO_{sh} > ZnO_{ap} > ZnO_{sp}$ with 29, 27, 26, and 19 nm respectively. The relationship between crystallite sizes and intensity ratios of (101) and (002) planes is shown in Figure 3.2.2 c. This showed the linear dependence of crystallite sizes on the $I_{(101)}/I_{(002)}$ intensity ratio. Further, an increase in the $I_{(101)}/I_{(002)}$ value shows elongation in the c-axis, a polar plane of ZnO, to minimize surface energy. Also, the crystallite sizes calculated from the XRD analysis are found to be smaller than the particle sizes calculated from the FESEM images which are due to the aggregation and growth of the nanoparticles to form nanoaggregates and flakes-like structures[166,167].

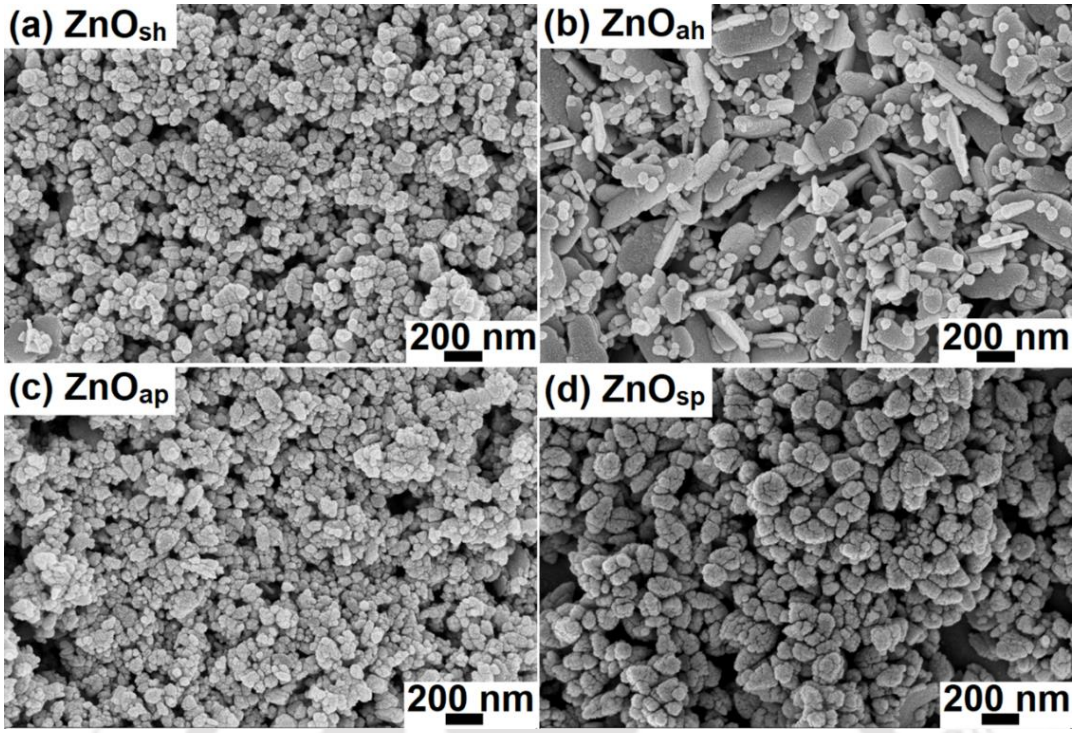


*Figure 3.2.1 FESEM images of (a) $ZnO_{sh}$, (b) $ZnO_{ah}$, (c) $ZnO_{sp}$ and (d) $ZnO_{sp}$*

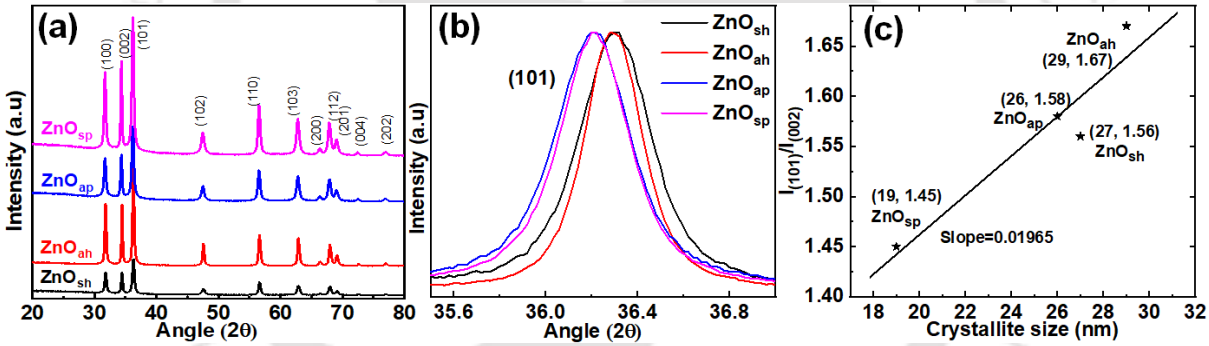


*Figure 3.2.2 XRD pattern for (a) $ZnO_{sh}$, $ZnO_{ah}$, $ZnO_{ap}$, $ZnO_{sp}$, (b) comparison of normalized (101) plane, (c) relative study of crystallite sizes to intensity ratio $I_{(101)}/ I_{(002)}$ of the ZnO synthesized calculated from XRD data*

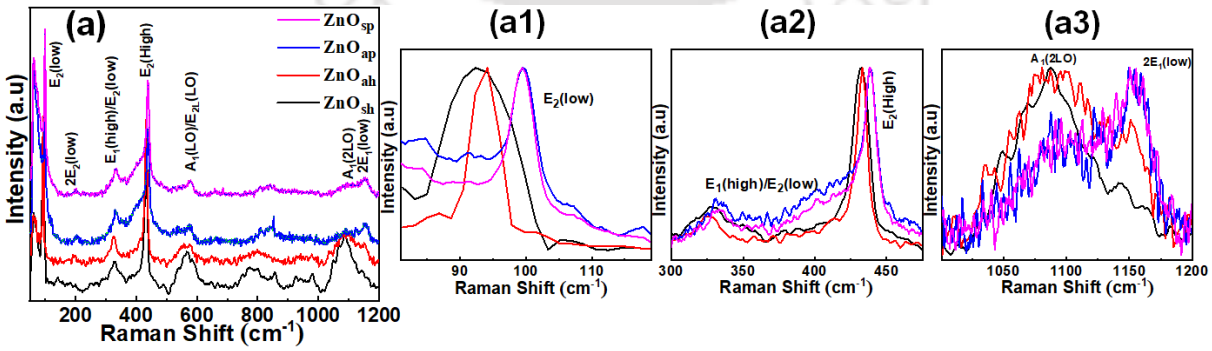


*Figure 3.2.3 Comparison of Raman spectra for (a) four ZnO synthesized from zinc sulphate and zinc acetate source with hydrothermal and precipitation method; $ZnO_{sp}$, $ZnO_{ap}$, $ZnO_{ah}$, and $ZnO_{sh}$ [normalized peak shift comparison for ZnO samples for the (a1) $E_2$(low), (a2) $E_1$(high) and $E_2$(high), (a3) $A_1$(2LO) and $2E_1$(low) peaks*

The Raman spectra of four ZnO; $ZnO_{ah}$, $ZnO_{ap}$, $ZnO_{sh,}$ and $ZnO_{sp}$ show high crystallinity with wurtzite phase structure significant peaks (Figure 3.2.3 a); $E_2$(high) at 433, 438, 433 and 438 $cm^{-1}$ respectively, as agreed with XRD analysis. Complementing XRD result analysis, Raman spectra show similar behavior where the same peak positions of $E_2$(high) were seen for ZnO samples of similar synthesis methods i.e., $ZnO_{ah}$ & $ZnO_{sh}$ at 433 $cm^{-1}$ and $ZnO_{ap}$ & $ZnO_{sp}$ at 438 $cm^{-1}$, regardless of the varied zinc source. The shifting of Raman $E_2$(high) and $E_2$(low) peak by 5 $cm^{-1}$ (Figure 3.2.3 a1, a2) is contributed by the change in d-spacing resulting from crystallite size variation. Also, the alteration in the reaction environment creates shifting in ZnO vibration peaks by creating defects, strain, and stress-causing localization of phonons and subsequently peak shift. Due to the changes in bond length, chemical bond vibration also shifts to lesser or higher wavenumbers based on the increase or decrease in bond length correspondingly[168]. Thereby, due to smaller bond length and lesser crystallite sizes in $ZnO_{ap}$ and $ZnO_{sp,}$ $E_2$(high) is observed at 438 $cm^{-1}$ as compared to hydrothermally synthesized $ZnO_{ah}$ and $ZnO_{sh}$ at 433 $cm^{-1}$. In conclusion, based on crystallite sizes, hydrothermally synthesized ZnO firstly shows larger crystallite sizes than precipitately synthesized ZnO albeit varied zinc source and secondly, it shows lesser lattice strain with a change in lattice spacing. Other ZnO Raman peaks; $E_2$(low), $2E_2$(low), $E_1$(high)/$E_2$(low), $A_1$(LO), $A_1$(2LO) and $2E_1$(low) were seen at ~99, ~203, ~334, ~577, ~1094 and ~1155 $cm^{-1}$ respectively (Figure 3.2.3 a). The high intensity of $E_2$(high) shows good crystalline quality with $C_{6V}$ symmetry, where $O^{2-}$ and $Zn^{2+}$ are interconnected by surrounding $Zn^{2+}$ ions with four $O^{2-}$ ions and vice versa. In summary, shifting in $E_2$(high) is associated with the intermolecular Zn-O bond stress, vacancies, defects, particle size variation, and dislocations.

### ***3.2.2 ZnO formation mechanism***

The resulting ZnO synthesized from the $ZnSO_4.7H_2O$ source shows smaller crystallite sizes when compared to ZnO synthesized from $Zn(CH_3COO)_2.2H_2O$ source, as a moderate amount of $OH^-$ ions are present from $Zn(CH_3COO)_2.2H_2O$ dissociation in $H_2O$ resulting in pH>7. Whereas, a moderate amount of $H^+$ ions are generated when $ZnSO_4.7H_2O$ is dissociated in $H_2O$ and shows an acidic medium with pH<7. Therefore, the presence of more $OH^-$ ions enhances the rapid growth of the crystal in zinc acetate solution precipitating out larger crystallite size ZnO nanoparticles[166,169]. The ZnO crystals are found to be oriented in the polar surface of (101) growth direction. The mechanism of nucleation and growth of ZnO nanoparticles with different zinc sources are illustrated in Table 3.2.1 with a sequence of reactions that occurred following the numbering.

*Table 3.2.1. Reaction sequence for the preparation of ZnO with two different zinc sources*[167,170]

| Equation | Zinc Sulphate source | Zinc Acetate source |
|---|---|---|
| 1. | $ZnSO_4.7H_2O \xrightarrow{aq.\ medium} Zn^{2+} + SO_4^{2-} + 7H^+ + 7OH^- \rightarrow Zn(OH)_2$ | $Zn(CH_3COO)_2.2H_2O \xrightarrow{aq.\ medium} Zn^{2+} + 2(CH_3COO)^- + 2H^+ + 2OH^-$ |
| 2. | $Zn^{2+} + 2OH^- \xrightarrow{H_2O} Zn(OH)_2$ | |
| 3. | $Zn(OH)_2 \xrightarrow{NaOH} [Zn(OH)_4]^{2-}$ | |
| 4. | $SO_4^{2-} \xrightarrow{NaOH} Na_2SO_4$ Or $SO_4^{2-} \xrightarrow{NaOH} NaHSO_4$ | $(CH_3COO)^- \xrightarrow{NaOH} NaCH_3COO$ |
| 5. | $the\ Zn(OH)_2 \xrightarrow{H_2O} [Zn(OH)_4]^{2-}$ | |
| 6. | $[Zn(OH)_4]^{2-} \xrightarrow{heat/drying} ZnO + H_2O$ <br> $Zn(OH)_2 \xrightarrow{heat/drying} ZnO + H_2O$ | |

The zinc sources ($ZnSO_4.7H_2O$ or $Zn(CH_3COO)_2.2H_2O$) are dissociated into $Zn^{2+}$ and $SO_4^{2-}$ or $CH_3COO^-$ ions in the reaction medium ($H_2O$) with the formation of the first non-zero charged precursor zinc complex, $Zn(OH)_2$, a process called nucleation. The process marks a toll point of manifold ZnO seed formation in the initial stage, believed to form "burst nucleation" when heat and vigorous stirring are applied continuously (Table 3.2.1- Eq. 1 and 2). This led to the formation of homogeneous nuclei, building up supersaturation from the dissociation of zinc salt with water molecules[171]. Table 3.2.1 shows the sequence of reactions for the formation of nuclei and crystal growth, taking place in the formation of ZnO nanoparticles. With the addition of basic aq. NaOH solution as shown in Eq. 3 (Table 3.2.1), the pH of the colloidal solution is lowered, therefore, the growth process dominates the nucleation regime of forming zinc hydroxide molecules. Subsequently, the polycondensation process of Zn-OH took place, creating Zn-O-Zn entities with aq. NaOH solution[167,169,172,173].

### ***3.2.3 Photocatalytic degradation***

To test the performance of the four synthesized $ZnO_{sh}$, $ZnO_{ah}$, $ZnO_{ap}$, and $ZnO_{sp}$ nanoparticles, photocatalytic degradation of 50 ml 10 ppm RhB dye solution under the illumination of UVC light was evaluated. Figure 3.2.4 a shows the degradation curves of the pollutant in the presence of a photocatalyst. ZnO synthesized using a zinc acetate source in the precipitation method, $ZnO_{ap}$ exhibited the highest degradation efficiency of 91% for the total reaction time of 3 hr.

The lowest degradation efficiency is shown by the hydrothermally synthesized ZnO nanoparticles ($ZnO_{ah}$) with the largest crystallite size of 29 nm. The $ZnO_{ap}$ also showed the highest degradation rate of 0.0093 $min^{-1}$. Table 3.2.2 summarises the data obtained from the XRD analysis, photocatalytic degradations, and degradation rates. The proper mechanism of pollutant degradation in the presence of ZnO photocatalyst is well known and the advanced oxidation process for pollutant decomposition under the influence of reactive oxygen species has been explained in detail.

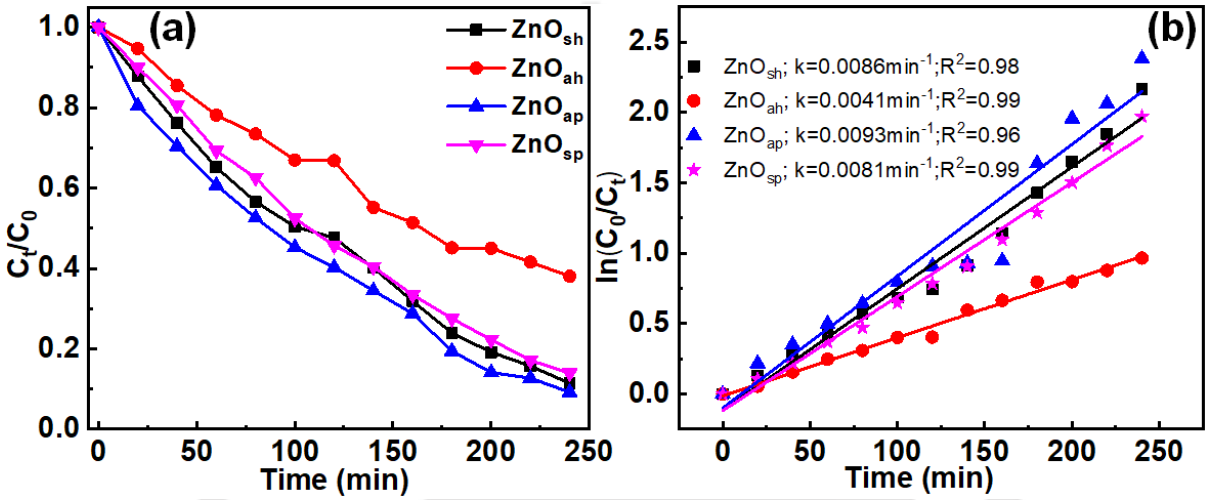


*Figure 3.2.4 (a) Photocatalytic degradation of RhB under the UVC light irradiation, and (b) degradation rate calculation using first-order rate kinetics*

*Table 3.2.2 Summary of results obtained: crystallite size, photocatalytic efficiency, and degradation rate of the ZnO nanoparticles prepared using different zinc sources and synthesis methods*

| | ***$ZnO_{sh}$*** | ***$ZnO_{ah}$*** | ***$ZnO_{ap}$*** | ***$ZnO_{sp}$*** |
|---|---|---|---|---|
| ***Method*** | Zinc sulphate + hydrothermal | Zinc acetate + hydrothermal | Zinc acetate + precipitation | Zinc sulphate + precipitation |
| ***Crystallite size*** | 27 nm | 29 nm | 26 nm | 19 nm |
| ***Efficiency (η)*** | 89% | 62% | 91% | 87% |
| ***Rate ($min^{-1}$)*** | 0.0086 | 0.0041 | 0.0093 | 0.0081 |

### *3.2.3 Findings of Part B (Optimisation of reaction parameters)*

- Four different ZnO nanoparticles: $ZnO_{sh}$, $ZnO_{ah}$, $ZnO_{ap,}$ and $ZnO_{sp}$ are synthesized with two different zinc sources: $ZnSO_4.7H_2O$ and $Zn(CH_3COO)_2.2H_2O$ and two synthesis methods: hydrothermal and precipitation method.
- Among these four ZnO samples synthesized ($ZnO_{sh}$, $ZnO_{ah}$, $ZnO_{ap,}$ and $ZnO_{sp}$), ZnO synthesized from the hydrothermal method and $Zn(CH_3COO)_2.2H_2O$ source shows the largest crystallite size while ZnO synthesized from $ZnSO_4.7H_2O$ source with precipitation method showed the smallest crystallite size.
- ZnO nanoparticles prepared via the precipitation method showed smaller crystallite sizes as compared with the hydrothermal method indicating that the maintenance of the same temperature and pressure inside a hydrothermal reaction process led to the rapid growth of ZnO crystals.
- ZnO nanoparticles synthesized using a zinc acetate source and prepared via precipitation method showed the highest degradation rate and efficiency of 91% in 3 hr reaction time. Thus, the $Zn(CH_3COO)_2.2H_2O$ source is used as the zinc precursor to prepare ZnO samples to tune the physicochemical properties for an enhanced efficiency triggered by natural sunlight in the later part of the thesis (Chapter 3, part C).

## Part C: Effect of synthesis medium on the ZnO nanoparticles

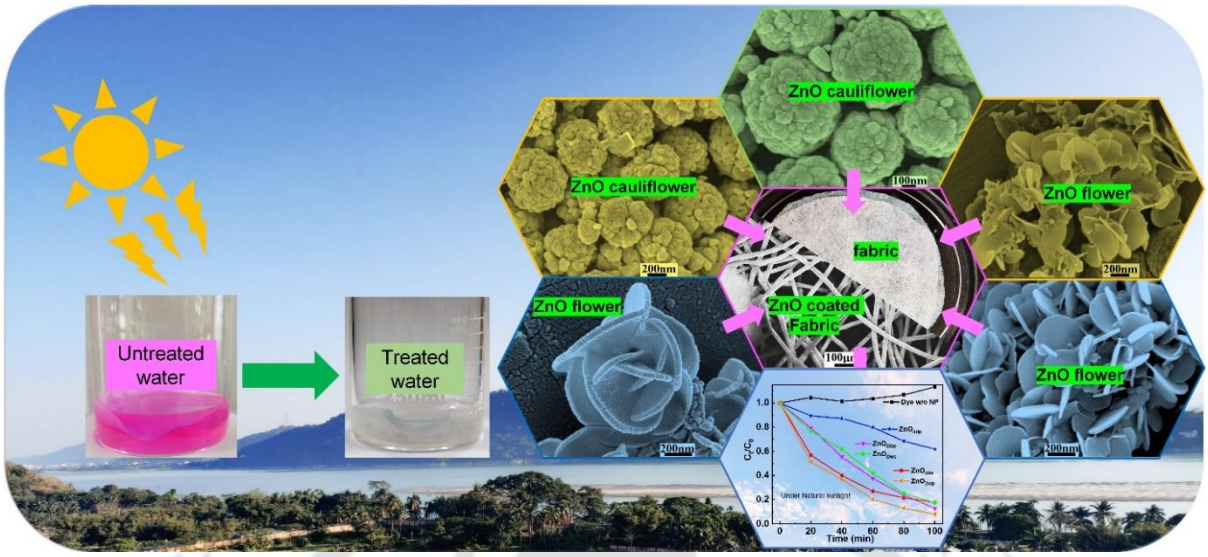


***Graphical Abstract of Part C***

*Thongam, D. D.; Chaturvedi, H. Induced Defect and ZnO Nano-Flower Formation by N, N, Dimethylformamide Solvent for Natural Sunlight Responsive Floating Photocatalytic Advanced Oxidation Process. Chemosphere 2023, 313 (August 2022), 137600. https://doi.org/10.1016/j.chemosphere.2022.137600.*

### 3.3 ZnO nanoflower formation and introducing defects through different synthesis medium

Tuning nanoparticle physicochemical properties for top-notch performance in a colloidal system has been a prime research area in the field of nanotechnology and material science. The understanding and development of growth behavior methods and growth kinetics assist a promising tool to modulate the desired characteristics in engineering nanoparticle physicochemical and optical properties. The shape, size, crystal defects, and surface properties of a nanoparticle play a vital role in determining its physicochemical, optical, and electronic properties[174,175]. Hence, studying the effect of crystal growth behavior in a bottom-up chemical synthesis approach in variable reaction parameters on nanoparticle characteristics is a much-needed task for a material scientist and nanotechnologist. The reaction parameters like type of solvent, precursor, solution pH, temperature, use of surfactants, synthesis method, etc. influence nucleation and growth rate, agglomeration, and coalescence producing unique intrinsic nanoparticle properties[146,172,176,177]. Therefore, as surface charge plays a vital role in a colloidal system and tuning desired physicochemical properties, planning, and selection of suitable reaction parameters are of foremost priority[148,174,178,179]. To reduce the aggregation and

surface energy or charge, surfactants are normally utilized for controllable nanoparticle shape and size while compromising on the reduction and passivation of surface area-related properties and defects.

In the photocatalytic reactions, the role of defects had been shown by L.Zhang et al. by introducing deliberate defects onto the photocatalyst by using defective linkers with different functional groups and acid dissociation constant where an optimal defect concentration provided better performance while too many defects reduced the photocatalytic activity by acting as the recombination site[180]. While adding defects and modifying photocatalyst characteristics are methods for boosting photocatalytic performance, combining two or more compounds allows for the synergistic improvement of photocatalytic performance. This chapter describes how the three most significant challenges to the implementation of photocatalytic water treatment are being surmounted: (a) the development of natural sunlight active ZnO photocatalyst, (b) replacing slurry photocatalytic process by floating photocatalyst removing the controversy of photocatalyst retrieval, (c) re-use of face-mask fabric coated with ZnO photocatalyst for dye degradation.

### ***3.3.1 Structural analysis***

To determine the influence of synthesis medium and methods on the physicochemical properties of ZnO five different morphologies of ZnO nanoparticles are synthesized as given in Chapter 2, subheading 2.2.2, Table 2.3. The crystallite sizes calculated from the Debye-Scherrer formula, $I_{(101)}/I_{(002)}$ intensity ratios, and dislocation or defect density calculated from the XRD data are given in Table 3.3.1. The nature of crystallinity and purity is studied using the XRD pattern shown in Figure 3.3.1 a. The intense diffraction and absence of additional peaks show the successful formation of hexagonal wurtzite phase structure with high crystallinity and pure ZnO structures (JCPDS card no. 00-036-1451) as shown in Figure 3.3.1 b. With the use of DMF as the solvent, the ZnO (101) peaks are shifted to lower and higher angles concerning the ZnO prepared from DEG solvent indicating slight contraction and expansion in the unit cell volume. The XRD peak shifts also indicate an alteration or deformation in the structural and lattice parameters- lattice strain, crystallite sizes, lattice constants, etc.[143,181] While comparing, the $ZnO_{Dws}$ show the narrowest FWHM indicating the highest crystallite size of 46.9 nm.

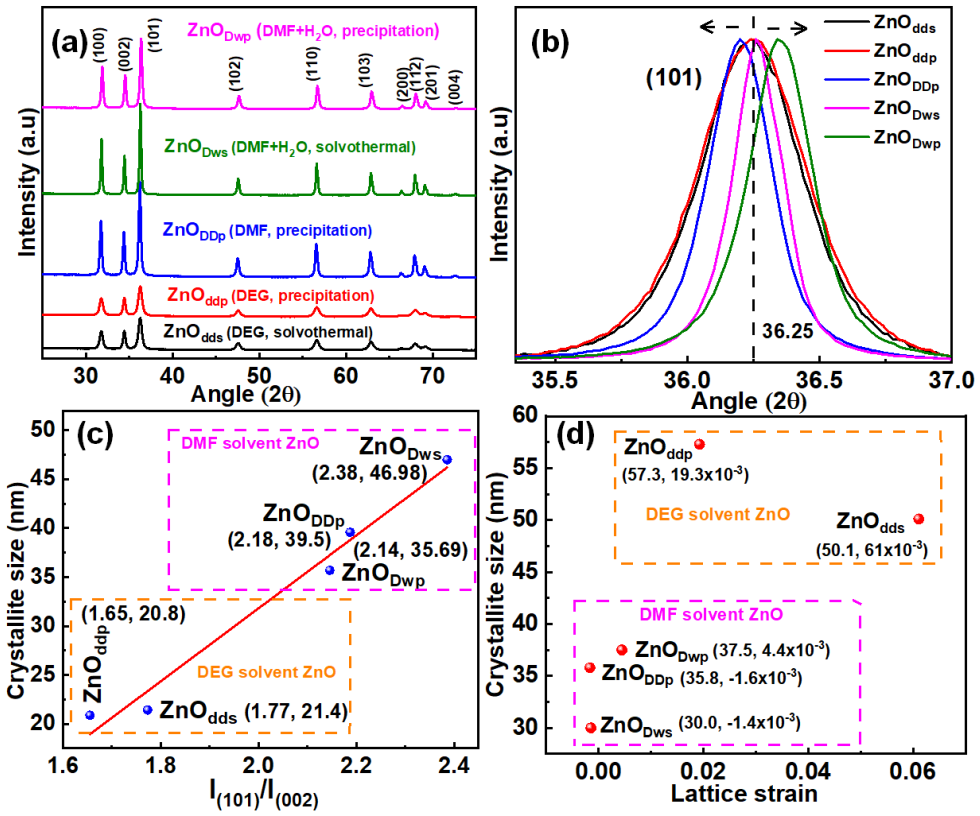


*Figure 3.3.1 (a) XRD analysis of $ZnO_{dds}$, $ZnO_{ddp}$, $ZnO_{DDp}$, $ZnO_{Dws}$, $ZnO_{Dwp}$, (b) normalized (101) plane comparison (c) relation between $I_{(101)}/I_{(002)}$ intensity ratio and crystallite size obtained from Debye-Scherrer formula (d) correlation between crystallite size and lattice strain calculated from the Size-Strain Plot analysis*

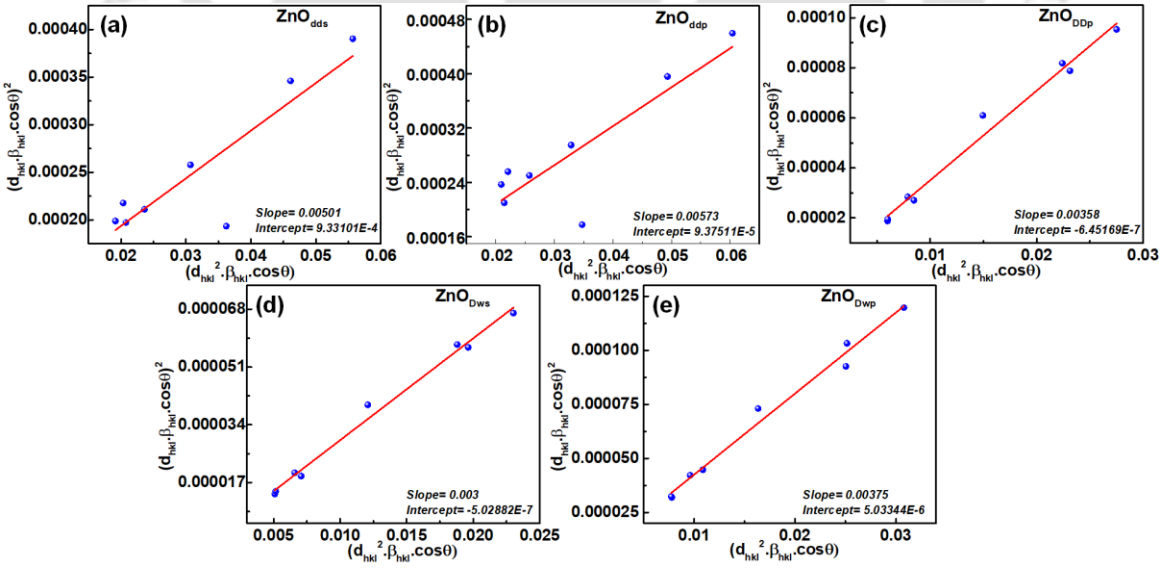


*Figure 3.3.2 Size-Strain plot analysis of (a) $ZnO_{dds}$, (b) $ZnO_{ddp}$, (c) $ZnO_{DDp}$, (d) $ZnO_{Dws}$, (e) $ZnO_{Dwp}$*

The relationship between crystallite size calculated from the Debye-Scherrer formula and the $I_{(101)}/I_{(002)}$ intensity ratio is illustrated by the linear fitted graph exhibited in Figure 3.3.1 c. With the increase in the intensity ratio $I_{(101)}/I_{(002)}$, the crystallite sizes calculated from the Debye-Scherrer formula also increase showing the linear dependency between the two factors. As compared to ZnO+DEG samples, ZnO+DMF samples show higher crystallite sizes as well as higher $I_{(101)}/I_{(002)}$ intensity ratios. The smaller FWHM and high-intensity ratio result in the higher crystallite size, $ZnO_{Dws}$ in this case with 46.98 nm.

Table 3.3.1 also contains information regarding the micro-strain and strain-induced crystallite sizes of these ZnO samples investigated through Size Strain Plot (SSP) analysis and its correlation with crystallite size is shown in Figure 3.3.2 d. In contrast with the crystallite size calculated from the Debye-Scherrer formula, the ZnO+DMF samples show less crystallite sizes and lattice strain as compared with the ZnO+DEG. Although SSP employs a combination of the Gaussian and the Lorentzian functions in considering the XRD peak profiles, this method might be less compatible with investigating the micro-strain and crystallite sizes for the ZnO samples in this case[182,183]. Multiple analyses of XRD parameters suggest that the solvents used in nanoparticle synthesis have a greater impact on the nanoparticles' lattice and structural parameters than the synthesis methods employed.

*Table 3.3.1 Intensity ratio i, Crystallite size (D), Dislocation density (δ), Micro-strain calculated from XRD data and Size-strain plot analysis*

| | **$ZnO_{dds}$** | **$ZnO_{ddp}$** | **$ZnO_{DDp}$** | **$ZnO_{Dws}$** | **$ZnO_{Dwp}$** |
|---|---|---|---|---|---|
| **Solvent, Method** | DEG, Solvothermal | DEG, Precipitation | DMF, Precipitation | DMF+$H_2O$, Solvothermal | DMF+$H_2O$, Precipitation |
| **Intensity ratio $i = \frac{I_{(101)}}{I_{(002)}}$, Crystallite size from Debye-Scherrer formula (nm)** | 1.77, 21.4 | 1.65, 20.8 | 2.07, 39.5 | 2.29, 46.9 | 2.04, 35.6 |
| **Dislocation density ($nm^{-2}$)** | $21.79x10^{-4}$ | $22.95x10^{-4}$ | $8.73x10^{-4}$ | $4.95x10^{-4}$ | $8.72x10^{-4}$ |
| **Crystallite size (nm) and Strain from Size-Strain Plot** | 50.1, $61x10^{-3}$ | 57.3, 19.3 $x10^{-3}$ | 35.8, -1.6 $x10^{-3}$ | 30.0, -1.41 $x10^{-3}$ | 37.5, 4.4 $x10^{-3}$ |

### ***3.3.2 Influence of synthesis medium and method on ZnO structures***

The ZnO samples prepared in DEG solvent show lesser crystallite sizes of 21.4 and 20.8 nm for $ZnO_{dds}$ and $ZnO_{ddp}$ as compared to the ZnO samples synthesized in DMF solvent showing 39.5, 46.9, and 35.6 nm for $ZnO_{DDp}$, $ZnO_{Dws}$, $ZnO_{Dwp}$ correspondingly (Table 3.3.1). The

crystallite sizes increase when the solvothermal method is adopted. The largest crystallite size was obtained by $ZnO_{Dws}$ with 46.9 nm when $H_2O$ was added to the DMF solvent in the solvothermal method. This may be due to the constant temperature and pressure maintained throughout the experiment in the solvothermal method favoring steady ZnO growth, thereby resulting in larger crystallite size. The smallest crystallite size is obtained in DEG solvent using the precipitation method with 20.8 nm ($ZnO_{ddp}$). With the addition of $H_2O$ molecules, the amount of $OH^-$ ions increases, enhancing crystal growth in the polar c-axis[184]. Therefore, these findings clearly state the importance of using a certain type of synthesis medium and method in tuning and engineering a particular type of nanomaterial. The highest dislocation density of $27.25x10^{-4}$ $nm^{-2}$ is obtained in $ZnO_{ddp}$ synthesized from the precipitation method using DEG as solvent (Table 3.3.2). The $ZnO_{Dws}$ (DMF+$H_2O$+solvothermal method) show the lowest defect density with $4.95x10^{-4}$ $nm^{-2}$.

### ***3.3.3 Morphological and surface analysis***

Varied morphologies of ZnO are seen with the change in reaction parameters— solvent types and synthesis routes. $ZnO_{dds}$ (DEG+solvothermal) and $ZnO_{ddp}$ (DEG+precipitation) show similar porous cauliflower morphologies where aggregated nanoparticles formed a floret as shown in Figure 3.3.3 (a, b). As these synthesized ZnO samples showed different morphologies due to nanoparticle aggregations and growth, its particle sizes are greater than the crystallite sizes calculated from the XRD analysis. The sizes of fully grown $ZnO_{dds}$ are 500-650 nm and individual florets are 170-200 nm in length and 120-190 nm breath. In $ZnO_{dds}$, uniform shapes and sizes of individual florets are seen (Figure 3.3.3 a inset). However, in $ZnO_{ddp}$, partially filled hollow balls (average diameter ~750 nm) by the collection of 40-60nm diameter nanospheres (Figure 3.3.3 b) are also sighted in addition to the cauliflower-like ZnO nanoparticles (Figure 3.3.3 a). Floret sizes of the $ZnO_{ddp}$ cauliflower are similar to that of $ZnO_{dds}$. Although similar cauliflower morphologies are formed in both ZnO, the partially filled ball formation is sighted only in $ZnO_{ddp}$, ascribed to the synthesis method.

With the change of solvent from DEG to DMF, self-assembly and oriented attachment of the petals-like structure take place where hydrangea flower-like structures are formed in combination with nano-aggregates. The $ZnO_{DDp}$ (DMF+precipitation) flower-like structure in Figure 3.3.3 c (inset) is of ~1 μm in size with an innermost petal length of ~190 nm. A fully grown multi-petaled $ZnO_{DDp}$ flower consists of 10-20 petals self-attached asymmetrically with smaller-length petals arranged in the core. The petal's thickness ranges from ~30 nm to ~50 nm and is arranged by self-assembly of nano aggregates of ~70 nm in diameter and exhibits porous

nature. When 5 ml of $H_2O$ is added to the DMF reaction medium ($ZnO_{Dws}$), the degree of petals disorientation-arrangement and nano aggregates formation increases, resulting in resembling asymmetrically connected hydrangea bunch (Figure 3.3.3 d). However, in the same reaction medium of $ZnO_{Dws}$, when solvothermal is replaced by precipitation method i.e., $ZnO_{Dwp}$, 20-100 nm nano aggregates, and flower-like structures are formed (Figure 3.3.3 e).

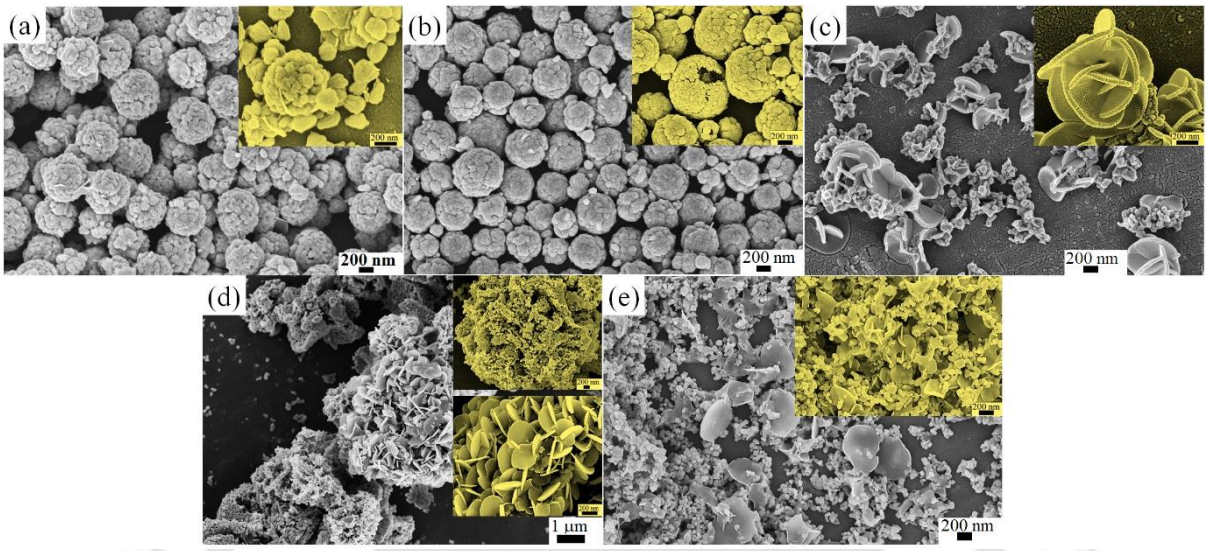


*Figure 3.3.3 FESEM images of (a) $ZnO_{dds}$, (b) $ZnO_{ddp}$, (c) $ZnO_{DDp}$, (d) $ZnO_{Dws}$, (e) $ZnO_{Dwp}$ (inset images show high-resolution images of the corresponding ZnO)*

Less than 5 asymmetrical interconnections of flakes are observed in $ZnO_{Dwp}$, with an average diameter of ~515 nm and ~19 nm thickness (Figure 3.3.3 e). As the nano-assemblies and flakes are formed by the self-arrangement of sub-nanoparticles, the surface exhibits a porous nature. The Brunauer-Emmett-Teller (BET) and Barrett-Joyner-Halenda (BJH) analysis for surface area analysis and pore size & volume analysis respectively are done for $ZnO_{ddp}$, $ZnO_{dds,}$ and $ZnO_{Dwp}$. The average pore diameter and surface area of $ZnO_{ddp}$, $ZnO_{dds}$ and $ZnO_{Dwp}$ are 6.89 nm and 18.59 $m^2/g$, 10.65 nm and 25.76 $m^2/g$, 24.5 nm and 14.51 $m^2/g$ respectively with the pore volume of $3.19x10^{-2}$ cc/g, $6.86x10^{-2}$ cc/g and $8.92x10^{-2}$ cc/g respectively. Although the surface area of $ZnO_{ddp}$ is greater than that of $ZnO_{Dwp}$, the pore diameters and pore volumes are larger in $ZnO_{Dwp}$. This may be due to the use of DMF for the $ZnO_{Dwp}$ preparation as dimethyl amine (DMA), a hydrolysate of DMF plays a major role attributed to its pore formation ability, high swelling degree of the amide molecules, and template ability. Due to the availability of lone pair electrons in DMA, DMA easily binds with the $Zn^{2+}$ positive ions forming a template and producing a higher surface area[185,186].

### *3.3.4 Optical properties*

The five different ZnO samples show broad emission in the near band edge (NBE) region and shallow emission in the visible region (Figure 3.3.4 a). The NBE is related to the band-band transition emission while the visible region emission originates from the ZnO defects present in crystal viz. oxygen/zinc vacancies/interstitials, doping, etc. where an intermediate energy level is formed between the conduction and valence band[187]. The intense NBE with broad-intensity green emission indicates good crystalline quality and optical properties[188].

Here, DMF-based ZnO nanoparticles show bigger and broader visible region emission spectra as compared to the DEG-based ZnO. This may be due to the defects created by the liberation of DMF molecules by calcination that are attached to the ZnO surface as DMF molecules act as a surfactant and structure-directing agent. Thus, DMF induces surface defects or creates open sites which are known for their active participation in photocatalytic reactions[189]. The charge carrier transfer dynamics in ZnO photocatalysts are studied using TRPL photoexcited by a 375 nm laser source. TRPL gives the information on photogenerated charge carrier lifetime, a crucial parameter to quantify charge carrier recombination as these parameters play a significant role in photocatalytic AOP.

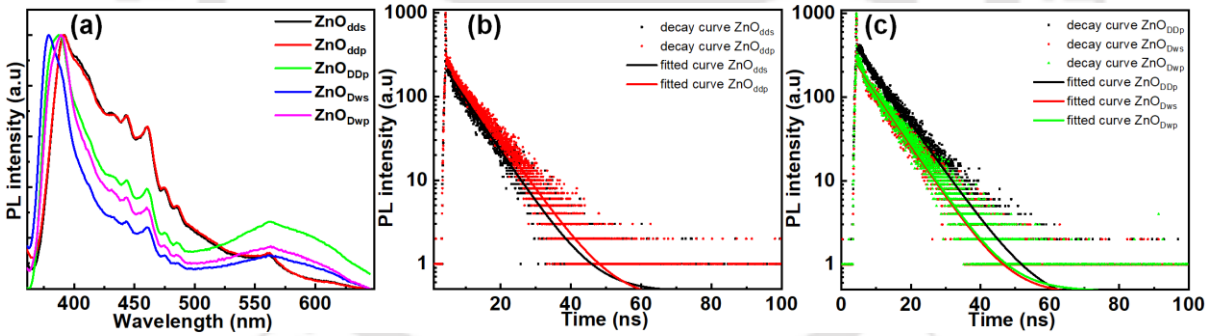


*Figure 3.3.4 (a) Photoluminescence spectra of ZnO samples, Time-resolved photoluminescence decay curve of (b) $ZnO_{dds}$, $ZnO_{ddp}$, and (c) $ZnO_{DDp}$, $ZnO_{Dws}$, $ZnO_{Dwp}$*

*Table 3.3.2 Photogenerated charge carrier lifetimes calculated from TR-PL analysis*

| Sample | $ZnO_{dds}$ | $ZnO_{ddp}$ | $ZnO_{DDp}$ | $ZnO_{Dws}$ | $ZnO_{Dwp}$ |
|---|---|---|---|---|---|
| $\chi^2$ | 1.007 | 1.007 | 1.000 | 1.002 | 1.006 |
| τ (ns) | 6.94 | 7.26 | 7.45 | 6.94 | 6.97 |

The photoluminescence decay profile against time for ZnO synthesized using DEG (Figure 3.3.4 b) and DMF (Figure 3.3.4 c) are plotted and fitted using mono-exponential curve fitting. The decay lifetimes calculated from the curve fittings are summarized in Table 3.3.3. The

lifetimes of $ZnO_{dds}$, $ZnO_{ddp}$, $ZnO_{DDp}$, $ZnO_{Dws}$, and $ZnO_{Dwp}$ are found to be 6.94 ns, 7.26 ns, 7.45 ns, 6.94 ns, and 6.97 ns respectively with $\chi^2$=~1, indicating a good curve fitting. The higher lifetimes in ZnO nanoparticles in the absence of doping indicate the presence of defect states, thereby providing higher carrier lifetimes.

### ***3.3.5 Influence of synthesis mediums and methods on ZnO growth kinetics and shape evolution***

As DEG and DMF are the main solvents in ZnO synthesis, the two dielectric values are taken as the primary determining factor. The coulombic attraction $E_R$, ($E_R = \frac{q_1 q_2}{4\pi\varepsilon r}$) signifies the repulsive forces which hinder the aggregation and coalescence of the nanoparticles, inversely dependent upon the dielectric constant. Thus, with the increase in dielectric constant, the $E_R$ value decreases thus representing higher growth of nanoparticles by aggregation[146]. Different morphologies of ZnO were obtained by using different ratios of solvents, for example, with the addition of polar and high dielectric constant solvent $H_2O$ into the reaction medium, ZnO nano-shuttles were formed. Also, nanoflowers were obtained when surfactants were introduced into the system due to the decrease in selectivity[190].

Here, in comparison, ZnO(DMF) has a higher growth rate than ZnO(DEG), as DMF has a higher dielectric constant (ε= 36.71) than DEG (ε= 31.69) i.e., as $E_R$ decreases with the increase in dielectric constant. Also, as no surfactants are used in the reaction and all the parameters are kept constant, the charge values of the ZnO nanoparticles are derived from the solvent molecules' ionization which is related to the solvent polarities. Since DEG polarity is higher than DMF, the aggregation and growth of ZnO nanoparticles are higher in the DEG solvent as compared with the DMF solvent nanoparticles[147]. Also, viscosity affects the nanoparticles' growth kinetics by hindering the primary nanoparticles' mobilities, resulting in the variation of particle collision rate inducing further aggregation and growth[191]. Thus, in analyzing the solvent effect, the solvents' intrinsic properties- dielectric constant, polarity, and viscosity played a crucial role in determining nanoparticle growth kinetics and hence the resulting ZnO morphologies that are prepared in different solvents.

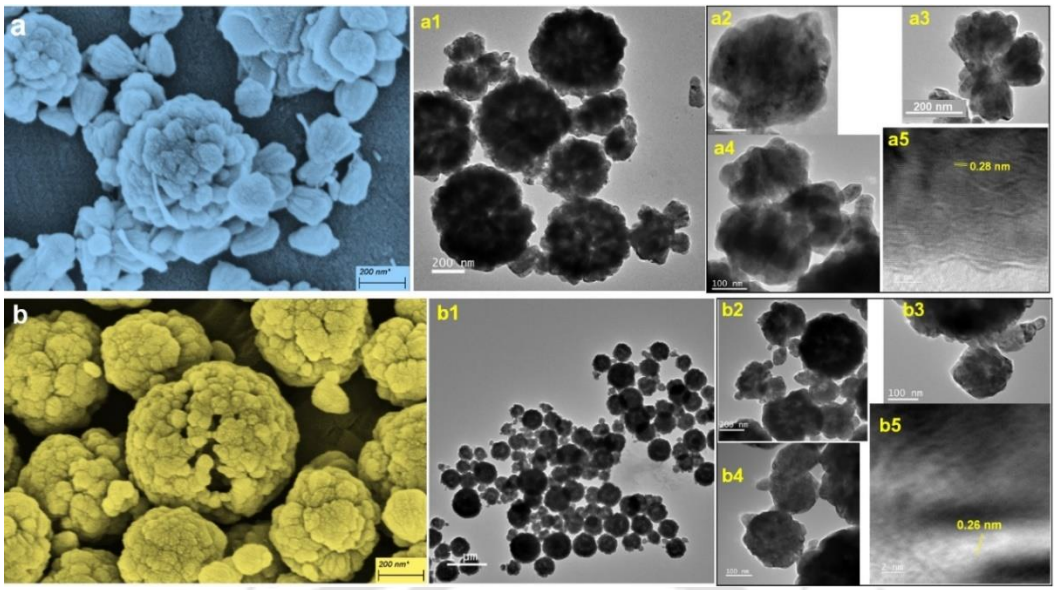


*Figure 3.3.5 FESEM images of (a) $ZnO_{dds,}$ (b) $ZnO_{ddp}$, TEM and HRTEM images of (a1-a5) $ZnO_{dds}$, (b1-b5) $ZnO_{ddp}$ synthesized using DEG solvent via solvothermal and precipitation method respectively showing the building blocks of ZnO cauliflower-like structure*

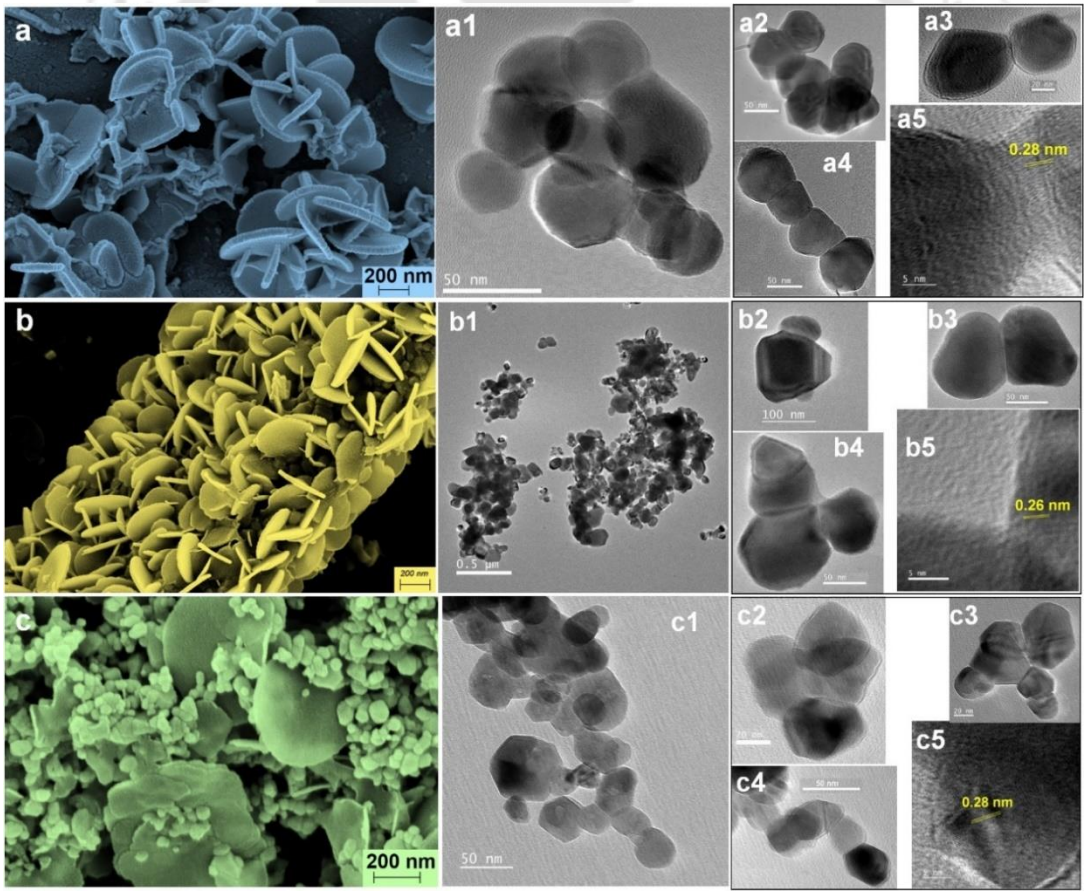


*Figure 3.3.6 FESEM images (a) $ZnO_{DDp}$, (b) $ZnO_{Dws}$, (c) $ZnO_{Dwp}$, TEM images of (a1-a5) $ZnO_{DDp}$, (b1-b5) $ZnO_{Dws}$, (c1-c5) $ZnO_{Dwp}$ illustrating the formation of flower ZnO structures with the petals like structure building blocks*

During the ZnO nanoparticles' crystal growth, oriented attachment, and self-assembly seem to take place forming flower-like structures followed by a coarsening process. The TEM images in Figure 3.3.5 reveal the process of cauliflower-like structure formation with the florets-like building blocks by self-assembly and oriented attachment. The building blocks of the cauliflower-like structure in $ZnO_{dds}$ and $ZnO_{ddp}$, look like a floret, flared at one end and tapered on the other (Figure 3.3.5 (a2-a4)). The tapered part of the florets joined together (Figure 3.3.5 (a3, a4)) to form matured cauliflower-like structures in Figure 3.3.5 a1. Similarly, self-assembly and oriented attachment also occur in $ZnO_{ddp}$ where tapered parts of the florets (Figure 3.3.5 (b2-b4)) are joined to form low-energy configurations exhibiting cauliflower and partially filled hollow ball structures (Figure 3.3.5 b, b1).

Due to the higher polarity and lower dielectric constant of DEG solvent, the primary ZnO nanoparticles are aggregated and showed faster growth kinetics thus forming florets and cauliflower-like structures by fast aggregation. From the HRTEM images, the interplanar d-spacings are found to be 0.28 nm and 0.26 nm for $ZnO_{dds}$ (Figure 3.3.5 a5) and $ZnO_{ddp}$ (Figure 3.3.5 b5) corresponding to the d-spacing value of (100) and (002) planes.

The use of DMF as a solvent result in hierarchical structures due to the formation of formic acid and dimethylamine (DMA) when hydrolysis takes place. The formation of DMA provides alkalinity to the solution by hydrolysis process[192]. M.Wang et al. showed the shape evolution of ZnO nanoparticles from nanoplates to nanoplate aggregation and self-assembled forming persimmon-shaped and further bowl-like structures by using optimal amounts of DMF to form $Zn^{2+}$-DMF intermediates. Thus, the formation of $Zn^{2+}$-DMF intermediates i.e., adsorption and desorption of DMF molecules on the $Zn^{2+}$ or ZnO surface controls the nanoparticle's growth rate in a specific direction thus acting as the structure-directing agent[192].

J.Zhou et al. studied the controllable properties of boehmite microspheres where an increase in DMF amount i.e., DMA, hydrolysate of DMF, can regulate the boehmites morphology formation with the sulfate ions[186]. The DMA acts as a structure-directing agent by providing alkalinity via hydrolysis which agrees with the results obtained in this paper for the formation of flower-like structures by self-oriented attachment of individual petals acting as the building blocks. The DMA molecules have a high binding ability due to the lone pairs present in the amine group binding easily with the $Zn^{2+}$ positive ions forming a template[185]. Figure 3.3.5 shows the FESEM and respective TEM and HRTEM images to understand the growth behavior. Figure 3.3.5 (a1- a4) shows the self-oriented attachment of the petals-like structure

of $ZnO_{DDp}$ (DMF+precipitation). The petals seem to form faceted structures and the attachment takes place in one of the facets as observed in Figure 3.3.5 (a3, a4), and the junction of two petals is seen in Figure 6 a5. The self-attachment of the petals-like structures is also observed in $ZnO_{Dwp}$ (DMF+ $H_2O$ + precipitation) in Figure 3.3.5 (c1-c4). Likewise, in $ZnO_{Dws}$ (DMF+$H_2O$+solvothermal), petals-like structures are joined to form a hydrangea-flower structure (Figure 3.3.5 (b2-b4)). The HRTEM images show interplanar d-spacings calculated from the Bragg's law equation (XRD data) are found to be 0.26 nm, 0.26 nm, and 0.28 nm for $ZnO_{DDp}$ (Figure 3.3.5 a5), $ZnO_{Dws}$ (Figure 3.3.5 b5), $ZnO_{Dwp}$ (Figure 3.3.5 c5) respectively.

### ***3.3.6 Photocatalytic degradation of RhB under Natural sunlight and UV light illumination and kinetics study***

The as-synthesized five different ZnO photocatalysts are used for photocatalytic RhB degradation to determine their potential application and performance as a photocatalyst. The photocatalytic experiments are triggered by two different light illuminations: (a) natural sunlight in the October sky and (b) UVC light. For the natural sunlight-triggered RhB degradation, floating ZnO-coated face-mask fabrics are dipped into the RhB solution and exposed to open sunlight. The microscopic images of bare fabric and ZnO-coated fabric are shown in Figure 3.3.7 (a, b). The uniform coating of ZnO on a single strand of the fabric is observed in Figure 3.3.7 (a, b) insets.

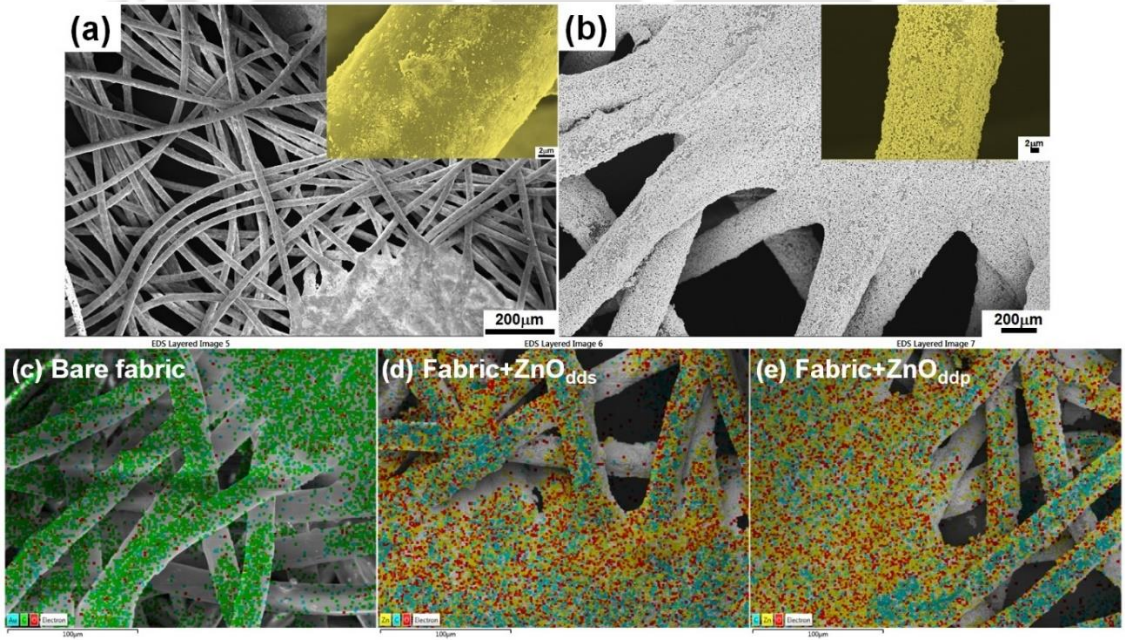


*Figure 3.3.7 FESEM images of the (a) bare face-mask fabric, (b) fabric coated with $ZnO_{ddp}$, ZnO photocatalyst distribution analysis using elemental mapping of (c) bare face-mask fabric, face-mask fabric coated with (d) $ZnO_{dds,}$ and (e) $ZnO_{ddp}$*

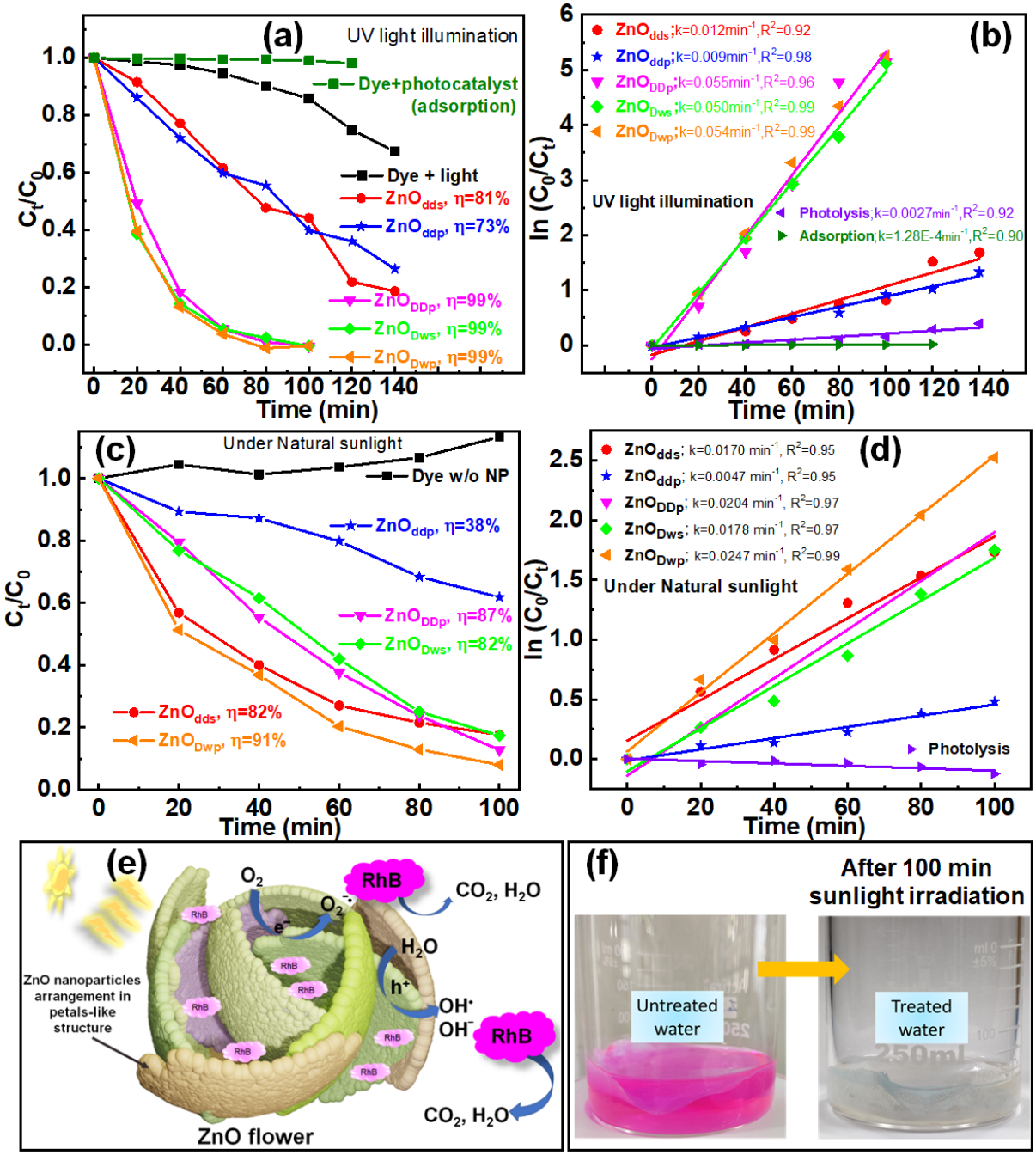


*Figure 3.3.8 Photocatalytic degradation plot of RhB against irradiation time and degradation rate constant calculation (a, b) for slurry system under UV light (36W), and (c, d) ZnO coated face-mask fabric under natural sunlight in October (120k Lux), (e) photocatalytic degradation of RhB on ZnO flower structure, and (f) before and after 100 min exposure to natural sunlight of RhB solution in the presence of ZnO coated fabric*

The uniform distribution of ZnO photocatalyst on each strand of the fabric is evident from the elemental mapping, shown in Figure 3.3.7 (d, e). Figure 3.3.7 c shows before ZnO coating elemental mapping, where carbon originated from the polymer face-mask fabric and gold (from gold coating) with negligible oxygen. The ZnO decorations in the face-mask fabrics are

presented in Figure 3.3.7 (d, e) for $ZnO_{dds}$ and $ZnO_{ddp}$ photocatalyst respectively as a representative analysis for all ZnO-coated fabrics.

The $C_t/C_0$ values against time (minutes) are used to describe the degradation curve plotted in Figure 3.3.8 a and 3.3.8 c for UV light illumination and natural sunlight for all the synthesized ZnO samples; where $C_t$=concentration at the time t and $C_0$=initial dye concentration at time t= 0 min. Under UV light illumination, 99% photocatalytic RhB degradation efficiencies are observed under 100min of illumination for the ZnO photocatalyst prepared in DMF solvent irrespective of the synthesis method and $H_2O$ addition in the synthesis medium. However, 81% and 73% degradation efficiencies are observed for $ZnO_{dds}$ and $ZnO_{ddp}$ synthesized using DEG solvent in 140 min UV light illumination time (Figure 3.3.8 a). In the dark condition in the presence of photocatalyst, no absorption and self-degradations are observed as indicated in Figure 3.3.8 a. A 32% self-degradation of RhB is observed by the photolysis under UV light in the absence of the photocatalyst. However, in the presence of photocatalyst nanoparticles, the RhB degradation increased sharply up to 99%.

With comparable results to UV-assisted degradation, a 91% degradation efficiency was observed under natural sunlight illumination under 100 min exposure time (Figure 3.3.8 c) by using face mask fabric decorated with $ZnO_{Dwp}$ (DMF+$H_2O$+precipitation). With 38% degradation efficiency under natural sunlight, $ZnO_{ddp}$ prepared by precipitation method in DEG solvent with no $H_2O$ addition achieved the lowest efficiency under the 100 min exposure. In the overall investigation and analysis, maximum degradation efficiencies are observed by the ZnO+DMF as compared with the ZnO+DEG samples. This may be due to the additional surface defects created by the liberation of DMF molecules via the calcination process. Further, the $ZnO_{ddp}$ showed the lowest degradation efficiencies under both UV and natural sunlight. This can be correlated with the pore size diameter and pore volumes of $ZnO_{ddp}$ (6.87 nm and $3.19x10^{-2}$ cc/g) which are found to be smaller than other samples despite having a surface area of 18.59 $m^2/g$ which is larger than that of $ZnO_{Dwp}$. Thus, it can be concluded that surface morphology, pore volume, and pore diameter played a major role in the photocatalytic degradation of RhB dye. In the absence of a photocatalyst in the dye solution, no self-degradation or absorption in the fabric is observed although a minor intensity change is detected which is believed to be the effect of sunlight exposure (Figure 3.3.8 c). Thus, this experiment also demonstrates the higher risk of exposing untreated dye waste to direct sunlight which might impose a major concern on the aquatic ecosystem and the nearby environment.

For the photocatalytic degradation of RhB under UV light illumination and natural sunlight, the k values obtained from the experimental data are plotted in Figure 3.3.8 (b, d) respectively.

### ***3.3.7 Influence of different ZnO morphologies on the photocatalytic performance***

From the degradation rate analysis shown in Figure 3.3.7 (b, d), under natural sunlight, $ZnO_{Dwp}$ (DMF+$H_2O$+precipitation) shows the highest degradation rate of 0.0247 $min^{-1}$ while $ZnO_{dds}$ (DEG+solvothermal) show the lowest with 0.017 $min^{-1}$. However, compared to natural sunlight illumination, UV light-assisted photocatalytic degradation shows a two-fold degradation rate and $ZnO_{ddp}$ (DMF+precipitation) shows the highest degradation with 0.0558 $min^{-1}$. In the overall photocatalytic AOP of RhB degradation, ZnO nanoparticles synthesized using DMF solvent demonstrate a higher degradation rate as compared to ZnO prepared from DEG solvent. This may be due to the defects or the open sites created by the liberation of DMF molecules from the ZnO surface, acting as photocatalytic reactive active sites[189]. Also, among the three ZnO synthesized using DMF, the ZnO synthesized from the precipitation method showed higher degradation performance. The surpassing photocatalytic degradation performance exhibited by the DMF solvent ZnO— $ZnO_{DDp}$, $ZnO_{Dws}$, and $ZnO_{Dwp}$ over DEG solvent ZnO— $ZnO_{dds}$, $ZnO_{ddp}$ may be attributed to the coexistence of different morphologies (flower, petals like and nano aggregates) as shown in Figure 3.3.3 and the creation of open sites on ZnO surface. A possible reaction mechanism is illustrated in Figure 3.3.7 e where more RhB molecules are accessible to the ZnO flower-petal surfaces while the cauliflower-like structure has closed surfaces thus enhancing the performance and efficiency. The major factors affecting photocatalytic performance are morphology, size, and surface properties like area, porosity, defects, pH, etc. Although $ZnO_{ddp}$ has the smallest crystallite size (20.8 nm), $ZnO_{Dwp}$ exhibits the best degradation performance despite obtaining a larger crystallite size of 33.8 nm. This anomalous behavior may be attributed to the formation of distinct and multiple architectures of ZnO obtained in the DMF solvent. However, if the crystallite size obtained from the size strain plot (SSP) is considered, $ZnO_{ddp}$ has the highest crystallite size of 57.3 nm with the highest dislocation density of $22.95 \times 10^{-4}$ $nm^{-2}$ (Table 3.3.2). Therefore, with the increasing dislocation density, the recombination rate of charge carriers also increases thereby limiting the photocatalytic performance. Also, from the experimental data obtained and result analysis, the values obtained from the SSP are in line with the well-known theory of size and disorder density effect on photocatalytic performance and efficiency. Further, the surface properties also contributed to varying the photocatalytic degradation efficiencies of the ZnO samples. S.Li et al. showed the dependence of photocatalytic efficiency in the pore sizes where macropores

assist in improving visible light adsorption yielding more photoexcitons and serving as intramolecular or interlayer delivery channels for charge communication[193]. The study deduced that the larger the pore sizes from micropores to mesopores and further to macropores, the visible light absorption was increased, undergoes multiple light scattering & reflections, and facilitates charge transport[193]. Thus, in this work, the ZnO sample ($ZnO_{Dwp}$) with the highest pore diameter and pore volume showed the highest degradation efficiency while the ZnO sample ($ZnO_{ddp}$) with the smallest pore diameter and pore volume exhibited the lowest efficiency. Thus, with the larger pore diameter, the photocatalytic activity increases by improving the visible light adsorption and photo-exciton generation and simultaneously serving as a channel for charge carriers' communication.

As seen in Table 3.3.3 and Figure 3.3.3 a, ZnO nanoparticles synthesized are found to exhibit the presence of defects i.e., oxygen interstitials in the ZnO crystals. The charge carriers excited by the laser source have lifetimes of 6.9-7.4 ns for all the samples, maximum by $ZnO_{DDp}$ with 7.45 ns and the lowest by $ZnO_{dds}$ and $ZnO_{Dws}$ with 6.94 ns. From the reaction rate calculation using UV light illumination, $ZnO_{DDp}$ shows the maximum degradation rate of RhB. Also, although $ZnO_{ddp}$ shows a similar carrier lifetime with $ZnO_{DDp}$ with 7.26 ns, the performances for the RhB degradation are exceeded by $ZnO_{Dws}$ and $ZnO_{Dwp}$ with carrier lifetimes of 6.94 and 6.97 ns. This anomalous behavior may be contributed by the formation of flower and petals-like structures which are thinner than cauliflower-like structures providing higher exposure and excess area for RhB molecule absorption and interaction. The higher charge carrier lifetimes and emission bands in the visible region indicated the presence of intrinsic defects aid in improving the in-situ generation of reactive oxygen species for degrading RhB molecules. The highly reactive oxygen comprises hydroxyl radical (OH•), hydroxyl ($OH^-$), singlet oxygen ($^1O_2$), superoxide radical ($\bullet O_2^-$), and peroxide ($H_2O_2$). Also, the defect states provide a mid-level energy band thereby increasing the photogenerated charge carrier lifetimes and reaction site.

So far, the reuse of face mask fabric for photocatalytic performance shows an appreciable result while using photocatalytic degradation of RhB triggered by the natural sunlight as shown in Figure 3.3.8 e. This allows the reuse of face-mask, paving the way for mitigating environmental pollution caused by the increasing disposal of surgical face masks due to the pandemic. Also, the use of natural sunlight in the successful degradation of RhB gives a promising solution for replacing external UV or artificial light sources for the photocatalytic AOP to treat polluted water as a practical application. Different architectures of ZnO obtained using DMF solvent

show lesser dislocation density, strain, and crystallite sizes (from SSP calculation). In addition, the formation of petals and flower-like structures provided higher exposure to the pollutant molecules for greater interaction as compared to the cauliflower-like structures. Thus, enhancing photocatalytic performance and efficiency as compared to the ZnO synthesized using DEG solvent.

### ***3.3.8 Findings of Part C (Optimisation of nanoparticle properties)***

- The use of different solvents results in obtaining different ZnO morphologies- nano aggregates, cauliflower, and hydrangea flower-like structures sited along with their building blocks.
- As particle interaction is defined by Coulomb's law, which is inversely dependent on solvents' dielectric constant, ZnO nanoparticles prepared in a higher dielectric constant (DMF) solvent have a higher growth rate.
- ZnO prepared in a higher polar solvent (DEG) observed higher aggregation. DMF acts as a structure-directing agent forming petals-like structures acting as the building block for flower formation by self-assembly and orientated-attachment process because of the DMA's ability to bind with positive charge $Zn^{2+}$.
- The liberation of DMF and DMF derivatives from the ZnO surface via calcination from surface defects.
- ZnO-coated face-mask fabrics were used as a floating photocatalyst for RhB degradation under natural sunlight illumination, overcoming the need for an additional photocatalyst retrieval process.
- A similar degradation efficiency of 91% dye removal in 100 min is obtained as compared with the slurry system triggered by UV light illumination of 99% by the ZnO samples prepared in DMF solvent.
- ZnO from DMF solvent shows better performance and degradation rate due to the synergy of the formation of surface defects, oxygen interstitial, open sites, and higher surface exposure by the petal-like structures.
- The synergy of the defect formation, petals-like morphologies, larger pore size and volume resulted in exhibiting higher degradation efficiencies under UV and sunlight irradiation.

## 3.4 Conclusion

- With the use of green synthesis method, the presence of bioactive compounds in aloe vera and lemon fruit extracts form metal complexes through the linkage of metal ions ($Zn^{2+}$) and the functional groups of the biomolecules. Thus, green synthesis is not suitable for the synthesis of nanoparticles with high crystallinity and purity.
- The use of $Zn(CH_3COO)_2.2H_2O$ for the ZnO synthesis in the hydrothermal method gives the largest crystallite size and ZnO synthesized from the $ZnSO_4.7H_2O$ source with the precipitation method shows the smallest crystallite size.
- Nanoparticles prepared via the precipitation method show lesser crystallite sizes than that of the hydrothermal method owing to the continuous agitation during the reaction and maintenance of the same temperature and pressure inside a hydrothermal.
- DMF acts as a structure-directing agent and a surfactant. The liberation of DMF and DMF-derivatives from the ZnO surface via calcination form surface defects.
- ZnO nanoparticles synthesized via precipitation method using $Zn(CH_3COO)_2$. showed the highest degradation rate of 0.0093 $min^{-1}$ and efficiency of 91% in 3 hr reaction time.
- ZnO from DMF solvent shows better performance and degradation rate due to the synergy of the formation of surface defects, oxygen interstitial, open sites, and higher surface exposure by the petal-like structures.
- A similar degradation efficiency of 91% dye removal in 100 min is obtained using ZnO-coated face-mask fabrics under natural sunlight as compared with the slurry system triggered by UV light illumination of 99% by the ZnO samples prepared in DMF solvent.

# Chapter 4

# Interaction and Charge Transfer Analysis on Different SWCNTs Functionalized by ZnO Nanoparticles

## Introduction

As an emerging research, carbon nanotubes are coupled with nanomaterials to produce a synergetic effect in the electrical, optical, and mechanical properties for numerous uses[194,195]. SWCNTs are also used as a scaffolding and anchoring backbone for designing nanomaterial growth in a specific array[126,196–198]. SWCNTs are functionalized by various methods; chemical or physical modifications incorporated with multiple organic or inorganic compounds via intimate interactions between the individuals with covalent or non-covalent attachment[126]. The non-covalent functionalization in composites shows complementing behavior due to the synergetic effect for both the building blocks, uplifting overall performance e.g. functionalization of SWCNTs with metallic nanoparticles (Au/Ag) enhances the selective catalytic property and increases in charge carrier transfer[199]. The SWCNT-semiconductor oxide composites form p-n/Schottky heterojunction type interfaces depending upon the type of individuals used[200]. However, an in-depth investigation into the interaction between individual contributors in this composite is required. In addition, other SWCNT functionalization treatments like acid treatment, use of polymer, or expensive preparation techniques have to be replaced by an easy synthesis method. As a single strand of carbon nanotube (CNT) diameter is within 10 nm, it is impossible to separate a single CNT strand, thereby existing in a bundle of strands attached, due to the polydisperse nature of SWCNT during their productions (like mixed diameters, lengths, and chirality)[165,201]. Because of SWCNT's difficulty in dispersion, SWCNTs are functionalized with other molecules and compounds is a new way to support a stable dispersion in any desirable solvent, especially $H_2O$, thereby, eliminating the use of surfactants[202–204]. In a photocatalytic advanced oxidation process, the production and generation of charge carriers depend upon the charge carrier lifetimes. CNT-semiconductor oxide photocatalysts have desirable electronic properties while CNT acts as an $e^-$ transmitting channel photogenerated by the semiconductor nanomaterials, thus, enhancing $e^-$—$h^+$

separation/transfer and increasing charge carrier lifetimes through recombination inhibition. Single-Walled Carbon Nanotubes (SWCNTs) possess unique optical and electronic properties which highly depend upon the carbon nanotube diameter and chirality, the (n, m) values. That is, every distinct (n, m) nanotube has unique interband energy displaying specific electronic properties. In ZnO/MWCNT heterostructure, the MWCNT promotes interfacial $e^-$ transfer by acting as an $e^-$ acceptor. This process enhances $e^-$—$h^+$ separation in the composites, showing similar semiconductor-metal heterojunction characteristics where photogenerated $e^-$s of semiconductors are transferred to the carbon-based material, suppressing the recombination process[6,130,131]. Due to the high aspect ratio of CNTs and surface areas, the ZnO/CNT composites showed higher degradation efficiency as compared with the bare ZnO nanoparticles[141,142]. The enhancement of photocatalytic performance in the CNT/semiconductor oxides is well known, but the impact of the type of SWCNTs which are metallic and semiconducting on the charge transfer dynamics needs to be studied exclusively.

Charge carrier transfer dynamics in a photosystem have long been studied for their use as a foundation for numerous modern scientific applications to attain sustainable development goals mainly relating to environmental applications. This light-matter interaction and their charge transfer dynamics play a major role in advanced cutting-edge technologies mostly in the field of nanotechnology. The crucial step of heterogeneous photocatalysis is the generation of photoinduced charge carriers, their separation, transfer, and recombination. The efficiency of heterogeneous photocatalysis is enhanced by increasing the generation and separation of photogenerated charge carriers, inhibiting the recombination and hence improving the ROS generation. The photocatalytic reaction mechanisms follow different pathways for dissimilar materials and targeted applications. For contaminant mineralization, $e^-$s and $h^+$s are utilized in generating ROS. Whereas in water splitting, $h^+$s are consumed by $H_2O$ and $e^-$s by $H^+$, for $O_2/H_2$ generation[138]. Three competing pathways, namely, charge recombination, $h^+/e^-$ transfer, and energy transfer determine the photocatalytic quantum efficiency. In a more advanced approach, in heterostructures, these photogenerated excitons are separated by the influence of a built-in electric field developed in a heterojunction interface, thereby increasing charge carrier lifetime and their number partaking in redox reactions[127,205,206]. Thus, to investigate the charge transfer analysis and interaction between three electronically different SWCNTs that were procured from Nano Integris-IsoNanotubes with ZnO nanoparticles, SWCNTs are functionalized with ZnO and discuss the interaction through the concept of critical coagulation concentration.

## PART A: Functionalization of SWCNTs by ZnO: Analysis through Critical Coagulation Concentration

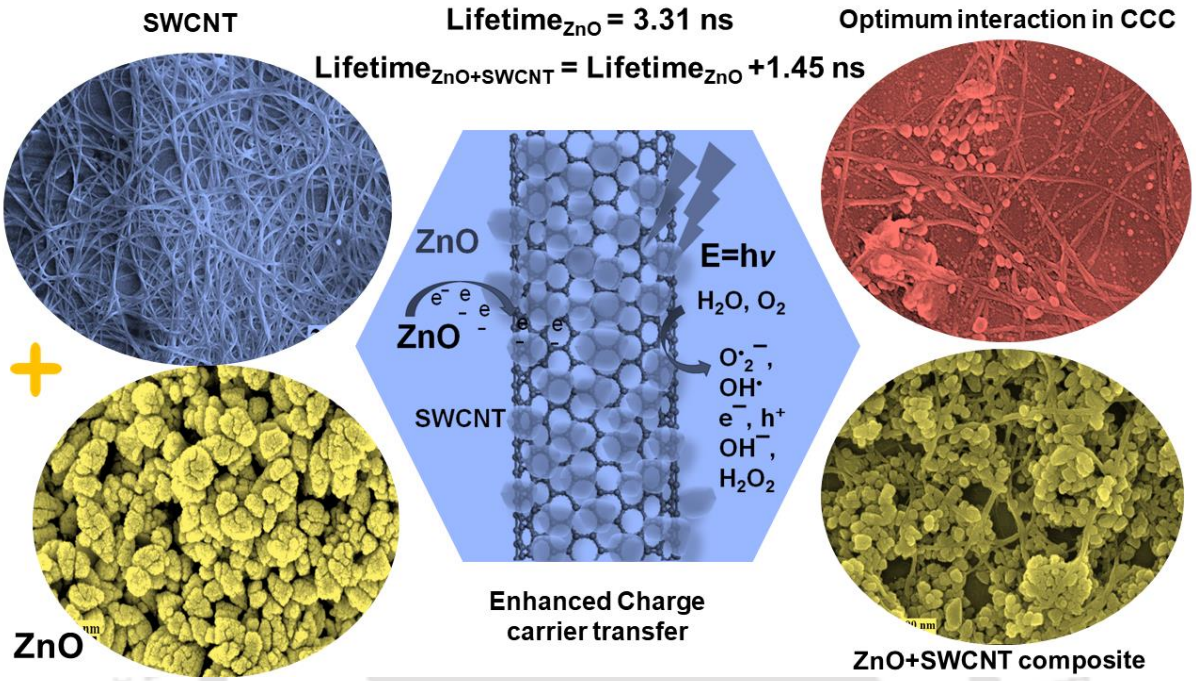


***Graphical Abstract of Part A***

*D.D. Thongam, H. Chaturvedi, Functionalization of Pristine, Metallic, and Semiconducting-SWCNTs by ZnO for Efficient Charge Carrier Transfer: Analysis through Critical Coagulation Concentration, ACS Omega. 7 (2022) 14784–14796. https://doi.org/10.1021/acsomega.2c00193.*

In Part A, ZnO nanoparticles that showed good photocatalytic performance in Chapter 3 which was synthesized using an acetate source in the precipitation method are selected. The three electronically different SWCNTs (metallic, semiconducting, and pristine: m-SWCNT, s-SWCNT, and p-SWCNT) that were procured from Nano Integris-IsoNanotubes are functionalized using ZnO nanoparticles by facile sonication process to retain SWCNTs and ZnO properties in the composites formed, while exhibiting a synergistic effect. The interaction of SWCNTs and ZnO in terms of charge carrier transfer through carrier lifetimes has been analyzed and a charge carrier separation and transfer mechanism has been illustrated and explained for better understanding. The impact of functionalization was studied from two different points of view: SWCNTs and ZnO through various characterization techniques and analysis.

## 4.1 Results and discussion of the SWCNTs functionalized by ZnO

### *4.1.1 Structural, physical, and interaction analysis of ZnO functionalized SWCNTs*

Morphological analysis of ZnO nanopowders exhibited the formation of porous rough surface quasi-spherical morphologies by aggregating smaller sub-nano-sized ZnO particles forming larger particles of 100-200 nm (Figure 3.2.1 c). A comparative study of the XRD and Raman analysis of ZnO and SWCNT+ZnO samples prepared in Figure 2.1.3 is shown in Figure 4.1.1. The XRD patterns of ZnO and SWCNT/ZnO composites show good crystallinity with hexagonal wurtzite phase structure of space group $P6_3mc$. In the m-SWCNT+ZnO, s-SWCNT+ZnO, and p-SWCNT+ZnO composite nanoparticles, the eleven significant peaks of ZnO (JCPDS card number 00-036-1451) were recorded. A broad hump between 20°-30° was seen in all the composites, corresponding to the (002) plane of SWCNT (Figure 4.1.1 a). No other impurity peaks were seen and sharp intense peaks indicate high crystallinity of the prepared samples. The crystallite size of the ZnO is found to be 19 nm and is used to functionalize the three different SWCNTs; metallic, semiconducting, and pristine-SWCNTs. For the ZnO functionalized SWCNTs, no significant (101) plane peak shift is observed in the XRD analysis (Figure 4.1.1 b). The crystallite size of ZnO is increased from 19 nm to 30, 32, and 30 nm when m-SWCNT+ZnO, s-SWCNT+ZnO and p-SWCNT+ZnO were formed. Also, $I_{101}/I_{002}$ intensity ratios are increased in the composites (Figure 4.1.1 c) from 1.45 to 2.58, 2.74 and 2.8 for p-SWCNT+ZnO, s-SWCNT+ZnO and m-SWCNT+ZnO correspondingly. A linear dependence between the $I_{101}/I_{002}$ intensity ratio and crystallite sizes is also seen for the composites. The increase in crystallite sizes of ZnO and intensity ratios may be attributed to the change in surface free energy originating from the addition of SWCNTs and the application of external sonication energy. This shows the enhancement in c-axis growth orientation. This also summarized that due to the continuous agitation provided by extra sonication energy, crystal growth in a particular orientation (101) is enhanced with the addition of SWCNTs.

Due to the complete coverage of SWCNT surfaces by ZnO particles and lesser SWCNT quantities, a trivial broad peak is observed between 20° to 30° in the XRD pattern (Figure 4.1.1 a), owing to the overpowering crystal orientations of ZnO. However, in Raman spectroscopy, the molecular vibration and stretching of ZnO (Figure 4.1.1 d) are dominated by the bond vibrations of SWCNT. High-intensity Raman peaks corresponding to SWCNTs: radial breathing mode (RBM), D, G (split into $G^-$ and $G^+$), and G` or 2D bands with a negligible audience of ZnO vibrations (Figure 4.1.1 e) are seen.

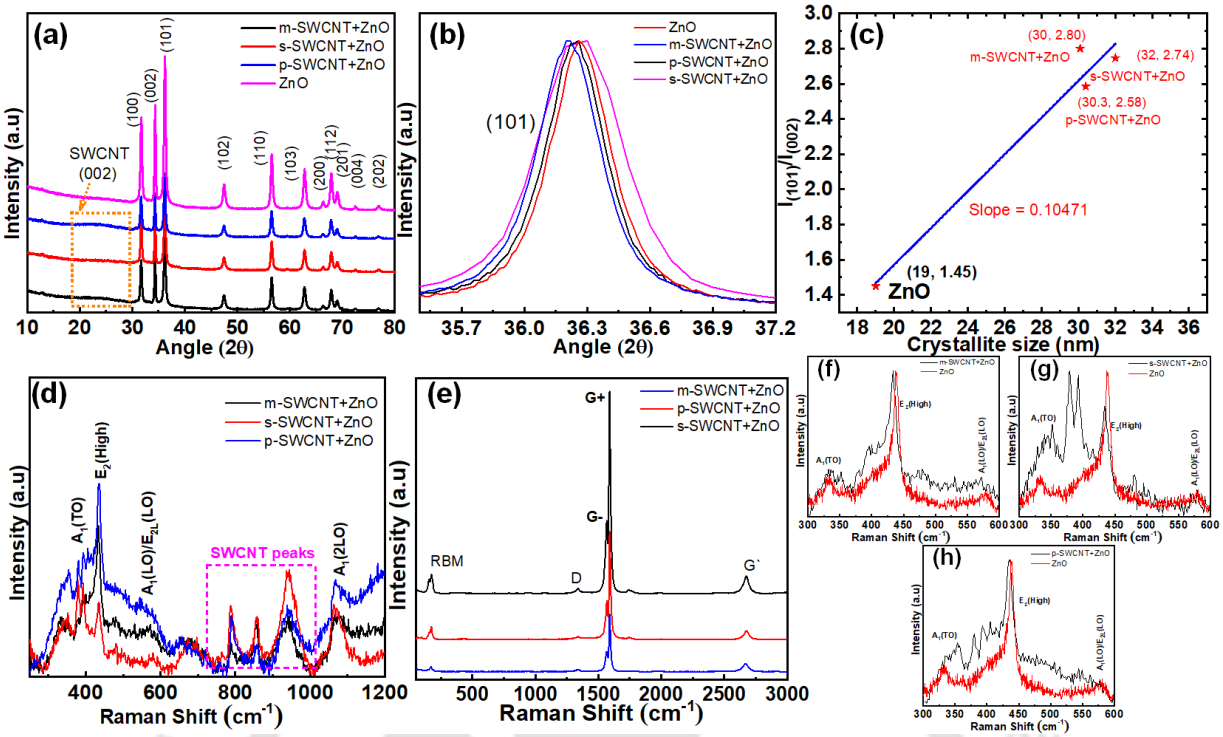


*Figure 4.1.1 Comparative structural and vibrational analysis of ZnO, m-SWCNT+ZnO, s-SWCNT+ZnO and p-SWCNT+ZnO with (a) XRD pattern, (b) (101) peak comparison, (c) $I_{(101)}/I_{(002)}$ and crystallite size plot, (d) Raman spectra from ZnO point of view, (e) Raman spectra from SWCNT point of view, and peak shift comparison for $E_2$(high) peak of ZnO, and ZnO functionalized (f) m-SWCNT+ZnO, (g) s-SWCNT+ZnO, and (h) p-SWCNT+ZnO*

The structural, phonon, and electrical properties of the composites are analyzed from two perspectives: (a) ZnO $E_2$(high) mode, and (b) RBM, D, G, and G` band of intrinsic SWCNTs individually for the corresponding functionalization. Figure 4.1.1 (d, e) shows the comparison of Raman spectra of m-SWCNT+ZnO, s-SWCNT+ZnO, and p-SWCNT+ZnO from the ZnO and SWCNTs point of view respectively. Major dominant Raman peaks corresponding to ZnO; $E_2$(high), $A_1$(LO)/$E_{2L}$(LO) at ~338 $cm^{-1}$ and ~580 $cm^{-1}$ respectively were also seen to be present, with additional peaks at 800-1000 $cm^{-1}$ corresponding to SWCNTs[207]. Shifting of $E_2$(high) Raman peak positions to lesser wavenumbers was observed in the ZnO functionalized SWCNTs by 4 $cm^{-1}$ for m-SWCNT (Figure 4.1.1 f) and s-SWCNT and 2 $cm^{-1}$ for p-SWCNTs (Figure 4.1.1 g, h). This is due to the tensile stress and mechanical activation influenced by the presence of SWCNTs in ZnO that results in increasing bond length, thereby shifting in the Raman peak. These Raman peak shifts are resulted due to the deviation in electron distribution, indicating charge transfer between the constituting materials[208–211].

### *4.1.2 Charge carrier transfer analysis between SWCNT and ZnO*

To investigate the charge transfer in ZnO functionalized SWCNT, further analysis on Raman shift has been carried out. A study of 15 different Raman spectra of each functionalized sample was taken and compared by selecting 6 spectra as shown in Figure 4.2, exhibiting the extreme shifts in both directions— blueshift, redshift, and no-shift. The comparison is done from SWCNT perspectives, selecting three characteristic SWCNT peaks; RBM, G ($G^+$, $G^-$), and G` band for all ZnO+SWCNTs samples compared with the corresponding intrinsic SWCNTs. The Raman redshift or blueshift and increase or decrease in peak intensities are an indicator of SWCNTs' role as an electron donor or acceptors in the functionalization as SWCNTs are ambipolar. The amount of shift in wavenumbers is found to be a source of calculating the number of charge densities[209–213]. A.M.Rao et al.[211] studied the change in charge carrier density of SWCNTs with chemical doping using electron donor and acceptor dopants hence altering thermal and electrical properties. The $G^+$ band of SWCNTs shifted to lower wavenumbers in the presence of electron donor molecules (K, Rb) and shifted to a higher wavenumber when paired with electron acceptor molecules ($I_2$, $Br_2$)[211]. Figures 4.1.2 (a, b, c), 4.1.3 (a, b, c), and 4.1.3 (d, e, f) show the comparison of normalized RBM, G and G` band of the ZnO functionalized SWCNTs; m-SWCNT+ZnO, s-SWCNT+ZnO and p-SWCNT+ZnO to intrinsic SWCNTs respectively. Figure 4.1.2 d shows the collective distribution of Raman shift to their intrinsic SWCNTs for all the functionalized samples; m-SWCNT+ZnO, s-SWCNT+ZnO, and p-SWCNT+ZnO. Three characteristic peaks, RBM, G and G` of m-SWCNT+ZnO, $G^-$ and G` band of p-SWCNT+ZnO, and G` band of the s-SWCNT+ZnO show both blueshift and redshift with varied values. This anomalous behavior may have occurred due to variable degrees of absorption, functionalization, interaction, and charge transfer between SWCNTs and ZnO nanoparticles as SWCNTs are ambipolar. This is also contributed by the presence of different defects and varied influences of ZnO in electronically different SWCNT's carbon-carbon bonds uniquely as well as different diameters and chirality of SWCNTs. However, a major shift from all the distribution is being considered in this study and the distribution is shown in Figures 4.1.2 d.

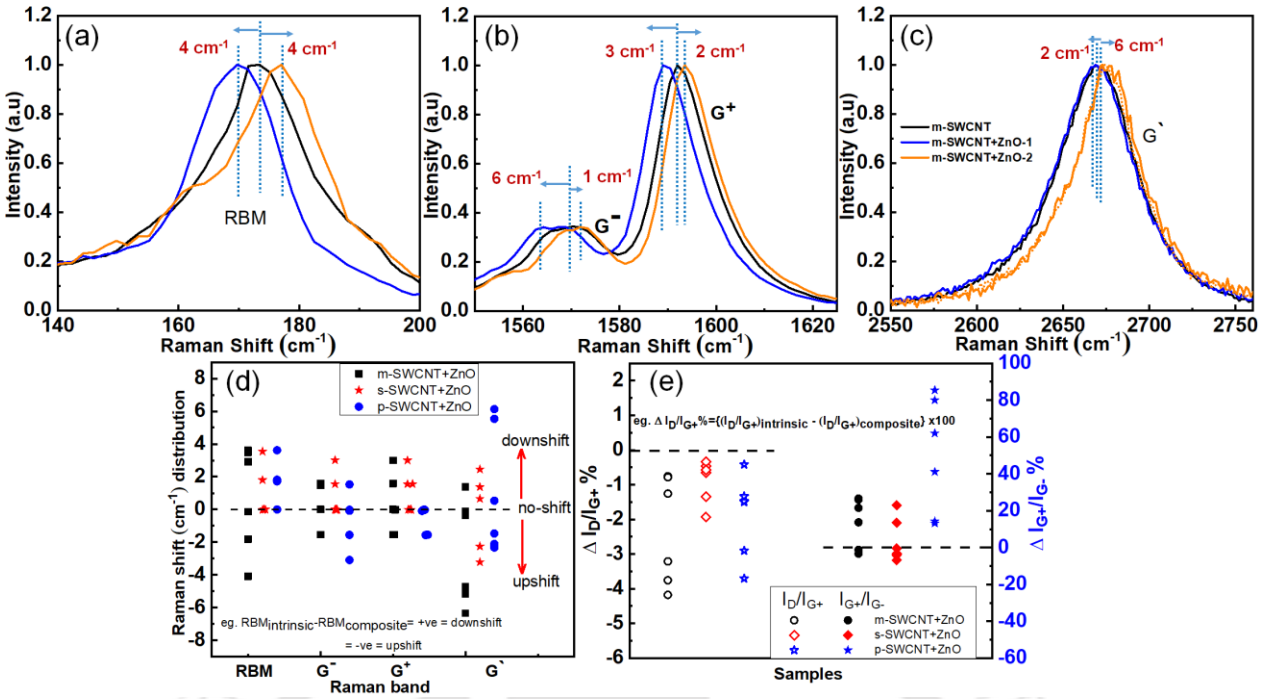


*Figure 4.1.2 Effect of functionalization in Raman peak in comparison taken from six different points: (a) RBM, (b) G-band, (c) G`-band for m-SWCNT+ZnO compared with m-SWCNT, (d) distribution of RBM, G-, G+ and G` band peak shift for six different readings of the same sample for the three ZnO functionalized SWCNTs with the corresponding intrinsic SWCNTs, (e) distribution of intensity ratios $\Delta I_D/I_{G+}$, $\Delta I_{G+}/I_{G-}$ for the three samples- m-SWCNT+ZnO, s-SWCNT+ZnO, p-SWCNT+ZnO and intrinsic-SWCNT taken for the six readings*

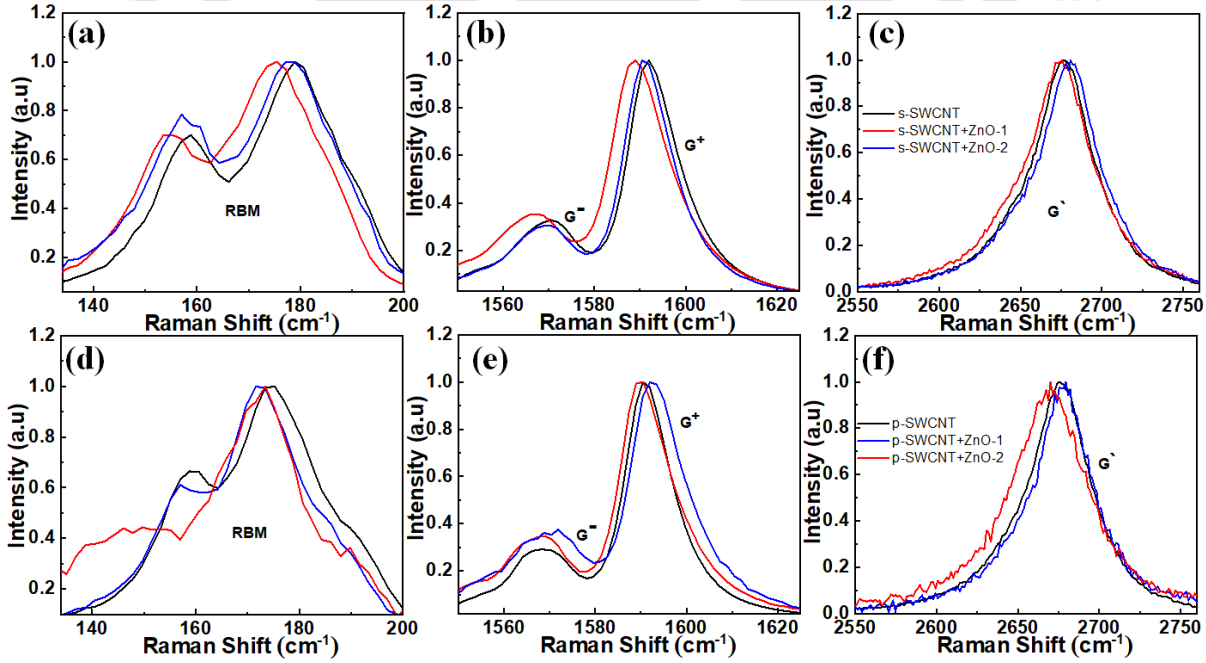


*Figure 4.1.3 Effect of functionalization in Raman peak in comparison: (a, d) RBM, (b, e) G-band from, (c, f) G`-band for s-SWCNT+ZnO and p-SWCNT+ZnO compared with the intrinsic s-SWCNT and p-SWCNT respectively*

A maximum redshift of ~4 $cm^{-1}$ in RBM is seen in all three functionalized SWCNTs as compared to their intrinsic SWCNTs counterparts except for m-SWCNT+ZnO, where a maximum blueshift of ~4 $cm^{-1}$ is also seen (Figure 4.1.2 a, d). For s-SWCNT+ZnO, $G^-$ and $G^+$ band exhibit maximum redshift of ~3 $cm^{-1}$ each, with an increased $G^-$ intensity (Figure 4.1.3 b). However, an opposite trend is seen in p-SWCNT+ZnO, where the $G^-$ showed a blueshift of ~3 $cm^{-1}$ (with increased $G^-$ intensity, Figure 4.1.3 e) and ~1 $cm^{-1}$ for the $G^+$ band. The G` bands of m-SWCNT+ZnO, s-SWCNT+ZnO, and p-SWCNT+ZnO are blue-shifted by ~6 $cm^{-1}$, ~3 $cm^{-1}$ and ~2 $cm^{-1}$, and are redshifted by 2 $cm^{-1}$, 3 $cm^{-1}$ and 6 $cm^{-1}$ respectively, as compared to their respective intrinsic SWCNT counterparts (Figure 4.1.2 (c, d), Figure 4.1.3 c, 4.1.3 f). Some readings show no Raman shift which shows the delicate method of functionalization and composite formation while retaining individual dignities in physical, electronic, and phonon properties of SWCNTs. These shifts and alterations in G band intensity are also a source of determining the amount of charge density as well as the type of dopant; either donor or acceptor[201,211,214]. Thus, charge transfer occurred between the two constituting materials and hence resulted in the shifting of exciton energies. Other factors like uniaxial mechanical strain in SWCNTs or alteration in the structural integrity of $sp^2$-hybridized C atoms cause shifting of G-band[209–211]. This is also due to the decrease in tube-tube interaction by increasing the inter-tubular spaces between individual nanotubes when ZnO is loaded[215]. The D-band or distortion band of SWCNTs gives information regarding the presence of defects, dislocations, nanotube ends, and chemical functionalization. The blueshifts in D-band in all three SWCNT+ZnO samples are due to the functionalization of SWCNTs by ZnO nanoparticles besides indicating the introduction of defects, distortion, and delocalization of electron density. The redshift in the G band ($G^+$, $G^-$) for all SWCNT+ZnO samples indicates the formation of physical non-covalent functionalization when ZnO adheres to SWCNT surfaces[208]. To be brief, it is noteworthy that, the functionalization of electronically different SWCNTs- metallic, semiconducting, and pristine SWCNTs surface by ZnO nanoparticles is based on chemical functionalization with non-covalent van der Waals interaction. The individual properties are retained with additional evidence of charge transfer, changing charge carrier density as some non-Raman peak shifts are observed in all three SWCNT+ZnO samples. In this non-covalent interaction, the semiconductor oxides interact by wrapping or physical absorption in the carbon nanotube walls, thereby retaining electronic and structural properties via maintaining the original aromatic systems of nanotubes.

Apart from concluding the non-covalent interaction between SWCNT and ZnO, the collective distribution of $\Delta I_D/I_{G+}$ % and $\Delta I_{G+}/I_{G-}$ % for the six selected readings of all ZnO functionalized SWCNTs as compared to their corresponding intrinsic SWCNTs is shown in Figure 4.1.2 e. For m-SWCNT+ZnO, s-SWCNT+ZnO and p-SWCNT+ZnO, the $\Delta I_D/I_{G+}$ % values are decreased by a maximum of ~4%, ~2% and ~3% sequentially from their intrinsic SWCNT. And, as compared to the $\Delta I_{G+}/I_{G-}$ % value of intrinsic SWCNT, the $\Delta I_{G+}/I_{G-}$ % values of m-SWCNT+ZnO, s-SWCNT+ZnO and p-SWCNT+ZnO are increased by ~26 %, ~22 % and ~85 % respectively. The decrease in $\Delta I_D/I_{G+}$ values in SWCNT+ZnO is due to the formation of defects as the origin of the D band is related to the $sp^3$ hybridization of the C atom also known as the defect/distortion-induced band. The change from $sp^2$ to $sp^3$ hybridization of C atoms in CNT is due to the chemical modification resulting from functionalization[216]. However, a maximum of 0.051 decrease in $I_D/I_{G+}$ value indicates the formation of very few minute defects in the p-SWCNT+ZnO as compared to other SWCNT/ZnO composites formed by the sputtering process which was observed to be ~6[217].

The value of $I_D/I_{G+}$ value of the SWCNT+ZnO has increased from 0.027 to $0.069_{max}$ (six readings of $I_D/I_{G+}$ values lie between 0.034 and 0.069) for m-SWCNT+ZnO, 0.020 to $0.040_{max}$ (six readings of $I_D/I_{G+}$ values lie between 0.024 and 0.040) for s-SWCNT+ZnO, and 0.014 to $0.051_{max}$ (six readings of $I_D/I_{G+}$ values lie between 0.019 and 0.051) for p-SWCNT+ZnO from their intrinsic SWCNT counterparts. These indicate the introduction of defects due to composite formation and functionalization with higher structural quality. The distribution of $\Delta I_{G+}/I_{G-}$ % value for all six readings and three samples lies in the positive direction, which indicates the decrease in $I_{G+}/I_{G-}$ value relative to their intrinsic SWCNTs. Some readings show no change in $I_{G+}/I_{G-}$ value, implying the retained property of SWCNTs after functionalization. The changes in the $I_{G+}/I_{G-}$ intensity ratio of SWCNT and ZnO functionalized SWCNT also reveal the signature of charge transfer information between SWCNT and ZnO. The decrease in $I_{G+}/I_{G-}$ value indicates the increasing intensity of the $G^-$ band and the decreasing intensity of the $G^+$ band. The increase in the $G^-$ band represents the increasing metallicity of SWCNTs by acting as an electron acceptor[209]. Among the three different types of SWCNTs; metallic, semiconducting, and pristine SWCNTs, p-SWCNTs show a maximum decrease in $I_{G+}/I_{G-}$ ratio by almost 85%, depicting maximum charge transfer occurring between p-SWCNTs and ZnO. Hence, in summary, it can be concluded that despite the difference in optical and electronic properties of the three electronically different SWCNTs, in the three mentioned functionalized SWCNTs (m-SWCNT+ZnO, s-SWCNT+ZnO, and p-SWCNT+ZnO), ZnO semiconductor

oxide acted as an electron donor and SWCNT, an ambipolar material acted as an electron acceptor. As a result, this charge transfer process enhances charge carrier lifetimes by ~1ns in all the functionalized SWCNTs as compared to intrinsic ZnO, indicating a reduction in charge carrier recombination. As charge transfer plays a crucial role in the application of photocatalysis, it is speculated that an increase in charge carrier lifetime in the SWCNT+ZnO composites by charge transfer assists in elevating the photocatalytic process. Therefore, it is worthwhile to investigate and study the charge transfer mechanism between SWCNTs and ZnO as illustrated in Figure 4.1.4 and Table 4.1.1.

Figure 4.1.4 (a, b, c) show FESEM images of the stably dispersed m-SWCNT, s-SWCNT, and p-SWCNT in DMF solvent. The tubular structural analysis is done by using FETEM shown in Figure 4.1.5. From Figure 4.1.4 (d, e, f), it is evident that the interaction between SWCNTs and ZnO is less although ZnO nanoparticles are attached to the tube surface. The presence of an excess amount of ZnO particles (50 mg) as compared to SWCNTs (3 ml of 1 mg/20 ml solution) is seen in all three composites and homo-aggregations of ZnO are found to be dominant.

The crystallinity of ZnO is also shown by the Selected Area Electron Diffraction (SAED) pattern in Figure 4.1.5 a3. The SAED pattern m-SWCNT (Figure 4.1.5 b3) shows amorphous structures donated by the two rings corresponding to (002) and (004) planes. The (002) plane of SWCNT and ZnO diffraction planes are observed in Figure 4.1.5 c3 in the m-SWCNT+ZnO sample.

On account of verifying the existence of charge transfer between the constituting materials, intermolecular charge transfer is investigated by measuring carrier lifetimes using a TRPL spectrophotometer. The calculated carrier lifetimes are shown in Table 4.1.1. The lifetimes of charge carriers are found to have increased by ~1 ns in SWCNT+ZnO. This supports Raman analysis of charge carrier transfer from n-type ZnO (electron donor) to ambipolar SWCNTs (electron acceptor), thereby forming a heterojunction interface. Notably, the carrier lifetime of m-SWCNT+ZnO lies in-between s-SWCNT+ZnO and p-SWCNT+ZnO and follows the order of s-SWCNT+ZnO> m-SWCNT+ZnO> p-SWCNT+ZnO> ZnO; 4.76> 4.62> 4.24> 3.31 ns (Figure 4.1.6 a). This may be due to the presence of m-SWCNTs and s-SWCNTs in p-SWCNTs in ~1:3 ratio. Thus, the easy charge carriers transfer from semiconductor oxides (~2.9 eV of ZnO calculated from UV-Vis absorption Tauc's plot shown in Figure 4.1.6 b inset) is facilitated by SWCNTs because of the bandgap difference.

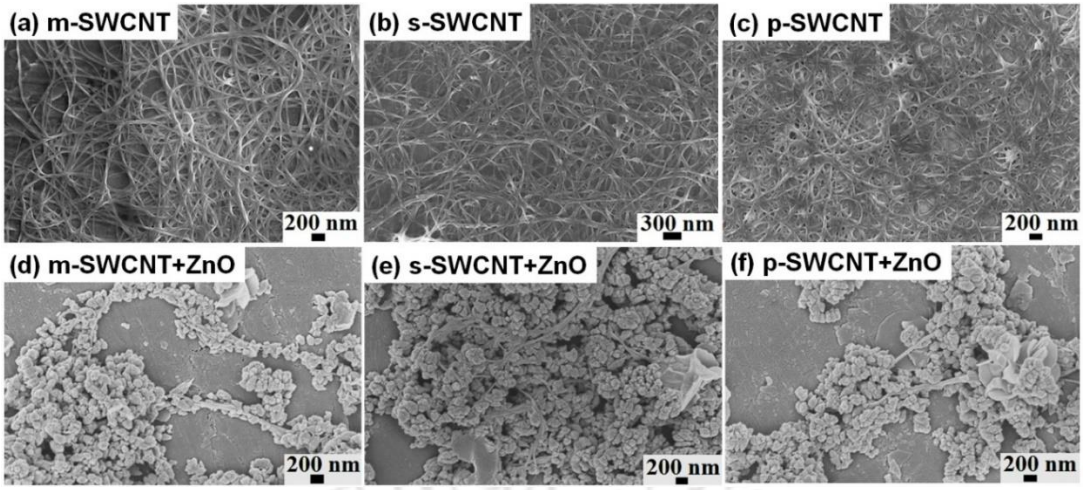


*Figure 4.1.4 FESEM images of (a) m-SWCNT, (b) s-SWCNT, (c) p-SWCNT, (d) m-SWCNT+ZnO, (e) s-SWCNT+ZnO and (f) p-SWCNT+ZnO*

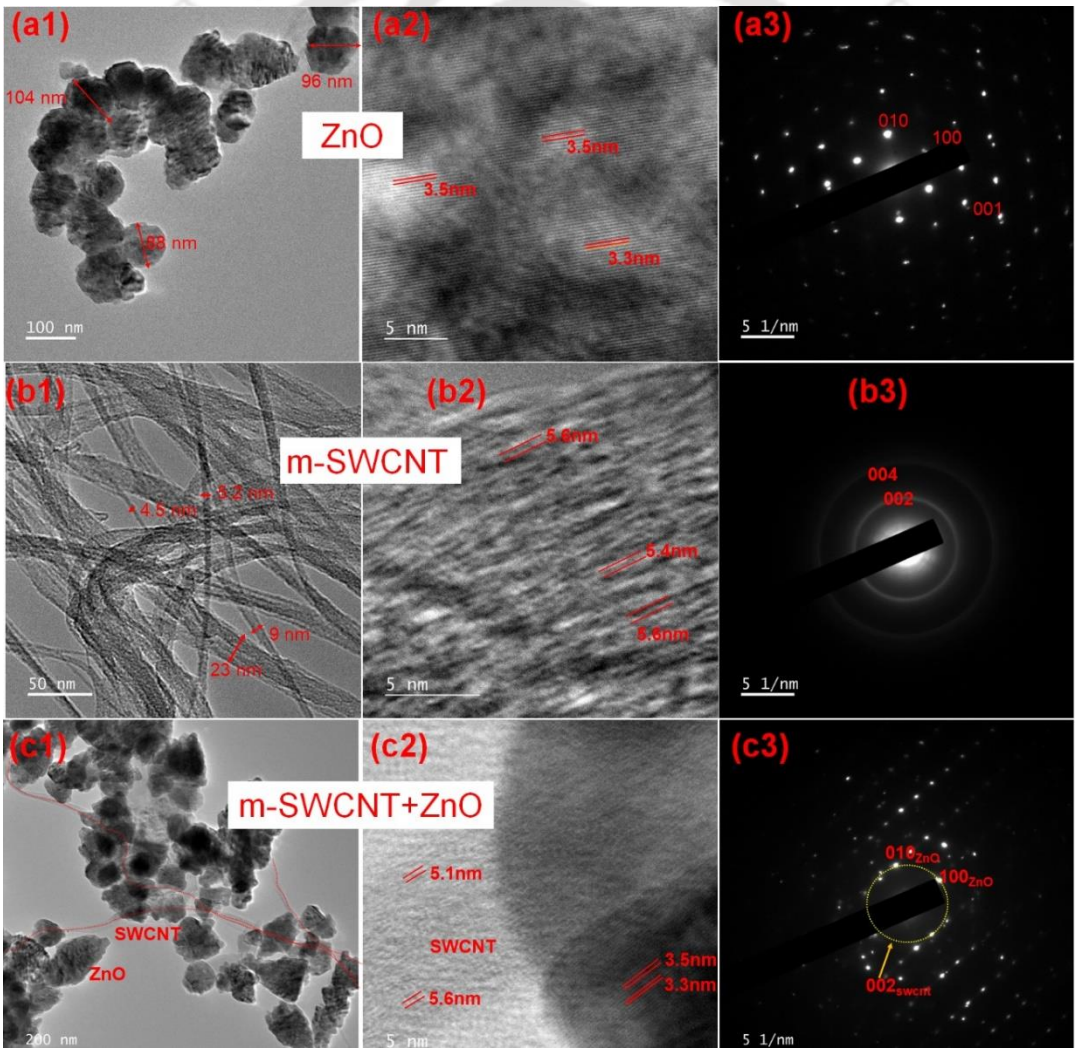


*Figure 4.1.5 FETEM (a1, b1, c1), HRTEM (a2, b2, c2) and Selected Area Electron Diffraction (SAED) pattern (a3, b3, c3) analysis of ZnO, m-SWCNT, m-SWCNT+ZnO respectively*

*Table 4.1.1 Carrier lifetime of ZnO and ZnO functionalized with three optically and electronically different SWCNTs*

| **Samples/ Parameters** | **ZnO** | **m-SWCNT+ZnO** | **s-SWCNT+ZnO** | **p-SWCNT+ZnO** |
|---|---|---|---|---|
| Lifetime (ns) ±2ps | 3.31 | 4.62 | 4.76 | 4.24 |
| $\chi^2$ | 1.280 | 1.076 | 1.036 | 1.155 |

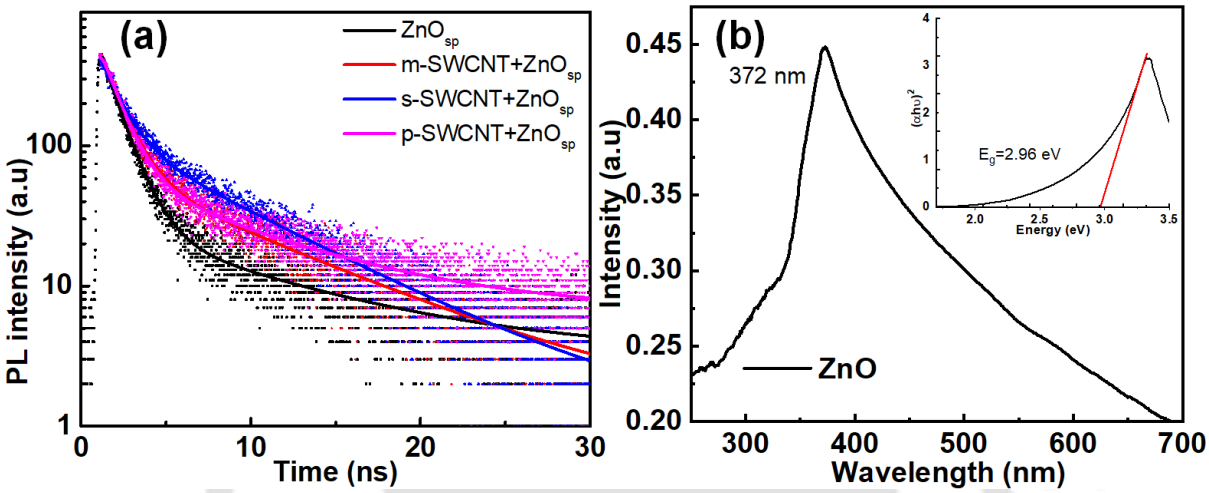


*Figure 4.1.6 (a) Carrier decay graph of ZnO, m-SWCNT+ZnO, s-SWCNT+ZnO, and p-SWCNT+ZnO, and (b) UV-Vis absorption spectra of ZnO (inset: Tauc's plot)*

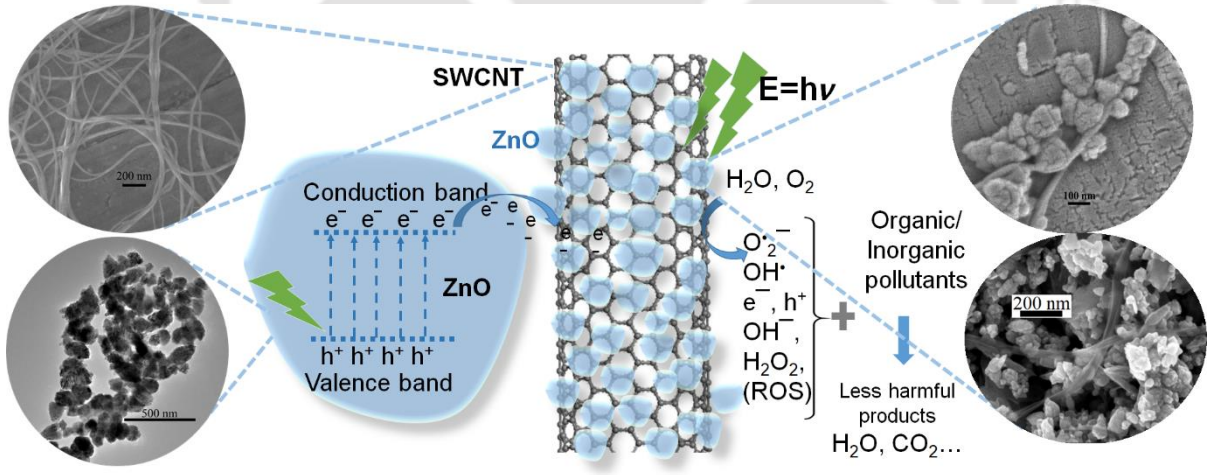


*Figure 4.1.7 Illustration diagram of ZnO particles attached to the SWCNT surfaces and intermolecular charge transfer between ZnO and SWCNT for the potential photocatalytic water treatment process*

The attachment of ZnO particles to SWCNT surfaces with intermolecular charge transfer from wide bandgap ZnO semiconductor oxide to no or lesser bandgap SWCNTs is illustrated in Figure 4.1.7. The basic step of charge carrier dynamics is considered to be commenced when electrons are excited from the valence band to the conduction band of ZnO, triggered by the

illumination of light energy greater than or equal to the bandgap energy. The photoexcited electrons of ZnO are separated at the p-n heterojunction interface of s-SWCNT+ZnO, and Schottky junction of m-SWCNT+ZnO. As a result, the separated electrons are transferred and conducted to the respective SWCNTs in the SWCNT+ZnO composites as SWCNTs are a good conductivity of electricity providing a driving force, while holes stay back in ZnO[206,218]. This charge separation inhibits the recombination of electrons and holes. Therefore, considering the potential application in photocatalytic reactions, it is speculated that with the increase in charge separation, the generation of highly reactive oxygen species (ROS) is found to be enhanced when additional photogenerated $e^-$s combined with $H_2O$ molecules and $O_2$ for photocatalytic water treatment application. This mentioned ROS includes $H_2O_2$, $O_2\bullet^-$, $OH^-$, OH•, etc. which further assist in degrading or decomposing organic/inorganic pollutants in water into less harmful by-products (illustrated in Figure 4.1.7)[136].

Summarizing from all the analysis and discussions, three electronically different SWCNT are functionalized by ZnO forming composites: m-SWCNT+ZnO, s-SWCNT+ZnO, and p-SWCNT+ZnO are successfully performed by the facile sonication method by preserving their individual properties. Also, it is to be emphasized that photogenerated charge carriers are separated at the heterojunction interface and transferred from donor ZnO to SWCNTs acceptors, increasing the charge carrier lifetimes. Thus, the enhancement in carrier lifetime due to charge transfer between SWCNT and ZnO provides plenty of future applications mostly in photocatalysis, sensors, devices, fuel generation, and photo-related applications. Hence, these photoexcited charge carriers are separated in the SWCNTs/ semiconductor oxide interface inhibiting charge recombination, thus, increasing the generation of reactive oxygen species by interactions in the case of photocatalytic water treatment.

### ***4.1.3 Determination and analysis of critical coagulation concentration***

To enhance the intermolecular interaction between ZnO and SWCNTs with the optimum quantity for functionalization and composite formation, critical coagulation concentration (CCC) of different SWCNTs was studied using ZnO as the coagulant. The stability of nanotube dispersion is studied by its aggregation properties using ionic coagulants and is described by the Schulze-Hardy rule (SH) and modified-Derjaguin-Landau-Verwey-Overbeek (modified-DLVO) colloidal interaction theories. Critical coagulation concentration is used to study colloidal stability referring to the minimum concentration of a coagulant required to induce coagulation of a stable colloidal solution. For experimental analysis and calculation of CCC, this value is given by SH rule, $CCC \propto z^{-6}$, where, z=valence of the coagulant ion. Theoretically,

CCC is calculated from two approaches- by interaction energy (traditional calculation method) and interaction force, when their maximum value reaches zero[219,220]. The underlying mechanism for the attraction between SWCNTs and ZnO is based on hetero-aggregations, where the involved molecules are different, possessing different surface charge densities. In addition, in the early stage of aggregation, homo-aggregation of SWCNTs and ZnO takes place, which later shifts towards hetero-aggregation processes. The aggregation rate is determined by $dN_{12}/dt = kN_1N_2$ ; where: k=rate constant, $N_1$, $N_2$= number concentrations of particle 1 and 2 (here, 1= ZnO and 2= SWCNT), $N_{12}$= number concentration of dimer, and t= time. At high salt concentrations, diffusion-controlled aggregation (DCA) occurs, as hydrodynamic interactions and van der Waals forces have a minor effect. But, at low salt concentration, particles undergo slow aggregation known as reaction-controlled aggregation (RCA), as extra energy is required to overcome the energy barrier developed due to the electrical double layer. The transition between slow and fast aggregation regimes, separated by CCC, highly depends upon salt concentration and surface charge densities[221].

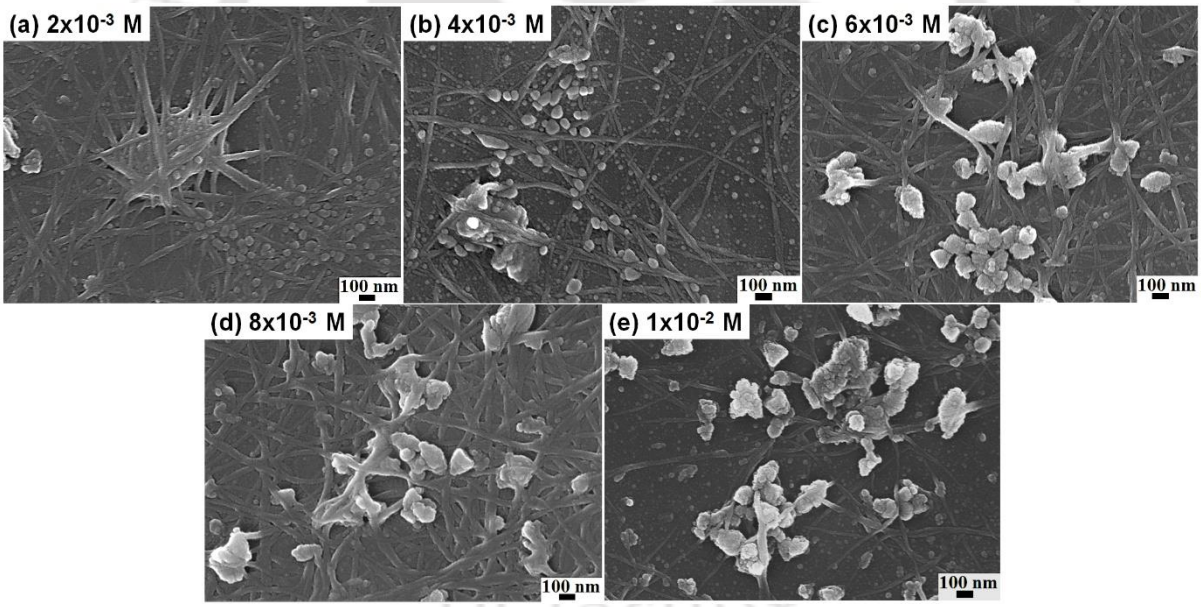


*Figure 4.1.8 FESEM images of m-SWCNT+ZnO supernatant (drop cast 3 times) in determining CCC by various molarity of ZnO coagulant (a) 2x10$^{-3}$, (b) 4x10$^{-3}$, (c) 6x10$^{-3}$, (d) 8x10$^{-3}$ and (e) 1x10$^{-2}$ M*

Here, to show morphological interactions between SWCNT and ZnO, m-SWCNT coagulation for 2x10$^{-3}$ to 1x10$^{-2}$ M ZnO concentrations is used, as the CCC befall under this range. Figure 4.1.8 (a-e) show FESEM images of the supernatant (three times drop cast) when different molarities of ZnO (2x10$^{-3}$, 4x10$^{-3}$, 6x10$^{-3}$, 8x10$^{-3}$ and 1x10$^{-2}$ M) are used for coagulating stably dispersed m-SWCNT suspension in DMF. From the images, by increasing ZnO concentrations

from 2 mM to 10 mM, the amount of ZnO and SWCNTs suspended in the supernatant decreased as expected. This shows that with the addition of ZnO nanoparticles, SWCNTs are agglomerated by the influence of the coagulant. A similar interaction was seen in FESEM images shown in Figure 4.1.4 (d-f). In conjunction with the previous results obtained from Raman spectroscopy, it can be concluded that sub-nano ZnO particles have attached to SWCNT surfaces non-covalently. Owing to the bigger aggregate sizes of ZnO particles (~100-200 nm) and its affinity to aggregate, many stable ZnO aggregates outside SWCNT surfaces are also sighted.

Figure 4.1.9 (a, b, c) show UV-Vis absorption spectra of m-SWCNT, s-SWCNT, and p-SWCNT respectively when ZnO coagulants in a series of molar concentrations ranging from $1x10^{-2}$ to $1x10^{-8}$ M are introduced into the stably dispersed SWCNT solution. From the absorption spectra, the absorption at ~370 nm originates from ZnO nanoparticles (Figure 4.1.6 b) stably suspended in the supernatant. These peak intensities corresponding to SWCNT decrease with the increase in ZnO concentration beyond doubt ($1x10^{-8} > 1x10^{-6} > 1x10^{-4} > 2x10^{-4} > 4x10^{-4} > 6x10^{-4} > 8x10^{-4} > 1x10^{-3} > 2x10^{-3} > 4x10^{-3} > 6x10^{-3} > 8x10^{-3} > 1x10^{-2}$ M) while the peak of ZnO followed the opposite trend. Thus, showing maximum intensity at $1x10^{-8}$ M and minimum at $1x10^{-2}$ M ZnO concentration is apparent. It is seen that a negligible amount of SWCNTs is dispersed in the supernatant of all three functionalizations for $1x10^{-2}$ M ZnO concentration.

Each peak in SWCNT UV-Vis absorption spectra corresponds to a certain SWCNT of specific chirality and diameter. From the absorption wavelength of each van Hove peak, SWCNT diameters are calculated using the tight-binding model, where, band-gap energy is inversely proportional to the diameter of SWCNT[222],

for m-SWCNTs: $E_{11}^{M}(eV) = 6a_0\gamma_0/E = 2.47/d_t$ ----- eq. 1

for s-SWCNTs: $E_{11}^{S}(eV) = 2a_0\gamma_0/E = 0.85/d_t$ ----- eq. 2

$E_{22}^{S}(eV) = 4a_0\gamma_0/E = 1.65/d_t$ ----- eq. 3

$E_{33}^{S}(eV) = 8a_0\gamma_0/E = 3.29/d_t$ ----- eq. 4

where; $d_t$= diameter of nanotube in nm, $a_0$= C-C bond length= 0.142nm, $\gamma_0$= hopping energy = ~2.9 eV, E(eV)= 1240/λ(nm). The van Hove singularities are energy levels that resulted from 1D quantum confinement of the electronic states in carbon nanotubes when a 2D graphene sheet rolled up, having a high density of states[223]. In m-SWCNT dispersion with ZnO coagulant (Figure 4.1.9 a), a broad prominent 1D van Hove singularity transition is seen at 550-800 nm

with small bumps in between 400-550nm. The broad peak in higher wavelength is attributed to the first transition of metallic SWCNT, $M_{11}$. The lesser wavelength absorption at 400-550 nm is attributed to the second van Hove transition, $M_{22}$ of m-SWCNT. For m-SWCNT, only the first two transitions $M_{11}$ and $M_{22}$ are observed as the van Hove singularities spacing is large[223,224]. Whereas, in s-SWCNT, first (1400-1800nm), second (800-1200nm), and third (400-600nm) transitions ($S_{11}$, $S_{22}$, and $S_{33}$ respectively) are seen when electrons are elevated from van Hove singularities valence band to their corresponding conduction band. The electronic and optical properties of the SWCNTs depend on the nanotube diameters, length, and chirality. In these one-dimensional SWCNTs, the density of states is not a continuous function of energy but descends gradually and increases in discontinuous spikes forming Van Hove singularities that are caused by the rolling of graphene sheets into tubular one-dimensional nanotube structures. Thus, optical transitions in SWCNTs occur between the same valence and conduction states or crossover transitions. However, the energies between the Van Hove singularities depend on the nanotube structures—length, diameter, and chirality. In absorption spectroscopy, by the absorption of light, the electrons in the Van Hove singularities of the valence band are excited to the corresponding energy levels in the conduction band. That is, for the optical absorbance, electronic transitions occur from the occupied Van Hove singularities to the unoccupied Van Hove singularities. The different peaks in the absorption spectra arise from the different species of SWCNTs i.e., different diameters, lengths, and chirality of SWCNTs. Also, the presence of defective or non-defective SWCNTs affects the peak structures in the absorption spectra. In addition to this, the centrifugation process also impacts the spectra as the process removes the aggregated nanotubes from the solution and remains the individual nanotubes in the solution[223,224].

Here, Figure 4.1.9 b shows several small significant van Hove singularities between ~450-750nm corresponding to $S_{33}$ transitions. As the p-SWCNT sample is composed of both semiconducting and metallic SWCNTs, the $M_{11}$, $M_{22}$, and $S_{33}$ transitions are evident. The intensities of these peaks decrease due to the increase in coagulation with the increase in ZnO molar concentration. This indicates the formation of large aggregates via van der Waals's attractive forces between SWCNT/ZnO, ZnO/ZnO, and SWCNT/SWCNT (homo- and hetero-molecular aggregations). Thereby, the number of suspended SWCNTs is reduced by repressing electrostatic double-layer (EDL) repulsive forces between the NTs with the influence of ZnO coagulant. Due to the introduction of ZnO into the stably dispersed SWCNT suspensions, ZnO interacts with SWCNTs, reducing the surface energy barrier of the nanotube. Thus, the

attractive van der Waals forces overpower double-layer repulsive forces thereby initiating the aggregate formation and coagulation processes.

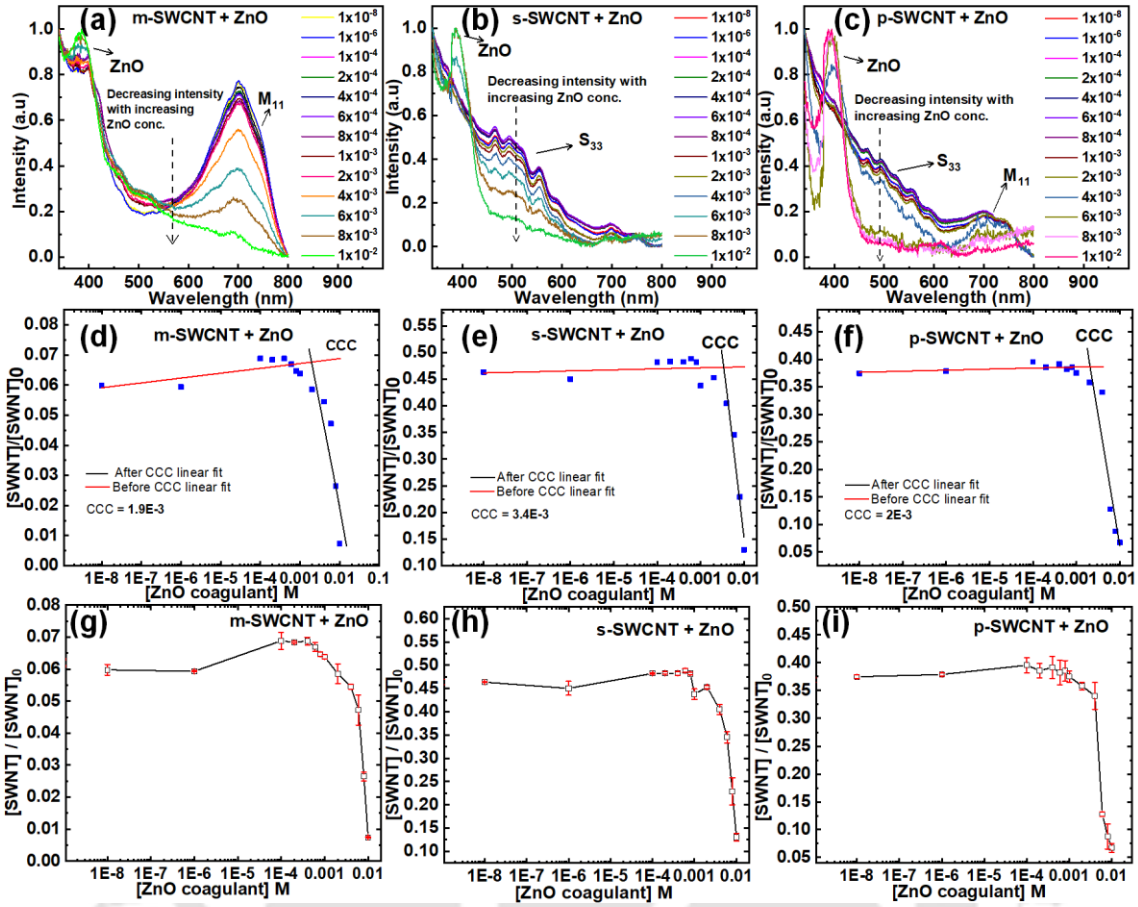


*Figure 4.1.9 (a, b, c) UV-Vis absorption spectra (normalized) of the supernatant of m-SWCNT, s-SWCNT, and p-SWCNT respectively with different ZnO coagulant concentrations ranging from $1x10^{-8}$ M to $1x10^{-2}$ M, (d, e, f) determination of CCC by linear fitting of before (red) and after (black) the CCC of m-SWCNT, s-SWCNT, and p-SWCNT with ZnO coagulant, and an average of triplicate experiments with calculated standard deviation for (g) m-SWCNT (h) s-SWCNT, (i) p-SWCNT with ZnO as a coagulant*

To delve deeper into the interaction mechanism between SWCNT and ZnO in the CCC process, the aggregate and supernatant of the coagulant-added solutions are separated and explored through normalized UV-Vis absorption analysis. A representative study and analysis were done for $10^{-3}$ M concentration series, where CCC befall for m-SWCNT (Figure 4.1.10). The increase in ZnO coagulant molar concentration from DMF (controlled) i.e., no coagulant or 0 mM (Figure 4.1.10 a) to $1x10^{-2}$ M (Figure 4.1.10 g), the SWCNT quantity in the supernatant is decreased which is undisputed. From Figure 4.1.10 a, it is apparent that the centrifugation effect is absent in the whole experiment, thereby the reduction in SWCNT quantity in the supernatant is wholly due to the coagulation formed by adding ZnO. The lesser intensity of the 600-800 nm peak in the aggregates is undoubtedly due to the suppression by the highly intense ZnO

peak seen at ~370nm. SWCNTs have high van der Waals interaction between individual nanotubes and are chemically dispersed stably due to the interplay of attractive van der Waals force and electrostatic double-layer repulsive forces/ energy. However, at near-CCC, the interfacial interaction played a major role with shorter intermolecular distances, increasing the rate of aggregation[203].

The absorption at 500nm is utilized as the CCC determination point for all SWCNT suspensions (m-SWCNTs, s-SWCNTs, and p-SWCNTs). The supernatants after coagulation and centrifugation are carefully collected without disturbing the aggregates and separated for CCC analysis. The experiments were executed in triplicates. The average of these three results was taken and standard deviations were calculated as shown in Figure 4.1.9 (g, h, i). Chiefly, the calculated average values were taken to calculate the CCC value with linear fitting as shown in Figure 4.1.9 (d, e, f) for m-SWCNT, s-SWCNT, and p-SWCNT respectively and found to be ~$1.9x10^{-3}$ M, $3.4x10^{-3}$ M and $2x10^{-3}$ M respectively. This indicates the involvement of close interaction between semiconductor oxide ZnO and SWCNTs, which will enhance efficient charge transfer between hetero-molecules. The difference in CCC values for three different SWCNTs is due to the different dielectric and electronic properties of metallic and semiconducting SWCNTs as finite dielectric constants depend upon bandgap energy. The finite dielectric constant of s-SWCNT is less than 5 (where the dielectric value is inversely proportional to the square of the bandgap) and a large absolute value for m-SWCNT[225]. In addition to the dielectric properties, the surface charge distribution, zeta potential, and chirality of SWCNTs differentiate the overall SWCNT properties[225,226]. This distinctive dissimilarity in CCC value also gave rise to the result that different chemical reactivity occurred for m-SWCNT and s-SWCNT toward the same ZnO particles. The CCC value of p-SWCNT lies in between the CCC values of m-SWCNT and s-SWCNTs. Like other analysis results, this behavior is contributed by the mixed presence of both metallic and semiconducting SWCNTs in pristine SWCNTs.

The determination of CCC by the SH rule is based on the classical DLVO theory under the assumption of certain morphology, iconicity of the counterions (valence of counter ion), and constant surface potential during the interaction[227]. Although the SH rule of CCC determination is applicable in the case of ionic coagulants for SWCNTs coagulation[228], it also shows a deviation in some experimental coagulation studies. This deviation may be due to the molecular nature of the coagulant (similar in our case), large molecular size as compared to ionic radii, and most importantly the nature of surface potentials. Therefore, in the case of molecular

interactions, the SH rule is controversial to give CCC value. Also, DLVO theory is built on the assumption that two particles are interacting in an infinite volume which contradicts our experimental evaluation where an infinite number of particles are interacting in a finite volume[227].

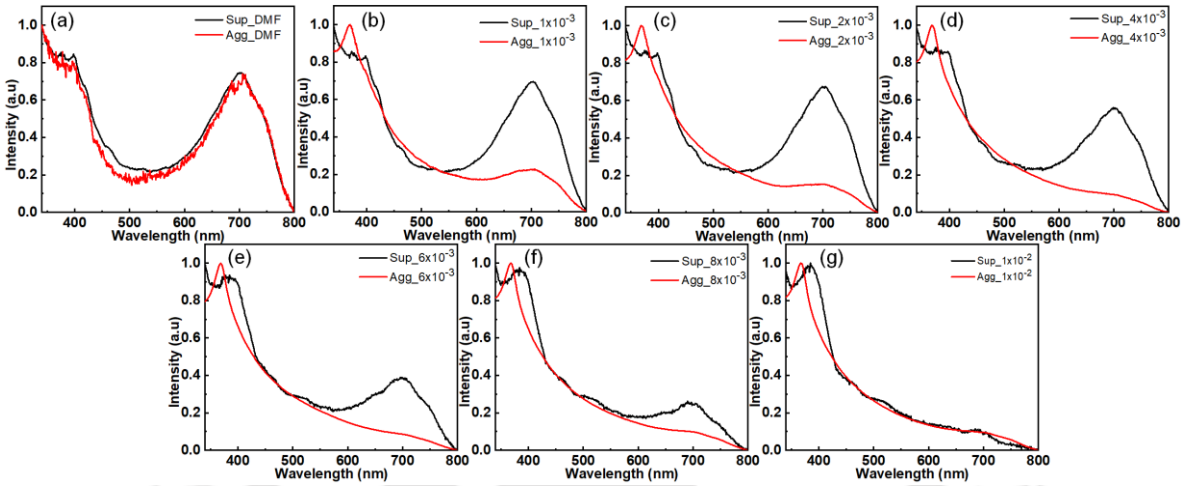


*Figure 4.1.10 UV-Vis absorption spectra (normalized) showing the intensity difference in supernatants and aggregates of m-SWCNTs separated during CCC experiment for ZnO concentration of (a) 0 mM or DMF alone, (b) 1x10$^{-3}$ M, (c) 2x10$^{-3}$ M, (d) 4x10$^{-3}$ M, (e) 6x10$^{-3}$ M, (f) 8x10$^{-3}$ M and (g) 1x10$^{-2}$ M*

The fast coagulation/ aggregation of the stably suspended SWCNTs in DMF starts at the CCC point. At the CCC point, the EDL repulsive forces that kept SWCNT dispersion stable reduce fully and the van der Waals force of attraction controls the aggregation kinetics. The particle aggregation follows RCA kinetics before CCC and is replaced by DCA after the CCC point where the EDL layer is below a threshold level by the hindrances created due to coagulant addition and disrupts surface energy distribution[203,229]. Another experimental result suggested that aggregation was triggered due to the direct binding of counter ions to SWCNT surfaces. This phenomenon reduces and neutralizes the nanotube's surface charges and was proved by using differently charged ionic coagulants carrying different charges: anionic and cationic, multi or monovalent[221,228]. It is assumed that the DLVO theory of sphere-plate interaction will be a suitable relationship to express surface potential barrier with van der Waals' interaction attractive forces and EDL repulsive forces where the morphology of ZnO will be taken as a sphere and the latter a plate-like structure[230,231]. However, it is difficult to choose a specific theory for this system as every system and the nature of particle morphologies are different from the assumptions taken in the original theories. Nonetheless, to explore the behaviors of interacting particles in a solution, the summation of repulsive EDL and attractive dispersion forces are recognized and accepted[228]. Here, as our study focuses on hetero-interaction, homo-

aggregations; ZnO-ZnO and SWCNT-SWCNT are being ignored where DLVO sphere-sphere and plate-plate model will be suitable to explain these interacting phenomena. In hetero-aggregations; SWCNT-ZnO, assuming ZnO as a spherical molecule, for this study, the net interaction energy analysis will also be suitable for taking the sphere-cylinder model using Hamaker's approach for simplicity and applicability. It has been noted that in a small separation distance, the EDL interaction may act as attractive as the two interacting molecules have an asymmetric distribution of EDL although the molecules possess the same surface potentials. In smaller separation distances, the EDL is strongly affected by the curvature effect[220,232]. In the end, there is a need to investigate the interaction energy or force for different structures like carbon nanotubes. Therefore, the CCCs of the three electronically different SWCNTs; m-SWCNT, s-SWCNT, and p-SWCNT with ZnO coagulant are calculated experimentally where the optimum interaction is assumed to occur. It is concluded that the interaction between SWCNTs and ZnO is apt to be explained by the sphere-cylinder model. Also, due to the variation in dielectric value and type of the SWCNTs, the CCC values of m-SWCNT, s-SWCNT, and p-SWCNT differed as dielectricity is dependent on the energy band gaps.

### ***4.1.4 Key findings in Part A***

- In the functionalization and composites formation, ZnO sub-nano particles are attached and anchored on SWCNT surfaces, thereby exhibiting distortion-dislocation and strain.
- The crystallite sizes of the composites were increased due to the additional sonication process and incorporation of SWCNTs.
- Due to the charge transfer and interaction between SWCNTs and ZnO, the carrier lifetimes were increased by ~1ns, and an increase in metallicity is seen in s-SWCNT+ZnO.
- The carrier lifetime value of p-SWCNT+ZnO (4.24ns) lies in-betweens s-SWCNT+ZnO (4.76ns) and m-SWCNT+ZnO, (4.62ns) because of the mixed presence of m-SWCNT and s-SWCNT in p-SWCNT.
- The interaction between SWCNT and ZnO has been due to the retardation in EDL of SWCNTs by overpowering repulsive forces by the attractive van der Waals force of attraction, thereby forming a bond between the coagulant and SWCNT suspensions.
- The CCC of p-SWCNT (2E-4) lies in between m-SWCNT (1.9E-4) and s-SWCNT (3.4E-4) in alignment with the carrier lifetime values.
- s-SWCNT shows a maximum CCC value as compared to the other two SWCNTs.

## PART B: ZnO Self-Assembled on Electronically Different SWCNTs

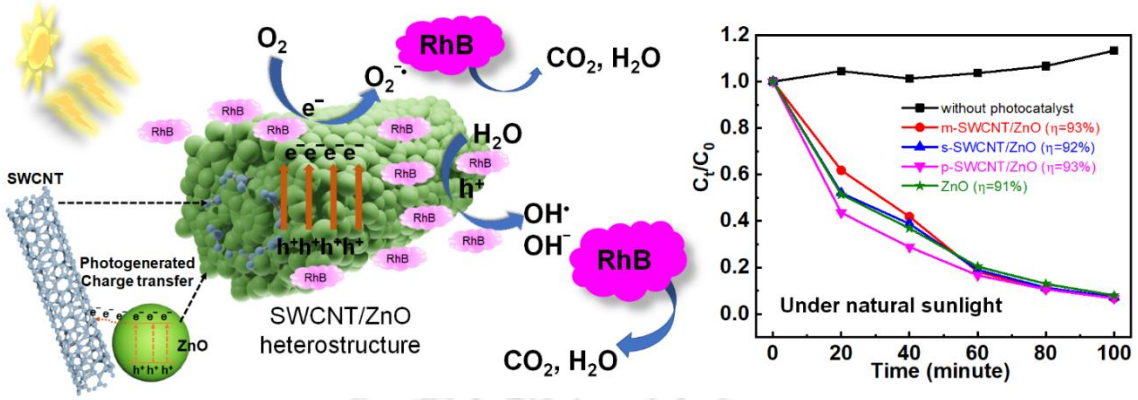


***Graphical Abstract of Part B***

***Publication: Thongam, D. D. & Chaturvedi, H. Heterostructure charge transfer dynamics on self-assembled ZnO on electronically different single-walled carbon nanotubes. Chemosphere 323, 138239 (2023), 10.1016/j.chemosphere.2023.138239***

In continuation of the work done in Part A of this chapter on examining the charge transfer analysis on the ZnO functionalized SWCNTs and SWCNT+ZnO composites, here we grow and assemble ZnO nanoparticles onto three electronically different SWCNT surfaces (metallic, semiconducting, and pristine that were procured from Nano Integris-IsoNanotubes) by facile precipitation method SWCNTs (m-SWCNTs, s-SWCNTs, p-SWCNTs). Using advanced characterization techniques, the three SWCNT/ZnO heterostructures and pure ZnO are studied and compared for the heterogeneous AOP. To the best of our knowledge, there is no comparative study on the charge transfer dynamics for the self-assembled ZnO with electronically different SWCNTs. Therefore, we report on a comparative study of the structural, chemical, optical, and photocatalytic performance of three different SWCNT/ZnO heterostructures with bare ZnO. The impact of different SWCNTs/ZnO heterostructures on charge transfer and separation mechanisms are also analyzed and compared with illustrated diagrams and band edge positions. The impact of charge carrier lifetime on the reaction rate kinetics for rhodamine B degradation is studied using a pseudo-first-order kinetics model for all the samples. We examined the AOP performance for all the samples under UV light and natural sunlight for up to five repeated photocatalytic experiments to determine their stability and reusability.

## 4.2 Results and discussion of the ZnO Self-Assembled on different SWCNTs

### *4.2.1 Structural analysis*

To enhance the interaction between ZnO and SWCNTs in the SWCNT/ZnO nanocomposites, ZnO nanoparticles are self-assembled onto three electronically distinctive SWCNTs using a precipitation reaction. Here, ZnO nanoparticles are anchored onto SWCNTs, establishing a bond with the SWCNT's hydroxyl/carboxyl/formaldehyde group. These SWCNTs are stably dispersed in DMF solvent by the van der Waals interaction with DMF molecules along with CH-π and dipole-π weaker polar interactions. Thus, limiting composite formation with ZnO due to the intramolecular junction generated between SWCNT and DMF molecules[233]. However, stable and efficient three different SWCNT/ZnO heterostructure photocatalysts are synthesized via a facile chemical precipitation method. Figure 1a depicts the XRD patterns obtained following calcination: m-SWCNTs/ZnO, s-SWCNTs/ZnO, p-SWCNTs/ZnO in comparison with bare ZnO nanoparticles.

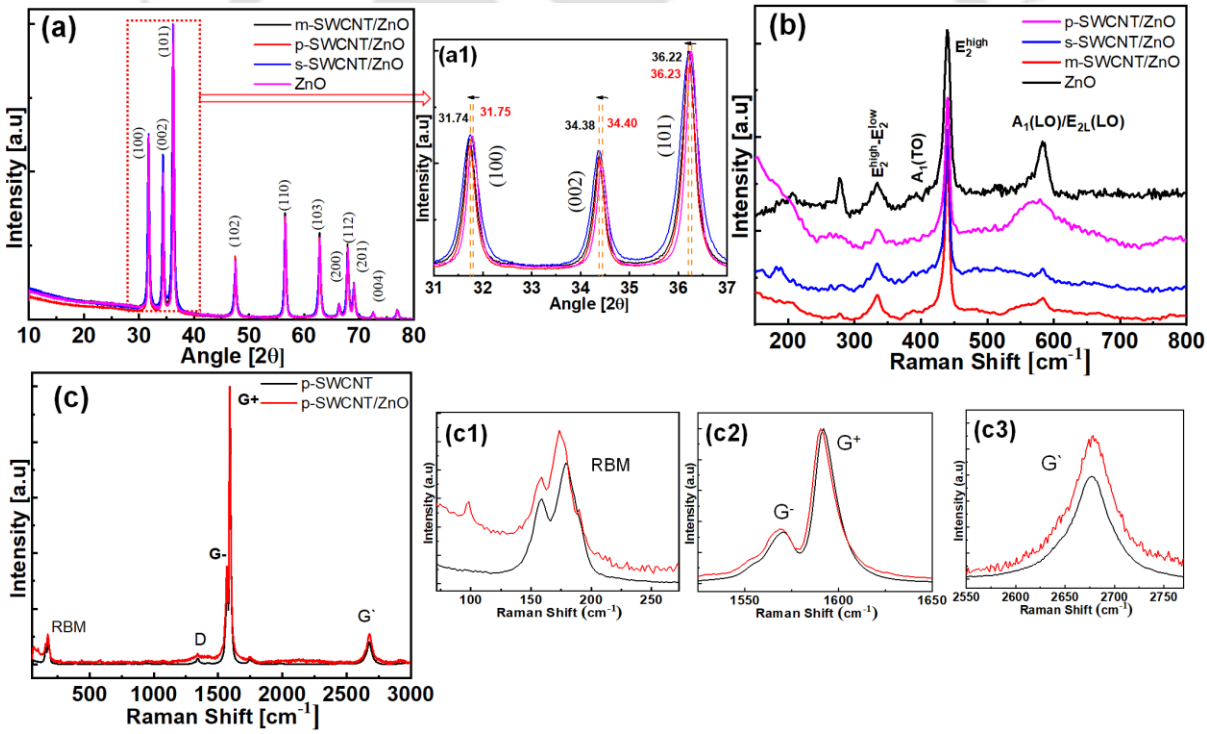


*Figure 4.2.1 (a) XRD analysis for the SWCNT/ZnO heterostructures with pure ZnO, (a1) comparison and peak shift of the (100), (002) and (101) plane, (b) Raman spectra from the SWCNT points of view, (c) Comparison of Raman spectra for the p-SWCNT/ZnO with pure p-SWCNT for the full range and (c1, c2, c3) RBM, G, and G` band respectively*

The SWCNT/ZnO form wurtzite ZnO crystal structure exhibits eleven significant peaks: (100), (002), (101), (102), (110), (103), (200), (112), (201), (004), and (202). As DMF plays multiple

roles in the chemical synthesis process: solvent, surfactant, reductant, and structure-directing agent, the DMF molecules surround the metal ions thereby forming complex ions. Undergoing the calcination process, the surface absorbed DMF molecules were liberated forming catalytically active sites[189].

A negligible peak shift of 0.02˚ toward the lower 2θ angle is seen for all samples with maximum peak broadening in s-SWCNT/ZnO heterostructure as seen in the comparative analysis in Figure 4.2.1 a1. Thus, the crystallite size of s-SWCNT/ZnO heterostructure, 23 nm, is found to be the lowest as calculated from the Debye-Scherrer formula among other samples of crystallite sizes 31 nm, 37 nm, and 35 nm for m-SWCNT/ZnO, p-SWCNT/ZnO, and bare ZnO respectively. From the ZnO perspective, Figure 4.2.1 b compares the Raman spectra of ZnO and SWCNT/ZnO heterostructure. No peak shifts are seen in $E_2^{high}$ peak that corresponds to the wurtzite structure of ZnO, thus, it can be concluded that negligible structural changes and distortions are imposed by the SWCNTs. This also may be attributed to the utilization of a low quantity of SWCNTs for the SWCNT/ZnO heterostructures. However, minor peak shifting is seen in the radial breathing mode (RBM), G-band (graphitic in-plane mode), D-band (disorder-induced band), and G` band (second harmonic D-band). These peak shifts are shown in Figure 4.2.1c and 4.2.1 (c1, c2, c3) for the comparison of pure p-SWCNTs with p-SWCNT/ZnO. The peak shifting originated from the deviation in electron distribution which also indicates charge transfer characteristics. The correlation between Raman shift and charge transfer phenomena is being studied in our previous work with the study of charge transfer dynamics in ZnO functionalized SWCNT and SWCNT+ZnO composites[234].

### ***4.2.2 Morphological analysis***

The de-bundled stably dispersed SWCNTs used to prepare SWCNT/ZnO heterostructures are shown in Figure 4.2.2 (a, b, c) for m-SWCNTs, s-SWCNT and p-SWCNTs. The average nanotubes diameter is 8-10 nm. ZnO exhibited the formation of differing morphologies-nanoaggregates, flakes, and flowers (Figure 4.2.2 d, e). Aside from nanoaggregates and floral ZnO morphologies formed from the supplementary precursors, elongated structures decorated with ZnO sub-nanoparticles are seen for SWCNT/ZnO heterostructures (Figure 4.2.3 a, b, c). The coral-like structures with elongated stems are formed by ZnO sub-nanoparticles aggregated on the SWCNTs surfaces through oriented attachment and self-assembly processes. The detailed structures of the heterostructures are shown in Figure 4.2.3 (a1, b1, c1).

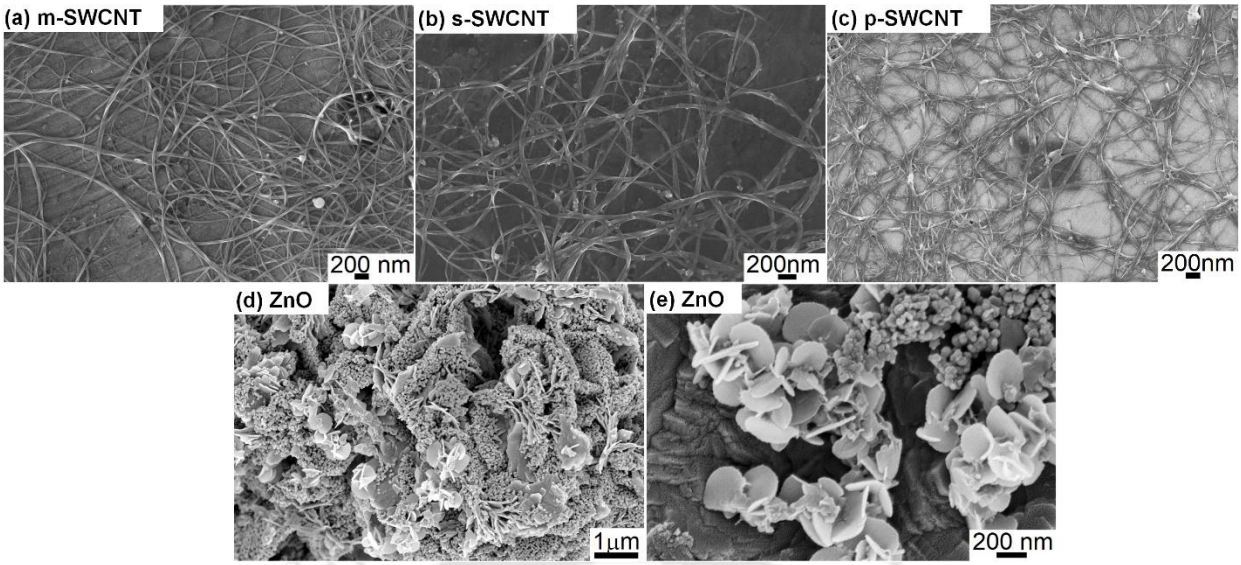


*Figure 4.2.2 FESEM images of the stably dispersed (a) m-SWCNT, (b) s-SWCNT, (c) p-SWCNT which are used for SWCNT/ZnO heterostructure preparations, (d, e) ZnO showing the formation of different morphologies*

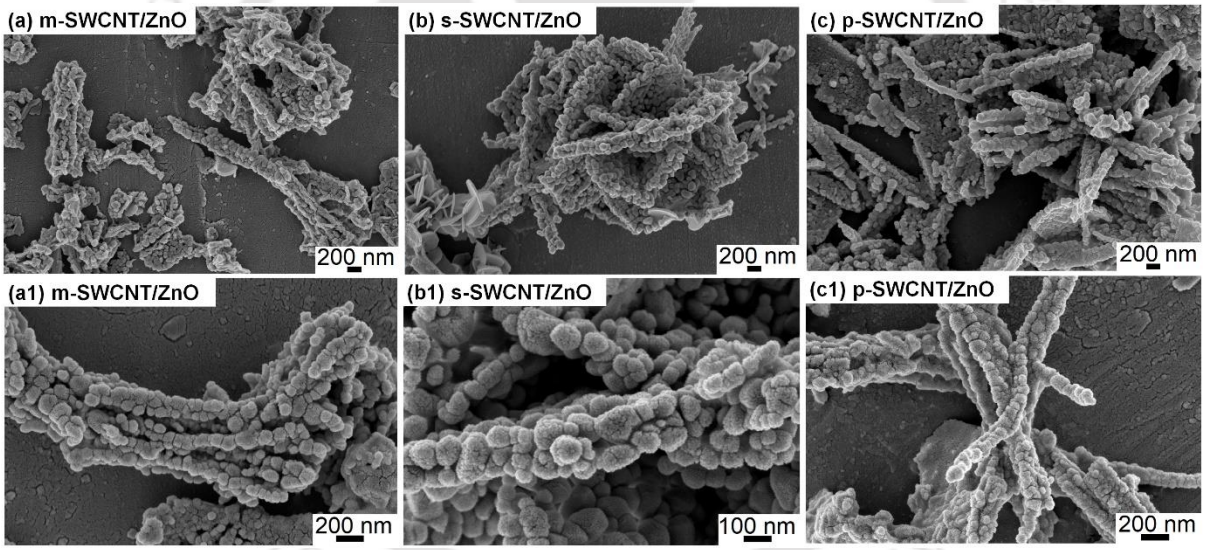


*Figure 4.2.3 FESEM images of (a, a1) m-SWCNT/ZnO, (b, b1) s-SWCNT/ZnO, and (c, c1) p-SWCNT/ZnO heterostructures*

The surface structures of the heterostructures formed by oriented attachment and self-assembled aggregation of ZnO sub-nanoparticles show a bubble and spongy nature. The ZnO nanoparticles are completely formed on the SWCNT surfaces by attaching $Zn^{2+}$ ions to the functional groups present on the SWCNT surface since no ZnO-uncovered SWCNTs are seen[233]. The SWCNT/ZnO heterostructures: m-SWCNT/ZnO, s-SWCNT/ZnO, and p-SWCNT/ZnO show similar morphologies with 20-50 nm thickness i.e., a 10-30 nm ZnO shell is formed over the SWCNTs. Here, the heterostructure nanoparticles sizes calculated from the

FESEM analysis is found to be in accordance with the crystallite sizes calculated from the XRD analysis.

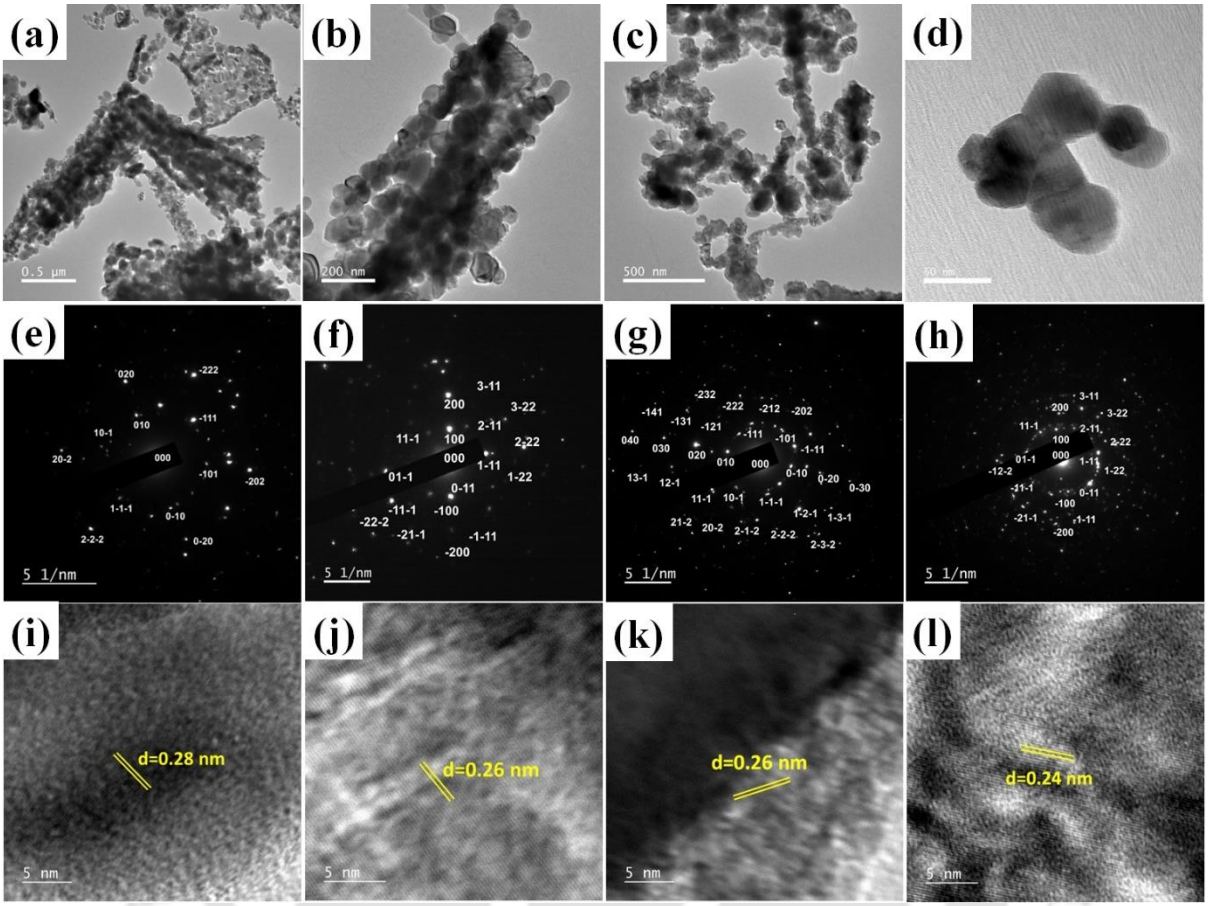


*Figure 4.2.4 TEM images of (a) m-SWCNT/ZnO, (b) s-SWCNT/ZnO, (c) p-SWCNT/ZnO, (d) ZnO, SAED pattern for (e) m-SWCNT/ZnO, (f) s-SWCNT/ZnO, (g) p-SWCNT/ZnO, (h) ZnO and HRTEM images of (i) m-SWCNT/ZnO, (j) s-SWCNT/ZnO and (k) p-SWCNT/ZnO and (l) ZnO*

Figure 4.2.4 (a, b, c, d) show the TEM images of m-SWCNT/ZnO, s-SWCNT/ZnO, p-SWCNT/ZnO, and ZnO respectively. These images confirmed that SWCNT serves as an anchoring tube for the formation of ZnO nanoparticles. Therefore, the ZnO-coated SWCNTs may be recognized by their darker color compared to their side edges. The SAED patterns of SWCNT/ZnO heterostructures and ZnO show a polycrystalline nature. The unique SAED diffraction spots displayed in Figure 4.2.4 (e, f, g, h) indicate the establishment of crystallographic orientation of ZnO crystals. All the diffraction points were calculated and indexed using CrysTBox software by comparing them with the standard ZnO diffraction patterns[235]. The interplanar distance, d-spacings calculated from the HRTEM images of m-SWCNT/ZnO, s-SWCNT/ZnO, p-SWCNT/ZnO and ZnO are 0.28 nm, 0.26 nm, 0.26 nm, and 0.24 nm corresponding to the (100), (002) and (101) planes of ZnO (Figure 4.2.4 (i, j, k, l)).

### *4.2.3 Optical properties and photogenerated charge transfer*

Figure 4.2.5 (a, b) displays the UV-Vis absorption spectra of SWCNT/ZnO heterostructures, bare ZnO, and pure SWCNTs. In contrast to the single 374 nm absorption peak by ZnO nanoparticles, SWCNT/ZnO heterostructures display redshift and blueshift absorption peaks with broad absorption peaks across the visible spectrum. These visible region absorption peaks originated from the SWCNTs associated with ZnO as shown in Figure 5 b.

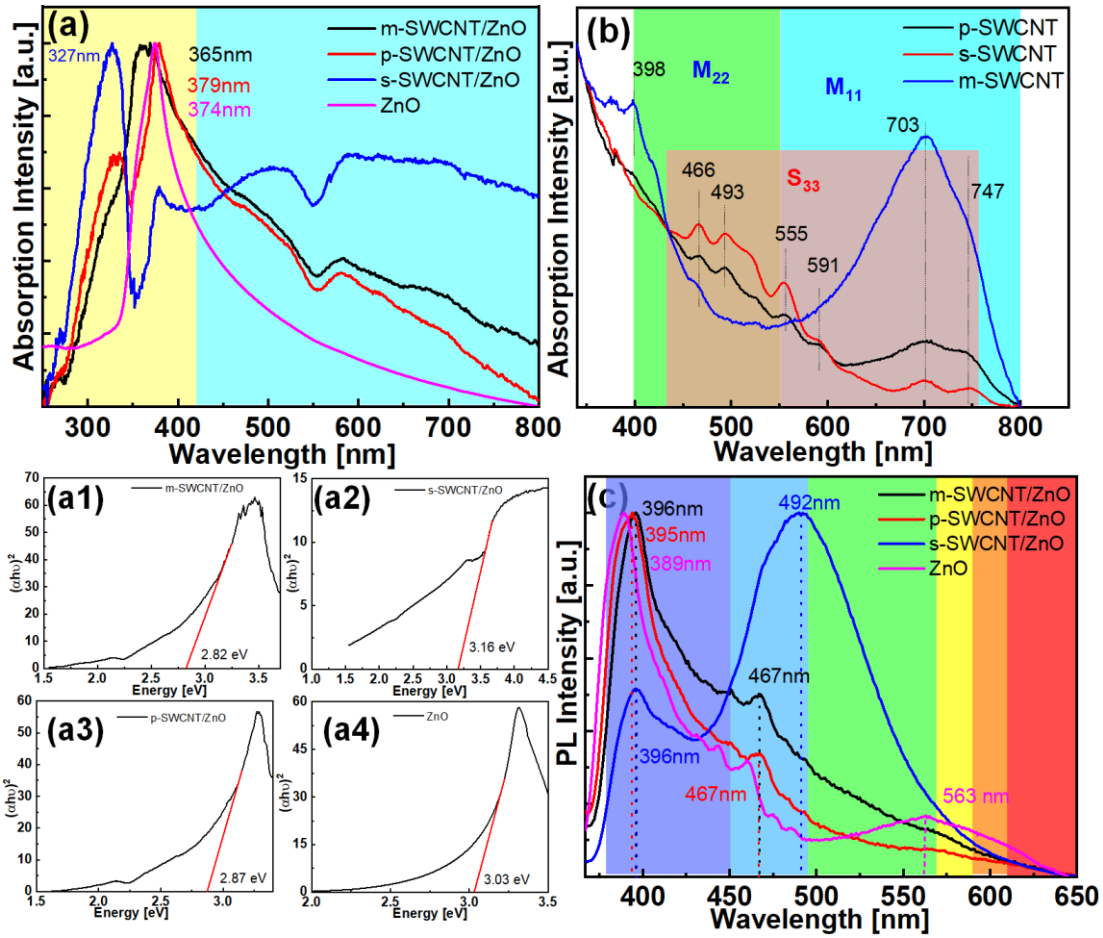


*Figure 4.2.5 Optical property analysis using (a) normalized UV-Vis absorption, (a1, a2, a3, a4) Tauc plot of m-SWCNT/ZnO, s-SWCNT/ZnO, p-SWCNT/ZnO, ZnO respectively, (b) UV-Vis absorption spectra of pure m-SWCNT, p-SWCNT and s-SWCNT, and (c) normalized PL emission spectroscopy*

As discussed in the previous report, the visible region absorption peak is due to the one-dimensional van Hove singularity transition corresponding to $M_{11}$ and $M_{22}$ for m-SWCNT, $S_{33}$ for s-SWCNTs and a combination of $M_{11}$, $M_{22}$, and $S_{33}$ peaks in p-SWCNT as p-SWCNTs consist of m-SWCNT and s-SWCNT mixture[234]. The optical energy band gap of the SWCNT/ZnO heterostructures and ZnO nanoparticles is calculated from Tauc's plot. the

optical band gaps are determined by extrapolating to the zero absorbance as shown in Figure 4.2.5 (a1, a2, a3, a4).

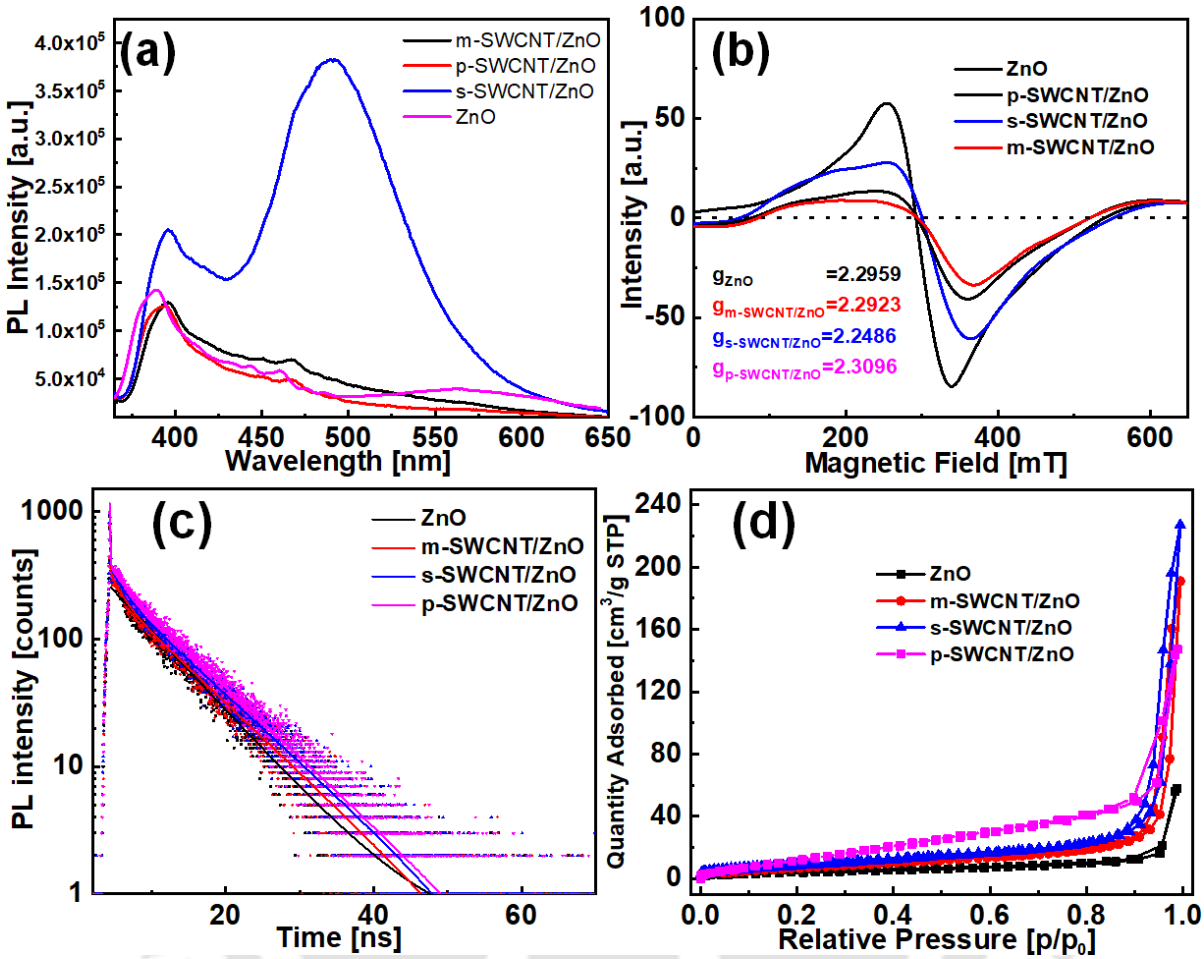


*Figure 4.2.6 (a) PL emission spectra and (b)ESR spectra of ZnO, m-SWCNT/ZnO, s-SWCNT/ZnO, and p-SWCNT/ZnO heterostructures, (c) Charge carrier lifetime analysis using time-resolved photoluminescence spectroscopy and (d) Nitrogen adsorption-desorption isotherm measured for ZnO, m-SWCNT/ZnO, s-SWCNT/ZnO, and p-SWCNT/ZnO*

The ZnO, m-SWCNT/ZnO, s-SWCNT/ZnO, and p-SWCNT/ZnO heterostructures show optical bandgaps of 3.03 eV, 2.82 eV, 3.16 eV, 2.87 eV respectively, showing blue shift as compared to the bare ZnO optical band gap energy (3.3 eV). Depending on the kind of SWCNTs used, the $E_g$ varies; the usage of s-SWCNTs exhibits the largest blue shift with $E_g$=3.16 eV. This is consistent with the link between crystallite size and absorbance, which displays a blue shift with smaller particles. In addition, an Urbach's tail formation is seen for s-SWCNT/ZnO heterostructure (Figure 4.2.5 a2), indicating the formation of mid-gap defect energy states. As a result, shifting bandgaps indicate the appearance of defects and a decrease in crystallite size[236,237]. The apparent absorption of the SWCNT/ZnO heterostructures is caused

by the presence of SWCNTs, as demonstrated by the absorption spectra of pure SWCNTs (Figure 4.2.5 b).

Using the distinctive peaks in the photoluminescence (PL) spectra, Figure 4.2.5 c provides more insight into the creation of the crystal defects. The 492 nm centered broad blue-green PL emission peak is observed due to the electron transition between the valence band of ZnO and surface-related defects such as oxygen vacancies and zinc interstitial sites. This is consistent with the UV-Vis absorption analysis of s-SWCNT/ZnO for mid-gap defect energy state formation. Furthermore, the heterostructures show blue emission peaks due to the presence of zinc interstitial defects. The 563 nm green emission peak indicates the presence of oxygen vacancies in the ZnO crystal[236,238]. However, ~2.6 eV emission is dedicated to the oxygen anti-site defect sites due to the excess oxygen stoichiometry in ZnO nanoparticles[236].

The PL emission intensity also expresses the information regarding the radiative recombination rate. From Figure 4.2.6 a, s-SWCNT/ZnO shows the highest PL intensity whereas m-SWCNT/ZnO and p-SWCNT/ZnO show lower PL intensity as compared to the pure ZnO nanoparticles. The formation of defects in pure ZnO and SWCNT/ZnO heterostructures is also verified by the ESR signal shown in Figure 4.2.6 b. The presence of an ESR signal in pure ZnO is attributed to defects, especially surface defects originating from the liberation of DMF molecules upon calcination. The g-values representing electron properties in a specific environment are found to be greater than the free electron g-value (=2.0036), indicating electron delocalization[239]. The changes in g-value and ESR signal intensities suggest charge transfer at the heterostructure interface by fostering intense electronic interaction between the individuals, hence encouraging the production of a magnetic field. M. Sayed et al. reported the g-factor shifting towards the higher or lower depending upon the direction of charge transfer in the heterojunction formed[240]. In this circumstance, electronic and charge transfer interactions between different SWCNT and ZnO differ owing to the dissimilar electronic characteristics of metallic, semiconducting, and pristine SWCNT, thus, displaying the g-factor shift and varying peak intensities for various SWCNT/ZnO heterostructures. The larger the deviation of the g-factor, the larger the interaction and charge transfer in the heterojunction, thereby increasing the generation of internal magnetic field[240]. Since the recombination of photogenerated charge carriers is vital to the photocatalytic advanced oxidation process, the charge carrier lifetimes of ZnO and SWCNT/ZnO heterostructures are computed by fitting an exponential curve to the TRPL spectra (Figure 4.2.6 c).

*Table 4.2.1 Photogenerated charge carrier lifetimes from TRPL spectroscopy and Summary of BET surface area, total pore volume, and average pore diameter of the ZnO, m-SWCNT/ZnO, s-SWCNT/ZnO, and p-SWCNT/ZnO*

| | **m-SWCNT/ZnO** | **p-SWCNT/ZnO** | **s-SWCNT/ZnO** | **ZnO** |
|---|---|---|---|---|
| $\chi^2$ | 1.004 | 1.001 | 1.001 | 1.006 |
| **Exponential fitting** | Tri-fit | Tri- fit | Tri- fit | Mono- fit |
| $\tau_{avg}^{amp}$ **(ns)** | 7.19 | 7.41 | 7.37 | 6.97 |
| $\tau_{avg}^{int}$ **(ns)** | 7.86 | 7.90 | 8.08 | 6.97 |
| **BET surface area ($m^2/g$)** | 29.66 | 61.64 | 35.20 | 14.51 |
| **Total pore volume ($cm^3/g$)** | 0.255 | 0.227 | 0.317 | 0.089 |
| **Average pore diameter (nm)** | 34.38 | 14.78 | 36.09 | 24.59 |

Due to the existence of crystal defects, photogenerated charge carriers are confined and gradually relaxed to the ground state by phonon emission[241]. The optical decay curve is fitted by using mono-exponential and tri-exponential fit for the ZnO and SWCNT/ZnO heterostructures as shown in Figure 4.2.6 c. Although two distinct methods have been used to compute lifetimes, the amplitude-weighted average lifetime is often utilized to evaluate energy transfer or charge transfer between donor and acceptor[120,126]. The calculated lifetimes and their $\chi^2$ values are sorted in Table 4.2.1. The charge carrier lifetimes of the SWCNT/ZnO heterostructures are increased from 6.97 ns to 7.19 ns, 7.41 ns, and 7.37 ns (amplitude-weighted) when ZnO nanoparticles are decorated on the m-SWCNT, p-SWCNT, and s-SWCNT. The increase in average lifetimes may be ascribed to the interaction and charge transfer between SWCNTs and ZnO in the SWCNT/ZnO heterostructures. The increase in charge carrier lifetimes in the self-assembled SWCNT/ZnO heterostructures as compared to ZnO functionalized SWCNTs reported previously[234], the self-assembled SWCNT/ZnO heterostructures have greater interaction between the individual components, resulting in higher probability of charge transfer. Because SWCNT has a lower band gap than ZnO, it acts as a metal, making it an electron acceptor and ZnO an electron donor in SWCNT/ZnO heterostructures[138].

### *4.2.4 Surface analysis*

The Brunauer-Emmett-Teller (BET) surface area and Barrett-Jayner-Halenda (BJH) pore sizes and volumes of the ZnO, m-SWCNT/ZnO, s-SWCNT/ZnO, and p-SWCNT/ZnO heterostructures are summarized in Table 4.2.1. The nitrogen absorption-desorption isotherm curves are shown in Figure 4.2.6 d showing type IV isotherm curve indicating mesopores formation. With the formation of SWCNT/ZnO heterostructures, the BET surface areas are increased from 14.51 $m^2/g$ for ZnO to 29.66 $m^2/g$, 35.20 $m^2/g$, and 61.64 $m^2/g$ for m-SWCNT/ZnO, s-SWCNT/ZnO, and p-SWCNT/ZnO respectively. The average pore diameter and pore volumes are also increased from 24.59 nm and 0.08 $cm^3/g$ for ZnO to 34.38 nm and 0.25 $cm^3/g$, 36.09 nm and 0.31 $cm^3/g$, 14.78 nm and 0.22 $cm^3/g$ for m-SWCNT/ZnO, s-SWCNT/ZnO, p-SWCNT/ZnO respectively. The p-SWCNT/ZnO shows the highest BET surface area with the lowest average pore diameter. The pore volume of the SWCNT/ZnO was 3.5 times larger than that of ZnO and 4.2 times larger in BET surface area. Therefore, with the formation of SWCNT/ZnO heterostructures, the surface area, pore size, and pore volume are increased to manifold as compared with that of pure ZnO. The increase in surface area indicates the enhancement in surface active sites for pollutant absorption and interaction on the nanoparticle surfaces in the photocatalytic reactions.

### *4.2.5 XPS analysis*

The elemental composition, oxidation state, binding energy, and chemical states are analyzed and investigated using XPS analysis for ZnO and SWCNT/ZnO heterostructures. Figure 4.2.7 a shows the XPS analysis of ZnO and the high-resolution survey of O and Zn are shown in Figure 4.2.7 (a1, a2). The effect and information of the chemical and oxidation states of the elements in m-SWCNT/ZnO and p-SWCNT/ZnO heterostructures are acquired from the XPS survey analysis in Figure 4.2.7 (b, c), with the high-resolution analysis of the individual elements C, O, and Zn in Figure 4.2.7 (b1, b2, b3) and (c1, c2, c3) correspondingly. A weak C 1*s* core level signal exhibited at 285 eV in the ZnO is assigned to the direct C-O bonding originating from the surface hydroxyl C-OH configuration[236]. However, prominent peaks of C1*s* core signals are observed in m-SWCNT/ZnO and p-SWCNT/ZnO heterostructures and are deconvoluted into three signals using Gauss fitting at 284 eV, 286 eV, and 288 eV in the high-resolution spectrum (Figure 4.2.7 b1, c1). The peaks at 284 eV and 286 eV are assigned to the $sp^2$-hybridized C=C and $sp^3$-hybridized C-C bonds for CNTs in the SWCNT/ZnO heterostructures[242]. The 288 eV peaks in the SWCNT/ZnO correspond to the O-C=O bonding[243,244]. For ZnO, the O 1*s* peak is deconvoluted into two peaks- 530 eV and 532 eV

corresponding to the $O^{2-}$ lattice oxygen in ZnO and $O^{2-}$ defect or vacancies showing in the larger binding energy[245]. However, for SWCNT/ZnO heterostructure shows three deconvoluted O 1*s* peaks at 530 eV, 531 eV, and 533 eV which are due to the $O^{2-}$ lattice oxygen, $O^{2-}$ defect or vacancies, and absorbed -OH on the surface[244]. The shift in the binding energies in ZnO and SWCNT/ZnO heterostructures may be due to the change in the chemical environment of oxygen, changing the local electrostatic situations[246]. The existence of surface-absorbed oxygen in the SWCNT/ZnO heterostructure indicates the bond formation of carbon from SWCNTs with zinc at the oxygen vacancies through -O-Zn-C[244]. Thus, this provides the information of chemical bond formation between ZnO and SWCNTs forming heterojunctions. The strong doublet peaks of Zn 2*p* shown in Figure 4.2.7 (a2, b3, c3) at 1022 eV and 1044 eV binding energies match the chemical environment of $Zn^{2+}$ 2*p*3/2 and $Zn^{2+}$ 2*p*1/2 confirming the +2-oxidation state of Zn and ZnO formation in the pure ZnO and SWCNT/ZnO heterostructure. No other peaks of Zn are seen, indicating the prevalence of +2 zinc oxidation state in all the samples[236,244,247].

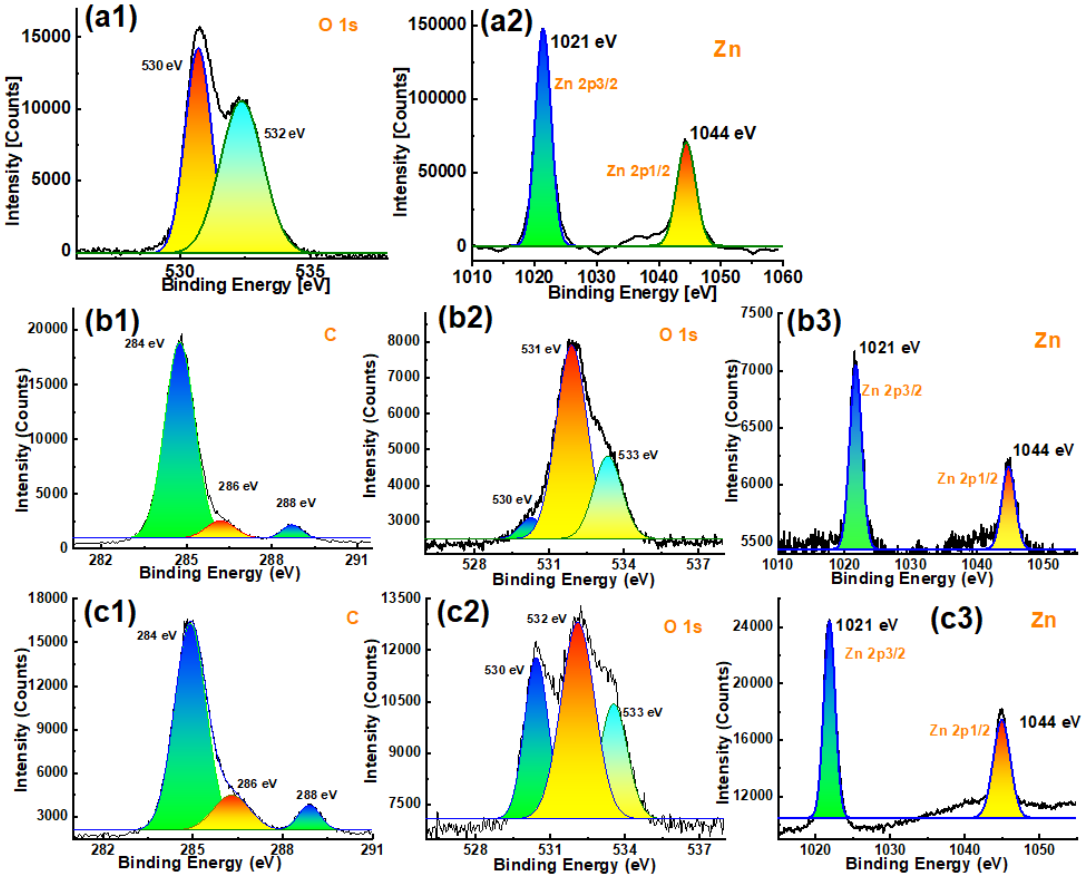


*Figure 4.2.7 High resolution XPS survey spectra of (a1, b2, c2) ZnO, (a2, b3, c3) m-SWCNT/ZnO, and (b1, c1) p-SWCNT/ZnO.*

### *4.2.6 Photocatalytic degradation of RhB by UV and natural sunlight*

The performance and charge transfer of ZnO and SWCNT/ZnO heterostructures are evaluated by the photocatalytic advanced oxidation process of RhB triggered by natural sunlight and UV light. The photocatalyst was used in the form of a floating photocatalyst where ZnO or SWCNT/ZnO nanoparticles were decorated on the 7 cm diameter two-layer disposable face mask fabric. Figure 4.2.8 a shows the photocatalytic degradation of RhB and the decrease in RhB intensity as a function of natural sunlight irradiation time. Triggered by natural sunlight, the highest efficiency of 93% RhB degradation is obtained by using m-SWCNT/ZnO and p-SWCNT/ZnO as compared with the 91% efficiency for ZnO. Without a photocatalyst, no self-degradation is seen under natural sunlight. The m-SWCNT/ZnO gives the highest degradation rate of 0.028 $min^{-1}$ and the lowest by ZnO with 0.024 $min^{-1}$ for the total sunlight illumination time of 100 min. Under 40 min of sunlight exposure, p-SWCNT/ZnO photocatalyst show maximum degradation rate and minimum by m-SWCNT/ZnO. This may be correlated with the maximum surface area exhibited by p-SWCNT/ZnO with 61.64 $m^2/g$, however, ZnO nanoparticles having the lowest surface area also produce comparable degradation results.

Considering the dependence of ROS generation reactions on redox potentials, the determination of band edge positions of the photocatalyst is essential for analyzing photocatalytic mechanisms. The valence and conduction band edge positions for ZnO, m-SWCNT/ZnO, s-SWCNT/ZnO, and p-SWCNT/ZnO calculated from the Mulliken electronegativity theory are shown in Figure 4.2.8 c. The computed band edge locations show that the valence band potentials are more positive than the oxidation potentials of $H_2O/OH•$ (2.72 V vs SHE) and $OH•/OH$ (2.29 V vs SHE), which is favorable for the oxidation of $H_2O$ or hydroxyl species absorbed on the photocatalyst surface. The photogenerated $h^+$ in the valence band will react with $H_2O$ and $OH^-$, leading to the production of OH• radicals which will disintegrate pollutant molecules into $H_2O$ and $CO_2$[132,248,249]. The photogenerated electrons either participated in the reduction of $O_2$ to $HO_2•$ or transferred to SWCNTs inhibiting charge carrier recombination. As the conduction band of ZnO and SWCNT/ZnO are more negative than the oxidation potential of $O_2/HO_2•$ (-0.046 V vs SHE), the photogenerated electrons reacted with the dissolved $O_2$ to form $HO_2•$ radicals[132]. Thus, the production of OH• and $HO_2•$ will induce a series of reactions for the continuous generation of ROS into the reaction system[250].

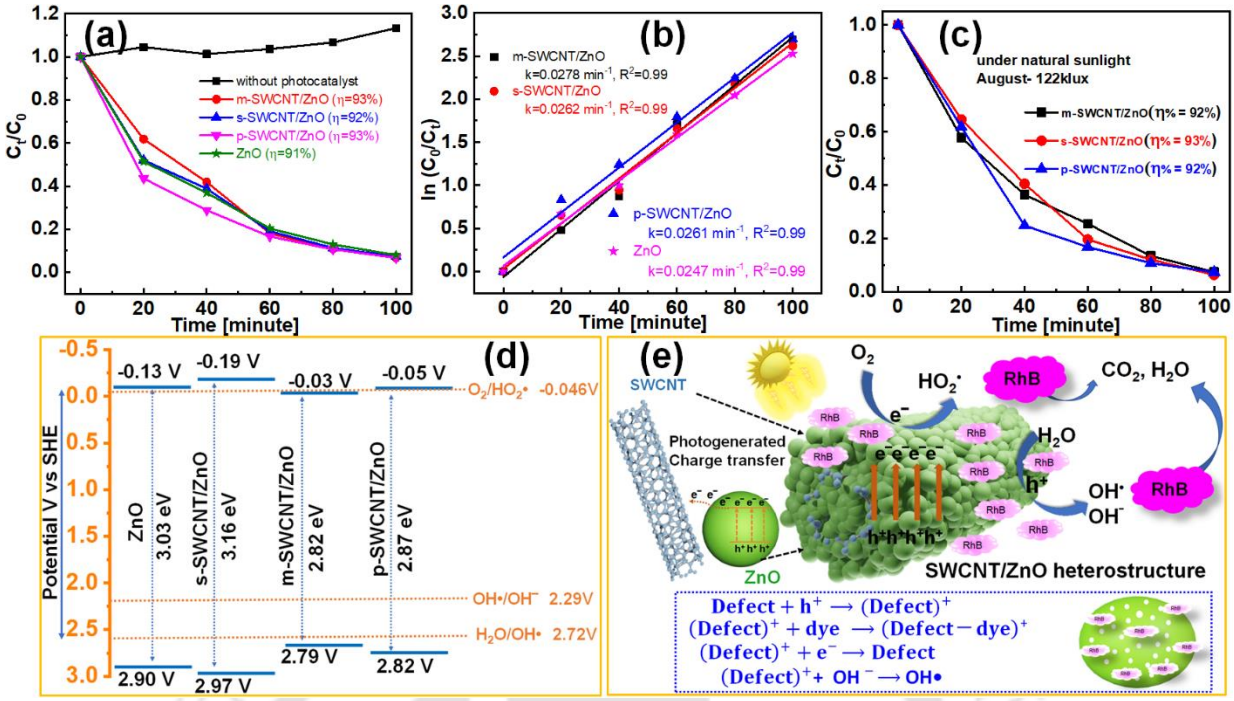


*Figure 4.2.8 (a) Normalized photo-catalytic degradation curve of RhB dye in terms of absorption intensity concerning time under the natural sunlight using the face-mask fabric coated with the photocatalyst, (b) photocatalytic degradation rate vs irradiation time, (c) band edge position calculated using Mulliken electronegativity theory, and (d) charge transfer and RhB degradation by advanced oxidation process*

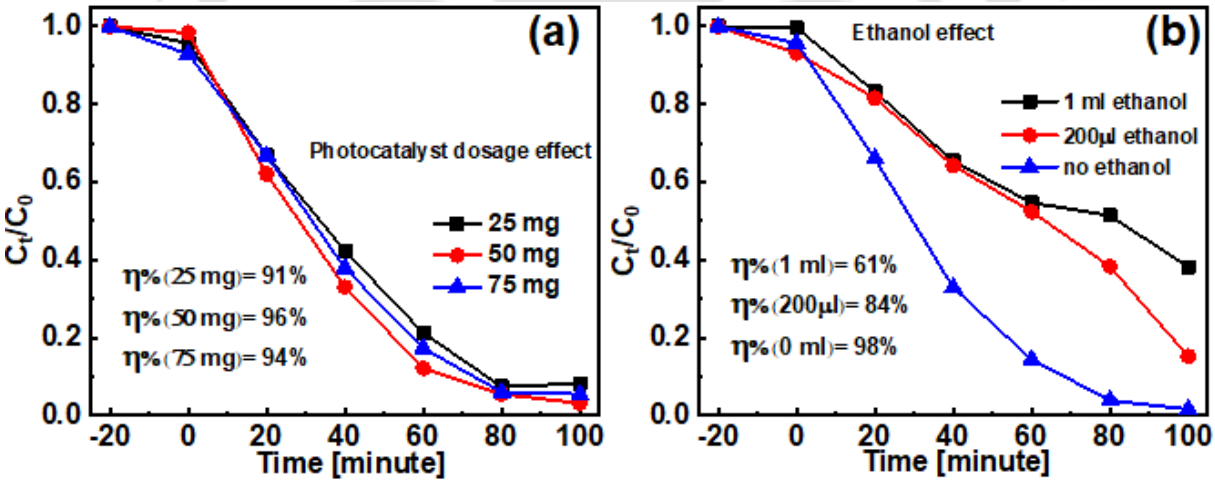


*Figure 4.2.9 Photocatalytic degradation curve of (a) m-SWCNT/ZnO to check dosage effect and (b) s-SWCNT/ZnO to check the ethanol effect*

A hypothetical charge transfer and reaction mechanism shown in Figure 4.2.8 e gives the degradation of RhB dye with the production of ROS like hydroperoxyl radicals ($HO_2$•), hydroxy radicals (OH•), and hydroxyl ions ($OH^-$) via reduction of molecular $O_2$, oxidation of $H_2O$ and in-situ formed $H_2O_2$. The RhB adsorption and degradation occur on the ZnO surface with photogenerated charge transfer between ZnO to SWCNTs via establishing conductive

pathways, effectively boosting charge carrier lifetimes. Although the photocatalyst was adorned and fixed on the face-mask fabric as a floating photocatalyst, it produces a remarkably quick breakdown of persistent organic dye when exposed to sunlight. With the AOP process in the presence of SWCNT/ZnO photocatalyst under natural sunlight, a complete degradation of RhB dye is seen in 100 min. The same tests were repeated in August using a SWCNT/ZnO photocatalyst to degrade RhB. Comparable to the photocatalytic degradation outcomes of October, s-SWCNT/ZnO, m-SWCNT/ZnO, and p-SWCNT/ZnO heterostructures demonstrate a 93%, 93%, and 92% efficiency with 122 klux sunlight intensity (Figure 4.2.8 c). The defects created in the ZnO crystal by the desorption and liberation of DMF molecules act as an active catalytic reaction site as this result surpassed the results obtained by using ZnO photocatalyst prepared from DEG solvent under natural sunlight. The longer lifetime of photogenerated charge carriers (via charge transfer) contributes to the formation of more reactive oxygen species in the reaction media, which is accountable for the enhanced performance and efficiency accomplished by SWCNT/ZnO heterostructures.

### ***4.2.7 Effect of photocatalyst dosage***

Photocatalytic degradation efficiency is heavily influenced by many factors, but the photocatalyst dosage used in the AOP is particularly crucial as the pollutant adsorption and degradation occur on the surface. Furthermore, it plays a key role in controlling the amount of light entering the reactor, the percentage of pollutant molecules interacting with the photocatalyst surface, and the generation of photogenerated charged particles and ROS[127,129,238,251]. With the use of m-SWCNT/ZnO nanoparticles under UV light, three photocatalyst dosages are tested (25 mg, 50 mg, and 75 mg) in our study to determine the effect of catalyst dosage on RhB degradation. With an increase in the photocatalyst dosage from 25 mg to 50 mg, the efficiency (η%) was found to increase from 91% to 96% (Figure 4.2.9 a). As the number of charge carrier generator photocatalysts increased two-fold, ROS generation increased as well, resulting in the greater interaction between photocatalysts and light. Additionally, in this case, by increasing the photocatalyst dosage, the active sites are also increased, boosting dye-photocatalyst interactions. However, a further increase in photocatalyst dosage to 75 mg resulted in a lowering η% from 96% to 94% (Figure 4.2.9 a). This anomalous behavior of declining photocatalytic efficiency is contributed by the blocking of light penetration to the reaction system causing turbidity by the excess photocatalyst added. As a result, the photocatalyst's efficiency is diminished due to the turbidity's effect on the light-photocatalyst interaction and, by extension, the ROS formation. There is also the possibility

that it is caused by an increase in the recombination of charge carriers[127,129,205,251]. Thus, based on the findings, a concentration of 50 mg was chosen as the optimal value to degrade 50 ml 10 ppm RhB. To test the stability, reusability, and lifetime of the photocatalyst, the photocatalyst was repeatedly used five times after washing and drying in between each iteration in sunlight and UV light to achieve maximum RhB degradation efficiency.

### *4.2.8 Effect of ethanol on photocatalytic efficiency*

In the advanced oxidation process of heterogeneous photocatalysis, the main point is the in-situ generation of strong oxidation species- hydroxyl radicals (OH•) under the influence of photon energy and a photocatalyst. Thus, in this work, the role of OH• radical in the photocatalytic degradation of RhB under UV light is tested by adding ethanol as a sacrificing agent for the OH• and $h^+$ scavenger. With no ethanol, 98% degradation efficiency was obtained, however, the degradation efficiency was decreased from 84% to 61% when ethanol was used in 200 µl and 1ml as the OH• and $h^+$ scavenger (Figure 4.2.9 b). This shows the dominant role of OH• radicals and $h^+$ in the heterogeneous photocatalytic degradation of RhB. The OH• radicals are generated by multiple ways- oxidation of $H_2O$ dissolved $O_2$, and cleavage of $H_2O_2$ by the photogenerated $h^+$ in the valence band of the photocatalyst[250,252]. The OH• radical is known to be one of the strongest oxidants in the AOP process with an oxidation potential of 2.8 V (vs normal hydrogen electrode potential), decomposing persistent organic pollutants into non-toxic $CO_2$ and $H_2O$[253]. Other OH• radicals and $h^+$ scavengers- alcohols like methanol, isopropyl alcohol, and triethanolamine are also used in other cases to unveil the major role played by OH• radicals [121,205,254,255]. However, in the photocatalytic degradation of RhB using $Bi_2WO_6$, adding ethanol resulted in no significant change in the degradation efficiency, indicating the minor role played by the OH• radical[256]. As discussed in the mechanism section, this peculiar OH• radical involvement in AOP results from the relative placements of the photocatalyst's band edges with respect to the reduction potential.

### *4.2.9 Cycle and stability test under UV and natural sunlight illumination*

To assess the stability, reusability, and lifetime of the prepared ZnO and three SWCNT/ZnO heterostructures, five repeated iterations were conducted for the photocatalytic decomposition of RhB were performed under UV light illumination and natural sunlight (Figure 4.2.10). The photocatalysts were collected after each cycle, washed, and dried for the next iterations and were repeated five times. For the UV light cycle test, the m-SWCNT/ZnO was dispersed and illuminated with UV light while stirring continuously. A photocatalytic efficiency of 94% was

achieved after the 5th cycle for m-SWCNT/ZnO photocatalyst, while a maximum of 95% was achieved in the 4th cycle under 100 min illumination time. Consequently, the photocatalyst is shown to be highly stable and reusable after the 5th cycle by retaining its surface, chemical, and optical properties, without exhibiting photo-corrosion or degradation in its efficiency (Figure 4.2.10 b). It is noteworthy, however, that despite the photocatalyst's high efficiency after every cycle, the degradation rate differs with each cycle, being higher than the degradation rate observed after the 1st cycle (Figure 4.2.10 b).

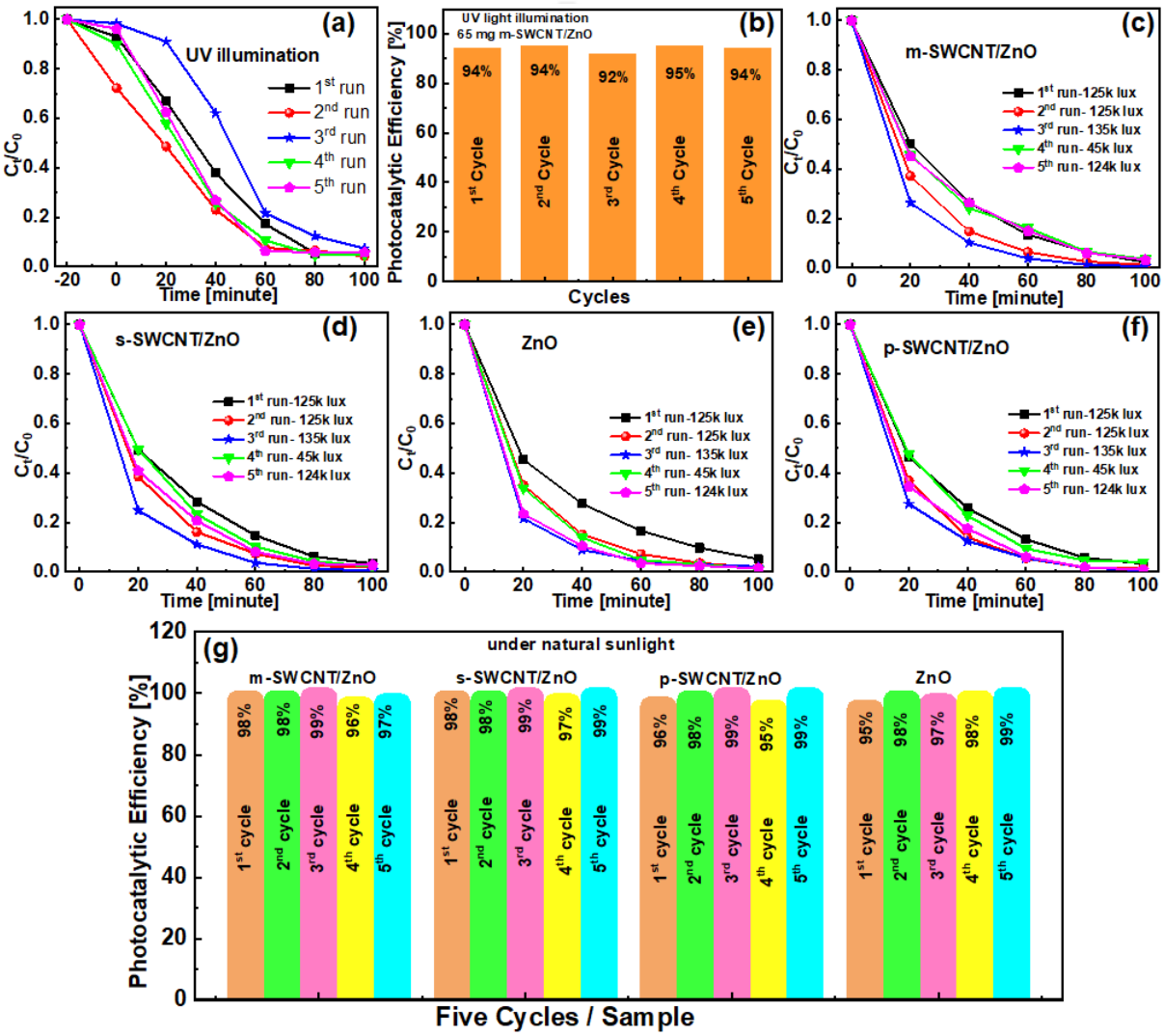


*Figure 4.2.10 Stability and reusability test with five repeated iterations of RhB photocatalytic decompositions under (a) UV light illumination, (b) efficiency chart, and (c, d, e, f) natural sunlight without stirring for m-SWCNT/ZnO, s-SWCNT/ZnO, ZnO and p-SWCNT/ZnO, respectively, (g) photocatalytic efficiency chart of all the samples under the natural sunlight for five collective cycles*

Photocatalyst stability was also tested for all samples under natural sunlight on sunny days to determine their effectiveness for photocatalytic decomposition and in an attempt to show

sustainability, an approach for large-scale application. Figure 4.2.10 (c, d, e, f) show the degradation curves of m-SWCNT/ZnO, s-SWCNT/ZnO, ZnO, and p-SWCNT/ZnO respectively for the five repeated experiments under sunlight with different sunlight intensities (due to change of day). The degradation efficiency for all samples increases as the sunlight intensity increases from 125 klux to 135 klux (Figure 4.2.10 g).

When the sun intensity was 45 klux due to the cloudy day, SWCNT/ZnO heterostructures showed the lowest degradation rate. A 99% RhB degradation was observed after the $5^{th}$ cycle. Though the overall photocatalytic efficiency was the same for all samples in all cycles, the highest degradation rate occurred in the highest sun intensity of 135 klux (Figure 4.2.10 g). This very high degradation efficiency in natural sunlight by the generated samples demonstrates the photocatalyst's ability to absorb a wide range of spectrum- ultraviolet, visible, and infrared radiations. In light of all the results and analysis, the prepared samples ZnO, m-SWCNT/ZnO, s-SWCNT/ZnO, and p-SWCNT/ZnO are found to be highly stable and reusable, while retaining their photocatalytic properties. Concerning UV light illumination photocatalytic degradation with continuous stirring, natural sunlight-triggered photocatalysis shows greater efficiency simply by allowing sunlight to penetrate without shaking or applying external forces.

### ***4.2.10 Key findings in Part B***

- ZnO nanoparticles are self-assembled and undergo oriented attachment on three electronically different SWCNTs, acting as an anchor for ZnO nanoparticles.
- The broad absorption PL emission spectra and ESR analyses clearly show the existence of defects that are attributed to interstitials and oxygen/zinc vacancies in heterostructures and charge transfer. These defect sites are also generated by the liberation of DMF molecules bound to the ZnO surface, which acted as a structure-directing agent and surfactant.
- These defects are found to enhance the photocatalytic degradation efficiency of RhB by complete degradation in 100 mins under natural sunlight by using face-mask fabric coated with ZnO and SWCNT/ZnO heterostructures.
- This increase in charge carrier lifetimes enhances in RhB degradation and the highest degradation rate of 0.0278 $min^{-1}$ is obtained by using floating face mask fabric coated with m-SWCNT/ZnO heterostructures.
- The photocatalytic degradation effectiveness is shown to have minimal influence on photocatalyst dosages by the s-SWCNT/ZnO heterostructure. By showing 99% degradation

efficiency in direct sunlight after the 5$^{th}$ cycle, the generated samples—ZnO and SWCNT/ZnO heterostructures—are discovered to be stable and recyclable.

- After being exposed to UV radiation for five repeated photocatalytic experiments, the samples remain stable and recyclable with no deterioration in the overall efficiencies.
- OH• radicals and $h^+$ were found to play major roles in the RhB photocatalytic degradation by using the prepared samples.

## 4.3 Conclusion

- In the functionalization and composite formation, ZnO sub-nano particles are attached and anchored on SWCNT surfaces, thereby exhibiting distortion-dislocation and strain onto the SWCNT.
- Due to the charge transfer and interaction between SWCNTs and ZnO, the carrier lifetimes were increased by ~1 ns, and an increase in metallicity is seen in s-SWCNT functionalized by ZnO nanoparticles. Further increases in charge carrier lifetimes are seen in the SWCNT/ZnO heterostructure formation.
- In the ZnO functionalized SWCNTs, the carrier lifetime value of p-SWCNT+ZnO, s-SWCNT+ZnO, and m-SWCNT+ZnO is 4.24 ns 4.76 ns, and, 4.62 ns. However, in ZnO self-assembled on different SWCNTs, the charge carrier lifetimes of the m-SWCNT/ZnO, p-SWCNT/ZnO, and s-SWCNT/ZnO heterostructures are 7.19 ns, 7.41 ns and 7.37 ns respectively.
- In SWCNT/ZnO heterostructures, the broad absorption PL emission spectra and ESR analyses clearly show the existence of defects that are attributed to interstitials and oxygen/zinc vacancies in heterostructures and charge transfer. These defect sites are also generated by the liberation of DMF molecules bound to the ZnO surface, which acted as a structure-directing agent and surfactant.
- These defects are found to enhance the photocatalytic degradation efficiency of RhB by complete degradation in 100 mins under natural sunlight by using face-mask fabric coated with ZnO and SWCNT/ZnO heterostructures.
- This increase in charge carrier lifetimes enhances in RhB degradation and the highest degradation rate of 0.0278 $min^{-1}$ is obtained by using floating face mask fabric coated with m-SWCNT/ZnO heterostructures.
- The photocatalytic degradation efficiencies depend upon photocatalyst dosages.
- By showing 99% degradation efficiency in direct sunlight after the $5^{th}$ cycle, the generated samples—ZnO and SWCNT/ZnO heterostructures—are discovered to be stable and recyclable.
- OH• radicals and $h^+$ are found to play major roles in the RhB photocatalytic degradation using SWCNT/ZnO heterostructures.

# Chapter 5

# Dependence of Photocatalytic Performance on Different Charge Transfer Pathways

## Introduction

In complex nanostructures, hetero-structured interfaces are formed with energy band-alignment to enhance the flow of charge carriers[257]. Based on the valence band (VB) and conduction band (CB) positions between two semiconductor oxides, these heterojunctions are categorized into four different types: (a) Type I- Straddling gap, (b) Type II- Staggered gap, (c) Type II- Z-scheme, and (d) Type III- Broken gap. Detailed analysis of the charge carrier transfer kinetics and band-gap engineering of multicomponent hetero-structures for photocatalysis have been discussed in Chapter 1, subsection 1.5[250]. Type I and Type II heterostructure photocatalysts provide efficient charge generation or separation in the heterojunction interface providing charge transfer pathways and hence a highly sought research field. The main principle behind the composite heterostructure lies in the architecture where the heterojunction interface carries a crucial role in separating photogenerated charge particles[258]. The driving force of the charged particle separation lies in the band energy difference developed by the band alignment of the conduction band (CB) and valence band (VB) of the contributing materials in the heterojunction interface[258]. With the alteration in the contributing materials and the sequencing, the variation in the charge transfer pathways affects the photocatalyst performance ex. $TiO_2$/ZnO shows better sensing performance as compared to ZnO/$TiO_2$[259].

To design composite heterostructures, the selection of suitable semiconductor oxides among the available materials for appropriate band alignment is important. Mostly employed photocatalysts include wide band-gap semiconductors— ZnO (bandgap $E_g$ ~ 3.37 eV) and anatase-$TiO_2$ ($E_g$ ~ 3.2 eV) for their less toxicity and ability to tune physicochemical and optical properties with a controlled approach in the synthesis parameters[258]. In addition to these wide band-gap semiconductor oxides, $Fe_3O_4$ is also an emerging choice in the field of photocatalysis contributing to its magnetic properties and exhibiting the photo-Fenton process in photocatalytic reactions. Attracting the subject to sustainability, the use of carbon-based nanoparticles like activated carbon, carbon nanotubes, graphene, and graphitic carbon nitride

($g\text{-}C_3N_4$) has attracted much attention but is supported by a co-catalyst[260–262]. Although activated carbon is easily available and prepared from widely available resources- rice husk, fruit peels, sugarcane scrapes, etc., they are mainly used for the absorption of pollutants rather than elimination. Also, carbon nanotubes and graphene are expensive and due to their complex preparation methods, their uses are limited and are only used as an anchor for the main protagonist photocatalysts like ZnO, $TiO_2$, $SnO_2$, etc. Thus, in this emerging decade, $g\text{-}C_3N_4$ has been in the limelight for its wide range of applications- $H_2$ generation, $CO_2$ reduction, photoelectronic applications, sensors, and mainly photocatalytic water treatment[263–266]. Graphitic carbon nitride ($g\text{-}C_3N_4$) is potentially serving as a photocatalyst because of its cheap, metal-free, non-toxic material properties, easy preparation, and suitable physicochemical and thermodynamic properties. It is easily prepared by the condensation or direct heating of nitrogen-rich organic compounds— urea[267,268], melamine[269,270], cyanamide[266,271], dicyandiamide[266,271] at an optimized synthesis temperature of 550ºC which results in exfoliated $g\text{-}C_3N_4$ with high surface area and successful conversion of most reactants into $g\text{-}C_3N_4$[264,272,273]. Depending on the condensation temperature, the band gap of $g\text{-}C_3N_4$ is varied from 2.6–2.8 eV absorbing UV and blue light in the visible spectrum by the inter-band transition[49,272,274]. It has a strong reduction ability due to the highly negative conduction band position and is responsible for the generation of photogenerated electrons, which plays a vital role in AOP. Apart from many praiseworthy qualities of $g\text{-}C_3N_4$, it has low oxidant ability due to the upper edge of the valence band which is undesirable for the photocatalytic AOP application. $g\text{-}C_3N_4$ is known to show a high recombination rate of photoinduced electrons and holes, leading to diminishing photocatalytic efficiency. Thus, modifications in the properties or composite formations are needed to enhance the photocatalytic activity.

The $g\text{-}C_3N_4$ shows low specific surface area, lower charge separation, higher charge recombination rate, and low solar energy conversion, the creation of defects or vacancies- carbon or nitrogen can modify the chemical and optical band gap, increase the surface area, convert defects into active reaction sites, and promote charge transfer to lower the recombination rate[269,270,275,276]. Another approach includes the composite formation of $g\text{-}C_3N_4$ with semiconductor oxides or semiconductor nanoparticles which will form different charge transfer heterojunction interfaces, thus enhancing the charge separation and migration and modifying solar energy conversion which affects the photocatalytic performance[277–279]. Different charge transfer mechanisms like Z-scheme (ex. $TiO_2/g\text{-}C_3N_4$/carbon dots[280], $g\text{-}C_3N_4/ZnO$[281], $MoS_2/TiO_2/g\text{-}C_3N_4$[282], $Ag/g\text{-}C_3N_4/ZnO$[277]), S-scheme (ex. $\alpha\text{-}Fe_2O_3/g\text{-}C_3N_4$

nanocomposites[283]), Type-II charge transfer (ex. ZnO/g-$C_3N_4$[284], CdS/$ZnIn_2S_4$/g-$C_3N_4$[285]), etc. are seen in the heterojunction interface of the individuals in the composites to enhance the charge separation and thus the photocatalytic performance. Although these improved photocatalysts demonstrate great performance and efficiency, their utilization is also limited by the need for high-power light sources such as xenon, tungsten, or mercury lamps with 550W-300W power.

Based on the above problems, we develop different types of composites with different types of charge transfer pathways in the heterojunction interface. The dependence of photocatalytic performance on the charge transfer pathways: Type I—ZnO/$Fe_3O_4$, Type II— ZnO/$TiO_2$, and Z-scheme— g-$C_3N_4$/ZnO are analyzed and discussed.

## PART A: Charge transfer dynamics in Composite Heterostructures

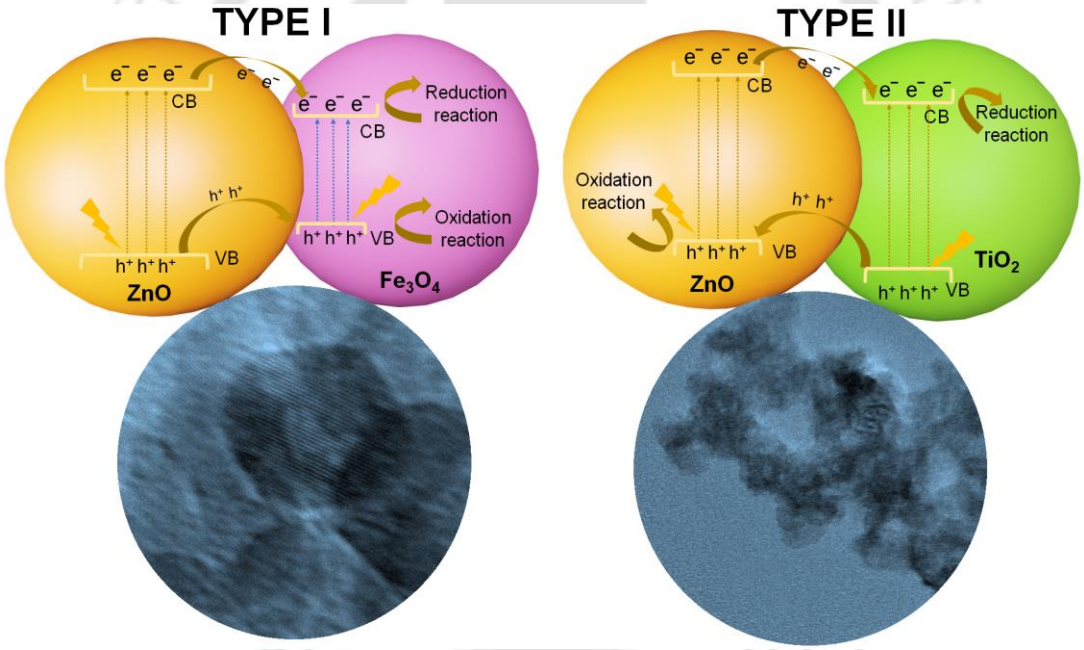


***Graphical abstract of Part A***

Part A of this chapter will show the development of two different complex heterostructures showing different charge transfer pathways: Type I and Type II charge transfer depending upon the energy bandgap of the individual component— ZnO/$Fe_3O_4$ and ZnO/$TiO_2$. The effect of the charge transfer pathways, type of heterostructure interface, and physicochemical, and optical properties on photocatalytic performance under UV light illumination will be studied.

## 5.1 Results and Discussions for the $ZnO/TiO_2$ and $ZnO/Fe_3O_4$ Composite Heterostructures

### *5.1.1 Structural analysis*

The structural and phase analysis of the synthesized $ZnO/TiO_2$ and $ZnO/Fe_3O_4$ composite heterostructures in comparison with the pure $TiO_2$ and $Fe_3O_4$ are confirmed by the XRD analysis shown in Figure 5.1.1. The $TiO_2$ and $Fe_3O_4$ procured are of 24 and 33 nm average crystallite sizes as calculated from the Debye-Scherrer formula by taking the first three peaks. As seen from the XRD peaks, the procured $TiO_2$ showed both anatase and rutile structures with the anatase-$TiO_2$ in high content. The peaks (PDF card no. 00-064-0863) at 27.4°, 36°, and 41.1° corresponding to the (110), (101), and (111) planes of rutile-$TiO_2$ structure (PDF card no. 00-017-0543). The procured $Fe_3O_4$ XRD peaks correspond to the magnetite-$Fe_3O_4$ with cubic structure belonging to the $Fd\bar{3}m$ (227) space group. The $ZnO/Fe_3O_4$ and $ZnO/TiO_2$ XRD peaks showed the presence of both individual oxide planes in the composite heterostructures. A majority of the peaks are dedicated to the ZnO hexagonal structure in both composites.

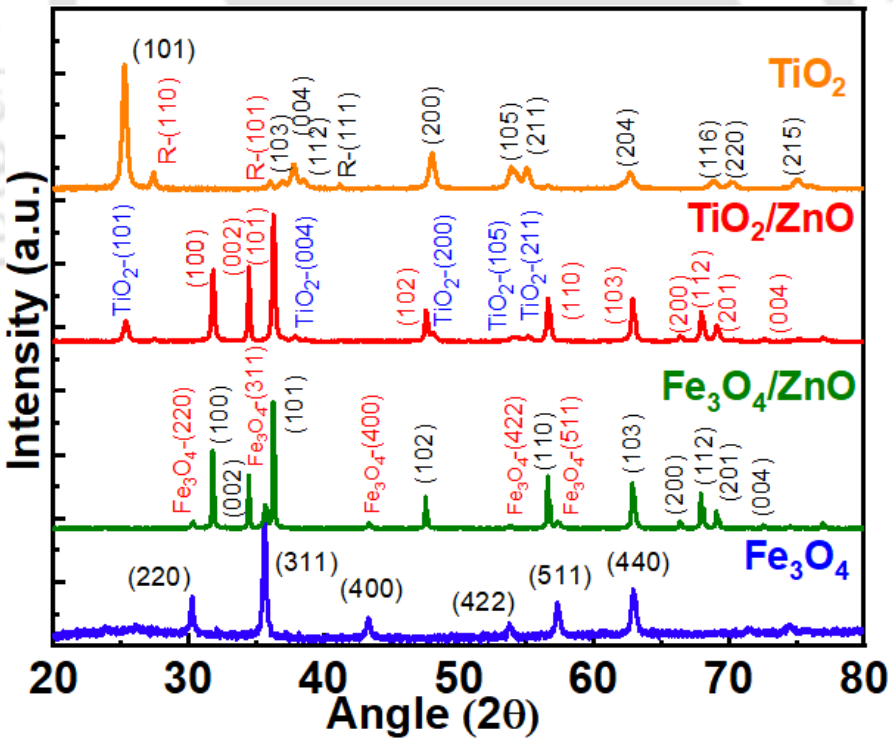


*Figure 5.1.1 XRD pattern and Raman spectra of the $TiO_2$, $Fe_3O_4$, $ZnO/TiO_2$, and $ZnO/Fe_3O_4$ composite heterostructures*

This indicated the formation of ZnO crystal planes (PDF card no. 00-036-1451) and its high intensity as compared to the $TiO_2$ or $Fe_3O_4$ peaks exhibited high crystallinity and crystal sizes. Therefore, in conclusion from the XRD diffraction analysis, the ZnO particles coexist with the $TiO_2$ and $Fe_3O_4$ in the $ZnO/Fe_3O_4$ and $ZnO/TiO_2$ composite heterostructures, forming a heterojunction interface with no additional impurity present in the sample.

### ***5.1.2 Morphological analysis***

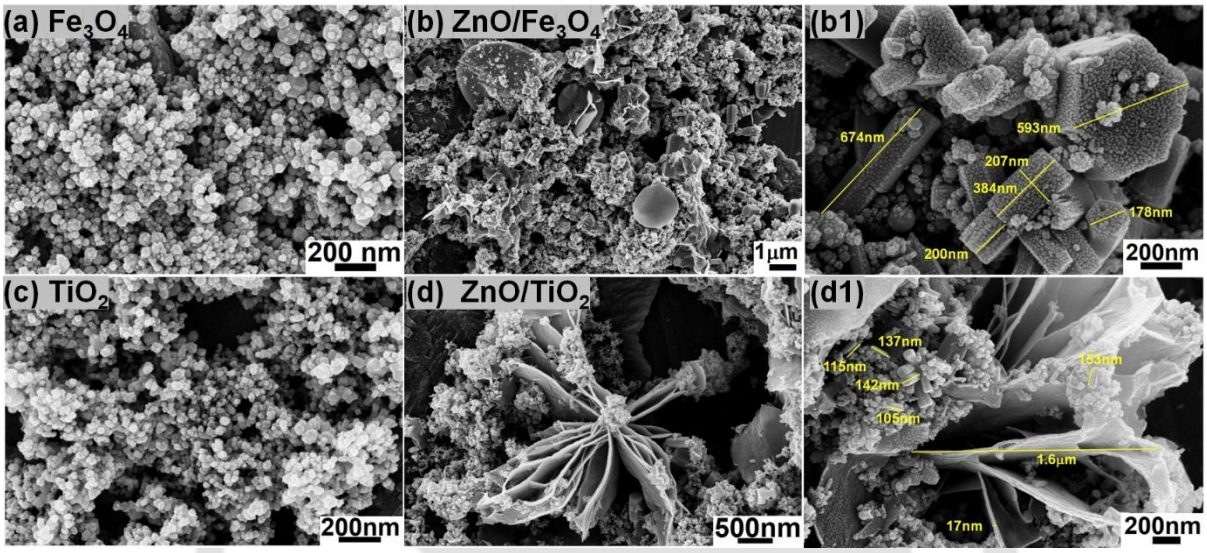


*Figure 5.1.2 FESEM images of (a) $Fe_3O_4$, (b, b1) $ZnO/Fe_3O_4$, (c) $TiO_2$, (d, d1) $ZnO/TiO_2$*

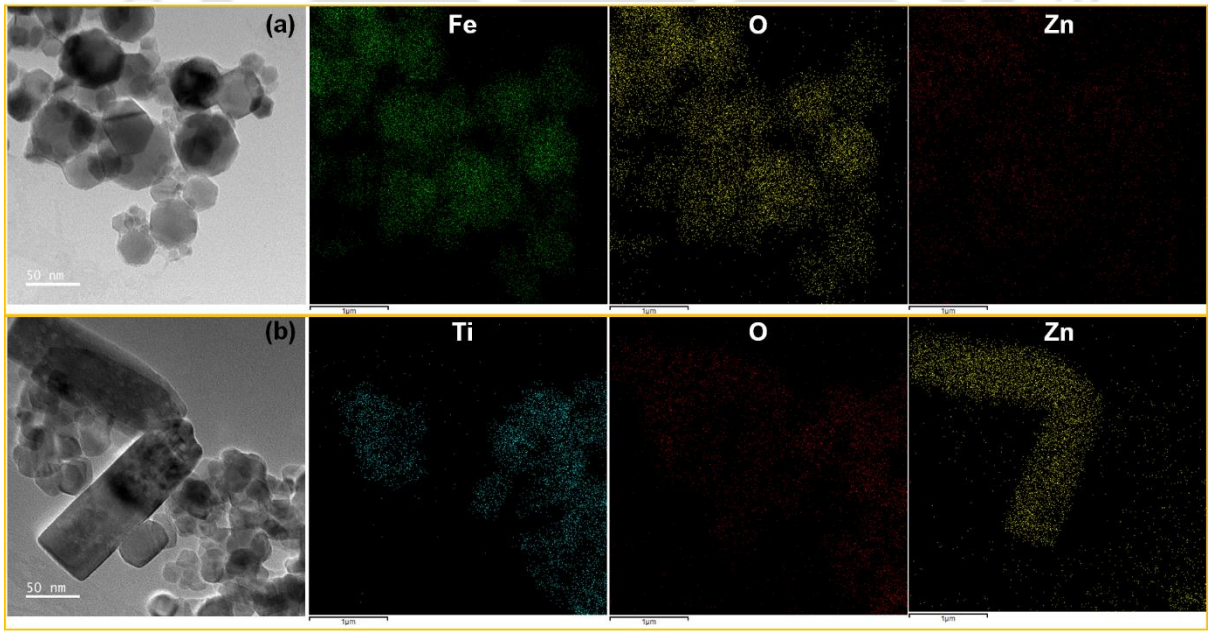


*Figure 5.1.3 Elemental mapping of (a) $ZnO/Fe_3O_4$, and (b) $ZnO/TiO_2$*

The morphological analysis of the $ZnO/Fe_3O_4$ and $ZnO/TiO_2$ composite heterostructures are analyzed with the FESEM (Figure 5.1.2 (b, d)) and FETEM electron microscopy images

(Figure 5.1.3). The procured $Fe_3O_4$ and $TiO_2$ showed aggregated nanoparticles forming hexagons and nanoparticles clusters respectively as seen from the FESEM analysis shown in Figure 5.1.2 (a, c) respectively. The average nanoparticle aggregate sizes of $Fe_3O_4$ and $TiO_2$ are ~50 nm and ~40 nm respectively which are greater than the corresponding crystallite sizes calculated from the XRD analysis. In the ZnO/$Fe_3O_4$ composite heterostructures (Figure 5.2.1 b, b1), nanoparticles undergo aggregation and growth forming hexagonal rods of variable length and breadth by the aggregation of sub-nanoparticles, and flaky structures. The ZnO/$TiO_2$ composites show the formation of rods and flower-like structures.

The elemental mapping analysis is done to investigate the distribution of the elements in the ZnO/$Fe_3O_4$ (Figure 5.1.3 a) and ZnO/$TiO_2$ (Figure 5.1.3 b) composite nanoparticles. As the composites showed $TiO_2$, $Fe_3O_4$, and ZnO crystal planes, it is assumed that formed composites exclude the occurrence of zinc doping. From the XRD and FESEM analysis, as ZnO nanoparticles are larger than the $TiO_2$, and $Fe_3O_4$ nanoparticles, in the ZnO/$Fe_3O_4$ composites, the hexagonal particles are found to be $Fe_3O_4$ particles whereas the uniform distribution of zinc is also observed. In the ZnO/$TiO_2$ composite heterostructure, the larger flake-like structure is found to be ZnO, and the smaller particles are the $TiO_2$. Also, titanium is seen to be present in the flaky structure other than the $TiO_2$ nanoparticles. Also, in the $TiO_2$ distribution area, uniform zinc distribution is seen. Thus, these indicate the formation of independent ZnO nanoparticles in addition to the ZnO coordination with the $TiO_2$ and $Fe_3O_4$ nanoparticles.

Further, the morphology and structure of the ZnO/$Fe_3O_4$, and ZnO/$TiO_2$ composite heterostructure were analyzed with FETEM, HRTEM images, and SAED pattern analysis as shown in Figure 5.1.4 (c, d) in comparison to those of $Fe_3O_4$ and $TiO_2$ (Figure 5.1.4 a and b). The $Fe_3O_4$ and $TiO_2$ nanoparticles ranges of different sizes range from ~10 nm to ~50 nm. The $Fe_3O_4$ nanoparticles showed hexagonal shape morphologies regardless of the size. The HRTEM images showed d-spacings of 0.25 nm corresponding to the (311) plane of $Fe_3O_4$. $TiO_2$ nanoparticles exhibited rectangular-shaped morphologies and showed a d-spacing value of 0.35 nm corresponding to the (101) plane of $TiO_2$. From the SAED analysis, the $Fe_3O_4$ and $TiO_2$ nanoparticles showed ring patterns indicating the polycrystalline nature. In ZnO/$Fe_3O_4$ composite heterostructure FETEM analysis, hexagonal $Fe_3O_4$ nanoparticles as evident from the elemental analysis, are seen with sizes similar to the independent $Fe_3O_4$ nanoparticles. However, in the FETEM analysis of ZnO/$TiO_2$ composite heterostructure, particles corresponding to individual ZnO and $TiO_2$ nanoparticles are seen where $TiO_2$ nanoparticles sizes are similar to the procured $TiO_2$ (Figure 5.1.4 b) and ZnO nanoparticles are of larger flake

like structures, ~175 nm in length and ~50 to 70 nm in breadth which are much greater than the crystallite sizes calculated from the XRD analysis. In the HRTEM images of ZnO/$Fe_3O_4$ and ZnO/$TiO_2$ composite heterostructures, two values of different d-spacings 0.25 nm & 0.28 nm, and 0.35 nm & 0.24 nm corresponding to the (311) plane of $Fe_3O_4$, (100) planes ZnO, (101) plane of $TiO_2$ and (101) plane of ZnO respectively. These also indicate the formation of small ZnO nanoparticles forming heterojunctions. Also, in the SAED analysis, the crystal planes of $Fe_3O_4$ & ZnO, and ZnO & $TiO_2$ are observed together, thus indicating the coexistence and formation of heterojunction interfaces.

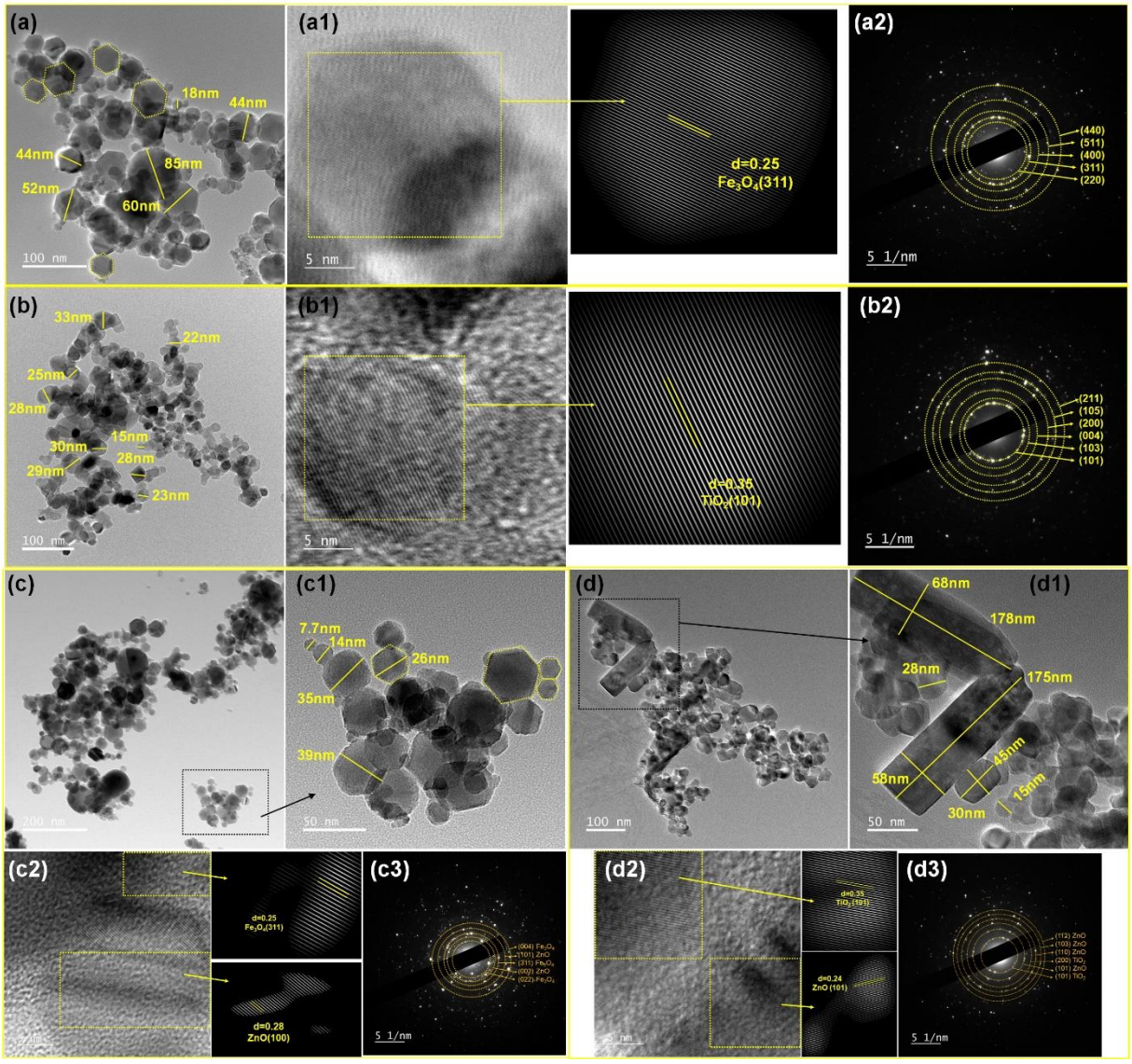


*Figure 5.1.4 FETEM, HRTEM images and SAED of (a, a1, a2) $Fe_3O_4$, (b, b1, b2) $TiO_2$, (c, c2, c3) ZnO/$Fe_3O_4$, and (d, d1, d2, d3) ZnO/$TiO_2$ heterostructures correspondingly*

To see the composite formation, XPS analysis is shown in Figure 5.1.5 (a, b) for the procured $TiO_2$ and $Fe_3O_4$ respectively, and Figure 5.1.5 (c, d) for the ZnO/$Fe_3O_4$ and ZnO/$TiO_2$

composite heterostructures. In $TiO_2$, the peaks correspond to Ti2*p*— 458 eV and 464 eV indicating Ti2*p*3/2 and Ti2*p*1/2. This is consistent with the $Ti^{4+}$ formation of $TiO_2$. The O1*s* peak is deconvoluted into two peaks— 529 eV and 530 eV. The first O1*s* peak represents the lattice O bound to $Ti^{4+}$, i.e., bulk oxide ($O^{2-}$), and the later peak corresponds to the hydroxyl (OH) species influence from the water molecules on the sample surface[286]. In the $Fe_3O_4$, the Fe2*p* peaks are deconvoluted into four major peaks— 710 eV, 712 eV, 717 eV, 724 eV, and 729 eV. The peaks at 710 eV and 724 eV correspond to the Fe2*p*3/2 and Fe2*p*1/2 indicating the presence of both $Fe^{2+}$ and $Fe^{3+}$ in the sample which is consistent with the formation of $Fe_3O_4$. The peak Fe2*p*3/2 at 710 eV is the core level electrons attributing to the octahedral sites of $Fe^{3+}$. $Fe_3O_4$, alternatively written as $FeO{\bullet}Fe_2O_3$ consists of two oxidation states of iron— $Fe^{2+}$ and $Fe^{3+}$ occupying the tetrahedral and octahedral interstices of the cubic spinel-type structure. The energy peak at 710 eV is attributed to $Fe^{2+}$ with a corresponding satellite at 717 eV. The O1s peak is deconvoluted into three peaks— 530 eV, 532 eV, and 533 eV. The lowest binding energy at 530 eV corresponds to the lattice $O^{2-}$ in $Fe_3O_4$. The peak at 532 eV and 533 eV represents the surface absorbed $OH^-$ and oxygen in the bidentate bond.

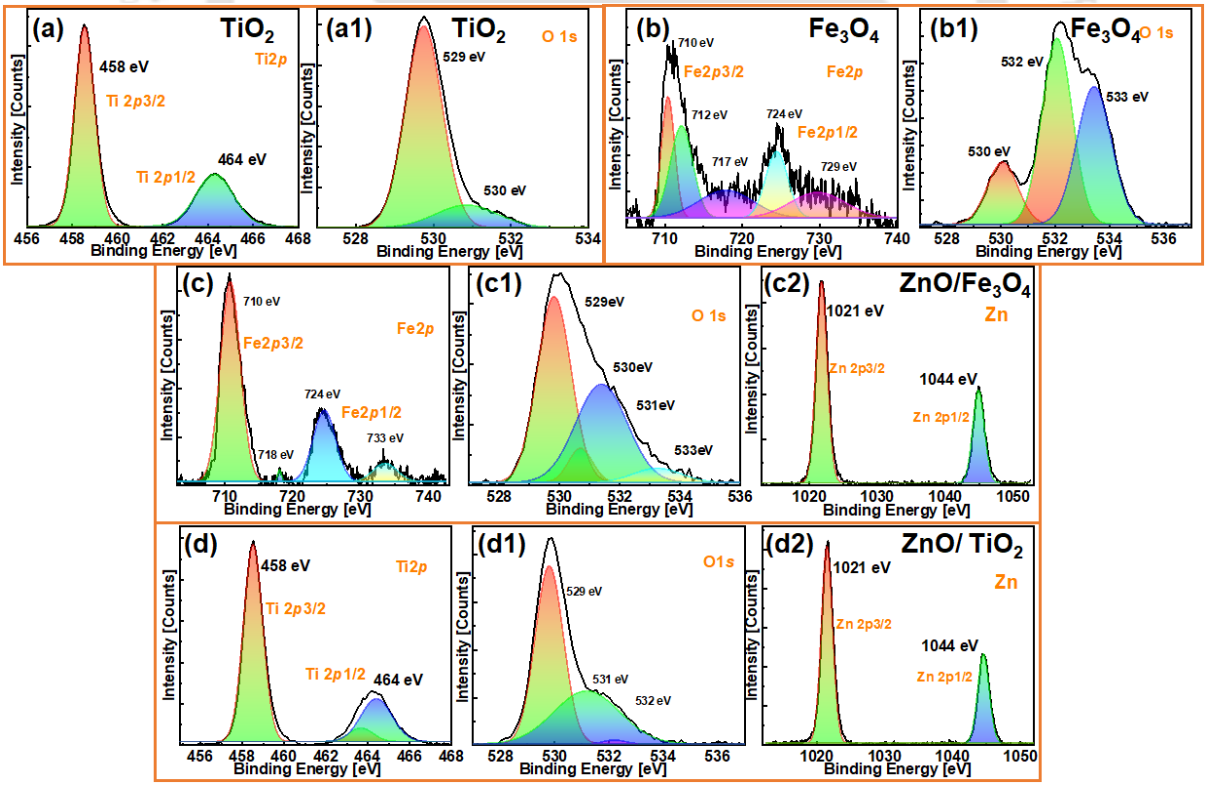


*Figure 5.1.5 High resolution XPS analysis of (a, a1) $TiO_2$, (b, b1) $Fe_3O_4$, (c, c1, c2) $ZnO/Fe_3O_4$, (d, d1, d2) $ZnO/TiO_2$*

In the $ZnO/Fe_3O_4$ heterostructure composite, the corresponding peaks of Fe2*p*3/2 and Fe2*p*1/2 are present at 710 eV and 724 eV with the satellite peaks at 718 eV and 733 eV. This indicates

the unchanging oxidation state of iron i.e., the properties of $Fe_3O_4$. The deconvolution of Zn2*p* peaks at 1021 eV and 1044 eV corresponding to the Zn2*p*3/2 and Zn2*p*1/2 indicates the $Zn^{2+}$ in the ZnO structure. The deconvoluted peaks of O1s indicate the lattice $O^{2-}$ of ZnO and $Fe_3O_4$, the higher binding energies are from the surface absorbed OH and COOH as seen from the $Fe_3O_4$ XPS analysis. In the ZnO/$TiO_2$ heterostructure XPS analysis, Ti2*p*3/2 and Ti2*p*1/2 which is consistent with the $Ti^{4+}$ formation of $TiO_2$. Also, the Zn2*p* peaks at 1021 eV and 1044 eV (Zn2*p*3/2 and Zn2*p*1/2) indicate the $Zn^{2+}$ formation of ZnO. The XPS analysis of ZnO/$Fe_3O_4$ and ZnO/$TiO_2$ heterostructure composites indicates the coexistence of the ZnO & $Fe_3O_4$ and ZnO & $TiO_2$ forming heterojunction interfaces.

### ***5.1.3 Charge transfer mechanism in the composite heterojunction interface***

From the literature review, ZnO/$TiO_2$ shows Type II and ZnO/$Fe_3O_4$ shows Type I heterostructure charge transfer pathways[250,287,288]. Possible charge transfer pathways for the ZnO/$Fe_3O_4$ and ZnO/$TiO_2$ composite heterostructures are illustrated in Figure 5.1.6. In Type I, straddling type heterojunction interface, the photogenerated electrons and holes are transferred from one semiconductor to another semiconductor. In short, the photogenerated electrons from the higher conduction band are transferred to the lower conduction band whereas holes are transferred from the lower valence band to the higher valence band of the comparison in the heterojunction interfaces. As depicted by C. Cheng et al, ZnO/$TiO_2$ show staggered Type II charge transfer where the photogenerated electrons and holes are separated in the heterojunction interface and oxidation and reduction take place on different semiconductor surfaces, unlike Type II charge transfer that occurs in a single semiconductor surface[250]. In the case of ZnO/$TiO_2$, the photogenerated holes are transferred from the valence band of $TiO_2$ to the valence band of ZnO while the electrons are transferred from the conduction band of ZnO to the conduction band of $TiO_2$[288]. Whereas in the ZnO/$Fe_3O_4$ composite heterostructure, Type I heterojunction charge transfer, the photogenerated electrons from the conduction band of ZnO are transferred to the conduction band of the $Fe_3O_4$, as the energy level of the conduction band of the ZnO lies above the Fermi level of $Fe_3O_4$ also, the holes are transferred from the valence band of ZnO to the valence band of $Fe_3O_4$[289,290].

In some reported papers, the electron from the conduction band of $Fe_3O_4$ is migrated to the ZnO[291], however, O. Długosz et al suggested that the Type-I charge transfer between the heterojunction interface is thermodynamically favorable[292]. Thus, in the two heterostructures, the energy level differences developed in the heterojunction act as a driving force of the charge migration, inhibiting the charge recombination and thus enhancing the photocatalytic

performance[292]. To validate the resulting performance and hypothesis of the existence of charge transfer, time-resolved photoluminescence spectroscopy is studied and shown in Figure 5.1.7 for the composite heterostructures with 375 nm laser excitation.

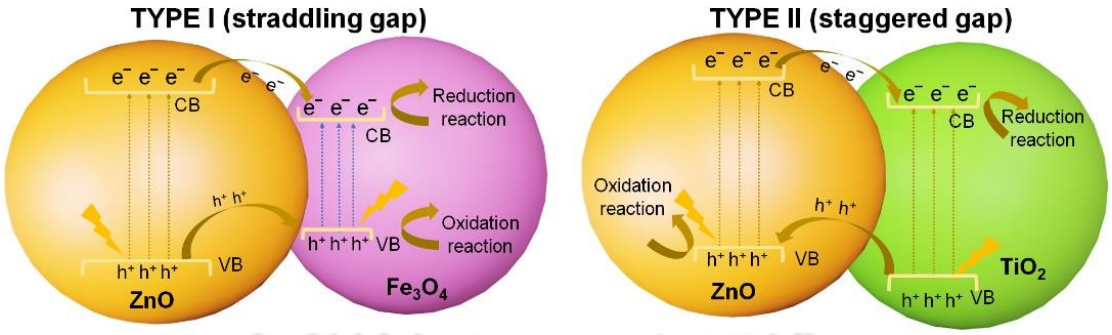


*Figure 5.1.6. Charge transfer pathways in the heterojunction interface of ZnO/$Fe_3O_4$, and ZnO/$TiO_2$*

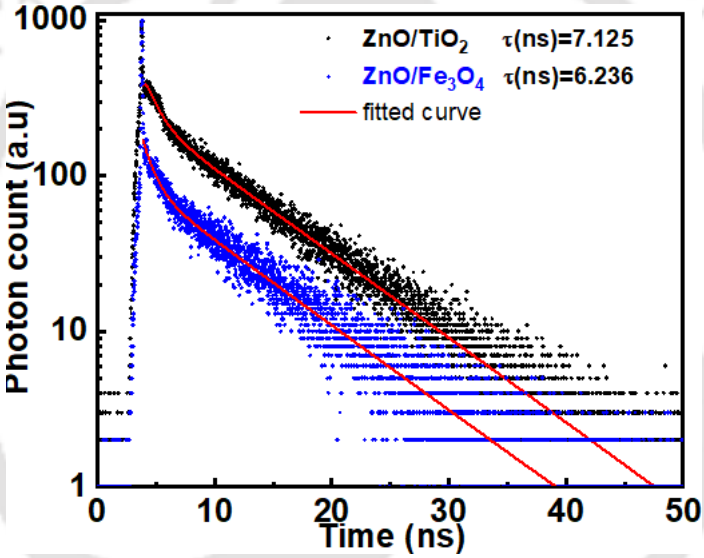


*Figure 5.1.7 Time-Resolved Photoluminescence TRPL spectroscopy of ZnO/$TiO_2$ and ZnO/$Fe_3O_4$ composite heterostructures*

From the obtained charge carrier lifetimes calculation, ZnO/$Fe_3O_4$ heterostructure has an average charge carrier lifetime of 6.236 ns while ZnO/$TiO_2$ heterostructure has an average charge carrier lifetime of 7.125 ns. Thus, this indicates the charge carrier transfer enhancement in the ZnO/$TiO_2$ composite structures, validating the better charge transfer between ZnO and $TiO_2$.

### *5.1.4 Photocatalysis and charge transfer mechanism in the composite heterojunction interface*

The degradation kinetics of the aqueous RhB solution were monitored under UV light illumination to determine the photocatalytic activity and performance of the composite heterostructures. After 100-120 mins, the degradation is almost constant with an overall 85-90 % dye degradation as seen in Figure 5.1.8 a. The efficiency and performance of the RhB dye degradation are shown in Figure 5.1.8 a, where the degree of degradation concerning the original concentration is plotted against the total reaction time of 140 min. Figure 5.1.8 b shows the pseudo-first-order degradation kinetics plot for the $ZnO/TiO_2$ and $ZnO/Fe_3O_4$ composite heterostructure as the photocatalyst under UV light irradiation. The rate of degradation is determined using the lining fitting curve plotted for the pseudo-first-order kinetics equation where the slope gives the numerical value of the reaction rate. The reaction rate is compared based on the correlation factor, the value of $R^2$ of the linear fitting curve obtained based on the experimental data. The higher value of $R^2$ gives a good criterion for the selection of the specific degradation kinetics rate model[293]. Based on the obtained data as shown in Figure 5.1.8 b, the pseudo-first-order reaction rates for $ZnO/TiO_2$ and $ZnO/Fe_3O_4$ composite heterostructure photocatalyst are 0.014 $min^{-1}$ ($R^2$= 0.98) and 0.011 $min^{-1}$ ($R^2$=0.97) respectively. The photo-generated electrons and holes in the mid-gap energy states are transferred to the conduction band of $TiO_2$ and valence band of ZnO of the semiconductor respectively, thus enhancing the reduction and oxidation process during the photocatalytic degradation of RhB dye[294].

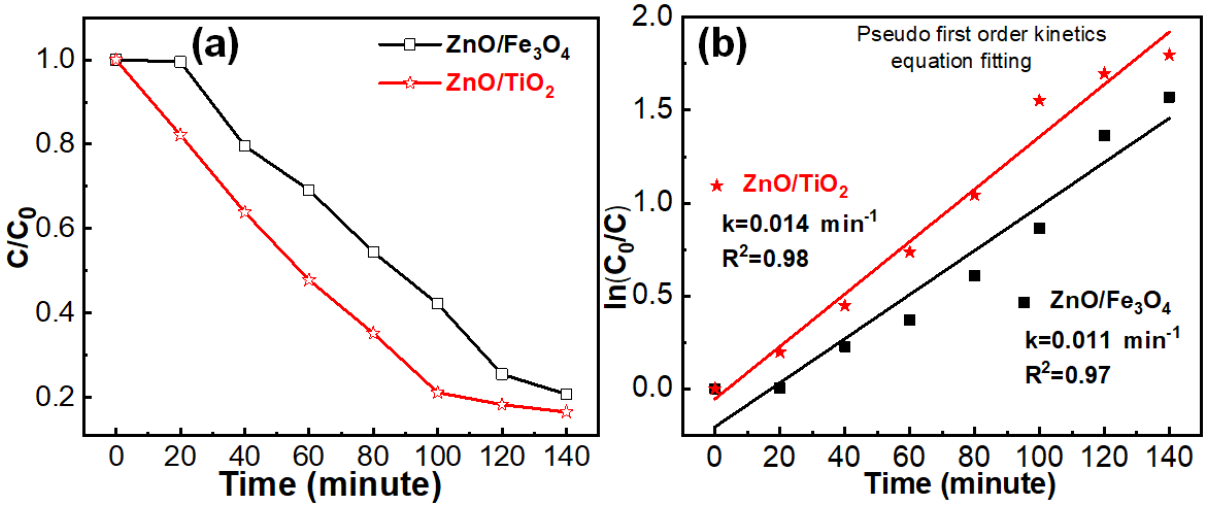


*Figure 5.1.8. (a) Photocatalytic degradation curve, and (b) degradation kinetic of RhB for pseudo-first-order kinetics of $ZnO/TiO_2$ and $ZnO/Fe_3O_4$ heterostructure composites under the UV-light irradiation*

The process of photocatalytic dye degradation is well known to everyone; in brief, it follows five major steps— (i) light adsorption, (ii) photogeneration of charge i.e., electrons and holes, (iii) separation and transfer of photogenerated charges, (iv) generation of reactive oxygen species and reduction or oxidation/ charge recombination, and (v) desorption of reactant products. The reactive oxygen species (ROS) produced— $O^{2\bullet-}$, •OH, $OH^-$, $HO_2$•, $H_2O_2$, by the influence of photogenerated electrons and holes reacting with the $H_2O$, attacked the unsaturated bonds of the dye molecules hence converting them into $CO_2$ and $H_2O$ as the final product[295]. In addition to the ROS generated, it is reported that $Fe^{3+}$ acts as electron trap sites, and $Fe^{2+}$ is oxidized to $Fe^{3+}$ generating more •OH radicals. The higher degradation rate of RhB dye using ZnO/$TiO_2$ composite heterostructure can be attributed to the involvement of both semiconductor surfaces for oxidation and reaction (as depicted in Type II charge transfer pathways) and also, it is contributed by the formation of mid-gap energy states. Also, it can be attributed to the difference in the electron diffusion speed from the ZnO core to the shell, where it is faster in the $TiO_2$ shell case as compared to the electron diffusion to the $Fe_3O_4$ shell. This may be due to the larger difference in the energy bandgap alignment between the constituting materials in the ZnO/$Fe_3O_4$ composite heterostructures. Thus, based on the study of both Type I and Type II charge transfer heterostructures, it is concluded that the Type II ZnO/$TiO_2$ composite heterostructure shows a higher photocatalytic activity with higher charge carrier lifetime than Type I ZnO/$Fe_3O_4$ composite heterostructures.

### ***5.1.5 Key findings of Part A***

- In summary, ZnO/$Fe_3O_4$ and ZnO/$TiO_2$ composite heterostructures are synthesized using the chemical synthesis method.
- Type II ZnO/$TiO_2$ composite heterostructures show greater photocatalytic performance degradation rate of 0.014 $min^{-1}$ as compared to that of Type I ZnO/$Fe_3O_4$.
- The higher photodegradation rate of ZnO/$TiO_2$ is due to the presence of defects and faster electron diffusion from ZnO to $TiO_2$ with a charge carrier lifetime of 7.125 ns.
- The lower photodegradation rate of 0.011 $min^{-1}$ by using ZnO/$Fe_3O_4$ photocatalyst is possibly due to the one surface participation in the photocatalytic redox reaction.
- The larger energy band level difference between ZnO and $Fe_3O_4$ in the heterojunction interface slows down the charge transfer diffusion in the heterostructure interface giving rise to a lower charge carrier lifetime of 6.236 ns. Thus, the photocatalytic performance is affected by the charge transfer pathways followed in the heterojunction interface.

## PART B: Charge transfer dynamics in g-$C_3N_4$/ZnO heterojunction interface

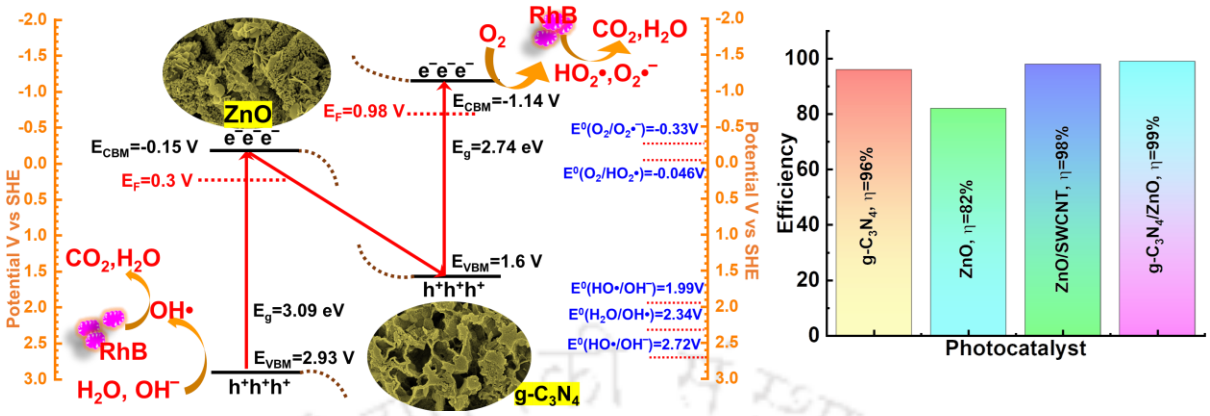


***Graphical Abstract of Part B***

In this part of the chapter, charge transfer dynamics are studied in the g-$C_3N_4$/ZnO complex heterostructure. The formation of the Z-scheme charges transfer pathway in the g-$C_3N_4$/ZnO heterojunction interface is studied in detail based on the optical and electronic properties analysis. The photocatalytic performances of these photocatalysts tested are found to be responsive to the natural sunlight for the advanced oxidation process. This part also shows the successful approach in eliminating the use of high-power triggering light sources and continuous stirring during the photocatalysis process.

## 5.2 Results and Discussion of the g-$C_3N_4$/ZnO heterostructure

### *5.2.1 Structural analysis*

The structural and crystallographic analysis is presented in Figure 5.2.1 a for XRD and Figure 5.2.1 b for Raman. The g-$C_3N_4$ nanoparticles prepared by the one-step thermal polymerization method show the formation of bulk g-$C_3N_4$ characteristics with two distinctive planes- (100) at 13.04º corresponding to the in-plane trigonal N linkage of tri-s-triazine repeating structural units and (002) plane at 27.6º attributed by the stacking of interplanar conjugated aromatic rings of g-$C_3N_4$[270,296]. In the g-$C_3N_4$/SWCNT nanocomposite, the (001) peak of carbon nanotubes is at 12.26º in addition to the (100) and (002) peaks of g-$C_3N_4$. With the nine highly intense clear peaks, ZnO shows high crystallinity and purity in the absence of impurity peaks forming the hexagonal wurtzite phase structure of space group P63mc(186).

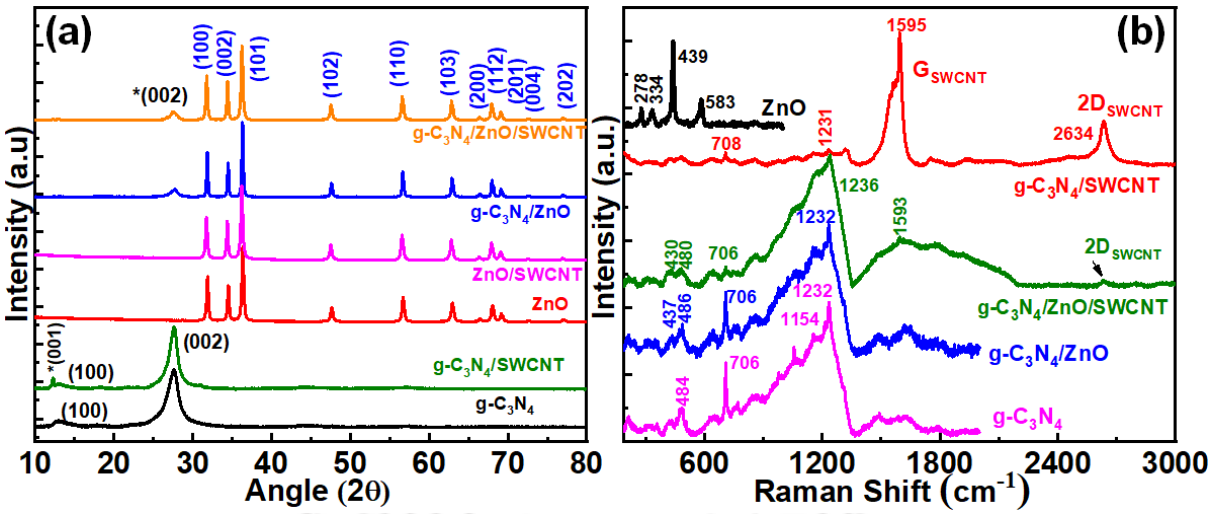


*Figure 5.2.1 (a) XRD spectra, and (b)Raman spectra of g-$C_3N_4$, ZnO, g-$C_3N_4$/ZnO, ZnO/SWCNT, g-$C_3N_4$/SWCNT, and g-$C_3N_4$/ZnO/SWCNT*

In the g-$C_3N_4$/ZnO composites, the prominent ZnO peaks in addition to the (002) peak of g-$C_3N_4$ are seen with no significant peak position shifting. This indicates the integral maintenance of the structure with successful composite formation retaining the parent properties. The structural integrity is also confirmed by the Raman analysis as shown in Figure 5.2.1 b. With the formation of g-$C_3N_4$/ZnO composites, no significant peak shift is observed indicating the absence of chemical bonding between the individuals. The typical signature of the g-$C_3N_4$ formation is also indicated by the presence of heptazine ring breathing mode (tri-s-triazine breathing modes) at 706 $cm^{-1}$ and 1232 $cm^{-1}$ for the stretching vibration modes of C=N and C—N heterocycles[273,297]. The vibration peak at ~480 $cm^{-1}$ and ~980 $cm^{-1}$ represents the C–N heterocycles and in-plane N radial vibration in g-$C_3N_4$[273,277]. However, it also indicates the fingerprints of melamine in the sample as it originates from the breathing 1 mode of melamine triazine ring. This may be due to the incomplete conversion of melamine reactants into the g-$C_3N_4$ during the thermal polymerization reaction where melem is formed by thermal polymerization of the melamine heptazine units and further organized into the formation of g-$C_3N_4$ networks[298]. The ~1151 $cm^{-1}$, ~1408 $cm^{-1}$ & 1489 $cm^{-1}$, ~1581 $cm^{-1}$ & 1617 $cm^{-1}$ indicate the -$NH_2$ rocking, CN breathing and ring stretching mode of g-$C_3N_4$ respectively[273,299]. In the presence of ZnO nanoparticles in the binary and ternary composites, a minute peak at 430 $cm^{-1}$ and 437 $cm^{-1}$ are observed attributed to the $E_2$ high mode and a significant indicator of ZnO structure[300]. The g-$C_3N_4$ peaks are highly dominated by the SWCNT peaks in the binary g-$C_3N_4$/SWCNT composite where a highly intense G and 2D bands are observed at 1595 $cm^{-1}$ and 2634 $cm^{-1}$. Although insignificant, small peaks at ~1131 $cm^{-1}$, 1580 $cm^{-1}$ and 1593 $cm^{-1}$

are seen in g-$C_3N_4$, g-$C_3N_4$/ZnO, g-$C_3N_4$/ZnO/SWCNT composite, a signature of graphitic carbon structure[299].

### ***5.2.2 Morphology analysis***

The morphological analysis of the successfully prepared g-$C_3N_4$, ZnO, binary photocatalyst g-$C_3N_4$/ZnO, ZnO/SWCNT, g-$C_3N_4$/SWCNT, and ternary photocatalyst g-$C_3N_4$/ZnO/SWCNT are analyzed by the field emission scanning electron microscopy (FESEM). With porous network structures and aggregated nanoparticles, the prepared g-$C_3N_4$ shows irregular shapes and sizes as shown in Figure 1a and inset. The network structures are found to be stacked by the nanoaggregates. The ZnO nanoparticles exhibited two different morphologies (Figure 5.2.2 b)- flakes of around 500 nm and nanoaggregates of around 30-40 nm. With the 1:1 mass ratio of g-$C_3N_4$ and ZnO nanoparticles, g-$C_3N_4$/ZnO composites are formed by sonication and its resulting morphology is shown in Figure 5.2.2 c. In the g-$C_3N_4$/SWCNT composite, the carbon nanotubes are distributed in the g-$C_3N_4$ nanoparticles. The ZnO/SWCNTs show similar morphology as discussed in the earlier article of ZnO self-assembled SWCNTs (here, pristine SWCNTs are used) where long nanoparticles aggregated are formed with SWCNTs as the skeleton surrounded by the ZnO nanoparticles (Figure 5.2.2 e).

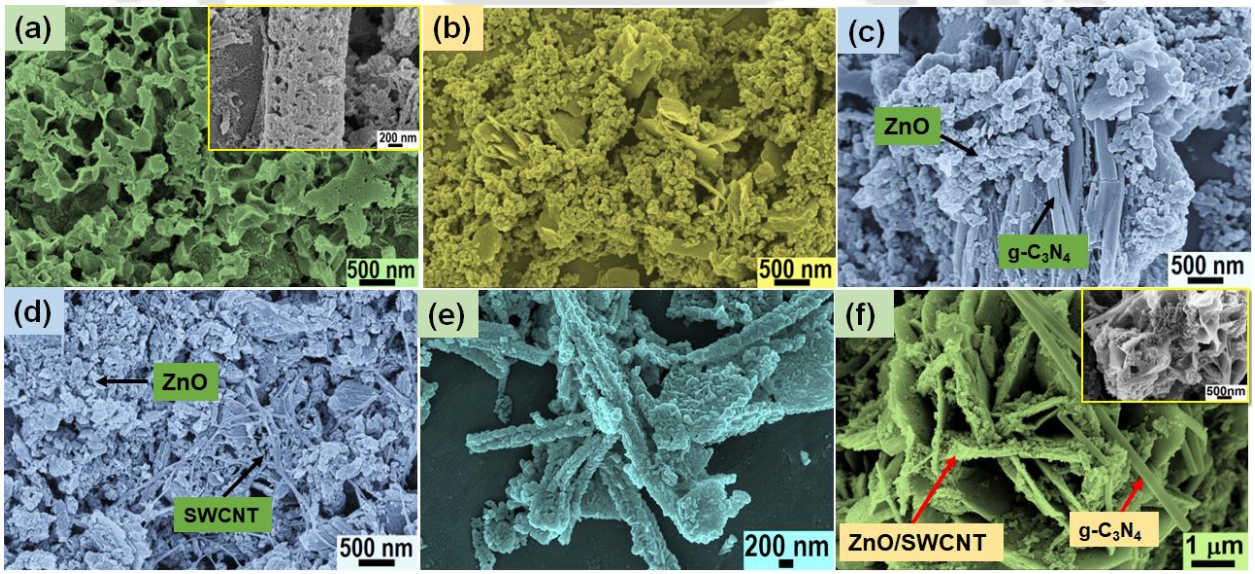


*Figure 5.2.2 FESEM images of (a) g-$C_3N_4$, (b) ZnO, (c) g-$C_3N_4$/ZnO, (d) g-$C_3N_4$/SWCNT (e) ZnO/SWCNT, and (f) g-$C_3N_4$/ZnO/SWCNT*

The elemental analysis and mapping of the individuals, binary and ternary composites are analyzed and presented in Figure 5.2.3 (a) g-$C_3N_4$, (b) ZnO, (c) g-$C_3N_4$/SWCNT, (d) ZnO/SWCNT, (e) g-$C_3N_4$/ZnO, and (f) g-$C_3N_4$/ZnO/SWCNT. In g-$C_3N_4$ and ZnO nanoparticles, carbon & nitrogen and zinc & oxygen are uniformly distributed with & the

particles. Further, in the binary- g-$C_3N_4$/ZnO, ZnO/SWCNT, g-$C_3N_4$/SWCNT, and ternary- g-$C_3N_4$/ZnO/SWCNT photocatalyst, the consistent distribution of elements across all particles indicates that individual nanoparticles have successfully combined to form composites.

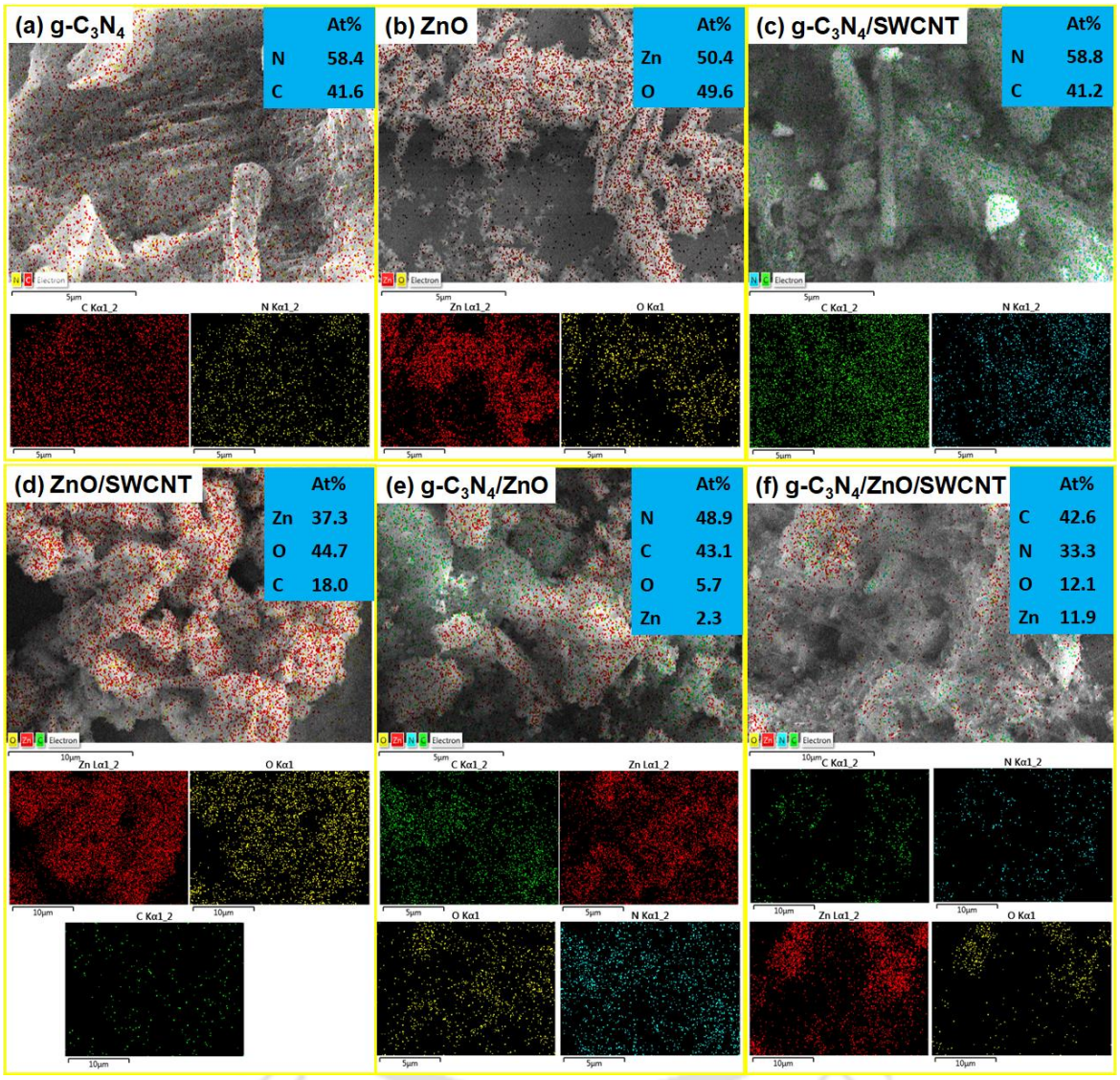


*Figure 5.2.3 Elemental analysis and mapping of (a) g-$C_3N_4$, (b) ZnO, (c) g-$C_3N_4$/SWCNT, (d) ZnO/SWCNT, (e) g-$C_3N_4$/ZnO, and (f) g-$C_3N_4$/ZnO/SWCNT*

The morphology and crystal structure of the individual photocatalyst (g-$C_3N_4$, ZnO, ZnO/SWCNT) are also analyzed using the FETEM, HRTEM, and SAED analysis as shown in Figure 5.2.4. The g-$C_3N_4$ shows a porous nature with variable pore sizes and diameters (Figure 5.2.4 a) where visible pore diameters range from 12 nm to 40 nm. The pores are observed here from an individual two-dimensional sheet-like structure that builds networks of variable thickness with thicknesses running from 14 nm to 40 nm, developing micropores. The HRTEM image (Figure 5.2.4 b) with a d-spacing of 0.33 nm corresponds to the (002) plane and the

diffused rings in the SAED pattern in Figure 5.2.4 c show an amorphous nature with the rings corresponding to the (100) and (002) planes of g-$C_3N_4$. The 100-250 nm sizes ZnO nanoparticles and ZnO/SWCNT show high crystallinity with distinctive bright spots which are indexed as shown in Figure 5.2.4 (f, i). The d-spacings of ZnO and ZnO/SWCNT are 0.26 nm corresponding to the (002) plane of ZnO.

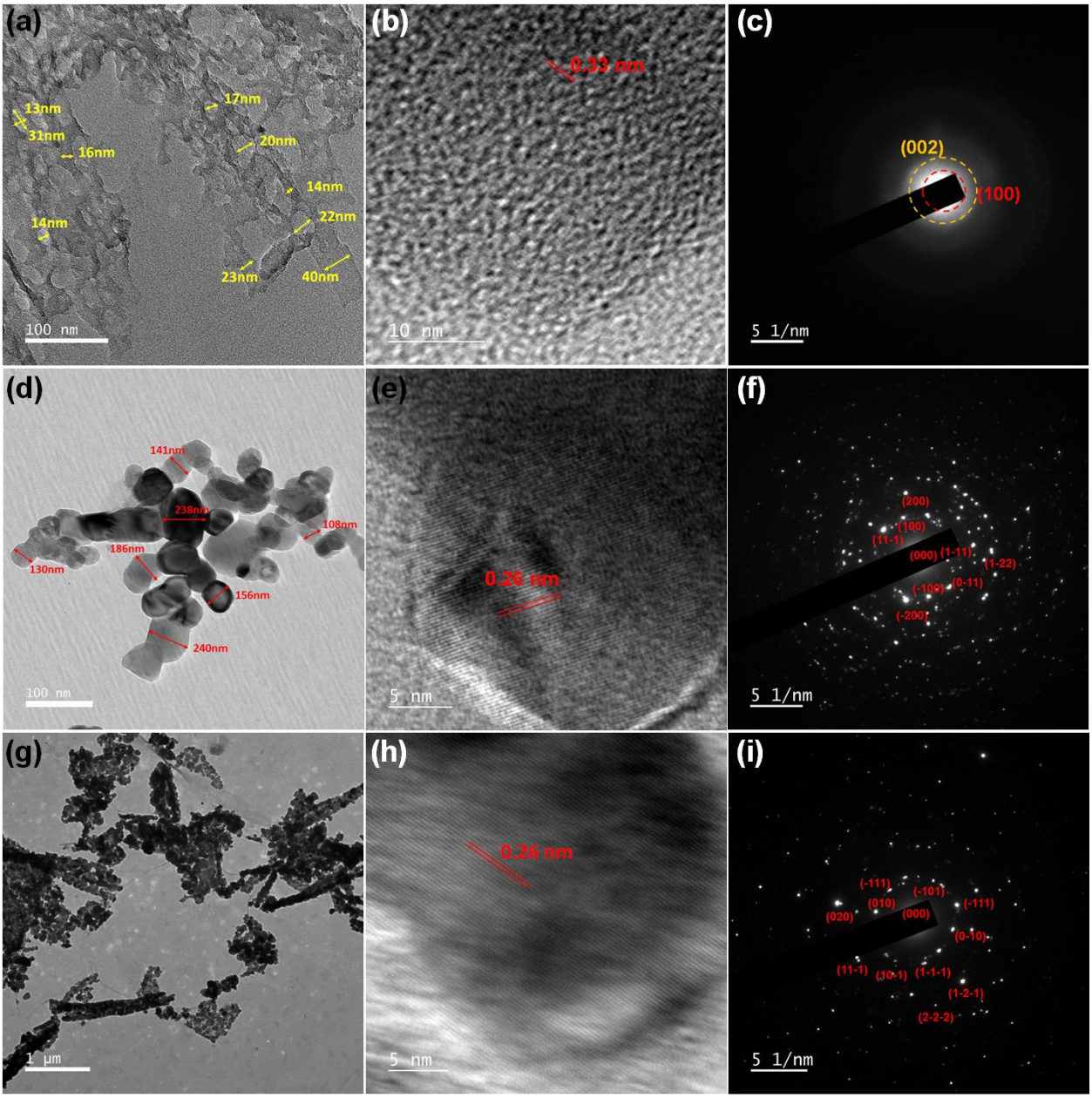


*Figure 5.2.4 (a, d, g) FETEM, (b, e, h) HRTEM, and (c, f, i) SAED pattern of g-$C_3N_4$, ZnO and ZnO/SWCNT nanoparticles*

### *5.2.3 XPS analysis*

As the binding energy of a sample indicates the major characteristics of a sample, XPS survey analysis was performed to investigate the oxidation state, electronic structure, chemical composition, and bonding of the samples. Figure 5.2.6 (a, b, c, d) represents the full survey spectrum of the individual photocatalyst ZnO, g-$C_3N_4$, and ZnO/SWCNT and binary g-$C_3N_4$/SWCNT composite. The high-resolution spectra of the O*1s* for the ZnO-based photocatalyst (ZnO, ZnO/SWCNT) are deconvoluted and observed peaks at 530 eV, 532 eV, and 534 eV which corresponds to the $O^{2-}$ ions surrounded by the Zn atom in the ZnO hexagonal wurtzite phase structure, oxygen vacancies, and -OH group chemisorbed onto the ZnO surface. In the Zn*2p* spectra, the two peaks at 1021 eV and 1044 eV correspond to the Zn$2p_{3/2}$ and Zn$2p_{1/2}$ respectively. The binding energy peak difference of 23 eV is within the standard ZnO reference value, indicating the +2 oxidation states of the Zn atoms in the ZnO nanoparticles[301–303].

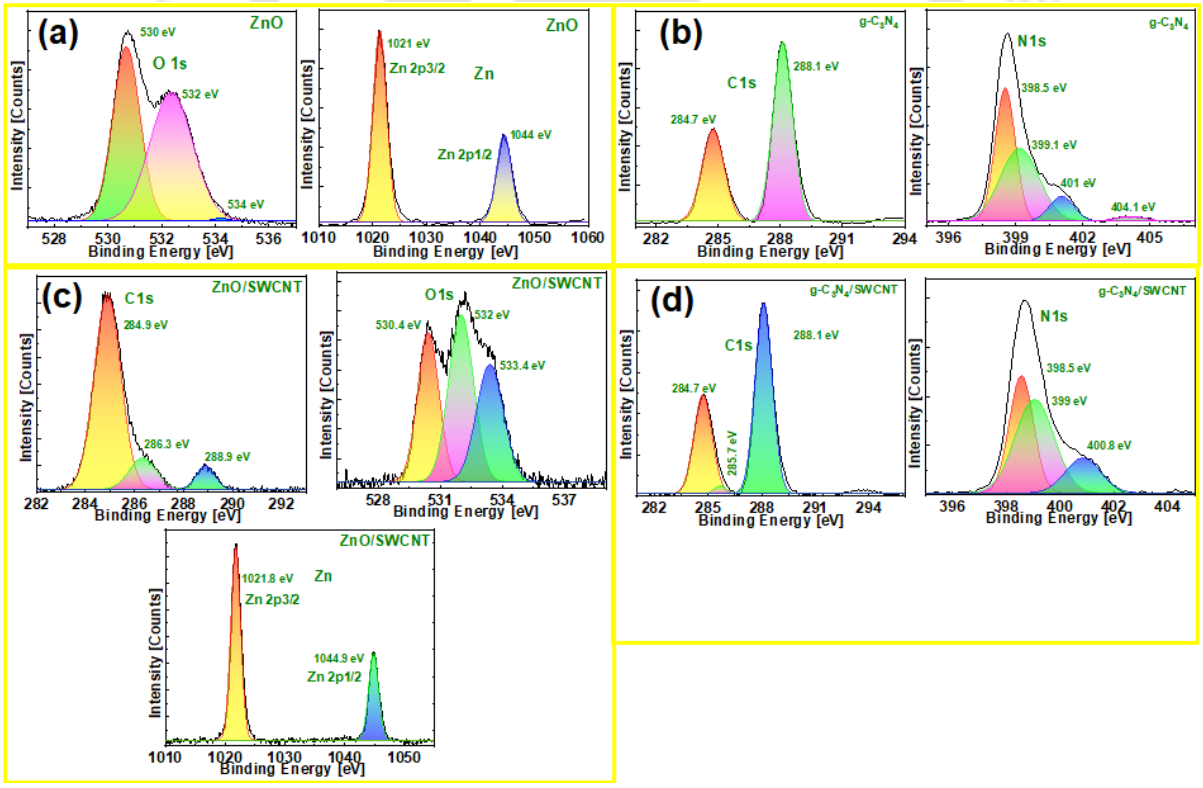


*Figure 5.2.5 High-resolution XPS analysis of (a) ZnO, (b) g-$C_3N_4$, (c) ZnO/SWCNT, and (d) g-$C_3N_4$/SWCNT*

In g-$C_3N_4$ XPS high-resolution deconvoluted spectrum, two peaks of C*1s* at 284.7 eV & 288.1 eV, and three peaks of N*1s* at 398.5 eV, 399.1 eV, 401 eV, & 404.1 eV are observed. The lower and higher binding energies of C*1s* spectra are assigned to the $sp^2$ C-C bond of graphitic carbon

or the pure graphitic site of carbon nitride and $sp^2$ carbon in the aromatic N-C=N structure of tri-s-triazine rings respectively[303,304]. The N*1s* peak of g-$C_3N_4$ was deconvoluted into its four basic units as shown in Figure 5.2.5 b; the $sp^2$ hybridized nitrogen (C-N=C) in triazine ring at 398.5 eV, $sp^3$ hybridized nitrogen (H-N-$(C)_2$ or N-$(C)_3$) in the aromatic moieties at 399.1 eV, residual amino functional groups or graphitic nitrogen (C-NH or C-N-$(H)_2$) at 401 eV, and π-excitation or π-π* transitions at 404.1 eV[267,298,305–307]. The ZnO/SWCNT show similar O*1s* and Zn*2p* high-resolution deconvoluted peaks (Figure 5.2.5 c) with the ZnO nanoparticles as exhibited in Figure 5.2.5 a with an additional C1s peak originated from the SWCNT in the composite. The C*1s* peaks at 284.9 eV, 286.3 eV, and 288.9 eV are attributed to the $sp^2$ hybridized C=C bond of carbon nanotubes, $sp^3$ hybridized C-O bond interaction, and π-π* transitions which are seen in graphene respectively[217,242]. In the g-$C_3N_4$/SWCNT composite (Figure 5.2.5 d), in addition to the signature C*1s* spectrum at 284.7 eV and 288.1 eV, an additional peak at 285 eV emerges due to the $sp^2$ hybridized C=C bond of carbon nanotubes. For the N*1s* spectra, three deconvoluted peaks at 398.5 eV, 399 eV, and 400.8 eV are observed which are similar to the N*1s* spectra of g-$C_3N_4$. Thus, from the XPS analysis, as no new oxidation states of the individual elements are observed, it can be concluded that the composites are formed by physical interaction rather than forming bonds between the individual photocatalysts.

### ***5.2.4 Photocatalysis***

Under the influence of natural sunlight, the photocatalytic advanced oxidation treatment of a typical pollutant of the textile industry, rhodamine B (RhB) was evaluated by using the synthesized photocatalyst. The individual photocatalyst; g-$C_3N_4$, ZnO, binary photocatalyst; g-$C_3N_4$/ZnO, ZnO/SWCNT, g-$C_3N_4$/SWCNT, and ternary photocatalyst; g-$C_3N_4$/ZnO/SWCNT are used to compare and study the efficiency by analyzing the charge transfer dynamics in the heterojunction interface of the individual photocatalyst. During the photolysis and adsorption process as shown in Figure 5.2.6 a, no significant change in the dye intensity is observed, indicating that negligible dye molecules have been degraded in the absence of a photocatalyst or absorbed onto the photocatalyst surface. A slight increase in dye intensity in photolysis is evidence of the harmful effect of dye molecules exposed to sunlight without proper treatment and hence its imposing toxicity in aquatic environments. In the presence of photocatalyst under natural sunlight exposure, RhB dye molecules are degraded with efficiencies (η) in the order of g-$C_3N_4$/ZnO (99%)> ZnO/SWCNT (98%)> g-$C_3N_4$ (96%) =g-$C_3N_4$/SWCNT (96%) > g-$C_3N_4$/ZnO/SWCNT (98%)< ZnO (82%). The ZnO-based composites- ZnO, ZnO/SWCNT, and

g-$C_3N_4$/ZnO showed the highest degradation efficiency (Figure 5.2.6 b). Despite having a lower energy bandgap of g-$C_3N_4$ (2.74 eV) in comparison with ZnO (3.09 eV), ZnO showed higher degradation efficiency. This may be due to the surface properties of ZnO like higher surface area and, the presence of surface defects acting as the reaction sites as discussed in the previous paper[308]. Among the Zn-based composites, g-$C_3N_4$/ZnO showed the highest degradation efficiency of 99% in the 1st run (Figure 5.2.6 b) and was reused again for the 2nd run, resulting in 96% efficiency.

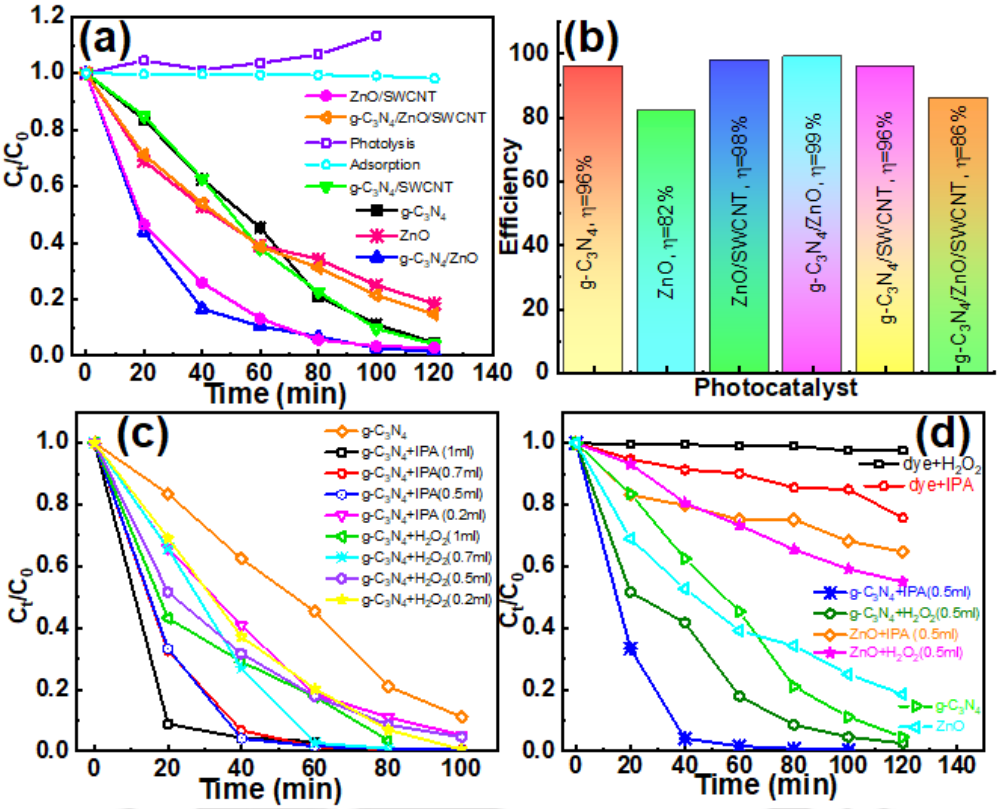


*Figure 5.2.6 (a) Photocatalytic degradation curve of RhB, and (b) photocatalytic efficiencies of the individual photocatalyst; g-$C_3N_4$, ZnO, binary photocatalyst; g-$C_3N_4$/ZnO, ZnO/SWCNT, g-$C_3N_4$/SWCNT, and ternary photocatalyst; g-$C_3N_4$/ZnO/SWCNT triggered by the natural sunlight, (c) effect of IPA and $H_2O_2$ in photocatalytic degradation, and (d) comparative degradation efficiencies of ZnO and g-$C_3N_4$ with the use of IPA and $H_2O_2$.*

The reproductivity and stability of the photocatalyst nanoparticles are tested as shown in Figure 5.2.7 for (a) g-$C_3N_4$, (b) ZnO, (c) g-$C_3N_4$/SWCNT, (d) ZnO/SWCNT, (e) g-$C_3N_4$/ZnO, and (f) g-$C_3N_4$/ZnO/SWCNT. The nanoparticles show similar photocatalytic efficiency in the 2nd run to that obtained in the 1st run under natural sunlight, thus proving its superior ability to be used as a powerful photocatalyst for organic pollutant removal efficiently. This reporting degradation method exempts the use of an external triggering light source and continuous stirring process during the reaction process overcoming the energy consumption setback and

reducing cost consumption while using cheap ZnO and carbon-based photocatalyst. A detailed summary of the efficiencies for all the photocatalysts is given in Table 5.1.

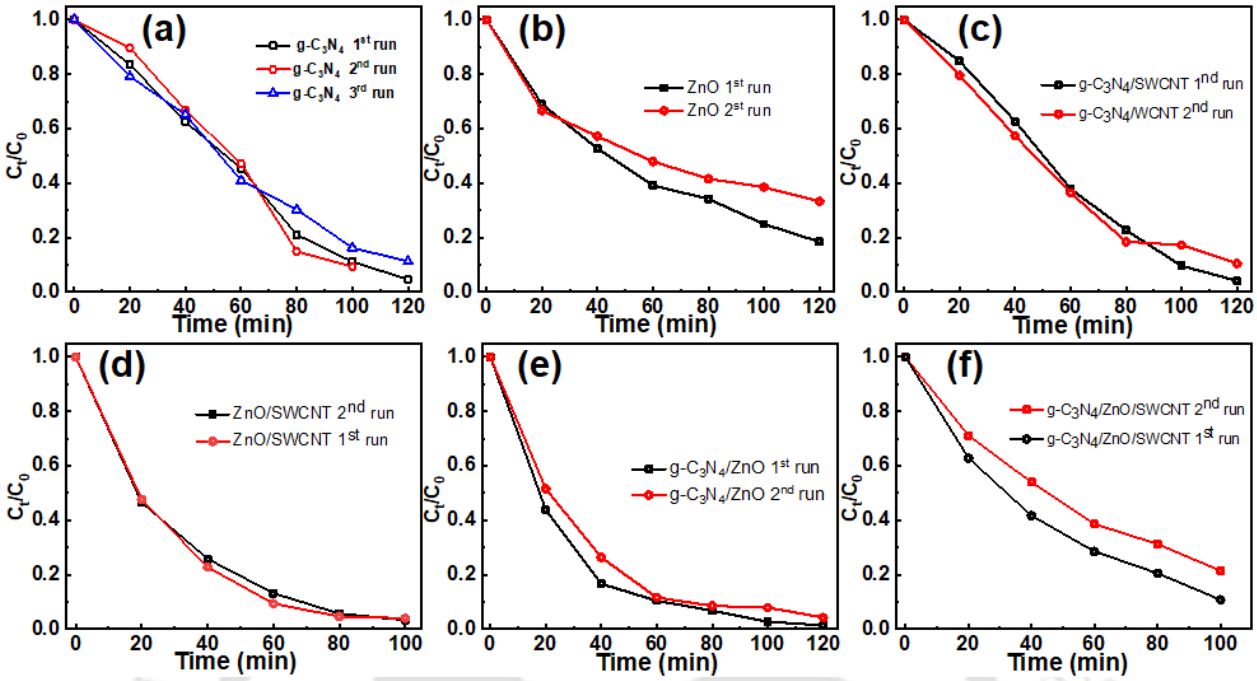


*Figure 5.2.7 Reusability and cyclic experiment of (a) g-$C_3N_4$, (b) ZnO, (c) g-$C_3N_4$/SWCNT, (d) ZnO/SWCNT, (e) g-$C_3N_4$/ZnO, and (f) g-$C_3N_4$/ZnO/SWCNT*

*Table. 5.1 Summary of reaction rate and photocatalysis efficiency*

| | **g-$C_3N_4$** | **ZnO** | **ZnO/SWCNT** | **g-$C_3N_4$/ZnO** | **g-$C_3N_4$/SWCNT** | **g-$C_3N_4$/ZnO/SWCNT** | **g-$C_3N_4$ +IPA (0.5ml)** | **g-$C_3N_4$ +$H_2O_2$ (0.5 ml)** | **ZnO +IPA (0.5 ml)** | **ZnO +$H_2O_2$ (0.5 ml)** |
|---|---|---|---|---|---|---|---|---|---|---|
| **Reaction rate ($min^{-1}$)** | 0.025 | 0.013 | 0.044 | 0.034 | 0.026 | 0.021 | 0.054 | 0.030 | 0.003 | 0.005 |
| **$R^2$** | 0.96 | 0.99 | 0.98 | 0.99 | 0.97 | 0.99 | 0.97 | 0.99 | 0.95 | 0.99 |
| **% Efficiency** | 96 | 82 | 98 | 99 | 96 | 86 | 99 | 98 | 36 | 46 |

To elucidate the photocatalytic reaction mechanism and the main reactive species for this specific advanced oxidation process, isopropyl alcohol (IPA) and $H_2O_2$ were used respectively in variable dosages (1 ml, 0.7 ml, 0.5 ml, and 0.2 ml) for the $h^+$ & OH•, and $e^-$ scavengers. IPA is known to be used as both $h^+$ and OH• scavengers in the photocatalytic AOP. The respected

degradation curve results are shown in Figure 5.2.6 c in the presence of g-$C_3N_4$ photocatalyst. With the addition of 1 ml, 0.7, ml, and 0.5 ml IPA in the reaction medium, the degradation efficiencies and rates are increased drastically with the highest values as compared to that of the use of $H_2O_2$. Although the degradation efficiency of g-$C_3N_4$+$H_2O_2$ (1 ml, 0.7 ml, 0.5 ml, and 0.2 ml) is less as compared to that of g-$C_3N_4$+IPA (1 ml, 0.7 ml, and 0.5 ml), it showed enhanced degradation rate and efficiency as compared to the bare g-$C_3N_4$ photocatalyst. These findings verify the crucial part played by the photogenerated $e^-$s in this AOP triggered by natural light. This may be due to the smaller size of IPA that is absorbed onto the photocatalyst surface with strong dissociative or non-dissociative chemisorption, acting as the $e^-$ donor and also, inhibiting $h^+$—$e^-$ recombination. Thus, assisting in the generation of more $O_2\bullet^-$ radicals through the reduction reaction of $O_2$ by the generated $e^-$s[283,309,310]. With the consumption of $h^+$ by the IPA scavengers, the photocatalytic degradation of RhB by using g-$C_3N_4$ photocatalyst exhibits the dominant nature of reduction reactions than the oxidation reactions. Further, as the degradation efficiency of g-$C_3N_4$+$H_2O_2$ is higher as compared to that of bare g-$C_3N_4$, $h^+$ also acted as a helping hand as $H_2O_2$ acts as the $e^-$ scavengers. The importance of $e^-$s in photocatalysis is also demonstrated by the photolysis of dye in the absence of a photocatalyst under natural sunlight. In the presence of ZnO photocatalyst, with the addition of 0.5 ml of IPA and $H_2O_2$ into the reaction medium, the degradation efficiencies and rates decreased from 82% to 36% and 46% respectively. In the case of ZnO photocatalyst, the use of $H_2O_2$ generates higher efficiency than IPA. $H_2O_2$ is also well known for its ability to generate OH• radicals and $OH^-$ ions when reacting with $e^-$. However, the direct photolysis of $H_2O_2$ is weak because of its small molar absorption coefficient of less than 1 $M^{-1}cm^{-1}$ for the triggering light of wavelength above 300 nm. Thus, in the ZnO photocatalyst system, the photogenerated $e^-$s are consumed by the added $H_2O_2$ and block the direct reduction of the dye molecules. As IPA acts as the $h^+$ and OH• radical scavengers, the number and concentration of ROS participating in the AOP has increased which led to a decrease in photocatalytic degradation efficiencies and rate. This anomalous behavior of the IPA and $H_2O_2$ effect on g-$C_3N_4$ and ZnO photocatalyst may also be attributable to the band edge positions.

### ***5.2.5 Charge transfer analysis and mechanism of photocatalysis***

In a composite photocatalyst, the photocatalytic activity is determined by the charge transfer efficiency, generation of ROS, and band edge positions in the heterojunction interface. These three determining factors of photocatalytic efficiency have been examined by investigating the band edge positions using Tauc plots obtained from UV-Vis absorption spectra and UPS

spectra as shown in Figure 5.2.8 and Figure 5.2.9 for g-$C_3N_4$, ZnO, ZnO/SWCNT, g-$C_3N_4$/ZnO, g-$C_3N_4$/SWCNT, and g-$C_3N_4$/ZnO/SWCNT. Here, ZnO/SWCNT is regarded as an individual photocatalyst as ZnO nanoparticles are self-assembled onto the SWCNTs via the chemical synthesis process, thus assumed as one. The bandgap ($E_g$) energies of the as-synthesized nanoparticles are calculated from Tauc's plot using Eq. 2. The valence band and conduction band energies are deduced from the band gap energies using Eq. 3 and 4 respectively. Therefore, from Figure 5.2.8 (a, b, c), the $E_g$ of g-$C_3N_4$, ZnO, and ZnO/SWCNT are calculated to be 2.74 eV, 3.09 eV, and 2.93 eV. With the formation of composites, the bandgap energies have decreased to 2.33 eV, 2.65 eV, and 2.10 eV respectively for g-$C_3N_4$/ZnO, g-$C_3N_4$/SWCNT, and g-$C_3N_4$/ZnO/SWCNT which suggest the heterojunction formation between the individuals.

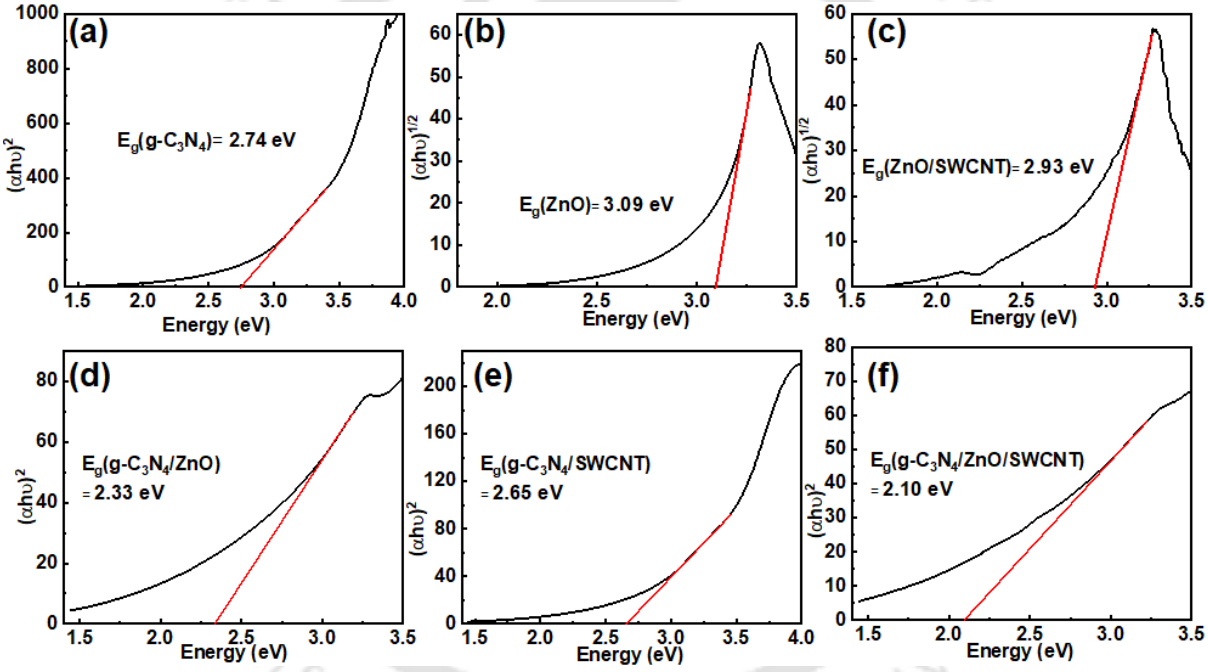


*Figure 5.2.8 Tauc plots of (a) g-$C_3N_4$, (b) ZnO, (c) ZnO/SWCNT, (d) g-$C_3N_4$/ZnO, (e) g-$C_3N_4$/SWCNT, and (f) g-$C_3N_4$/ZnO/SWCNT*

The complete electronic structures of the g-$C_3N_4$ and ZnO nanoparticles are determined from the UPS photoemission spectra as shown in Figure 5.2.9 (a, b) respectively using the He I ($h\upsilon$= 21.22 eV) photon energy source. The low and high binding energy cut-offs ($E_L$ and $E_H$) are derived from the UPS spectra by drawing corresponding tangent lines of the linear portion in the respective regions. The work function ($\phi$) of the photocatalyst is the difference between the vacuum level and the fermi level which is calculated by subtracting the width of the UPS spectrum from the incident He I photon energy[311,312], i.e., $\phi = 21.22 - (E_H - E_L)$. From

calculation, the Fermi level of g-$C_3N_4$ and ZnO is 0.98V vs SHE and 0.3 V vs SHE. With the formation of g-$C_3N_4$/ZnO, g-$C_3N_4$/SWCNT, and g-$C_3N_4$/ZnO/SWCNT composites, the Fermi level increases to 1.81 V vs SHE, 1.87 V vs SHE, and 2.41 V vs SHE respectively with respect to g-$C_3N_4$, an indication of difficulty in pulling electrons to the vacuum level. However, analyzing deeply, the Fermi level decreases when compared with that of ZnO, an opposite behavior to that of g-$C_3N_4$. To elucidate the nature of enhanced photocatalytic activity by efficient charge transfer dynamics, the position of $E_{VBM}$ and $E_{CBM}$ are calculated using Eq. 3 and 4 and found to be 1.6 V & -1.14 V and 2.93 V & -0.15 V when converted to the relative values to the standard hydrogen electrode for g-$C_3N_4$ and ZnO respectively. With the formation of a heterojunction interface, the difference in the Fermi level results in the band bending[313].

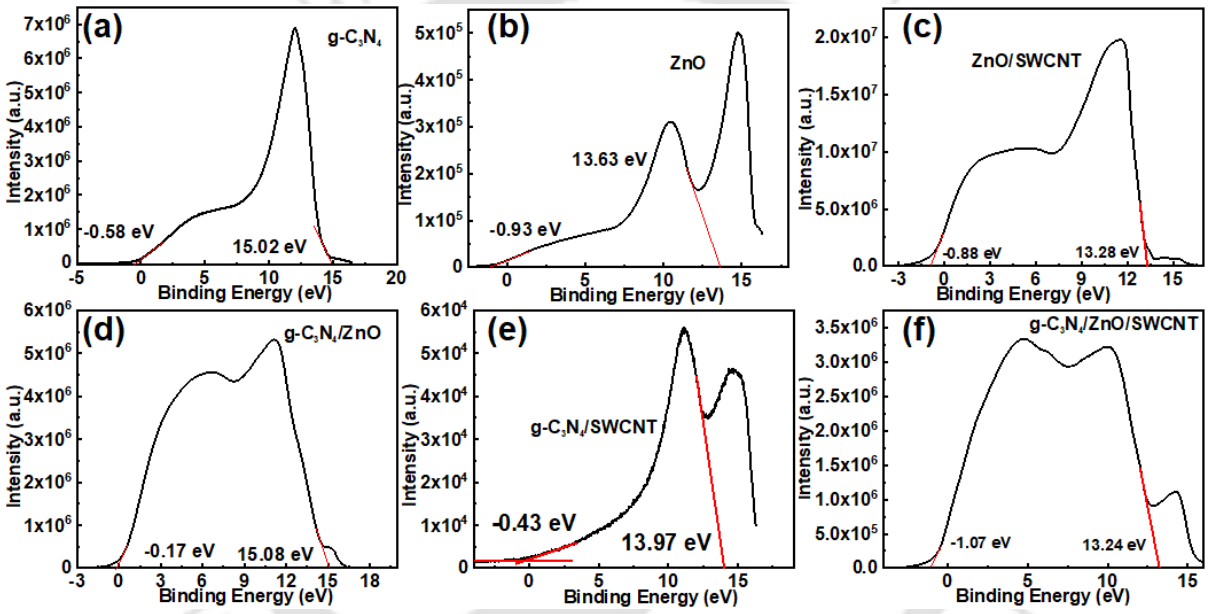


*Figure 5.2.9 UPS spectra of (a) g-$C_3N_4$, (b) ZnO, (c) ZnO/SWCNT, (d) g-$C_3N_4$/ZnO, (e) g-$C_3N_4$/SWCNT, and (f) g-$C_3N_4$/ZnO/SWCNT*

The newly formed energy levels of the composite nanoparticles are calculated from the Tauc plots and UPS spectra (Figure 5.2.8 (c-f) and Figure 5.2.9 (c-f)). With the formation of the g-$C_3N_4$/ZnO heterojunction interface, the Fermi level of the newly formed composite is estimated to be 1.81 V vs SHE, increased with respect to g-$C_3N_4$ and decreased with respect to ZnO. This finding epitomized the concept and evidence of charge transfer acting as an electron donor-acceptor, thus modifying the Fermi level when a heterojunction interface is introduced in a composite system. This same principle is applied to other composite: of g-$C_3N_4$/SWCNT, and g-$C_3N_4$/ZnO/SWCNT.

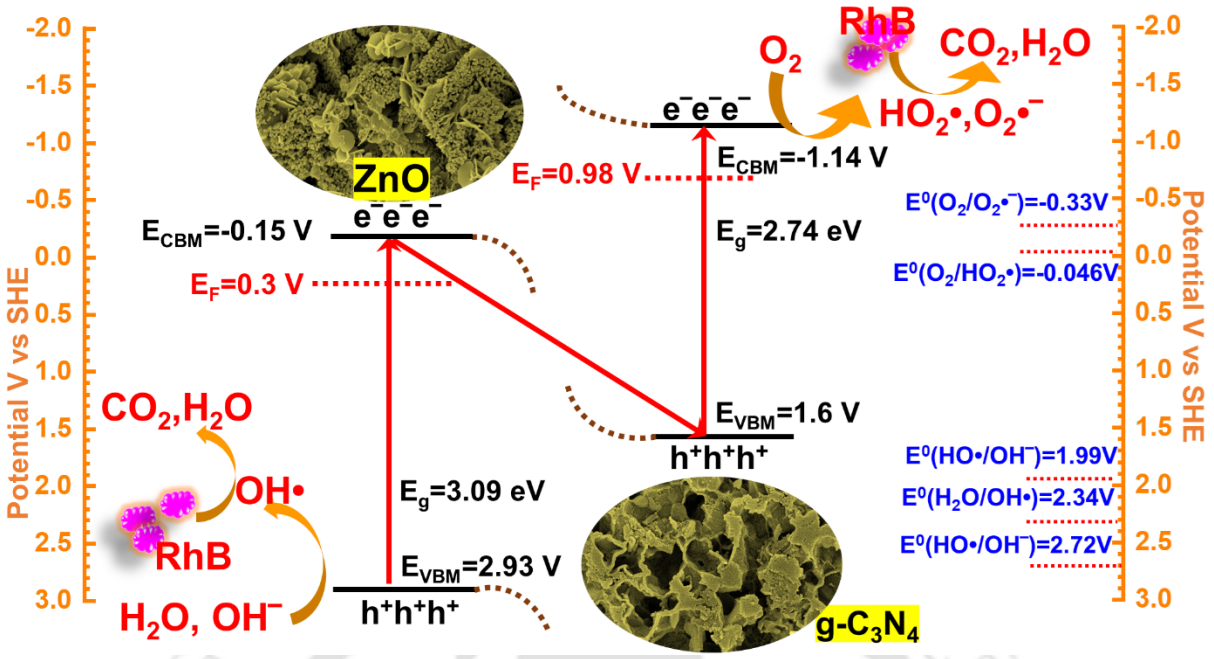


*Figure 5.2.10. Schematic diagrams of the energy-level distribution forming Z-scheme charge transfer in the g-$C_3N_4$/ZnO heterojunction interface for the photocatalytic degradation of RhB*

To understand deeply the energy level positions for the individual photocatalyst g-$C_3N_4$ and ZnO, and gain an insight into the charge transfer phenomena in the g-$C_3N_4$ and ZnO heterojunction formed, an elaborate schematic diagram is displayed in Figure 5.2.10. As the $E_F$ level of g-$C_3N_4$ is lower than the $E_F$ level of ZnO, the $E_{CBM}$ and $E_{VBM}$ of g-$C_3N_4$ bend upward while the band edges of ZnO bend downward in the heterojunction interface. The formation bend bending in the heterostructure interface is due to the differences in the Fermi levels of the contributing photocatalyst[313]. Thus, based on these band bending, the photogenerated charge transfer follows the Z-scheme mechanism where the photogenerated electrons of ZnO are transferred to the valence band of g-$C_3N_4$ causing electron-hole recombination. Z-scheme, a mimic of the natural photosynthesis process is known to improve quantum efficiency by the process of charge carrier recombination with inferior energy levels while maintaining the strong redox abilities of the photogenerated electrons and holes. The direct Z-scheme charge transfer is preferable as compared to the Type-II charge transfer as the charge carrier transportation is difficult in Type-II charge transfer owing to the strong Coulomb repulsion and the redox abilities are thermodynamically unfavorable for surface catalytic reactions[281,282]. Thus, Z-scheme charge transfer perpetuates the reducing ability of g-$C_3N_4$ conduction band electrons and oxidizing ability of ZnO valence band holes at the expense of the recombination of inferior oxidation and reduction ability holes and electrons[281].

From the energy band diagram and Z-scheme charge transfer mechanism in the g-$C_3N_4$ and ZnO heterojunction interface, the band edge positions determined the production of the type of reactive oxygen species by the photogenerated $h^+$s and $e^-$s. In this Z-Scheme, $e^-$s in ZnO are excited to the conduction band when exposed to sunlight leaving $h^+$ in the valence band. These photogenerated $e^-$s are transferred to the valence band of g-$C_3N_4$ and recombined leaving the $e^-$s possessing strong reducing ability in the CB of g-$C_3N_4$ and $h^+$s with strong oxidizing ability in the VB of ZnO. As the $E_{CBM}$ of g-$C_3N_4$ (-1.14 V) is more negative to that of the reduction potentials of $O_2$, i.e., $O_2 + e^- \rightarrow O_2^{\bullet -}$ $[-0.33V]$and $HO_2^{\bullet}[-0.046V]$, the $e^-$s in the CB of g-$C_3N_4$ reacts with the dissolved $O_2$ generating strong ROS: $O_2^{\bullet -}$ and $HO_2^{\bullet}$. The $E_{VBM}$ of ZnO is more positive (2.93 V) than the oxidation potential of $H_2O$ and OH•, i.e., $H_2O + h^+ \rightarrow OH^{\bullet}$ $[2.34\ V], HO^{\bullet} + h^+ \rightarrow HO^-[1.99\ V]$.[284,309,313] This charge transfer mechanism and production of the ROS for AOP supports and explains the increase in photocatalytic degradation of RhB in presence of g-$C_3N_4$ with the addition of IPA as the $h^+$ and HO• scavengers. The added IPA scavenges the photogenerated $h^+$s leaving es in the CB that has a strong reducing ability of $O^2$ thus generating more amount of superoxide ($O_2^{\bullet -}$) and hydroxide radicals ($HO_2^{\bullet}$) with additional $e^-$s donated by IPA to attack the unsaturated bonds of RhB thus degraded in time. Similarly, in the case of ZnO, with the addition of $H_2O_2$ in the reaction medium, $e^-$s are scavenged thus leaving $h^+$s with a strong oxidizing ability to produce HO• radicals. Thus, in conclusion, with the Z-scheme charge transfer in the g-$C_3N_4$/ZnO heterojunction interface, photogenerated $e^-$s and $h^+$s played a crucial role in the g-$C_3N_4$ and ZnO respectively for the photocatalytic degradation of RhB under natural sunlight.

### ***5.2.6 Key findings of Part B***

- In this part, g-$C_3N_4$ was prepared by a simple thermal polymerization process while ZnO was prepared by a solvothermal method using DMF solvent. The binary photocatalyst g-$C_3N_4$/ZnO, ZnO/SWCNT, g-$C_3N_4$/SWCNT, and ternary photocatalyst g-$C_3N_4$/ZnO/SWCNT were prepared by simple sonication process that showed responsive to natural sunlight.
- From the energy band structures and positions of the individual photocatalyst g-$C_3N_4$ and ZnO estimated using Tauc plot and UPS spectra, the g-$C_3N_4$/ZnO heterojunction interface showed Z-scheme charge transfer pathways.
- In the presence of g-$C_3N_4$, under natural sunlight, the addition of IPA enhances the efficiency from 95% to 99% with 1 ml, 0.7 ml, and 0.5 ml. And degradation efficiency of g-$C_3N_4$+(0.5 ml) $H_2O_2$ is higher (98%) as compared to that of bare g-$C_3N_4$ (96%).

- In the case of ZnO, with the addition of 0.5 ml of IPA and $H_2O_2$, the degradation efficiencies are decreased from 82% to 36% and 46% respectively.
- The Fermi energy level of the g-$C_3N_4$/ZnO composite was found to be higher than g-$C_3N_4$ and lower than that of ZnO, evidence of charge transfer acting as an electron donor-acceptor. In the Z-scheme charge transfer in the g-$C_3N_4$/ZnO heterojunction interface, photogenerated $e^-$s and $h^+$s played a crucial role in the g-$C_3N_4$ and ZnO respectively for the photocatalytic degradation of RhB under natural sunlight.
- This reporting degradation experiment method exempted the use of an external triggering light source and continuous stirring process during the reaction process, thus overcoming the energy consumption setback and reducing cost consumption while using cheap and less toxic photocatalysts— ZnO and carbon-based photocatalysts.

## 5.3 Conclusion

- $ZnO/Fe_3O_4$ and $ZnO/TiO_2$ composite heterostructures formed heterojunction interface forming Type I and Type II heterojunction interface, while the $g\text{-}C_3N_4/ZnO$ heterojunction interface showed Z-scheme charge transfer pathways.
- Z-scheme charge transfer showed greater photocatalytic performance than Type I and Type II composite heterostructures.
- The formation of different charge transfer pathways affects the photocatalytic performance. Designing a composite heterostructure interface enhances charge carrier lifetimes thus the efficiencies.
- The dominant ROS species for the AOP is determined by the band edge positions with respect to the oxidation and reduction potentials.

# Chapter 6

# Comparative study on photocatalyst performance

In this chapter, the photocatalytic performance of the nanoparticles synthesized has been compared in a categorized manner. The experiments for this performance comparison are performed under similar conditions using different photocatalysts and are shown in Figure 6.1 for UV light exposure and Figure 6.2 for the natural sunlight exposure experiment.

## 6.1 Comparison of photocatalyst performance under UV light illumination

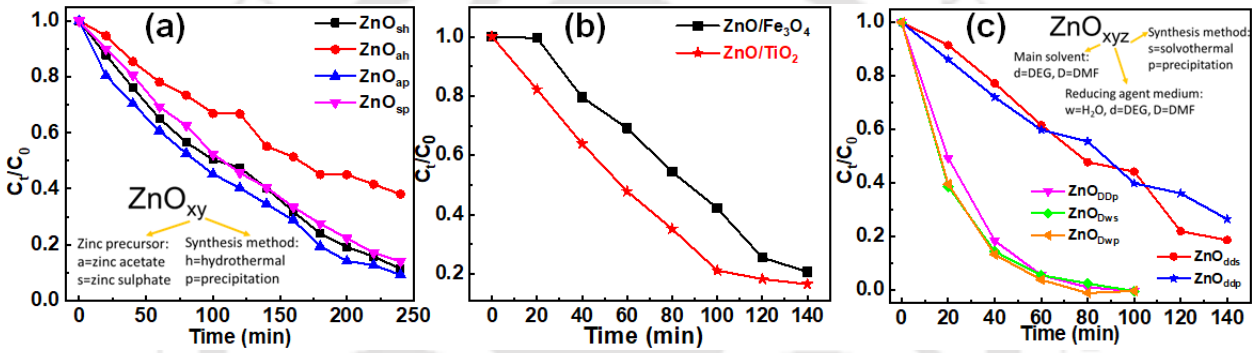


*Figure 6.1 Photocatalytic degradation curve under the UV-light illumination in the presence of (a) ZnO with zinc precursor and synthesis method variation, (b) ZnO/$Fe_3O_4$ & ZnO/$TiO_2$ heterostructure composites, and (c) ZnO from different solvents and synthesis method*

### ***6.1.1 Summary***

- With the use of different zinc precursors in two different synthesis methods, the $ZnO_{ap}$ synthesized using zinc acetate precursor in the precipitate method gave the highest photocatalytic efficiency at the given 250 min because of the lowest crystallite size.
- With the ZnO composite formation with $TiO_2$ and $Fe_3O_4$, ZnO/$TiO_2$ showed higher performance than ZnO/$Fe_3O_4$ at 140 min of illumination due to the presence of defects and faster electron diffusion from the ZnO to the $TiO_2$. This may also be due to the exposure of the surface for oxidation and reduction reaction, unlike ZnO/$Fe_3O_4$ which includes only one surface for redox reaction.
- With the use of different solvents for ZnO preparation, the ZnO prepared using DMF solvent gave the highest degradation efficiency at 100 min of exposure irrespective of the synthesis method. This is due to the synergy of the formation of flower-like structures,

crystal defects, and surface defects that are formed by the liberation of the DMF or its derivatives attached to the nanoparticle surface through calcination.

Thus, from all the analysis and comparison, DMF solvent was selected as the best parameter to influence the photocatalytic efficiency with the zinc acetate source.

## 6.2 Comparison of photocatalyst performance under natural sunlight

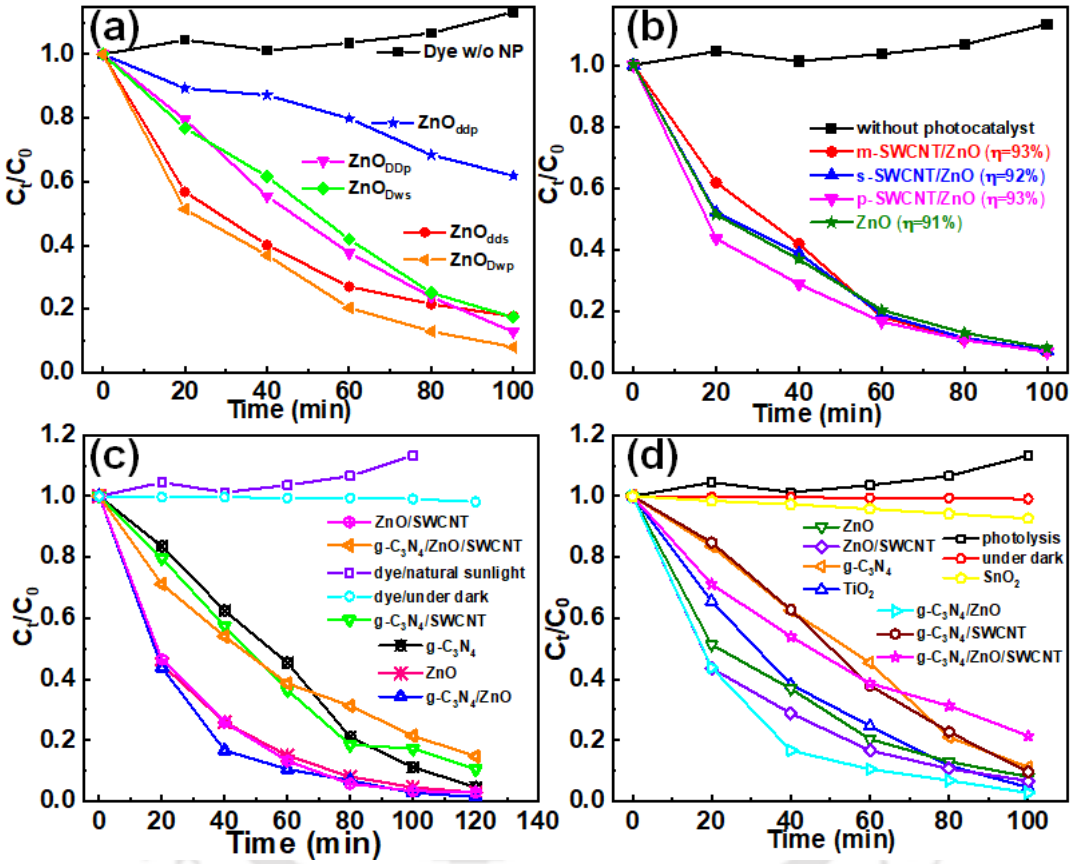


*Figure 6.2 Photocatalytic degradation curve under sunlight illumination in the presence of (a) ZnO from different solvents and synthesis methods, (b) ZnO self-assembled on three different SWCNTs, (c) ZnO-based composites, and (d) overall comparison with other photocatalysts*

### ***6.2.1 Summary***

- Under natural sunlight, with the use of different ZnO synthesized using different solvents (DEG, DMF) and methods (precipitation, solvothermal), ZnO prepared using DMF solvent following the precipitation method showed the highest performance for a given period of 100 min. This is due to the synergy of the formation of flower-like structures, crystal defects, and surface defects that are formed by the liberation of the DMF or its derivatives attached to the nanoparticle surface through calcination.

- With the use of three electronically different SWCNTs (metallic, semiconducting, and pristine-SWCNTs), the formation of ZnO self-assembled onto different SWCNTs showed an increase in degradation performances with different degradation rates. This may be due to the charge transfer between SWCNTs and ZnO with the formation of a heterojunction interface and the difference in the charge transfer rates owing to the different and unique properties of SWCNTs.
- With the use of ZnO/g-$C_3N_4$ photocatalyst and the formation of Z-scheme charge transfer in this heterojunction interface, the photocatalytic efficiencies are increased as compared with the individual photocatalyst and other composites. This is due to the increase in charge carriers' lifetimes owing to their charge transfer and the involvement of both ZnO and g-$C_3N_4$ photocatalyst surfaces for oxidation and reduction reactions.

Therefore, from the comparison it is concluded that ZnO nanoparticles prepared using DMF solvent are also responsive to natural sunlight and with the ZnO/SWCNT heterostructure composite formation, the performances are also increasing. ZnO nanoparticles in forming composites with another semiconductor oxide g-$C_3N_4$ give higher degradation efficiency. The photocatalytic efficiency depends upon the charge transfer pathways and the involvement of the photocatalyst surface for the photo-redox reactions.

# Chapter 7

# Concluding remarks and Future prospects

## 7.1 Conclusion

The objective of this thesis was to contribute towards an enhanced understanding of the charge transfer dynamics in heterostructure photocatalysts and tuning nanoparticle properties of the common transition metal oxide-based composites for photocatalytic advanced oxidation process under natural sunlight. To this end, the ZnO semiconductor was examined from the basic understanding and tuning by the chemical synthesis method. The role of defects: surface or crystal defects on the charge transfer and recombination is discussed with the synthesis of induced surface defects. Focus was placed on the charge transfer dynamics in the heterostructure interface of ZnO-SWCNT photocatalyst and the impact of different electronic properties of SWCNTs on charge transfer. To elucidate the difference in charge transfer and photocatalytic degradation performance, other composites and carbon-based semiconductor oxide photocatalysts are also prepared: ZnO@$TiO_2$, ZnO@$Fe_3O_4$, and ZnO/g-$C_3N_4$.

The first part of the **3rd chapter** discusses the biosynthesis growth mechanism of ZnO nanoparticles, using plant-based extracts as reducing agents: lemon fruit and aloe vera extracts. The nanoparticles are prepared by two different synthesis approaches facile chemical and hydrothermal processes with two different zinc sources: zinc acetate ($Zn(CH_3COO)_2.2H_2O$) and zinc sulphate ($ZnSO_4.7H_2O$). The ZnO-biomolecule complex is formed when $Zn^{2+}$ ions generated by dissociating zinc source link with the biomolecules through the metal ions and functional groups of biomolecules. In the second part of the 3rd chapter, different ZnO nanoparticles are synthesized from different zinc sources and synthesis methods. ZnO synthesized from the hydrothermal method and $Zn(CH_3COO)_2.2H_2O$ source shows the largest crystallite size and ZnO synthesized from $ZnSO_4.7H_2O$ source with precipitation method shows the smallest crystallite size. On the contrary, ZnO nanoparticles prepared via the precipitation method show lesser crystallite sizes as compared with the hydrothermal method which concludes that the maintenance of the same temperature and pressure inside a hydrothermal led to the rapid growth of ZnO crystal. The last part of this chapter highlights the formation of induced surface defects with the use of DMF solvents which are reaction active sites. This part overcomes three most significant challenges to the implementation of

photocatalytic water treatment: (a) the development of natural sunlight-active ZnO photocatalyst, (b) replacing slurry photocatalytic process by floating photocatalyst removing the controversy of photocatalyst retrieval, (c) re-use of face-mask fabric coated with ZnO photocatalyst for dye degradation. The use of different solvents results in obtaining different ZnO morphologies- nano aggregates, cauliflower, and hydrangea flower-like structures sited along with their building blocks. The ZnO photocatalysts are dip-coated on the face-mask fabric used as a floating photocatalyst for RhB degradation under natural sunlight illumination, thus removing the additional process of the photocatalyst retrieval process. A degradation efficiency of 91% dye removal in 100 min is obtained as compared with the slurry system triggered by UV light illumination of 99% by the ZnO samples prepared in DMF solvent. ZnO photocatalysts synthesized using DMF solvent show natural sunlight responsiveness, better performance, and degradation rate due to the synergy of the formation of surface defects, oxygen interstitial, open sites, and higher surface exposure by the petal-like structures.

In the **4$^{th}$ chapter**, interactions between three electronically different SWCNT and ZnO nanoparticles are analyzed with the charge transfer analysis for the AOP. In the first part, three electronically and optically different types of SWCNTs: metallic (m), semiconducting (s), and pristine (p) are functionalized by ZnO using a facile sonication method. In the functionalization and composites formation, ZnO sub-nano particles are attached and anchored on SWCNT surfaces, thereby exhibiting distortion-dislocation and strain. Due to the charge transfer and interaction between SWCNTs and ZnO, the carrier lifetimes were increased by ~1 ns, and an increase in metallicity is seen in s-SWCNT+ZnO. The carrier lifetime value of p-SWCNT+ZnO (4.24 ns) lies in-betweens s-SWCNT+ZnO (4.76 ns) and m-SWCNT+ZnO, (4.62 ns) because of the mixed presence of m-SWCNT and s-SWCNT in p-SWCNT. In the second part of the 4$^{th}$ chapter, ZnO nanoparticles are self-assembled onto three electronically different SWCNTs, and their charge transfer dynamics are investigated in Chapter 5. The defects created are found to enhance the photocatalytic degradation efficiency of RhB by achieving complete degradation in 100 mins under natural sunlight by using face-mask fabric coated with ZnO and SWCNT/ZnO heterostructures. Charge transfer and separation are observed and evident in the SWCNT/ZnO heterostructures, as measured by an increase in charge carrier lifetimes calculated from the TRPL and ESR analyses. This increase in charge carrier lifetimes enhances RhB degradation, and the highest degradation rate of 0.0278 min$^{-1}$ is obtained by using floating face mask fabrics coated with m-SWCNT/ZnO heterostructures. The photocatalytic degradation effectiveness is shown to have minimal influence on

photocatalyst dosages by the s-SWCNT/ZnO heterostructure. By showing 99% degradation efficiency in direct sunlight after the 5$^{th}$ cycle, the generated samples—ZnO and SWCNT/ZnO heterostructures—are discovered to be stable and recyclable.

In the **5$^{th}$ chapter**, different charge transfer mechanisms are studied-Type I, Type II, and Z-scheme charge transfer with the ZnO-based heterostructure composites. In the first part of this chapter, two composites: ZnO/$Fe_3O_4$ and ZnO/$TiO_2$ are synthesized using the precipitation method using the procured $TiO_2$ and $Fe_3O_4$ nanoparticles, and their charge transfer mechanisms are analyzed. In the ZnO/$TiO_2$ and ZnO/$Fe_3O_4$ composite heterostructures, ZnO nanoparticles show the highest particle sizes of 100-180 nm clusters while the $TiO_2$ and $Fe_3O_4$ nanoparticles are aggregated. Analysis showed the formation of a heterojunction interface with the non-changing oxidation states of the elements in the XPS analysis of the composites. The Type II ZnO/$TiO_2$ composite shows greater photocatalytic performance as compared to that of Type I ZnO/$Fe_3O_4$. The higher photodegradation rate of 0.014 min$^{-1}$ of ZnO/$TiO_2$ is due to the presence of defects or distortion mid-gaps and faster electron diffusion from the ZnO to $TiO_2$. Further, oxidation and reduction are assumed to occur in both the semiconductor surfaces as described by the Type II charge transfer mechanism. The lower photodegradation rate of 0.011 min$^{-1}$ by using ZnO/$Fe_3O_4$ photocatalyst is possibly due to the one surface participation in the photocatalytic redox reaction. Also, the larger energy band level difference between ZnO and $Fe_3O_4$ in the heterojunction interface may have slowed down the charge transfer diffusion in the heterostructure interface. In the second part of the 5$^{th}$ chapter, ZnO, g-$C_3N_4$, ZnO/SWCNT, ZnO/g-$C_3N_4$, g-$C_3N_4$/SWCNT, and ternary composite ZnO/SWCNT/g-$C_3N_4$ are prepared by a facile chemical synthesis process and sonication method. A hypothesis on the Z-scheme charge transfer dynamics formed in the ZnO/g-$C_3N_4$ heterojunction interface is depicted in this work for photocatalytic advanced oxidation process for water treatment applications. The prepared photocatalyst showed responsiveness to natural sunlight. From the energy band structures and positions of the individual photocatalyst g-$C_3N_4$ and ZnO estimated using Tauc plot and UPS spectra, the g-$C_3N_4$/ZnO heterojunction interface showed Z-scheme charge transfer pathways. In the presence of g-$C_3N_4$, under natural sunlight, the addition of IPA enhances the efficiency from 95% to 99% with 1 ml, 0.7 ml, and 0.5 ml. And degradation efficiency of g-$C_3N_4$+(0.5 ml) $H_2O_2$ is higher (98%) as compared to that of bare g-$C_3N_4$ (96%). In the case of ZnO, with the addition of 0.5 ml of IPA and $H_2O_2$, the degradation efficiencies are decreased from 82% to 36% and 46% respectively. The Fermi energy level of the g-$C_3N_4$/ZnO composite was found to be higher than g-$C_3N_4$ and lower than that of ZnO, evidence of charge transfer acting as an

electron donor-acceptor. In the Z-scheme charge transfer in the g-$C_3N_4$/ZnO heterojunction interface, photogenerated $e^-$s and $h^+$s played a crucial role in the g-$C_3N_4$ and ZnO respectively for the photocatalytic degradation of RhB under natural sunlight. This reporting degradation experiment method exempted the use of an external triggering light source and continuous stirring process during the reaction process, thus overcoming the energy consumption setback and reducing cost consumption while using cheap and less toxic photocatalysts— ZnO and carbon-based photocatalysts.

## 7.2 Prospects

This dissertation shows that a photocatalytic advanced oxidation process using a ZnO-based photocatalyst can be an effective method for cleaning water by removing organic compounds. A thorough investigation of the properties, modifications, and uses of ZnO was provided. ZnO has received the most research attention among the numerous different photocatalysts for a long time and has also been employed in this thesis. ZnO is known for its non-toxicity, cheap, easily tuneable properties, and its wide range of applications. However, its uses are limited by its wide-bandgap energy and high photogenerated charge carrier recombination. In this thesis, the surface, physical, chemical, and optical properties of ZnO are being modified by optimizing the ZnO synthesis parameters which resulted in exhibiting responsiveness to natural sunlight for effective AOP. Also, this work showed the successful use of a face mask as the photocatalyst anchoring substrate for the floating photocatalyst of AOP under natural sunlight. This opens the possibility of using in the large-scale application of ZnO nanomaterial through the slurry system or floating photocatalyst with the incorporation of membrane technology for efficient performance. With the use of g-$C_3N_4$, the ZnO/g-$C_3N_4$ composites showed the highest efficiency and were responsive to natural sunlight. This also provides a new way of using cheap nanomaterials for photocatalytic water treatment in large-scale applications.

## 7.3 Research articles published based on the thesis work

***Research article***

(i) D.D. Thongam, H. Chaturvedi, Functionalization of Pristine, Metallic, and Semiconducting-SWCNTs by ZnO for Efficient Charge Carrier Transfer: Analysis through Critical Coagulation Concentration, ACS Omega. (2022). *https://doi.org/10.1021/acsomega.2c00193*.

(ii) D.D. Thongam, H. Chaturvedi, Induced defect and ZnO nano-flower formation by N, N, dimethylformamide solvent for natural sunlight responsive floating photocatalytic advanced oxidation process, Chemosphere. 313 (2023) 137600. *https://doi.org/10.1016/j.chemosphere.2022.137600*.

(iii) D.D. Thongam, H. Chaturvedi, Heterostructure charge transfer dynamics on self-assembled ZnO on electronically different single-walled carbon nanotubes, Chemosphere. 323 (2023) 138239. *https://doi.org/10.1016/j.chemosphere.2023.138239.*

***Review article***

*(i) Thongam, D. D., & Chaturvedi, H. (2021). Advances in nanomaterials for heterogeneous photocatalysis. Nano Express, 2(1), 012005. https://doi.org/10.1088/2632-959x/abeb8d*

***Conference Proceeding***

*(i) Thongam, D. D., & Chaturvedi, H. (2020). Effect of biochemical compounds on ZnO nanomaterial preparation using aloe vera and lemon extracts. Materials Today: Proceedings, 44, 4299–4304. https://doi.org/10.1016/j.matpr.2020.10.548*

*(ii) Thongam, D. D., & Chaturvedi, H. (2021). Self-assembled ZnO nanomaterials on single-walled carbon nanotube surfaces for heterogeneous catalysis. ACS Spring Meeting 2021, https://doi.org/10.1021/scimeetings.1c00802*

***Book Chapter***

*(i) Thongam, D. D., & Chaturvedi, H. (2021). Chapter 12 - Nanomaterials for climate change and water pollution mitigation (B. Thokchom, P. Qiu, P. Singh, & P. K. B. T.-W. C. in the E. of G. C. C. Iyer (eds.); pp. 277–314). Elsevier. https://doi.org/https://doi.org/10.1016/B978-0-12-820200-5.00005-1*

***Submitted***

*(i) Thongam, D. D.; Chaturvedi, H. Understanding Charge Carrier Dynamics in Type I and Type II composite Heterostructures for photocatalysis: ZnO@$TiO_2$, ZnO@$Fe_3O_4$*

*(ii) Thongam, D. D.; Chaturvedi, H. Charge transfer dynamics in binary g-$C_3N_4$/ZnO and ternary photocatalyst g-$C_3N_4$/ZnO/SWCNT activated by natural sunlight heterojunction interface*

## Reference


1. Fujishima, A. & Honda, K. Electrochemical photolysis of water at a semiconductor electrode. *Nature* **238**, 37–38 (1972).

2. Kamat, P. V. Quantum Dot Solar Cells. Semiconductor Nanocrystals as Light Harvesters. *J. Phys. Chem. C* **112**, 18737–18753 (2008).

3. Tasbihi, M. *et al.* Photocatalytic reduction of CO2 to hydrocarbons by using photodeposited Pt nanoparticles on carbon-doped titania. *Catal. Today* **328**, 8–14 (2019).

4. Herrmann, J.-M. Heterogeneous photocatalysis: fundamentals and applications to the removal of various types of aqueous pollutants. *Catal. Today* **53**, 115–129 (1999).

5. Li, J. & Zhang, J. Z. Optical properties and applications of hybrid semiconductor nanomaterials. *Coord. Chem. Rev.* **253**, 3015–3041 (2009).

6. Sudhagar, P. *et al.* Exploring Graphene Quantum Dots/TiO2 interface in photoelectrochemical reactions: Solar to fuel conversion. *Electrochim. Acta* **187**, 249–255 (2016).

7. Latthe, S. S. *et al.* A mechanically bendable superhydrophobic steel surface with self-cleaning and corrosion-resistant properties. *J. Mater. Chem. A* **3**, 14263–14271 (2015).

8. Faraldos, M., Kropp, R., Anderson, M. A. & Sobolev, K. Photocatalytic hydrophobic concrete coatings to combat air pollution. *Catal. Today* **259**, 228–236 (2016).

9. Rodenas, P. *et al.* Quantum Dot Based Heterostructures for Unassisted Photoelectrochemical Hydrogen Generation. *Adv. Energy Mater.* **3**, 176–182 (2013).

10. Gupta, J., Bhargava, P. & Bahadur, D. Fluorescent ZnO for imaging and induction of DNA fragmentation and ROS-mediated apoptosis in cancer cells. *J. Mater. Chem. B* **3**, 1968–1978 (2015).

11. Rozhkova, E. A. *et al.* A High-Performance Nanobio Photocatalyst for Targeted Brain Cancer Therapy. *Nano Lett.* **9**, 3337–3342 (2009).

12. Singh, S. & Tandon, P. Catalysis: A brief review on Nano-Catalyst. *J. Energy Chem. Eng.* **2**, 106–115 (2014).

13. Thongam, D. D., Gupta, J., Sahu, N. K. & Bahadur, D. Investigating the role of different reducing agents, molar ratios, and synthesis medium over the formation of ZnO nanostructures and their photo-catalytic activity. *J. Mater. Sci.* **53**, 1110–1122 (2018).

14. Gupta, J. & Bahadur, D. Visible Light Sensitive Mesoporous Cu-Substituted ZnO Nanoassembly for Enhanced Photocatalysis, Bacterial Inhibition, and Noninvasive Tumor Regression. *ACS Sustain. Chem. Eng.* **5**, 8702–8709 (2017).

15. Prakash, A. & Bahadur, D. Chemically derived defects in zinc oxide nanocrystals and

their enhanced photo-electrocatalytic activities. *Phys. Chem. Chem. Phys.* **16**, 21429–21437 (2014).

16. Stock, N. L., Peller, J., Vinodgopal, K. & Kamat, P. V. Combinative sonolysis and photocatalysis for textile dye degradation. *Environ. Sci. Technol.* **34**, 1747–1750 (2000).

17. Peller, J., Wiest, O. & Kamat, P. V. Synergy of combining sonolysis and photocatalysis in the degradation and mineralization of chlorinated aromatic compounds. *Environ. Sci. Technol.* **37**, 1926–1932 (2003).

18. Peleyeju, M. G. *et al.* Photoelectrocatalytic water treatment systems: Degradation, kinetics and intermediate products studies of sulfamethoxazole on a TiO2-exfoliated graphite electrode. *RSC Adv.* **7**, 40571–40580 (2017).

19. Cardenas-Morcoso, D. *et al.* Photocatalytic and Photoelectrochemical Degradation of Organic Compounds with All-Inorganic Metal Halide Perovskite Quantum Dots. *J. Phys. Chem. Lett.* **10**, 630–636 (2019).

20. Luo, X., Zhang, S. & Lin, X. New insights on degradation of methylene blue using thermocatalytic reactions catalyzed by low-temperature excitation. *J. Hazard. Mater.* **260**, 112–121 (2013).

21. Huang, Y. *et al.* Cerium-based hybrid nanorods for synergetic photo-thermocatalytic degradation of organic pollutants. *J. Mater. Chem. A* **6**, 24740–24747 (2018).

22. Li, X., Zhang, G. & Pan, H. Experimental study on ozone photolytic and photocatalytic degradation of H 2S using continuous flow mode. *Journal of Hazardous Materials* vols 199–200 255–261 at https://doi.org/10.1016/j.jhazmat.2011.11.006 (2012).

23. Lindström, B. & Pettersson, L. J. A Brief History of Catalysis. *CATTECH* **7**, 130–138 (2003).

24. Wisniak, J. The History of Catalysis. From the Beginning to Nobel Prizes. *Educ. Química* **21**, 60–69 (2010).

25. Widegren, J. A. & Finke, R. G. A review of the problem of distinguishing true homogeneous catalysis from soluble or other metal-particle heterogeneous catalysis under reducing conditions. *J. Mol. Catal. A Chem.* **198**, 317–341 (2003).

26. Cole-Hamilton, D. J. Homogeneous catalysis - New approaches to catalyst separation, recovery, and recycling. *Science (80-. ).* **299**, 1702–1706 (2003).

27. Mills, A. & Le Hunte, S. An overview of semiconductor photocatalysis. *J. Photochem. Photobiol. A Chem.* **108**, 1–35 (1997).

28. Ravelli, D., Dondi, D., Fagnoni, M. & Albini, A. Photocatalysis. A multi-faceted concept for green chemistry. *Chem. Soc. Rev.* **38**, 1999–2011 (2009).

29. Berardi, S. *et al.* Molecular artificial photosynthesis. *Chem. Soc. Rev.* **43**, 7501–7519 (2014).

30. Yang, X. & Wang, D. Photocatalysis: From Fundamental Principles to Materials and Applications. *ACS Appl. Energy Mater.* **1**, 6657–6693 (2018).

31. Kitsiou, V., Filippidis, N., Mantzavinos, D. & Poulios, I. Heterogeneous and homogeneous photocatalytic degradation of the insecticide imidacloprid in aqueous solutions. *Appl. Catal. B Environ.* **86**, 27–35 (2009).

32. Kositzi, M., Poulios, I., Malato, S., Caceres, J. & Campos, A. Solar photocatalytic treatment of synthetic municipal wastewater. *Water Res.* **38**, 1147–1154 (2004).

33. Jamil, T. S., Roland, H., Michael, H. & Jens-Uwe, R. Homogeneous photocatalytic processes for degradation of some endocrine disturbing chemicals under UV irradiation. *J. Water Process Eng.* **18**, 159–168 (2017).

34. Baur, E. Photolysis and electrolysis. *Helv. Chim. Acta* **1**, 186–201 (1918).

35. Baur, E. The photolysis of methylene blue sensitised by zinc oxide. *Trans. Faraday Soc.* **21**, 627–629 (1926).

36. Egerton, G. S. The role of hydrogen peroxide in the photo-chemical degradation of cotton sensitized by vat dyes and some metallic oxides. *J. Text. Inst. Trans.* **39**, T305–T318 (1948).

37. Egerton, G. S. The Mechanism of the Photochemical Degradation of Textile Material. *J. Soc. Dye. Colour.* **65**, 764–780 (1949).

38. Ashton, D., Clibbens, D. & Probert, M. E. Some Experimental Observations on the Photochemical Degradation of Dyed Cotton. *J. Soc. Dye. Colour.* **65**, 650–658 (1949).

39. Serpone, N. & Emeline, A. V. Semiconductor Photocatalysis — Past, Present, and Future Outlook. *J. Phys. Chem. Lett.* **3**, 673–677 (2012).

40. Emeline, A. V, Kuznetsov, V. N., Ryabchuk, V. K. & Serpone, N. On the way to the creation of next generation photoactive materials. *Environ. Sci. Pollut. Res.* **19**, 3666–3675 (2012).

41. Fresno, F., Portela, R., Suárez, S. & Coronado, J. M. Photocatalytic materials: recent achievements and near future trends. *J. Mater. Chem. A* **2**, 2863–2884 (2014).

42. G M Schwab, and & Gossner, K. Heterogeneous Catalysis. *Annu. Rev. Phys. Chem.* **14**, 177–204 (1963).

43. Serpone, N., Emeline, A. V, Horikoshi, S., Kuznetsov, V. N. & Ryabchuk, V. K. On the genesis of heterogeneous photocatalysis: A brief historical perspective in the period 1910 to the mid-1980s. *Photochemical and Photobiological Sciences* vol. 11 1121–1150 at https://doi.org/10.1039/c2pp25026h (2012).

44. Ren, H., Koshy, P., Chen, W.-F., Qi, S. & Sorrell, C. C. Photocatalytic materials and technologies for air purification. *J. Hazard. Mater.* **325**, 340–366 (2017).

45. Boyjoo, Y., Sun, H., Liu, J., K. Pareek, V. & Wang, S. A Review on Photocatalysis for Air Treatment: From Catalyst Development to Reactor Design. *Chem. Eng. J.* (2016)

doi:10.1016/j.cej.2016.06.090.

46. Gupta, J., Bhargava, P. & Bahadur, D. Morphology dependent photocatalytic and magnetic properties of ZnO nanostructures. *Phys. B Condens. Matter* **448**, 16–19 (2014).

47. Singh, S., Barick, K. C. & Bahadur, D. Fe3O4 embedded ZnO nanocomposites for the removal of toxic metal ions, organic dyes and bacterial pathogens. *J. Mater. Chem. A* **1**, 3325–3333 (2013).

48. Chandrasekaran, S. *et al.* Recent advances in metal sulfides: from controlled fabrication to electrocatalytic, photocatalytic and photoelectrochemical water splitting and beyond. *Chem. Soc. Rev.* **48**, 4178–4280 (2019).

49. Hao, H. & Lang, X. Metal Sulfide Photocatalysis: Visible-Light-Induced Organic Transformations. *ChemCatChem* vol. 11 1378–1393 at https://doi.org/10.1002/cctc.201801773 (2019).

50. Wang, N., Yang, G., Wang, H., Sun, R. & Wong, C.-P. Visible Light-Responsive Photocatalytic Activity of Boron Nitride Incorporated Composites. *Front. Chem.* **6**, (2018).

51. Zeng, Y. *et al.* A three-dimensional graphitic carbon nitride belt network for enhanced visible light photocatalytic hydrogen evolution. *J. Mater. Chem. A* **4**, 19003–19010 (2016).

52. Wilker, M. B., Schnitzenbaumer, K. J. & Dukovic, G. Recent progress in photocatalysis mediated by colloidal II-VI nanocrystals. *Isr. J. Chem.* **52**, 1002–1015 (2012).

53. Zeng, C., Tian, B. & Zhang, J. silver halide/silver iodide@silver composite with excellent visible light photocatalytic activity for methyl orange degradation. *J. Colloid Interface Sci.* **405**, 17–21 (2013).

54. Mac Dougall, J. E. *et al.* Synthesis and Characterization of III-V Semiconductor Clusters: GaP in Zeolite Y. *J. Am. Chem. Soc.* **111**, 8006–8007 (1989).

55. Asahi, R., Morikawa, T., Ohwaki, T., Aoki, K. & Taga, Y. Visible-Light Photocatalysis in Nitrogen-Doped Titanium Oxides. *Science (80-. ).* **293**, 269–271 (2001).

56. Kumar, S. *et al.* Cost-effective and eco-friendly synthesis of novel and stable N-doped ZnO/g-C3N4 core-shell nanoplates with excellent visible-light responsive photocatalysis. *Nanoscale* **6**, 4830–4842 (2014).

57. Riaz, R. *et al.* Self-assembled nitrogen-doped graphene quantum dots (N-GQDs) over graphene sheets for superb electro-photocatalytic activity. *Appl. Surf. Sci.* **480**, 1035–1046 (2019).

58. Zhuo, S., Shao, M. & Lee, S.-T. Upconversion and Downconversion Fluorescent Graphene Quantum Dots: Ultrasonic Preparation and Photocatalysis. *ACS Nano* **6**, 1059–1064 (2012).

59. Jiang, J., Li, H. & Zhang, L. New Insight into Daylight Photocatalysis of AgBr@Ag: Synergistic Effect between Semiconductor Photocatalysis and Plasmonic Photocatalysis. *Chem. – A Eur. J.* **18**, 6360–6369 (2012).

60. Kale, M. J., Avanesian, T. & Christopher, P. Direct photocatalysis by plasmonic nanostructures. *ACS Catal.* **4**, 116–128 (2014).

61. Wang, C., Xie, Z., Dekrafft, K. E. & Lin, W. Doping metal-organic frameworks for water oxidation, carbon dioxide reduction, and organic photocatalysis. *J. Am. Chem. Soc.* **133**, 13445–13454 (2011).

62. Magalhães, F., Moura, F. C. C. & Lago, R. M. TiO2/LDPE composites: A new floating photocatalyst for solar degradation of organic contaminants. *Desalination* **276**, 266–271 (2011).

63. Kalam, A. *et al.* Modified solvothermal synthesis of cobalt ferrite (CoFe2O4) magnetic nanoparticles photocatalysts for degradation of methylene blue with H2O2/visible light. *Results Phys.* **8**, 1046–1053 (2018).

64. Tang, J. & Ye, J. Correlation of crystal structures and electronic structures and photocatalytic properties of the W-containing oxides. *J. Mater. Chem.* **15**, 4246–4251 (2005).

65. Yoshida, T., Yamaguchi, A., Umezawa, N. & Miyauchi, M. Photocatalytic CO2 Reduction Using a Pristine Cu2ZnSnS4 Film Electrode under Visible Light Irradiation. *J. Phys. Chem. C* **122**, 21695–21702 (2018).

66. Gupta, J., Barick, K. C. & Bahadur, D. Defect mediated photocatalytic activity in shape-controlled ZnO nanostructures. *J. Alloys Compd.* **509**, 6725–6730 (2011).

67. Kuriakose, S. *et al.* Facile synthesis of Au-ZnO plasmonic nanohybrids for highly efficient photocatalytic degradation of methylene blue. *Opt. Mater. (Amst).* **64**, 47–52 (2017).

68. Chithambararaj, A., Sanjini, N. S., Bose, A. C. & Velmathi, S. Flower-like hierarchical h-MoO3: New findings of efficient visible light driven nano photocatalyst for methylene blue degradation. *Catal. Sci. Technol.* **3**, 1405–1414 (2013).

69. Jiang, B. *et al.* Core-shell structure CdS/TiO2 for enhanced visible-light-driven photocatalytic organic pollutants degradation. *J. Sol-Gel Sci. Technol.* **66**, 504–511 (2013).

70. Rani, B., Punniyakoti, S. & Sahu, N. K. Polyol asserted hydrothermal synthesis of SnO2 nanoparticles for the fast adsorption and photocatalytic degradation of methylene blue cationic dye. *New J. Chem.* **42**, 943–954 (2018).

71. Hu, H., Chang, M., Wang, X. & Chen, D. Cotton fabric-based facile solar photocatalytic purification of simulated real dye wastes. *J. Mater. Sci.* **52**, 9922–9930 (2017).

72. Sboui, M., Nsib, M. F., Rayes, A., Swaminathan, M. & Houas, A. TiO2–PANI/Cork composite: A new floating photocatalyst for the treatment of organic pollutants under

sunlight irradiation. *J. Environ. Sci. (China)* **60**, 3–13 (2017).

73. Schneider, J. *et al.* Understanding TiO2 Photocatalysis: Mechanisms and Materials. *Chem. Rev.* **114**, 9919–9986 (2014).

74. Fox, M. A. & Dulay, M. T. Heterogeneous Photocatalysis. *Chem. Rev.* **93**, 341–357 (1993).

75. Linsebigler, A. L., Lu, G. & Yates, J. T. Photocatalysis on TiO2 Surfaces: Principles, Mechanisms, and Selected Results. *Chem. Rev.* **95**, 735–758 (1995).

76. Rauf, M. A., Meetani, M. A. & Hisaindee, S. An overview on the photocatalytic degradation of azo dyes in the presence of TiO2 doped with selective transition metals. *Desalination* vol. 276 13–27 at https://doi.org/10.1016/j.desal.2011.03.071 (2011).

77. Pera-Titus, M., García-Molina, V., Baños, M. A., Giménez, J. & Esplugas, S. Degradation of chlorophenols by means of advanced oxidation processes: A general review. *Appl. Catal. B Environ.* **47**, 219–256 (2004).

78. Emin, S. *et al.* Photoelectrochemical properties of cadmium chalcogenide-sensitized textured porous zinc oxide plate electrodes. *ACS Appl. Mater. Interfaces* **5**, 1113–1121 (2013).

79. Thongam, D. D. D. D., Gupta, J. & Sahu, N. K. N. K. Effect of induced defects on the properties of ZnO nanocrystals: surfactant role and spectroscopic analysis. *SN Appl. Sci.* **1**, 1–14 (2019).

80. Barick, K. C. *et al.* Effect of cetylpyridinium chloride on surface passivation and photocatalytic activity of ZnO nanostructures. *Journal of Environmental Chemical Engineering* vol. 3 1346–1355 at https://doi.org/10.1016/j.jece.2014.12.007 (2015).

81. Demchenko, A. Excitons in Carbonic Nanostructures. *C — J. Carbon Res.* **5**, 71 (2019).

82. Loeb, S. K. *et al.* The Technology Horizon for Photocatalytic Water Treatment: Sunrise or Sunset? *Environ. Sci. Technol.* **53**, 2937–2947 (2019).

83. Cates, E. L. Photocatalytic water treatment: So where are we going with this? *Environ. Sci. Technol.* **51**, 757–758 (2017).

84. Musial, J., Mlynarczyk, D. T. & Stanisz, B. J. Photocatalytic degradation of sulfamethoxazole using TiO2-based materials – Perspectives for the development of a sustainable water treatment technology. *Sci. Total Environ.* **856**, 159122 (2023).

85. Xue, Y. *et al.* Immobilization of photocatalytic materials for (waste)water treatment using 3D printing technology – advances and challenges. *Environ. Pollut.* **316**, 120549 (2023).

86. Baaloudj, O. *et al.* Techno-economic studies for a pilot-scale Bi12TiO20 based photocatalytic system for pharmaceutical wastewater treatment: From laboratory studies to commercial-scale applications. *J. Water Process Eng.* **48**, 102847 (2022).

87. Wang, D. *et al.* Engineering and modeling perspectives on photocatalytic reactors for water treatment. *Water Res.* **202**, 117421 (2021).

88. Jorge, N., Teixeira, A. R., Lucas, M. S. & Peres, J. A. Combined organic coagulants and photocatalytic processes for winery wastewater treatment. *J. Environ. Manage.* **326**, (2023).

89. Arabkhani, P. *et al.* Plant extracts-mediated green synthesis of zinc oxide/carbon nanofiber nanocomposites with highly efficient photocatalytic and antimicrobial properties for wastewater treatment. *J. Water Process Eng.* **54**, 104020 (2023).

90. Kumar, R. *et al.* Integrating K and P co-doped g-C3N4 with ZnFe2O4 and graphene oxide for S-scheme-based enhanced adsorption coupled photocatalytic real wastewater treatment. *Chemosphere* **337**, 139267 (2023).

91. Lin, Q. *et al.* Self-cleaning photocatalytic MXene composite membrane for synergistically enhanced water treatment: Oil/water separation and dyes removal. *Chem. Eng. J.* **427**, 131668 (2022).

92. Mendes-Felipe, C., Veloso-Fernández, A., Vilas-Vilela, J. L. & Ruiz-Rubio, L. Hybrid Organic–Inorganic Membranes for Photocatalytic Water Remediation. *Catalysts* **12**, 1–19 (2022).

93. Horváth, E. *et al.* Solar water purification with photocatalytic nanocomposite filter based on TiO2 nanowires and carbon nanotubes. *npj Clean Water* **5**, 1–11 (2022).

94. Borges, M. E., de Paz Carmona, H., Gutiérrez, M. & Esparza, P. Photocatalytic Removal of Water Emerging Pollutants in an Optimized Packed Bed Photoreactor Using Solar Light. *Catalysts* **13**, (2023).

95. Banoo, M. *et al.* Universal Piezo-Photocatalytic Wastewater Treatment on Realistic Pollutant Feedstocks by Bi4TaO8Cl: Origin of High Efficiency and Adjustable Synergy. *ACS Appl. Mater. Interfaces* **15**, 32425–32435 (2023).

96. Lu, Y., Zhang, H., Fan, D., Chen, Z. & Yang, X. Coupling solar-driven photothermal effect into photocatalysis for sustainable water treatment. *J. Hazard. Mater.* **423**, (2022).

97. Zhang, C. *et al.* Development of a novel solar energy controllable Linear fresnel photoreactor (LFP) for high-efficiency photocatalytic wastewater treatment under actual weather. *Water Res.* **208**, 117880 (2022).

98. Ameta, R., Solanki, M., Benjamin, S. & Ameta, S. Photocatalysis. in 135–175 (2018). doi:10.1016/B978-0-12-810499-6.00006-1.

99. Xi, G., Yue, B., Cao, J. & Ye, J. *Fe3O4/WO3 Hierarchical Core-Shell Structure: High-Performance and Recyclable Visible-Light Photocatalysis*. vol. 17 (2011).

100. Wang, H. *et al.* Semiconductor heterojunction photocatalysts: Design, construction, and photocatalytic performances. *Chem. Soc. Rev.* **43**, 5234–5244 (2014).

101. Tong, H. *et al.* Nano-photocatalytic Materials: Possibilities and Challenges. *Adv.*

*Mater.* **24**, 229–251 (2012).

102. Yin, W. J. *et al.* Band structure engineering of semiconductors for enhanced photoelectrochemical water splitting: The case of TiO2. *Phys. Rev. B - Condens. Matter Mater. Phys.* **82**, 45106 (2010).

103. Ghasemi, S., Rahimnejad, S., Setayesh, S. R., Rohani, S. & Gholami, M. R. Transition metal ions effect on the properties and photocatalytic activity of nanocrystalline TiO2 prepared in an ionic liquid. *J. Hazard. Mater.* **172**, 1573–1578 (2009).

104. Kamat, P. V. Photophysical, Photochemical and Photocatalytic Aspects of Metal Nanoparticles. *J. Phys. Chem. B* **106**, 7729–7744 (2002).

105. Choi, W., Termin, A. & Hoffmann, M. R. The role of metal ion dopants in quantum-sized TiO2: Correlation between photoreactivity and charge carrier recombination dynamics. *J. Phys. Chem.* **98**, 13669–13679 (1994).

106. Gupta, J. & Bahadur, D. Modulation in band gap and efficient charge separation in Cd substituted ZnO quantum dots with enhanced photocatalytic and antibacterial activity. *Mater. Res. Express* **6**, 045058 (2019).

107. Wang, P., Huang, B., Dai, Y. & Whangbo, M.-H. Plasmonic photocatalysts: harvesting visible light with noble metal nanoparticles. *Phys. Chem. Chem. Phys.* **14**, 9813–9825 (2012).

108. Cushing, S. K. *et al.* Transfer from Metal to Semiconductor. *J. Am. Chem. Soc.* **134**, 15033–15041 (2012).

109. Vaneski, A., Schneider, J., Susha, A. S. & Rogach, A. L. Colloidal hybrid heterostructures based on II-VI semiconductor nanocrystals for photocatalytic hydrogen generation. *Journal of Photochemistry and Photobiology C: Photochemistry Reviews* vol. 19 52–61 at https://doi.org/10.1016/j.jphotochemrev.2013.12.001 (2014).

110. Zhang, W., Wang, M., Zhao, W. & Wang, B. Magnetic composite photocatalyst ZnFe2O4/BiVO4: synthesis, characterization, and visible-light photocatalytic activity. *Dalt. Trans.* **42**, 15464–15474 (2013).

111. Xie, T., Liu, C., Xu, L., Yang, J. & Zhou, W. Novel heterojunction Bi2O3/SrFe12O 19 magnetic photocatalyst with highly enhanced photocatalytic activity. *J. Phys. Chem. C* **117**, 24601–24610 (2013).

112. Moniz, S. J. A., Shevlin, S. A., Martin, D. J., Guo, Z.-X. & Tang, J. Visible-light driven heterojunction photocatalysts for water splitting – a critical review. *Energy Environ. Sci.* **8**, 731–759 (2015).

113. Reddy, P. A. K. *et al.* Recent advances in photocatalytic treatment of pollutants in aqueous media. *Environ. Int.* **91**, 94–103 (2016).

114. Afroz, K., Moniruddin, M., Bakranov, N., Kudaibergenov, S. & Nuraje, N. A heterojunction strategy to improve the visible light sensitive water splitting performance of photocatalytic materials. *J. Mater. Chem. A* **6**, 21696–21718 (2018).

115. Polo, A., Grigioni, I., Dozzi, M. V. & Selli, E. Sensitizing effects of BiVO4 and visible light induced production of highly reductive electrons in the TiO2/BiVO4 heterojunction. *Catal. Today* **340**, 19–25 (2020).

116. Ge, J., Zhang, Y., Heo, Y. J. & Park, S. J. *Advanced design and synthesis of composite photocatalysts for the remediation of wastewater: A review*. *Catalysts* vol. 9 (2019).

117. Li, K. *et al.* A nanostructured CuWO4/Mn3O4 with p/n heterojunction as photoanode toward enhanced water oxidation. *Catal. Today* **335**, 173–179 (2019).

118. Liu, Y. *et al.* Two-dimensional g-C3N4/TiO2 nanocomposites as vertical Z-scheme heterojunction for improved photocatalytic water disinfection. *Catal. Today* **335**, 243–251 (2019).

119. Singh, S., Barick, K. C. & Bahadur, D. Shape-controlled hierarchical ZnO architectures: Photocatalytic and antibacterial activities. *CrystEngComm* **15**, 4631–4639 (2013).

120. Mitchell, E., Law, A. & Godin, R. Interfacial charge transfer in carbon nitride heterojunctions monitored by optical methods. *J. Photochem. Photobiol. C Photochem. Rev.* **49**, 100453 (2021).

121. Mitchell, E., Law, A. & Godin, R. Experimental determination of charge carrier dynamics in carbon nitride heterojunctions. *Chem. Commun.* **57**, 1550–1567 (2021).

122. Yao, Y., Li, G., Ciston, S., Lueptow, R. M. & Gray, K. A. Photoreactive TiO2/Carbon Nanotube Composites: Synthesis and Reactivity. *Environ. Sci. Technol.* **42**, 4952–4957 (2008).

123. Huang, W. *et al.* Constructing novel ternary composites of carbon quantum dots/Bi2MoO6/graphitic nanofibers with tunable band structure and boosted photocatalytic activity. *Sep. Purif. Technol.* **217**, 195–205 (2019).

124. Prakash, A., Singh, S., Gupta, J. & Bahadur, D. Highly efficient zinc oxide-reduced graphene oxide nanohybrids for photocatalytic degradation of dye under dark and UV light. *Mater. Res. Express* **6**, 1250b1 (2020).

125. Dresselhaus, M. S. S., Dresselhaus, G., Jorio, A., Souza Filho, A. G. G. & Saito, R. Raman spectroscopy on isolated single wall carbon nanotubes. *Carbon N. Y.* **40**, 2043–2061 (2002).

126. Vietmeyer, F., Seger, B. & Kamat, P. V. Anchoring ZnO particles on functionalized single wall carbon nanotubes. Excited state interactions and charge collection. *Adv. Mater.* **19**, 2935–2940 (2007).

127. Malekkiani, M., Heshmati Jannat Magham, A., Ravari, F. & Dadmehr, M. Facile fabrication of ternary MWCNTs/ZnO/Chitosan nanocomposite for enhanced photocatalytic degradation of methylene blue and antibacterial activity. *Sci. Rep.* **12**, 1–22 (2022).

128. Kuang, Z. *et al.* Charge Transfer from Photoexcited Semiconducting Single-Walled Carbon Nanotubes to Wide-Bandgap Wrapping Polymer. *J. Phys. Chem. C* **125**, 8125–

8136 (2021).

129. Ghasemipour, P., Fattahi, M., Rasekh, B. & Yazdian, F. Developing the Ternary ZnO Doped MoS2 Nanostructures Grafted on CNT and Reduced Graphene Oxide (RGO) for Photocatalytic Degradation of Aniline. *Sci. Rep.* **10**, 1–16 (2020).

130. Wang, Y. *et al.* Unique hole-accepting carbon-dots promoting selective carbon dioxide reduction nearly 100% to methanol by pure water. *Nat. Commun.* **11**, 1–9 (2020).

131. Zhang, W. De, Jiang, L. C. & Ye, J. S. Photoelectrochemical study on charge transfer properties of ZnO nanowires promoted by carbon nanotubes. *J. Phys. Chem. C* **113**, 16247–16253 (2009).

132. Tatykayev, B. *et al.* Synthesis of core/shell ZnO/RGO nanoparticles by calcination of ZIF-8/RGO composites and their photocatalytic activity. *ACS Omega* **2**, 4946–4954 (2017).

133. Schütt, F., Postica, V., Adelung, R. & Lupan, O. Single and Networked ZnO–CNT Hybrid Tetrapods for Selective Room-Temperature High-Performance Ammonia Sensors. *ACS Appl. Mater. Interfaces* **9**, 23107–23118 (2017).

134. Sampaio, M. J. *et al.* Synergistic effect between carbon nanomaterials and ZnO for photocatalytic water decontamination. *J. Catal.* **331**, 172–180 (2015).

135. Zhu, G. *et al.* A facile synthesis of ZnO/CNT hierarchical microsphere composites with enhanced photocatalytic degradation of methylene blue. *RSC Adv.* **5**, 72476–72481 (2015).

136. Sapkota, K. P., Lee, I., Hanif, M. A., Islam, M. A. & Hahn, J. R. Solar-light-driven efficient zno–single-walled carbon nanotube photocatalyst for the degradation of a persistent water pollutant organic dye. *Catalysts* **9**, 1–15 (2019).

137. Huang, Y. *et al.* Synthesis and characterization of CNT/TiO2/ZnO composites with high photocatalytic performance. *Catalysts* **8**, 1–6 (2018).

138. Prasadam, V. P., Huerta Flores, A. M., Audinot, J.-N. & Bahlawane, N. CNT-ZnO Core-Shell Photoanodes for Photoelectrochemical Water Splitting. *Coatings* **12**, 47 (2022).

139. Chaudhary, D., Singh, S., Vankar, V. D. & Khare, N. ZnO nanoparticles decorated multi-walled carbon nanotubes for enhanced photocatalytic and photoelectrochemical water splitting. *J. Photochem. Photobiol. A Chem.* **351**, 154–161 (2018).

140. Lv, T., Pan, L., Liu, X. & Sun, Z. Enhanced photocatalytic degradation of methylene blue by ZnO-reduced graphene oxide-carbon nanotube composites synthesized via microwave-assisted reaction. *Catal. Sci. Technol.* **2**, 2297–2301 (2012).

141. Byrappa, K. *et al.* Hydrothermal preparation of ZnO:CNT and TiO2:CNT composites and their photocatalytic applications. *J. Mater. Sci.* **43**, 2348–2355 (2008).

142. Arsalani, N., Bazazi, S., Abuali, M. & Jodeyri, S. A new method for preparing ZnO/CNT nanocomposites with enhanced photocatalytic degradation of malachite

green under visible light. *J. Photochem. Photobiol. A Chem.* **389**, 112207 (2020).

143. Bindu, P. & Thomas, S. Estimation of lattice strain in ZnO nanoparticles: X-ray peak profile analysis. *J. Theor. Appl. Phys.* **8**, 123–134 (2014).

144. Khorsand Zak, A., Abd. Majid, W. H., Abrishami, M. E. & Yousefi, R. X-ray analysis of ZnO nanoparticles by Williamson-Hall and size-strain plot methods. *Solid State Sci.* **13**, 251–256 (2011).

145. Chauhan, H. *et al.* Photoinduced ultrafast charge separation in colloidal 2-dimensional CdSe/CdS-Au hybrid nanoplatelets and corresponding application in photocatalysis. *Nanoscale* **8**, 15802–15812 (2016).

146. Liu, J. *et al.* Understanding the Solvent Molecules Induced Spontaneous Growth of Uncapped Tellurium Nanoparticles. *Sci. Rep.* **6**, 32631 (2016).

147. Ramya, R., Nideep, T. K., Nampoori, V. P. N. & Kailasnath, M. Understanding the role of alcohols in the growth behaviour of ZnO nanostructures prepared by solution based synthesis and their application in solar cells. *New J. Chem.* **43**, 17980–17990 (2019).

148. Ramya, M., Nideep, T. K., Nampoori, V. P. N. & Kailasnath, M. Solvent assisted evolution and growth mechanism of zero to three dimensional ZnO nanostructures for dye sensitized solar cell applications. *Sci. Rep.* **11**, 1–14 (2021).

149. Banerjee, P., Satapathy, M., Mukhopahayay, A. & Das, P. Leaf extract mediated green synthesis of silver nanoparticles from widely available Indian plants: Synthesis, characterization, antimicrobial property and toxicity analysis. *Bioresour. Bioprocess.* **1**, 1–10 (2014).

150. Fakhari, S., Jamzad, M. & Kabiri Fard, H. Green synthesis of zinc oxide nanoparticles: a comparison. *Green Chem. Lett. Rev.* **12**, 19–24 (2019).

151. Sai Priya, G., Kanneganti, A., Anil Kumar, K., Venkateswara Rao, K. & Bykkam, S. Bio Synthesis of Cerium Oxide Nanoparticles using Aloe Barbadensis Miller Gel. *Int. J. Sci. Res. Publ.* **4**, 1–4 (2014).

152. Thovhogi, N., Diallo, A., Gurib-Fakim, A. & Maaza, M. Nanoparticles green synthesis by Hibiscus Sabdariffa flower extract: Main physical properties. *Journal of Alloys and Compounds* vol. 647 392–396 at https://doi.org/10.1016/j.jallcom.2015.06.076 (2015).

153. Muthu, K. & Priya, S. Green synthesis, characterization and catalytic activity of silver nanoparticles using Cassia auriculata flower extract separated fraction. *Spectrochimica Acta - Part A: Molecular and Biomolecular Spectroscopy* vol. 179 66–72 at https://doi.org/10.1016/j.saa.2017.02.024 (2017).

154. Nnadozie, E. C. & Ajibade, P. A. Green synthesis and characterization of magnetite (Fe3O4) nanoparticles using Chromolaena odorata root extract for smart nanocomposite. *Materials Letters* vol. 263 at https://doi.org/10.1016/j.matlet.2019.127145 (2020).

155. Suresh, J., Pradheesh, G., Alexramani, V., Sundrarajan, M. & Hong, S. I. Green

synthesis and characterization of zinc oxide nanoparticle using insulin plant (Costus pictus D. Don) and investigation of its antimicrobial as well as anticancer activities. *Adv. Nat. Sci. Nanosci. Nanotechnol.* **9**, (2018).

156. Luque, P. A. *et al.* Green synthesis of zinc oxide nanoparticles using Citrus sinensis extract. *J. Mater. Sci. Mater. Electron.* **29**, 9764–9770 (2018).

157. Hossain, A. *et al.* Lemon-fruit-based green synthesis of zinc oxide nanoparticles and titanium dioxide nanoparticles against soft rot bacterial pathogen dickeya dadantii. *Biomolecules* **9**, (2019).

158. Rasli, N. I., Basri, H. & Harun, Z. Zinc oxide from aloe vera extract: two-level factorial screening of biosynthesis parameters. *Heliyon* **6**, e03156 (2020).

159. Sangeetha, G., Rajeshwari, S. & Venckatesh, R. Green synthesis of zinc oxide nanoparticles by aloe barbadensis miller leaf extract: Structure and optical properties. *Mater. Res. Bull.* **46**, 2560–2566 (2011).

160. Nasrollahzadeh, M., Sajjadi, M., Dadashi, J. & Ghafuri, H. Pd-based nanoparticles: Plant-assisted biosynthesis, characterization, mechanism, stability, catalytic and antimicrobial activities. *Adv. Colloid Interface Sci.* **276**, 102103 (2020).

161. Yang, Z., Liu, Q.-H. H. & Yang, L. The effects of addition of citric acid on the morphologies of ZnO nanorods. *Mater. Res. Bull.* **42**, 221–227 (2007).

162. Nava, O. J. *et al. Fruit peel extract mediated green synthesis of zinc oxide nanoparticles. Journal of Molecular Structure* vol. 1147 1–6 (2017).

163. Gaikwad, S. S. *et al.* Oxygen induced strained ZnO nanoparticles: An investigation of Raman scattering and visible photoluminescence. *J. Mater. Chem. C* **2**, 7264–7274 (2014).

164. Kaur, M. *et al.* Effect on the dielectric properties due to In–N co-doping in ZnO particles. *J. Mater. Sci. Mater. Electron.* **32**, 8991–9004 (2021).

165. Dresselhaus, M. S., Jorio, A., Hofmann, M., Dresselhaus, G. & Saito, R. Perspectives on carbon nanotubes and graphene Raman spectroscopy. *Nano Letters* vol. 10 751–758 at https://doi.org/10.1021/nl904286r (2010).

166. Kar, S., Dev, A. & Chaudhuri, S. Simple solvothermal route to synthesize ZnO nanosheets, nanonails, and well-aligned nanorod arrays. *J. Phys. Chem. B* **110**, 17848–17853 (2006).

167. Khan, M. F. *et al.* Sol-gel synthesis of thorn-like ZnO nanoparticles endorsing mechanical stirring effect and their antimicrobial activities: Potential role as nano-Antibiotics. *Sci. Rep.* **6**, 1–12 (2016).

168. Chai, G. L., Lin, C. S. & Cheng, W. D. First-principles study of ZnO cluster-decorated carbon nanotubes. *Nanotechnology* **22**, (2011).

169. Dakhlaoui, A., Jendoubi, M., Smiri, L. S., Kanaev, A. & Jouini, N. Synthesis, characterization and optical properties of ZnO nanoparticles with controlled size and

morphology. *J. Cryst. Growth* **311**, 3989–3996 (2009).

170. Yang, L. & Xiang, L. Influence of the mixing ways of reactants on ZnO morphology. *J. Nanomater.* **2013**, (2013).

171. Thanh, N. T. K. K., Maclean, N. & Mahiddine, S. Mechanisms of Nucleation and Growth of Nanoparticles in Solution. *Chem. Rev.* **114**, 7610–7630 (2014).

172. Herbst, M., Hofmann, E. & Förster, S. Nucleation and Growth Kinetics of ZnO Nanoparticles Studied by in Situ Microfluidic SAXS/WAXS/UV-Vis Experiments. *Langmuir* **35**, 11702–11709 (2019).

173. Shaba, E. Y., Jacob, J. O., Tijani, J. O. & Suleiman, M. A. T. A critical review of synthesis parameters affecting the properties of zinc oxide nanoparticle and its application in wastewater treatment. *Appl. Water Sci.* **11**, 48 (2021).

174. Becker, J., Raghupathi, K. R., St. Pierre, J., Zhao, D. & Koodali, R. T. Tuning of the crystallite and particle sizes of ZnO nanocrystalline materials in solvothermal synthesis and their photocatalytic activity for dye degradation. *J. Phys. Chem. C* **115**, 13844–13850 (2011).

175. Zhang, J. *et al.* Control of ZnO morphology via a simple solution route. *Chem. Mater.* **14**, 4172–4177 (2002).

176. Hezam, A. *et al.* Heterogeneous growth mechanism of ZnO nanostructures and the effects of their morphology on optical and photocatalytic properties. *CrystEngComm* **19**, 3299–3312 (2017).

177. Mclaren, A., Valdes-Solis, T., Li, G. & Tsang, S. C. Shape and Size Effects of ZnO Nanocrystals on Photocatalytic Activity. *J. Am. Chem. Soc.* **131**, 12540–12541 (2009).

178. Davis, K., Yarbrough, R., Froeschle, M., White, J. & Rathnayake, H. Band gap engineered zinc oxide nanostructures: Via a sol-gel synthesis of solvent driven shape-controlled crystal growth. *RSC Adv.* **9**, 14638–14648 (2019).

179. Liu, X. *et al.* Controllable synthesis and change of emission color from green to orange of ZnO quantum dots using different solvents. *New J. Chem.* **39**, 2881–2888 (2015).

180. Zhang, L. *et al.* Effects of different defective linkers on the photocatalytic properties of Cu-BTC for overall water decomposition. *Appl. Catal. B Environ.* **303**, 120888 (2022).

181. Mahata, M. K. *et al.* Incorporation of Zn2+ ions into BaTiO3:Er3+/Yb3+ nanophosphor: An effective way to enhance upconversion, defect luminescence and temperature sensing. *Phys. Chem. Chem. Phys.* **17**, 20741–20753 (2015).

182. Abdurahman, M. H., Abdullah, A. Z. & Shoparwe, N. F. A comprehensive review on sonocatalytic, photocatalytic, and sonophotocatalytic processes for the degradation of antibiotics in water: Synergistic mechanism and degradation pathway. *Chem. Eng. J.* **413**, 127412 (2021).

183. Sa'aedi, A., Akl, A. A. & Hassanien, A. S. Effective role of Rb doping in controlling the crystallization, crystal imperfections, and microstructural and morphological

features of ZnO-NPs synthesized by the sol-gel approach. *CrystEngComm* **24**, 4661–4678 (2022).

184. Liang, S. *et al.* Novel cone-like ZnO mesocrystals with co-exposed (1011) and (0001) facets and enhanced photocatalytic activity. *Inorg. Chem. Front.* **5**, 2257–2267 (2018).

185. Kundu, S. & Naskar, M. K. Al-Mg-Ca-Layered Double Oxides for Efficient Removal of As(V) from Water: The Role of Amides. *J. Chem. Eng. Data* **64**, 1594–1604 (2019).

186. Zhou, J. *et al.* N,N-dimethylformamide assisted facile hydrothermal synthesis of boehmite microspheres for highly effective removal of Congo red from water. *J. Colloid Interface Sci.* **583**, 128–138 (2021).

187. Gald, A., Santana, G., Güell, F., Mart, P. R. & Dutt, A. Photoluminescence of ZnO Nanowires : A Review. (2020).

188. Alvi, M. A., Al-Ghamdi, A. A. & ShaheerAkhtar, M. Synthesis of ZnO nanostructures via low temperature solution process for photocatalytic degradation of rhodamine B dye. *Mater. Lett.* **204**, 12–15 (2017).

189. Nagata, T. & Obora, Y. N, N-Dimethylformamide-Protected Single-Sized Metal Nanoparticles and Their Use as Catalysts for Organic Transformations. *ACS Omega* vol. 5 98–103 at https://doi.org/10.1021/acsomega.9b03828 (2020).

190. Wen, B., Huang, Y. & Boland, J. J. Controllable growth of ZnO nanostructures by a simple solvothermal process. *J. Phys. Chem. C* **112**, 106–111 (2008).

191. Pimentel, A. *et al.* Effect of solvents on ZnO nanostructures synthesized by solvothermal method assisted by microwave radiation: a photocatalytic study. *J. Mater. Sci.* **50**, 5777–5787 (2015).

192. Wang, M. *et al.* Nanoplate-assembled hierarchical cake-like ZnO microstructures: Solvothermal synthesis, characterization and photocatalytic properties. *RSC Adv.* **7**, 32528–32535 (2017).

193. Li, S. *et al.* Alkali and donor–acceptor bridged three-dimensional interpenetrating polymer networks boost photocatalytic performance by efficient electron delocalization and charge transfer. *Appl. Catal. B Environ.* **292**, 120153 (2021).

194. Alamro, F. S., Mostafa, A. M., Ahmed, H. A. & Toghan, A. Zinc oxide/carbon nanotubes nanocomposite: Synthesis, characterization and catalytic reduction of 4-nitrophenol via laser assistant method. *Surfaces and Interfaces* **26**, 101406 (2021).

195. Mostafa, A. M., Mwafy, E. A. & Toghan, A. ZnO nanoparticles decorated carbon nanotubes via pulsed laser ablation method for degradation of methylene blue dyes. *Colloids Surfaces A Physicochem. Eng. Asp.* **627**, 127204 (2021).

196. Park, S., Byoun, Y., Kang, H., Song, Y. J. & Choi, S. W. ZnO Nanocluster-Functionalized Single-Walled Carbon Nanotubes Synthesized by Microwave Irradiation for Highly Sensitive NO2 Detection at Room Temperature. *ACS Omega* **4**, 10677–10686 (2019).

197. Rauwel, P., Salumaa, M., Aasna, A., Galeckas, A. & Rauwel, E. A Review of the Synthesis and Photoluminescence Properties of Hybrid ZnO and Carbon Nanomaterials. *J. Nanomater.* **2016**, (2016).

198. Barazzouk, S., Hotchandani, S., Vinodgopal, K. & Kamat, P. V. Single-wall carbon nanotube films for photocurrent generation. A prompt response to visible-light irradiation. *J. Phys. Chem. B* **108**, 17015–17018 (2004).

199. Fort, A. *et al.* Highly Sensitive Detection of NO2 by Au and TiO2 Nanoparticles Decorated SWCNTs Sensors. *Sensors* **20**, 12 (2019).

200. Camilli, L. & Passacantando, M. Advances on Sensors Based on Carbon Nanotubes. *Chemosensors* **6**, 62 (2018).

201. Dresselhaus, M. S., Dresselhaus, G., Saito, R. & Jorio, A. Raman spectroscopy of carbon nanotubes. *Physics Reports* vol. 409 47–99 at https://doi.org/10.1016/j.physrep.2004.10.006 (2005).

202. Forney, M. W. & Poler, J. C. Sonochemical formation of methyl hydroperoxide in polar aprotic solvents and its effect on single-walled carbon nanotube dispersion stability. *J. Am. Chem. Soc.* **132**, 791–797 (2010).

203. Forney, M. W., Anderson, J. S., Ameen, A. L. & Poler, J. C. Aggregation Kinetics of Single-Walled Carbon Nanotubes in Nonaqueous Solvents: Critical Coagulation Concentrations and Transient Dispersion Stability. *J. Phys. Chem. C* **115**, 23267–23272 (2011).

204. Kharissova, O. V., Kharisov, B. I. & De Casas Ortiz, E. G. Dispersion of carbon nanotubes in water and non-aqueous solvents. *RSC Adv.* **3**, 24812–24852 (2013).

205. Sun, C. *et al.* Synthesis of 0D SnO2 nanoparticles/2D g-C3N4 nanosheets heterojunction: improved charge transfer and separation for visible-light photocatalytic performance. *J. Alloys Compd.* **871**, 159561 (2021).

206. Choi, M. S., Park, T., Kim, W. J. & Hur, J. High-performance ultraviolet photodetector based on a zinc oxide nanoparticle@single-walled carbon nanotube heterojunction hybrid film. *Nanomaterials* **10**, 395 (2020).

207. Schaper, N. *et al.* Controlled fabrication of quality zno nws/cnts and zno nws/gr heterostructures via direct two-step cvd method. *Nanomaterials* **11**, (2021).

208. Rao, R. *et al.* Blueshifted Raman scattering and its correlation with the [110] growth direction in gallium oxide nanowires. *J. Appl. Phys.* **98**, (2005).

209. Bakaraju, V., Prasad, E. S., Meena, B. & Chaturvedi, H. An Electronic and Optically Controlled Bifunctional Transistor Based on a Bio-Nano Hybrid Complex. *ACS Omega* **5**, 9702–9706 (2020).

210. Rao, C. N. R. & Voggu, R. Charge-transfer with graphene and nanotubes. *Mater. Today* **13**, 34–40 (2010).

211. Rao, A. M., Eklund, P. C., Bandow, S., Thess, A. & Smalley, R. E. Evidence for

charge transfer in doped carbon nanotube bundles from raman scattering. *Nature* **388**, 257–259 (1997).

212. Nguyen, V. T. *et al.* Phototransistors with Negative or Ambipolar Photoresponse Based on As-Grown Heterostructures of Single-Walled Carbon Nanotube and MoS2. *Adv. Funct. Mater.* **28**, 1–9 (2018).

213. Martel, R. *et al.* Ambipolar electrical transport in semiconducting single-wall carbon nanotubes. *Phys. Rev. Lett.* **87**, 256805-1-256805–4 (2001).

214. Calatayud, D. G. *et al.* Encapsulation of Cadmium Selenide Nanocrystals in Biocompatible Nanotubes: DFT Calculations, X-ray Diffraction Investigations, and Confocal Fluorescence Imaging. *ChemistryOpen* **7**, 144–158 (2018).

215. Nath, M., Teredesai, P. V., Muthu, D. V. S., Sood, A. K. & Rao, C. N. R. Single-walled carbon nanotube bundles intercalated with semiconductor nanoparticles. *Curr. Sci.* **85**, 956–960 (2003).

216. Kharissova, O. V., Kharisov, B. I. & Leija Gutiérrez, H. M. Functionalization of SWCNTs with amine derivatives and comparative solubilization studies. *J. Mater. Sci.* **53**, 466–478 (2018).

217. Duc Chinh, N. *et al.* pn-Heterojunction of the SWCNT/ZnO nanocomposite for temperature dependent reaction with hydrogen. *J. Colloid Interface Sci.* **584**, 582–591 (2021).

218. Park, Y. R., Liu, N. & Lee, C. J. Photoluminescence enhancement from hybrid structures of metallic single-walled carbon nanotube/ZnO films. *Curr. Appl. Phys.* **13**, 2026–2032 (2013).

219. Giordano, A. N., Chaturvedi, H. & Poler, J. C. Critical Coagulation Concentrations for Carbon Nanotubes in Nonaqueous Solvent. *J. Phys. Chem. C* **111**, 11583–11589 (2007).

220. Trefalt, G. & Borkovec, M. Overview of DLVO Theory. *Lab. Colloid Surf. Chem. Univ. Geneva* 1–10 (2014).

221. Ameen, A. A. *et al.* Aggregation kinetics of single-walled carbon nanotubes investigated using mechanically wrapped multinuclear complexes: Probing the tube-tube repulsive barrier. *Phys. Chem. Chem. Phys.* **16**, 5855–5865 (2014).

222. Ryabenko, A. G., Dorofeeva, T. V & Zvereva, G. I. UV – VIS – NIR spectroscopy study of sensitivity of single-wall carbon nanotubes to chemical processing and Van-der-Waals SWNT / SWNT interaction . Verification of the SWNT content measurements by absorption spectroscopy. **42**, 1523–1535 (2004).

223. Backes, C. & Stemmler, I. Absorption Spectroscopy as a Powerful Technique for the Characterization of Single-Walled Carbon Nanotubes. *Perkinelmer.Co.Uk* 4–9 (2013).

224. Ichida, M. *et al.* Absorption spectra of high purity metallic and semiconducting single-walled carbon nanotube thin films in a wide energy region. *Solid State Commun.* **151**, 1696–1699 (2011).

225. Krupke, R., Hennrich, F., Löhneysen, H. v. & Kappes, M. M. Separation of Metallic from Semiconducting Single-Walled Carbon Nanotubes. *Science (80-. ).* **301**, 344–347 (2003).

226. Blancon, J. C. *et al.* Direct measurement of the absolute absorption spectrum of individual semiconducting single-wall carbon nanotubes. *Nat. Commun.* **4**, 2542 (2013).

227. Liu, L., Moreno, L. & Neretnieks, I. A novel approach to determine the critical coagulation concentration of a colloidal dispersion with plate-like particles. *Langmuir* **25**, 688–697 (2009).

228. Giordano, A. N., Chaturvedi, H. & Poler, J. C. Critical coagulation concentrations for carbon nanojtubes in nonaqueous solvent. *J. Phys. Chem. C* **111**, 11583–11589 (2007).

229. Koh, B. & Cheng, W. Mechanisms of carbon nanotube aggregation and the reversion of carbon nanotube aggregates in aqueous medium. *Langmuir* **30**, 10899–10909 (2014).

230. Martines, E., Csaderova, L., Morgan, H., Curtis, A. S. G. & Riehle, M. O. DLVO interaction energy between a sphere and a nano-patterned plate. *Colloids and Surfaces A: Physicochemical and Engineering Aspects* vol. 318 45–52 at https://doi.org/10.1016/j.colsurfa.2007.11.035 (2008).

231. Hoek, E. M. V. & Agarwal, G. K. Extended DLVO interactions between spherical particles and rough surfaces. *J. Colloid Interface Sci.* **298**, 50–58 (2006).

232. Gu, Y. The electrical double-layer interaction between a spherical particle and a cylinder. *J. Colloid Interface Sci.* **231**, 199–203 (2000).

233. Pramanik, C., Gissinger, J. R., Kumar, S. & Heinz, H. Carbon Nanotube Dispersion in Solvents and Polymer Solutions: Mechanisms, Assembly, and Preferences. *ACS Nano* **11**, 12805–12816 (2017).

234. Thongam, D. D. & Chaturvedi, H. Functionalization of Pristine, Metallic, and Semiconducting-SWCNTs by ZnO for Efficient Charge Carrier Transfer: Analysis through Critical Coagulation Concentration. *ACS Omega* **7**, 14784–14796 (2022).

235. Klinger, M. More features, more tools, more CrysTBox. *J. Appl. Crystallogr.* **50**, 1226–1234 (2017).

236. Ferreira, N. S., Sasaki, J. M., Silva JR, R. S., Attah-Baah, J. M. & Macêdo, M. A. Visible-Light-Responsive Photocatalytic Activity Significantly Enhanced by Active [ V Zn + V O + ] Defects in Self-Assembled ZnO Nanoparticles. *Inorg. Chem.* **60**, 4475–4496 (2021).

237. Sharma, S. K. *et al.* Photocatalytic performance of yttrium-doped CNT-ZnO nanoflowers synthesized from hydrothermal method. *Mater. Today Chem.* **20**, 100452 (2021).

238. Hosseini, F., Kasaeian, A., Pourfayaz, F., Sheikhpour, M. & Wen, D. Novel ZnO-Ag/MWCNT nanocomposite for the photocatalytic degradation of phenol. *Mater. Sci.*

*Semicond. Process.* **83**, 175–185 (2018).

239. Buldu-Akturk, M., Toufani, M., Tufani, A. & Erdem, E. ZnO and reduced graphene oxide electrodes for all-in-one supercapacitor devices. *Nanoscale* **14**, 3269–3278 (2022).

240. Sayed, M. *et al.* EPR Investigation on Electron Transfer of 2D/3D g-C3N4/ZnO S-Scheme Heterojunction for Enhanced CO2 Photoreduction. *Adv. Sustain. Syst.* **6**, 2100264 (2022).

241. Strak, P. *et al.* Exact method of determination of the recombination mode from time resolved photoluminescence data. 1–22 (2017).

242. Erim, B., Ciğeroğlu, Z., Şahin, S. & Vasseghian, Y. Photocatalytic degradation of cefixime in aqueous solutions using functionalized SWCNT/ZnO/Fe3O4 under UV-A irradiation. *Chemosphere* **291**, 132929 (2022).

243. Ho, Y. M., Liu, J. W., Qi, J. L. & Zheng, W. T. Spectroscopic investigation on carbon nanotubes coated with ZnO nanoparticles. *J. Phys. D. Appl. Phys.* **41**, 065308 (2008).

244. Hanif, M. A. *et al.* Formation of chemical heterojunctions between ZnO nanoparticles and single-walled carbon nanotubes for synergistic enhancement of photocatalytic activity. *J. Photochem. Photobiol. A Chem.* **413**, 113260 (2021).

245. Dupin, J.-C., Gonbeau, D., Vinatier, P. & Levasseur, A. Systematic XPS studies of metal oxides, hydroxides and peroxides. *Phys. Chem. Chem. Phys.* **2**, 1319–1324 (2000).

246. Taucher, T. C., Hehn, I., Hofmann, O. T., Zharnikov, M. & Zojer, E. Understanding Chemical versus Electrostatic Shifts in X-ray Photoelectron Spectra of Organic Self-Assembled Monolayers. *J. Phys. Chem. C* **120**, 3428–3437 (2016).

247. Khanderi, J., Hoffmann, R. C., Gurlo, A. & Schneider, J. J. Synthesis and sensoric response of ZnO decorated carbon nanotubes. *J. Mater. Chem.* **19**, 5039–5046 (2009).

248. Abdullah, E. A. Band edge positions as a key parameter to a systematic design of heterogeneous photocatalyst. *Eur. J. Chem.* **10**, 82–94 (2019).

249. Mousavi, M., Habibi-Yangjeh, A. & Abitorabi, M. Fabrication of novel magnetically separable nanocomposites using graphitic carbon nitride, silver phosphate and silver chloride and their applications in photocatalytic removal of different pollutants using visible-light irradiation. *J. Colloid Interface Sci.* **480**, 218–231 (2016).

250. Thongam, D. D. & Chaturvedi, H. Advances in nanomaterials for heterogeneous photocatalysis. *Nano Express* **2**, 012005 (2021).

251. Bagheri, M., Najafabadi, N. R. & Borna, E. Removal of reactive blue 203 dye photocatalytic using ZnO nanoparticles stabilized on functionalized MWCNTs. *J. King Saud Univ. - Sci.* **32**, 799–804 (2020).

252. Liu, H., Wang, C. & Wang, G. Photocatalytic Advanced Oxidation Processes for Water Treatment: Recent Advances and Perspective. *Chem. – An Asian J.* **15**, 3239–

3253 (2020).

253. Akerdi, A. G. & Bahrami, S. H. Application of heterogeneous nano-semiconductors for photocatalytic advanced oxidation of organic compounds: A review. *Journal of Environmental Chemical Engineering* vol. 7 103283 at https://doi.org/10.1016/j.jece.2019.103283 (2019).

254. Bhuvaneswari, K., Palanisamy, G., Sivashanmugan, K., Pazhanivel, T. & Maiyalagan, T. ZnO nanoparticles decorated multiwall carbon nanotube assisted ZnMgAl layered triple hydroxide hybrid photocatalyst for visible light-driven organic pollutants removal. *J. Environ. Chem. Eng.* **9**, 104909 (2021).

255. Schneider, J. T., Firak, D. S., Ribeiro, R. R. & Peralta-Zamora, P. Use of scavenger agents in heterogeneous photocatalysis: truths, half-truths, and misinterpretations. *Phys. Chem. Chem. Phys.* **22**, 15723–15733 (2020).

256. Wang, B. *et al.* Synthesis of Spherical Bi 2 WO 6 Nanoparticles by a Hydrothermal Route and Their Photocatalytic Properties. *J. Nanomater.* **2015**, 1–7 (2015).

257. Sun, W. *et al.* Insight into the Transfer Mechanisms of Photogenerated Carriers for Heterojunction Photocatalysts with the Analogous Positions of Valence Band and Conduction Band: A Case Study of ZnO/TiO2. *J. Phys. Chem. C* **122**, 15409–15420 (2018).

258. Vasilaki, E., Vamvakaki, M. & Katsarakis, N. Complex ZnO-TiO2 Core-Shell Flower-Like Architectures with Enhanced Photocatalytic Performance and Superhydrophilicity without UV Irradiation. *Langmuir* **34**, 9122–9132 (2018).

259. Boyadjiev, S. I. *et al.* TiO 2 /ZnO and ZnO/TiO 2 core/shell nanofibers prepared by electrospinning and atomic layer deposition for photocatalysis and gas sensing. *Appl. Surf. Sci.* **424**, 190–197 (2017).

260. Kandy, M. M. Carbon-based photocatalysts for enhanced photocatalytic reduction of CO2 to solar fuels. *Sustain. Energy Fuels* **4**, 469–484 (2020).

261. Ge, J., Zhang, Y. & Park, S.-J. Recent Advances in Carbonaceous Photocatalysts with Enhanced Photocatalytic Performances: A Mini Review. *Materials (Basel).* **12**, 1916 (2019).

262. Azami, M., Haghighi, M. & Allahyari, S. Sono-precipitation of Ag2CrO4-C composite enhanced by carbon-based materials (AC, GO, CNT and C3N4) and its activity in photocatalytic degradation of acid orange 7 in water. *Ultrason. Sonochem.* **40**, 505–516 (2018).

263. Rajput, Y., Kumar, P., Zhang, T. C., Kumar, D. & Nemiwal, M. Recent advances in g-C3N4-based photocatalysts for hydrogen evolution reactions. *Int. J. Hydrogen Energy* **47**, 38533–38555 (2022).

264. Dong, G., Zhang, Y., Pan, Q. & Qiu, J. A fantastic graphitic carbon nitride (g-C3N4) material: Electronic structure, photocatalytic and photoelectronic properties. *J. Photochem. Photobiol. C Photochem. Rev.* **20**, 33–50 (2014).

265. Singh, P. P. & Srivastava, V. Recent advances in visible-light graphitic carbon nitride (g-C3N4) photocatalysts for chemical transformations. *RSC Adv.* **12**, 18245–18265 (2022).

266. Naseri, A., Samadi, M., Pourjavadi, A., Moshfegh, A. Z. & Ramakrishna, S. Graphitic carbon nitride (g-C3N4)-based photocatalysts for solar hydrogen generation: Recent advances and future development directions. *J. Mater. Chem. A* **5**, 23406–23433 (2017).

267. Kong, J.-Z. *et al.* Visible Light-Driven Photocatalytic Performance of N-Doped ZnO/g-C3N4 Nanocomposites. *Nanoscale Res. Lett.* **12**, 526 (2017).

268. Uma, R., Ravichandran, K., Sriram, S. & Sakthivel, B. Cost-effective fabrication of ZnO/g-C 3 N 4 composite thin films for enhanced photocatalytic activity against three different dyes (MB, MG and RhB). *Mater. Chem. Phys.* **201**, 147–155 (2017).

269. Fan, M. *et al.* Visible-light-drived high photocatalytic activities of Cu/g-C3N4 photocatalysts for hydrogen production. *RSC Adv.* **6**, 34633–34640 (2016).

270. Yang, X. *et al.* Facile synthesis of nitrogen-defective g-C3N4for superior photocatalytic degradation of rhodamine B. *RSC Adv.* **11**, 30503–30509 (2021).

271. Inagaki, M., Tsumura, T., Kinumoto, T. & Toyoda, M. Graphitic carbon nitrides (g-C3N4) with comparative discussion to carbon materials. *Carbon N. Y.* **141**, 580–607 (2019).

272. Ong, W. J., Tan, L. L., Ng, Y. H., Yong, S. T. & Chai, S. P. Graphitic Carbon Nitride (g-C3N4)-Based Photocatalysts for Artificial Photosynthesis and Environmental Remediation: Are We a Step Closer to Achieving Sustainability? *Chem. Rev.* **116**, 7159–7329 (2016).

273. Yuan, Y. *et al.* High-yield synthesis and optical properties of g-C 3 N 4. *Nanoscale* **7**, 12343–12350 (2015).

274. Liang, J. *et al.* A review on g-C3N4incorporated with organics for enhanced photocatalytic water splitting. *J. Mater. Chem. A* **9**, 12898–12922 (2021).

275. Kang, S. *et al.* Harmonious K-I-O co-modification of g-C3N4for improved charge separation and photocatalysis. *Inorg. Chem. Front.* **9**, 950–958 (2022).

276. Yu, X. *et al.* Point-Defect Engineering: Leveraging Imperfections in Graphitic Carbon Nitride (g-C 3 N 4 ) Photocatalysts toward Artificial Photosynthesis. *Small* **17**, 2006851 (2021).

277. Thang, N. Q. *et al.* High-efficient photocatalytic degradation of commercial drugs for pharmaceutical wastewater treatment prospects: A case study of Ag/g-C3N4/ZnO nanocomposite materials. *Chemosphere* **282**, 130971 (2021).

278. Lam, S.-M. M., Sin, J.-C. C. & Mohamed, A. R. A review on photocatalytic application of g-C3N4/semiconductor (CNS) nanocomposites towards the erasure of dyeing wastewater. *Mater. Sci. Semicond. Process.* **47**, 62–84 (2016).

279. Alaghmandfard, A. & Ghandi, K. A Comprehensive Review of Graphitic Carbon Nitride (g-C3N4)–Metal Oxide-Based Nanocomposites: Potential for Photocatalysis and Sensing. *Nanomaterials* **12**, (2022).

280. Su, Y. *et al.* Decoration of TiO2/g-C3N4 Z-scheme by carbon dots as a novel photocatalyst with improved visible-light photocatalytic performance for the degradation of enrofloxacin. *RSC Adv.* **7**, 34096–34103 (2017).

281. Nie, N., Zhang, L., Fu, J., Cheng, B. & Yu, J. Self-assembled hierarchical direct Z-scheme g-C3N4/ZnO microspheres with enhanced photocatalytic CO2 reduction performance. *Appl. Surf. Sci.* **441**, 12–22 (2018).

282. Jo, W. K., Adinaveen, T., Vijaya, J. J. & Sagaya Selvam, N. C. Synthesis of MoS2 nanosheet supported Z-scheme TiO2/g-C3N4 photocatalysts for the enhanced photocatalytic degradation of organic water pollutants. *RSC Adv.* **6**, 10487–10497 (2016).

283. Pham, V. Van *et al.* S-Scheme α-Fe2O3/g-C3N4Nanocomposites as Heterojunction Photocatalysts for Antibiotic Degradation. *ACS Appl. Nano Mater.* **5**, 4506–4514 (2022).

284. Paul, D. R. *et al.* ZnO-Modified g-C 3 N 4 : A Potential Photocatalyst for Environmental Application. *ACS Omega* **5**, 3828–3838 (2020).

285. Li, J. *et al.* In situ fabrication of a novel CdS/ZnIn 2 S 4 /g-C 3 N 4 ternary heterojunction with enhanced visible-light photocatalytic performance . *RSC Adv.* **12**, 32480–32487 (2022).

286. Krishnan, P. *et al.* Characterization of photocatalytic TiO2 powder under varied environments using near ambient pressure X-ray photoelectron spectroscopy. *Sci. Rep.* **7**, 1–11 (2017).

287. Karunakaran, C., Vinayagamoorthy, P. & Jayabharathi, J. Nonquenching of Charge Carriers by Fe 3 O 4 Core in Fe 3 O 4 /ZnO Nanosheet Photocatalyst. *Langmuir* 15031−15039 (2014) doi:dx.doi.org/10.1021/la5039409.

288. Cheng, C. *et al.* Enhanced photocatalytic performance of TiO2-ZnO hybrid nanostructures. *Sci. Rep.* **4**, 1–5 (2014).

289. Pham, H. L. *et al.* Rational design of magnetically separable core/shell Fe3O4/ZnO heterostructures for enhanced visible-light photodegradation performance. *RSC Adv.* **11**, 22317–22326 (2021).

290. López, Y. C., Acevedo-Peña, P., Ortega, G. A. & Reguera, E. Unraveling the Fe3O4 NPs role in self-assembled magnetic zinc oxide nanorods for methylene blue photodegradation. *J. Photochem. Photobiol. A Chem.* **421**, 113514 (2021).

291. Elshypany, R. *et al.* Elaboration of Fe3O4/ZnO nanocomposite with highly performance photocatalytic activity for degradation methylene blue under visible light irradiation. *Environ. Technol. Innov.* **23**, 101710 (2021).

292. Długosz, O., Szostak, K., Krupiński, M. & Banach, M. Synthesis of Fe3O4/ZnO

nanoparticles and their application for the photodegradation of anionic and cationic dyes. *Int. J. Environ. Sci. Technol.* **18**, 561–574 (2021).

293. Hasan, I., Shekhar, C., Bin Sharfan, I. I., Khan, R. A. & Alsalme, A. Ecofriendly Green Synthesis of the ZnO-Doped CuO@Alg Bionanocomposite for Efficient Oxidative Degradation of p-Nitrophenol. *ACS Omega* **5**, 32011–32022 (2020).

294. Yaghoubi, H. *et al.* Toward a Visible Light-Driven Photocatalyst: The Effect of Midgap-States-Induced Energy Gap of Undoped TiO 2 Nanoparticles. *ACS Catal.* **5**, 327–335 (2015).

295. Pham, H. L. *et al.* Novel 3D hierarchical nanostructure of Fe3O4/ZnO hybrid composites for enhanced solar light photocatalytic performance. *J. Mater. Sci. Mater. Electron.* **32**, 25018–25032 (2021).

296. Wang, Y. *et al.* Facile Synthesis of Self-Assembled g-C3N4 with Abundant Nitrogen Defects for Photocatalytic Hydrogen Evolution. *ACS Sustain. Chem. Eng.* **6**, 10200–10210 (2018).

297. Kobkeatthawin, T. *et al.* Photocatalytic Activity of TiO2/g-C3N4 Nanocomposites for Removal of Monochlorophenols from Water. *Nanomaterials* **12**, 2852 (2022).

298. Papailias, I. *et al.* Effect of processing temperature on structure and photocatalytic properties of g-C 3 N 4. *Appl. Surf. Sci.* **358**, 278–286 (2015).

299. Maślana, K., Kaleńczuk, R. J., Zielińska, B. & Mijowska, E. Synthesis and Characterization of Nitrogen-doped Carbon Nanotubes Derived from g-C3N4. *Materials (Basel).* **13**, 1349 (2020).

300. Singh, P., Kumar, R. & Singh, R. K. Progress on Transition Metal-Doped ZnO Nanoparticles and Its Application. *Ind. Eng. Chem. Res.* **58**, 17130–17163 (2019).

301. Wu, Z., Chen, X., Liu, X., Yang, X. & Yang, Y. A Ternary Magnetic Recyclable ZnO/Fe3O4/g-C3N4 Composite Photocatalyst for Efficient Photodegradation of Monoazo Dye. *Nanoscale Res. Lett.* **14**, (2019).

302. Mishra, D. K. *et al.* Carbon doped ZnO: Synthesis, characterization and interpretation. *J. Magn. Magn. Mater.* **329**, 146–152 (2013).

303. Zhu, Y. P., Li, M., Liu, Y. L., Ren, T. Z. & Yuan, Z. Y. Carbon-Doped ZnO hybridized homogeneously with graphitic carbon nitride nanocomposites for photocatalysis. *J. Phys. Chem. C* **118**, 10963–10971 (2014).

304. Vattikuti, S. V. P., Reddy, P. A. K., Shim, J. & Byon, C. Visible-Light-Driven Photocatalytic Activity of SnO 2 –ZnO Quantum Dots Anchored on g-C 3 N 4 Nanosheets for Photocatalytic Pollutant Degradation and H 2 Production. *ACS Omega* **3**, 7587–7602 (2018).

305. Papailias, I. *et al.* Novel torus shaped g-C3N4 photocatalysts. *Appl. Catal. B Environ.* **268**, 118733 (2020).

306. Li, X. *et al.* Synergistic effect of efficient adsorption g-C3N4/ZnO composite for

photocatalytic property. *J. Phys. Chem. Solids* **75**, 441–446 (2014).

307. Safaei, J. *et al.* Graphitic carbon nitride (g-C3N4) electrodes for energy conversion and storage: A review on photoelectrochemical water splitting, solar cells and supercapacitors. *J. Mater. Chem. A* **6**, 22346–22380 (2018).

308. Thongam, D. D. & Chaturvedi, H. Induced defect and ZnO nano-flower formation by N, N, dimethylformamide solvent for natural sunlight responsive floating photocatalytic advanced oxidation process. *Chemosphere* **313**, 137600 (2023).

309. Vital-Grappin, A. D. *et al.* The role of the reactive species involved in the photocatalytic degradation of hdpe microplastics using c,n-tio2 powders. *Polymers (Basel).* **13**, 1–18 (2021).

310. de Jesus Martins, N. *et al.* Facile preparation of ZnO:g-C3N4 heterostructures and their application in amiloride photodegradation and CO2 photoreduction. *J. Alloys Compd.* **856**, (2021).

311. Chen, K. *et al.* Electronic structure of heterojunction MoO2/g-C3N4 catalyst for oxidative desulfurization. *Appl. Catal. B Environ.* **238**, 263–273 (2018).

312. Wang, R. *et al.* Nanoscale 2D g-C3N4 decorating 3D hierarchical architecture LDH for artificial photosynthesis and mechanism insight. *Chem. Eng. J.* **448**, 137338 (2022).

313. Kim, D. & Yong, K. Boron doping induced charge transfer switching of a C3N4/ZnO photocatalyst from Z-scheme to type II to enhance photocatalytic hydrogen production. *Appl. Catal. B Environ.* **282**, 119538 (2021).